

ABSTRACT

Title of Document: Thermal and Hydraulic Performance of Heat Exchangers for Low Temperature Lift Heat Pump Systems

Hoseong Lee, Doctor of Philosophy, 2012

Directed By: Professor Reinhard Radermacher,
Department of Mechanical Engineering

The work presented in this dissertation focused on investigating and understanding the hydraulic and thermal design space and tradeoffs for low temperature difference high performance heat exchangers for a low temperature lift heat pump (LTLHP) system, which benefits from a small difference between the condensing and evaporating temperatures of a working fluid. The heat exchangers for the LTLHP application require a larger heat transfer area, a higher volume flow rate, and a higher temperature of heat source fluid, as compared to the typical high temperature lift heat pump system. Therefore, heat exchanger research is critical, and it needs to be balanced between the heat transfer and pressure drop performance of both fluids in the heat exchanger. A plate heat exchanger (PHX) was selected to establish a baseline of a low temperature lift heat exchanger and was investigated experimentally and numerically. The traditional PHX is designed to have the identical surface area and enhancements on both fluid sides for ease of production. However, fluid side heat transfer coefficients and heat transfer capacities can be drastically different, for example, single-phase water versus two-phase refrigerant. Moreover, the PHX needs to have a large cross sectional

flow area in order to reduce the heat-source fluid-side pressure drop. In the experimental test, the PHX showed a relatively low overall heat transfer performance and a large pressure drop of the heat source fluid side under LTLHP operating conditions. The CFD simulation was carried out to further improve the potential of the PHX performance. However, there were limitations in the PHX. It was concluded that the PHX was restricted by two main factors: one was a large pressure drop on the heat source fluid-side due to corrugated shape, and the other was low overall heat transfer performance due to the low refrigerant-side mass flux and resulting low heat transfer performance. A concept of a novel low temperature lift heat exchanger (LTLHX) has been developed based on the lessons learned from the PHX performance investigation for the application to the LTLHP. Geometries were newly defined such as a channel width, channel height, channel pitch, and plate flow gap. Two design strategies were applied to the novel heat exchanger development: the flow area ratio was regulated, and plates were offset. The design parameters of the novel heat exchanger were optimized with multi scale approaches. After developing the laboratory heat exchanger test facility and the prototype of the novel LTLHX, its performance was experimentally measured. Then the thermal and hydraulic performance of the novel LTLHX was validated with experimental data. The heat transfer coefficient correlations and the pressure drop correlations of both the water-side and refrigerant-side were newly developed for the novel LTLHX. The overall heat transfer performance of the novel LTLHX was more than doubled as compared to that of the PHX. Moreover, the pressure drop of the novel heat exchanger was drastically lower than that of the PHX. Lastly, the novel heat exchangers were applied to a water source heat pump system, and its performance was investigated with parametric studies.

Thermal and Hydraulic Performance of Heat Exchangers for Low Temperature Lift Heat Pump Systems

By

Hoseong Lee

Dissertation submitted to the Faculty of the Graduate School of the
University of Maryland, College Park, in partial fulfillment
of the requirements for the degree of
Doctor of Philosophy
2012

Advisory Committee:

Professor Reinhard Radermacher (Chair)

Professor Marino di Marzo

Associate Professor Bao Yang

Research Associate Professor Yunho Hwang

Associate Professor Kenneth Yu, Dean's representative

© Copyright by
Hoseong Lee
2012

Dedication

*to my wife, Juhee
with my love and respect*

Acknowledgement

First of all, I would like to thank my advisor, Dr. Reinhard Radermacher, for giving me the opportunity to conduct research at the Center for Environmental Energy Engineering (CEEE). Dr. Radermacher provided me with continuing support, advice and guidance. His guidance always balanced me between academic and professional work, and his leadership has been very inspiring. I would also like to thank the committee members, Dr. Kenneth Yu, Dr. Bao Yang, and Dr. Marino di Marzo for their advice, time and effort.

I would like to thank Dr. Yunho Hwang for his grateful consideration. His guidance and advice made this dissertation more valuable to the engineering and scientific community. Without his effort, this work would not have been possible. I would like to extend my gratitude to Jan Muehlbauer provided me great support regarding my experimental testing. In addition, his amazing ideas and solutions were very impressive.

I would like to thank every colleague in CEEE, especially Kyle Gluesenkamp, Magnus Eisele, Xing Xu, Daniel Leighton, and Jiazhen Ling who have been working with me since I joined the CEEE. They provided an enjoyable work environment. Moreover, they provided an intellectual atmosphere to discuss academic problems as well as global issues. I also would like to offer a special note of thanks for Song Li who has been conducting the project with me. He has shown very impressive diligence and trust to me.

Lastly, I would like to deeply thank my parents who love and trust me as ever. Without their endless love and toughing dedication, I cannot be here today. I also would

like to express my appreciation to my wife, Juhee who supported and trusted me as always. Her continuous love and sacrifice enable me to focus on the study. I am also grateful to my lovely sons, Junseo and Junu.

Table of Contents

CHAPTER 1.	Introduction	1
1.1	Low temperature lift heat pump.....	1
1.2	Literature review	6
1.2.1	Low temperature lift heat exchanger	6
1.2.2	Single-phase heat transfer and pressure drop in plate heat exchanger.....	9
1.2.3	Two-phase heat transfer and pressure drop in plate heat exchanger	13
1.2.4	In-tube flow boiling heat transfer	15
1.2.5	In-tube flow boiling pressure drop.....	30
1.2.6	CFD simulation for heat exchangers.....	32
1.2.7	Heat exchanger design optimization.....	35
1.3	Objective	38
1.4	Dissertation organization.....	39
CHAPTER 2.	Research Approach.....	41
2.1	Experimental setup.....	41
2.1.1	Test facility	41
2.1.2	Instrumentation and DAQ system.....	42
2.1.3	Energy balance.....	43
2.1.4	Uncertainty analysis.....	43
2.1.5	Data reduction.....	46
2.2	CFD simulation	47
2.2.1	CFD simulation for heat exchanger	47
2.2.2	PHX simulation.....	50
2.2.3	LTLHX simulation.....	55
2.3	Optimization.....	60
CHAPTER 3.	Baseline Test with Plate Heat Exchanger.....	63
3.1	Experimental test with water-to-water	63
3.1.1	Test conditions and test matrix	63
3.1.2	Test procedure.....	64
3.1.3	Test results of water-side heat transfer coefficient	65
3.1.4	Test results of water-side pressure drop.....	67
3.2	Experimental test results with R22	68
3.2.1	Test conditions and test matrix	68
3.2.2	Variation of water MFR with fixed water outlet temperature	69
3.2.3	Variation of water MFR with fixed water inlet temperature	73
3.2.4	Effect of the heat flux on the refrigerant-side heat transfer	75
3.2.5	Effect of refrigerant property	77
3.3	Experimental test results with ammonia	80
3.3.1	Test conditions and test matrix	80
3.3.2	Variation of water mass flow rate.....	81
3.3.3	Variation of refrigerant mass flow rate.....	85
3.3.4	Discussion.....	86
3.4	PHX performance comparison between R22 and ammonia	87

3.4.1	Comparison between R22 and ammonia for the PHX.....	87
3.4.2	Comparison with fixed heat transfer capacity	89
3.5	CFD simulation results.....	92
3.5.1	Contours of the PHX properties.....	92
3.5.2	Effect of LMTD on HTC and pressure drop.....	93
3.5.3	Effect of the turbulent models on the HX performance.....	94
3.5.4	Comparison between turbulent and laminar flow models	96
3.5.5	Comparison between CFD simulation and experimental results	98
3.5.6	Discussion	100
3.6	Conclusions of the chapter 3	102
CHAPTER 4.	Novel Low Temperature Lift Heat Exchanger	105
4.1	Introduction	105
4.2	Development of novel heat exchanger concept.....	105
4.3	Optimization of novel LTLHX	108
4.3.1	Overview of OAAO.....	108
4.3.2	DOE and meta-model building	109
4.3.3	The verification of meta-models.....	110
4.3.4	Pareto solutions and verifications	113
4.3.5	Conclusions for optimization.....	116
4.4	CFD simulation results.....	117
4.4.1	Contours of the LTLHX properties.....	117
4.4.2	Effect of LMTD on HTC and pressure drop.....	120
4.4.3	Prediction of novel LTLHX performance.....	121
4.5	Experimental test with water to water.....	123
4.5.1	Test conditions and matrix.....	123
4.5.2	Test results of water-side heat transfer coefficient	124
4.5.3	Test results of water-side pressure drop.....	125
4.5.4	Comparison between CFD simulation and experimental results	126
4.6	Experimental test results with R22	128
4.6.1	Test conditions and test matrix	128
4.6.2	Data reduction.....	128
4.6.3	Variation of water-side Reynolds number	129
4.6.4	Variation of R22 liquid Reynolds number.....	132
4.6.5	Variation of evaporation pressure.....	136
4.6.6	Performance comparison between PHX and novel LTLHX with R22.....	140
4.7	Experimental test results with ammonia	144
4.7.1	Test conditions and test matrix	144
4.7.2	Variation of water-side Reynolds number	144
4.7.3	Variation of ammonia liquid Reynolds number.....	146
4.7.4	Variation of evaporation pressure.....	148
4.7.5	Performance comparison between PHX and novel LTLHX with ammonia	149
4.8	Flow boiling heat transfer and pressure drop of novel LTLHX.....	152
4.9	Conclusions of the chapter 4	157
CHAPTER 5.	Water Source Pump System	159

5.1	Introduction	159
5.2	Cycle simulation of WSHP	159
5.2.1	Modeling approach	159
5.2.2	Modeling results.....	162
5.2.3	Parametric study with temperature difference	165
5.3	Cycle options for the WSHP	170
5.3.1	Modeling approach	170
5.3.2	Modeling results.....	172
5.4	Heat exchanger design	174
5.4.1	PHX design	176
5.4.2	Novel LTLHX design	178
5.4.3	Guideline of novel heat exchanger design for the LTLHP application	179
5.5	Conclusions of the chapter 5	180
CHAPTER 6.	Summary and Conclusions	183
CHAPTER 7.	List of Major Contributions and Future Work.....	187
7.1	List of major contributions	187
7.2	List of related publications	188
7.3	Future work	189
Appendix A.	Uncertainty Analysis	192
Appendix B.	Reproducibility experiments	195
Reference	197

List of Tables

Table 1.1: Summary of the PHX research	7
Table 1.2: Summary of distinguishing features of each correlation	12
Table 1.3: Summary of boiling heat transfer database for minichannels	28
Table 1.4: Comparison of the heat transfer correlations against the database	29
Table 1.5: Summary of CFD research for the heat exchanger	32
Table 1.6: Turbulent model in Fluent	34
Table 1.7: Guideline for the y^+ values.....	35
Table 1.8: Summary of heat exchanger optimization research with AAO technique	37
Table 2.1: Measurement instruments	42
Table 2.2: Typical propagation of uncertainty.....	45
Table 2.3: Test matrix of CFD simulation	54
Table 2.4: Parameters of novel LTLHX	56
Table 2.5: Parameter matrix of CFD simulation.....	59
Table 3.1: Test matrix of water-to-water test.....	64
Table 3.2: Test matrix of PHX with R22.....	69
Table 3.3: Test matrix of PHX with ammonia.....	80
Table 3.4: Comparison between ammonia and R22	90
Table 4.1. Normalized boundary conditions for design variables	109
Table 4.2: Validation of different meta-model building methods	111
Table 4.3: Optimum designs selected from Pareto solution set.....	115
Table 4.4: CFD simulation results (water-side).....	121
Table 4.5: Test matrix of water-to-water test.....	123
Table 4.6: Test matrix of novel heat exchanger.....	128
Table 4.7: Geometrical comparison between PHX and novel LTLHX.....	140
Table 4.8: Test matrix of novel heat exchanger.....	144
Table 5.1: Summary of design condition	161
Table 5.2: Simulation results of the PHX design with R22.....	177
Table 5.3: Simulation results of the PHX design with ammonia.....	177
Table 5.4: Simulation results of the novel LTLHX design with ammonia.....	178

List of Figures

Fig. 1.1: Typical heat pump VCC	2
Fig. 1.2: T-s diagram of heat pump VCC	2
Fig. 1.3: T-s diagram of heat pump VCC for Case 3	5
Fig. 1.4: Plate heat exchanger	8
Fig. 1.5: Flow principle of a plate heat exchanger (Courtesy of Alfa Laval)	9
Fig. 1.6: Parameters of plate (Ayub, Zahid H., 2003)	9
Fig. 2.1: Schematic of test facility	41
Fig. 2.2: Screenshot of Labview control program	43
Fig. 2.3: Flow chart of CFD simulation	48
Fig. 2.4: Parameters of plate heat exchanger	51
Fig. 2.5: Calculation domain for CFD simulation	53
Fig. 2.6: Computational grid system.....	53
Fig. 2.7: Variation of wall y^+ with position	55
Fig. 2.8: Water flow computational domain of initial design between horizontal ammonia channels.....	57
Fig. 2.9: Water flow computational domain of initial design between vertical ammonia channels.....	57
Fig. 2.10: Water flow computational domain of current prototype between horizontal ammonia channels.....	58
Fig. 2.11: Water flow computational domain of current prototype between vertical ammonia channels.....	58
Fig. 2.12: Variation of wall y^+ with position.....	60
Fig. 2.13: Flow chart of the optimization of novel heat exchanger	62
Fig. 3.1: Schematic of the water-to-water test facility.....	64
Fig. 3.2: Original Wilson Plot.....	66
Fig. 3.3: Modified Wilson plot for calibration of water-side heat transfer coefficient (X and Y are defined in Eqs. (3.3) and (3.4), respectively)	67
Fig. 3.4: Variation of pressure drop per length with Reynolds number	68
Fig. 3.5: Variation of capacity and LMTD with Reynolds number of water-side.....	70
Fig. 3.6: Variation of heat transfer coefficients with Reynolds number of water-side.....	71
Fig. 3.7: Experimental data with criterion of Thonon et al. (1995)	72
Fig. 3.8: Temperature profile with low and high water Reynolds numbers	73
Fig. 3.9: Variation of heat transfer coefficients with Reynolds number of water-side.....	74
Fig. 3.10: Variation of temperature profiles with different water Reynolds numbers.....	75
Fig. 3.11: Effect of heat flux on boiling heat transfer coefficient with water Reynolds number	77
Fig. 3.12: Variation of heat transfer coefficients with R22 flow rate	78
Fig. 3.13: Variation of heat transfer coefficients with evaporation temperature	80
Fig. 3.14: Variation of capacity and LMTD with water-side Reynolds number	81
Fig. 3.15: Variation of subcooling and superheating with water-side Reynolds number.	82
Fig. 3.16: Variation of temperatures with water-side Reynolds number	82
Fig. 3.17: Variation of heat transfer coefficients with water flow rate.....	84
Fig. 3.18: Experimental data of boiling number with criterion of Thonon et al. (1995) ..	84

Fig. 3.19: Refrigerant and water temperature profiles with low and high water Reynolds numbers for fixed water outlet temperature.....	85
Fig. 3.20: Variation of the capacity and LMTD with ammonia mass flux.....	86
Fig. 3.21: Variation of the heat transfer coefficient with ammonia mass flux.....	86
Fig. 3.22: Variation of capacity with water-side Reynolds number.....	88
Fig. 3.23: Variation of U value with water-side Reynolds number.....	88
Fig. 3.24: Variation of refrigerant-side HTC with water Reynolds number.....	89
Fig. 3.25: Contours of (a) static temperature of the plate.....	92
Fig. 3.26: Velocity vectors by velocity magnitude (unit: m/s).....	93
Fig. 3.27: Variation of HTC and pressure drop per length with LMTD.....	94
Fig. 3.28: Variation of HTC with Reynolds number and different turbulence models....	95
Fig. 3.29: Variation of pressure drop per length with Reynolds number.....	95
Fig. 3.30: Variation of Nusselt number with Reynolds number and different turbulence models.....	97
Fig. 3.31: Variation of pressure drop per length with Reynolds number.....	97
Fig. 3.32: Variation of heat transfer coefficient with water Reynolds number.....	99
Fig. 3.33: Variation of friction factor with water Reynolds number.....	100
Fig. 3.34: Computational domain of the wide gap PHX.....	101
Fig. 4.1: Schematic of novel heat exchanger.....	106
Fig. 4.2: Schematic of a single plate of novel LTLHX.....	107
Fig. 4.3: Side cut view of novel LTLHX.....	108
Fig. 4.4: Geometrical parameters distribution in DOE points [gap between the plates (x1), channel height (x2), channel width (x3), and summit width (x4)].....	110
Fig. 4.5: HTC deviation between meta-model prediction and CFD simulation result ...	112
Fig. 4.6: P/L deviation between meta-model prediction and CFD simulation result.....	113
Fig. 4.7: Variation of water-side HTC with pump power per unit length.....	114
Fig. 4.8: Contours of static temperature of water flow in LTLHX.....	117
Fig. 4.9: Contours of static temperature of wall in LTLHX.....	118
Fig. 4.10: Contours of absolute pressure of water flow in LTLHX.....	119
Fig. 4.11: Velocity vectors colored by velocity magnitude of water flow in LTLHX ...	119
Fig. 4.12: Velocity vectors colored by velocity magnitude of water flow in LTLHX (Enlarged figure from Fig. 4.12).....	120
Fig. 4.13: Variation of HTC and pressure drop per length with LMTD.....	121
Fig. 4.14: Variation of DP/L with water velocity and plate gap.....	122
Fig. 4.15: Variation of water-side HTC with water velocity and plate gap.....	123
Fig. 4.16: Wilson Plot of novel heat exchanger.....	125
Fig. 4.17: Variation of the friction factor with water-side Reynolds number.....	126
Fig. 4.18: Nusselt number comparison between CFD simulation and experimental results.....	127
Fig. 4.19: Friction factor comparison between CFD simulation and experimental results.....	127
Fig. 4.20: Variation of capacity and LMTD with water-side Reynolds number.....	130
Fig. 4.21: Variation of U values with water-side Reynolds number.....	130
Fig. 4.22: Variation of heat transfer coefficients with water-side Reynolds number.....	131
Fig. 4.23: Experimental data of boiling number with criterion of Thonon et al.....	132

Fig. 4.24: Variation of capacity and LMTD with Reynolds number of liquid refrigerant	133
Fig. 4.25: Variation of evaporation temperature with Reynolds number of liquid refrigerant.....	133
Fig. 4.26: Variation of U values with Reynolds number of liquid refrigerant.....	134
Fig. 4.27: Variation of heat transfer coefficients with Reynolds number of liquid refrigerant.....	135
Fig. 4.28: Variation of convective number and reduced pressure with Reynolds number of liquid refrigerant	135
Fig. 4.29: Variation of degrees of capacity and LMTD with evaporation pressure	136
Fig. 4.30: Variation of U values with evaporation pressure	137
Fig. 4.31: Variation of heat transfer coefficients with evaporation pressure.....	138
Fig. 4.32: Variation of convection number and reduced pressure with evaporation pressure	139
Fig. 4.33: Variation of degrees of superheating and subcooling with evaporation pressure	139
Fig. 4.34: Comparison of U values	141
Fig. 4.35: Comparison of DP/L.....	142
Fig. 4.36: Comparison of water-side heat transfer coefficient.....	143
Fig. 4.37: Comparison of the refrigerant-side heat transfer coefficient.....	143
Fig. 4.38: Variation of capacity and LMTD with Water-side Reynolds number	145
Fig. 4.39: Variation of U value with Water-side Reynolds number	145
Fig. 4.40: Variation of heat transfer coefficient with Water-side Reynolds number.....	146
Fig. 4.41: Variation of capacity and LMTD with ammonia liquid Reynolds number....	147
Fig. 4.42: Variation of U value with ammonia liquid Reynolds number	147
Fig. 4.43: Variation of heat transfer coefficient with ammonia liquid Reynolds number	148
Fig. 4.44: Variation of heat transfer coefficient with evaporation pressure	149
Fig. 4.45: Comparison of U value.....	150
Fig. 4.46: Comparison of DP/L.....	151
Fig. 4.47: Comparison of heat transfer coefficient	152
Fig. 4.48: Variation of boiling heat transfer coefficient with liquid refrigerant Reynolds number	153
Fig. 4.49: <i>HTC</i> comparison between correlation results and experimental data with ammonia and R22	154
Fig. 4.50: Variation of pressure drop with liquid refrigerant Reynolds number	155
Fig. 4.51: <i>DP</i> comparison between correlation results and experimental data.....	156
Fig. 5.1: Schematic diagram of ASHP.....	160
Fig. 5.2: Schematic diagram of WSHP	160
Fig. 5.3: Temperature of air and ground-water from 1/1/2010 to 2/28/2010	162
Fig. 5.4 Comparison of evaporator capacity between ASHP and WSHP	163
Fig. 5.5: Comparison of power between ASHP and WSHP.....	163
Fig. 5.6: Comparison of COP between ASHP and WSHP	164
Fig. 5.7: Comparison of UA value between ASHP and WSHP	165
Fig. 5.8: Variation of COP with delta T between water inlet and outlet	166
Fig. 5.9: Variation of power consumption with delta T between water inlet and outlet	167

Fig. 5.10: Variation of capacity and LMTD with delta T between water inlet and outlet	168
Fig. 5.11: Variation of UA value with delta T between water inlet and outlet.....	168
Fig. 5.12: Variation of MFR with delta T between water inlet and outlet.....	169
Fig. 5.13: Schematic diagram of WSHP1	171
Fig. 5.14: Schematic diagram of WSHP2.....	171
Fig. 5.15: COP of WSHP1 and WSHP2.....	172
Fig. 5.16: UA of WSHP1 and WSHP2.....	173
Fig. 5.17: Mass flow rates of water and refrigerant (ammonia)	174
Fig. 5.18: Flow chart of the heat exchanger design for LTLHP application	176
Fig. 5.19: Design guideline for novel heat exchanger for LTLHP application	180

Nomenclature

symbols

a	channel width, m
A	heat transfer area, m ²
b	corrugation depth, m
b	channel distance, m
Bo	boiling number, dimensionless $q G^{-1} h_{fg}^{-1}$
c	summit width, m
Co	convection number, dimensionless $((1-x) x^{-1})^{0.8} (\rho_g \rho_l^{-1})^{0.5}$
C_p	specific heat, J·kg ⁻¹ ·K ⁻¹
d	diameter, m
d_h	hydraulic diameter, m
DP/L	pressure drop per unit length, kPa·m ⁻¹
f	friction factor, dimensionless
Fr_{l0}	liquid Froude number, $G^2 \cdot \rho_l^{-1} \cdot g^{-1} \cdot D^{-1}$
G	mass flux, kg·m ⁻² ·s ⁻¹
h	heat transfer coefficient, W·m ⁻² ·K ⁻¹
k	thermal conductivity, W·K ⁻¹ ·m ⁻¹
L	length, m
L_p	plate length, m
\dot{m}	mass flow rate, kg·s ⁻¹
Nu	Nusselt number, dimensionless, $h d k^{-1}$
P	corrugation pitch, m
p	pressure, Pa
p_r	reduced pressure
Pr	Prandtl number, dimensionless
q	heat flux, kW m ⁻²
\dot{Q}	total heat transfer, kW
Re	Reynolds number, dimensionless, $G d \cdot \mu^{-1}$
ΔT	temperature difference, K
T	temperature, K

t	thickness of wall, m
U	overall heat transfer coefficient, $\text{W}\cdot\text{m}^{-2}\cdot\text{K}^{-1}$
U_m	fluid mean velocity, $\text{m}\cdot\text{s}^{-1}$
w	plate width, m
We	Weber number, $G^2\cdot d\cdot\rho^{-1}\cdot\sigma^{-1}$
X_{tt}	Martinelli parameter, $((1-x) x^{-1})^{0.9} (\rho_g \rho_l^{-1})^{0.9} (\mu_l \cdot \mu_g^{-1})^{0.1}$
β	corrugation angle, degree
ε	acceptable error, dimensionless
μ	dynamic viscosity, $\text{Pa}\cdot\text{s}$
ρ	density, $\text{kg}\cdot\text{m}^{-3}$
ϕ	enlargement factor, dimensionless

Acronyms

AAO	Approximation Assisted Optimization
ASHP	Air Source Heat Pump
CFD	Computational Fluid Dynamics
COP	Coefficient of Performance
DOE	Design of Experiment
DP	Differential Pressure
DP/L	Pressure Drop per unit Length, $\text{Pa}\cdot\text{m}^{-1}$
HTC	Heat Transfer Coefficient, $\text{W}\cdot\text{K}^{-1}\cdot\text{m}^{-1}$
LES	Large Eddy Simulation
LMTD	Logarithmic Mean Temperature Difference, K
LTL	Low Temperature Lift
LTLHP	Low Temperature Lift Heat Pump
LTLHX	Low Temperature Lift Heat Exchanger
MAS	Metamodel Acceptability Score
MED	Maximum Entropy Design
MFR	Mass Flow Rate
MOGA	Multi-objective Optimization Generic Algorithm
NODC	National Oceanographic Data Center

OAAO	Online Approximation Assisted Optimization
PHX	Plate Heat eXchanger
Poly0	zero order polynomial
Poly1	first order polynomial
Poly2	second order polynomial
PPCFD	Parallel Parameterized CFD
RBF	Radial Basis Function
RMAE	Relative Maximum Absolute Error
RNG	Re-Normalization-Group
RRMSE	Relative Root Mean Squared Error
RSM	Reynolds Stress Model
S-A model	Spalart-Allmaras Model
SST	Shear Stress Transport
WSHP	Water Source Heat Pump
VCC	Vapor Compression Cycle

Subscript

e	equivalent
f1	fluid 1
f2	fluid 2
h	hydraulic
in	inlet
l	laminar
out	outlet
r	refrigerant
s	plate surface
t	turbulent
w	water

CHAPTER 1. Introduction

1.1 Low temperature lift heat pump

As energy demand and cost are projected to increase dramatically due to population and income growth, enhancing energy efficiency of the energy conversion systems becomes more important than ever. One of such approaches is reducing the temperature lift of the vapor compression cycle, which is used for air conditioning and heat pump applications. Therefore, it comes to be more pivotal to conduct research on the heat pump system utilizing a small temperature lift.

A schematic diagram of the typical heat pump vapor compression cycle (VCC) is shown in Fig. 1.1. A working fluid (refrigerant) absorbs heat from the evaporator, and discharges the heat to the heat sink through the condenser. Fig. 1.2 shows the heat pump cycle in a temperature-entropy (T-s) diagram. As shown in the figure, the heat source temperature is higher than evaporating temperature, and the heat sink temperature is lower than the condensing temperature of the VCC.

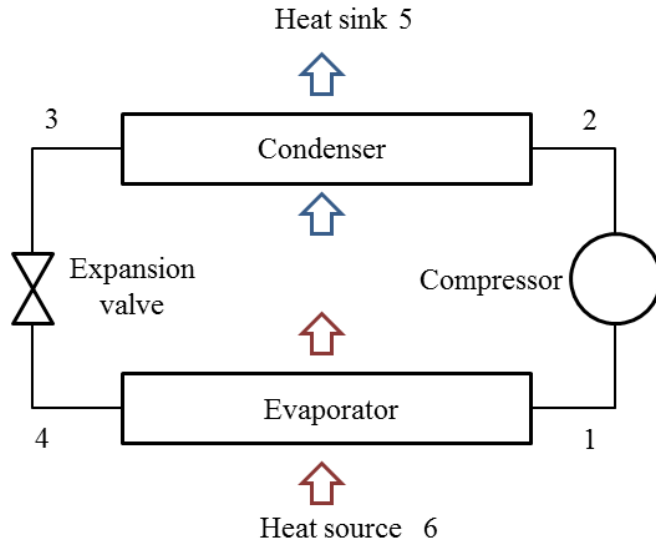


Fig. 1.1: Typical heat pump VCC

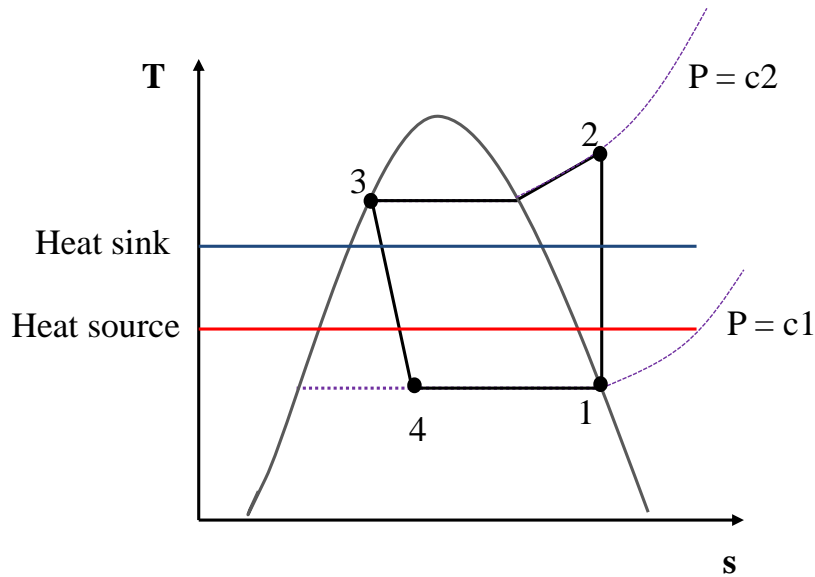


Fig. 1.2: T-s diagram of heat pump VCC

Work input to the VCC is mainly determined by two saturation temperatures: evaporating and condensing temperatures. As the temperature difference (ΔT) between two saturation temperatures decreases, or, as the cycle is operated at the low temperature lift, the system work also decreases. Therefore, reducing the temperature lift can increase the system efficiency. Heat pump system utilizing a small temperature difference

between a heat source and a heat sink is referred as a low temperature lift heat pump (LTLHP) hereafter. The system performance of the LTLHP can be improved due to the reduced power consumption, as compared to the typical heat pump. Several scenarios that can shift system operation from a large temperature lift system to a low temperature lift system are listed below. It should be noted that, in these scenarios, the VCC operates in a heating mode and the temperature of the heat sink is assumed to be constant.

- Case 1: Decrease in ΔT between heat source and working fluid
- Case 2: Increase in heat source-fluid temperature
- Case 3: Combination of Case 1 and Case 2

Case 1 is to reduce the temperature difference (ΔT) between the heat source and the working fluid in the heat exchangers. Overall heat transfer coefficient (U) can be expressed:

$$\dot{Q} = U \cdot A \cdot \Delta T \quad (1.1)$$

When heat transfer capacity (\dot{Q}) is fixed, either U or active heat transfer area (A) needs to be increased, in order to make ΔT small. U can be expressed:

$$\frac{1}{U} = \frac{1}{h_r} + \frac{t}{k} + \frac{1}{h_w} \quad (1.2)$$

The heat transfer coefficient of a heat source-fluid in single-phase is primarily dominated by the Reynolds number (Re), and Prandtl number (Pr). The heat transfer coefficient of a working fluid in two-phase is dominated by factors such as the Re , the quality of the fluid, and the heat flux. Furthermore, the Re is a function of velocity, viscosity, density, and hydraulic diameter. Therefore, U can be increased by increasing the flow rate of both fluids. Heat transfer area can be increased by using a larger heat exchanger. If the heat

exchanger size is increased to be infinite, then ΔT approaches to zero. In other words, the evaporating temperature almost approaches to heat source temperature.

Case 2 involves increasing the heat source temperature. As the heat source temperature increases, the evaporating temperature also increases. This can reduce the temperature difference between the evaporating and condensing temperatures. An air source heat pump system typically uses outside cold air as a heat source in winter season. Through replacing the cold air with warmer water, which can be resourced from either geothermal or solar thermal energy, the cycle is transitioned according to Case 2 parameters.

Case 3 is the application of both Case 1 and Case 2 through simultaneously decreasing ΔT and increasing the heat source temperature, as shown in Fig. 1.3. This would be the best option to reduce the temperature difference between evaporation and condensing temperatures in order to maximize the cycle efficiency. Therefore, this case was considered in this study.

The LTLHP with case 3 utilizes a small difference between heat source-fluid and working fluid temperatures, so that it requires a higher flow rate of heat source-fluid, a larger heat transfer area, and a higher heat source temperature than the typical temperature lift case. Since the flow rate is directly related to the operating cost, and the heat transfer area is related to the system's initial cost, the heat exchanger performance is a critical parameter to the LTLHP system's lift cycle cost.

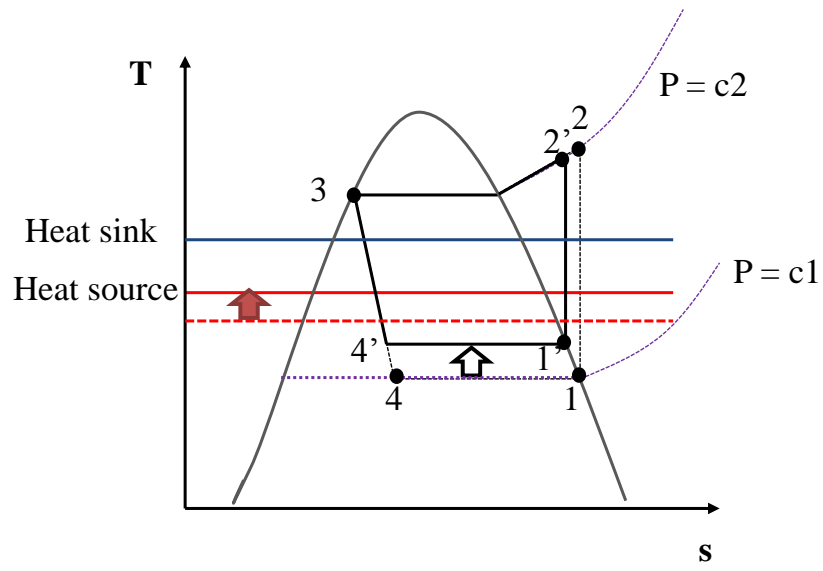


Fig. 1.3: T-s diagram of heat pump VCC for Case 3

1.2 Literature review

1.2.1 Low temperature lift heat exchanger

In this thesis, a low temperature lift heat exchanger (LTLHX) is defined as one used for the LTLHP that has a small difference between condensing and evaporating temperatures, and has a low approach temperature. Several heat exchangers could be used as the LTLHX such as a shell and tube type heat exchanger, plate-fin type heat exchanger, folded-tube heat exchanger, and plate heat exchanger. However, most of the studies were not about the heat exchanger performance, but the system performance (Garcia-Cascales et al., 2007; Cho and Yun, 2011; Buyukalaca et al., 2003; Murthy et al., 2004; Pinson et al., 2007; Faizal and Ahmed, 2012). Moreover, their research under LTLHP operating conditions is very limited. The plate heat exchanger (PHX) is the most widely used compact heat exchanger, due to its high thermal efficiency and ease of manufacturing and is open proposed for the LTLHP applications. Therefore, the PHX was reviewed as shown in Table 1.1. In order to compare the performance of the PHX, the fin-and-tube type heat exchanger was selected as a comparison heat exchanger. These heat exchangers were used for the application of heat pump and air-conditioning system. For the fin-and-tube type heat exchanger, the air-side heat transfer coefficient ranged from 10 to 200 $\text{W}\cdot\text{m}^{-2}\cdot\text{K}^{-1}$, and two-phase refrigerant heat transfer coefficient was almost 2,000 $\text{W}\cdot\text{m}^{-2}\cdot\text{K}^{-1}$. It is well known that the limitation of the fin-and-tube type heat exchanger is on the air-side heat transfer performance. For the PHX, the heat transfer coefficient of the heat source side (usually, water) ranged from 4,000 to 8,000 $\text{W}\cdot\text{m}^{-2}\cdot\text{K}^{-1}$, and refrigerant heat transfer coefficient was about 2,000 to 4,000 $\text{W}\cdot\text{m}^{-2}\cdot\text{K}^{-1}$. The heat transfer limitation of the PHX was on two-phase refrigerant heat transfer.

Table 1.1: Summary of the PHX research

Heat exchanger	Authors	Working fluid	Single-phase HTC ($W \cdot m^{-2} \cdot K^{-1}$)	Two-phase HTC ($W \cdot m^{-2} \cdot K^{-1}$)	Applications
Fin and tube type	Field data (2011)	R410A	10 - 200	2300	Heat pump
Fin and tube type	Castro et al. (2005)	R290	(typical range)	1600	Heat pump
Corrugated PHX	Han et al. (2003)	R410A		1200 - 4200	Heat pump
Corrugated PHX	Hsieh-Lin (2004)	R410A		2900 - 4100	Heat pump
Corrugated PHX	Thonon. (1995)	-		1800 - 2000	Heat pump
Corrugated PHX	Yan and Lin (1999)	R134a	4000 - 8000 (typical range)	2000 - 4000	Heat pump
Corrugated PHX	Longo and Gasparella (2007)	R410A		2000-4000	Heat pump
Corrugated PHX	Taboas et al. (2010)	Ammonia/water mixture		5000 - 15000	Absorption cycle
Plain PHX	Jorge et al. (2004)	water	1500 - 2300	-	Food industry

Most of the studies about the PHX were conducted by considering only one fluid side, such as either heat source fluid-side (Muley and Manglik, 1999; Kumar, 1984; Wanniarachchi, 1995; Martin, 1996; Kim, 1999; Thonon, 1995) or two-phase refrigerant-side (Yan and Lin, 1999; Hsieh and Lin, 2002; Han et al., 2003; Yan et al., 1999; Longo 2008, 2009, 2010; Longo and Gasparella, 2004). Several studies about the PHX performance were carried out by considering the relation between both fluids sides. However, their operating conditions were mostly for the conventional heat pump system. The Djordjevic and Kabelac (2008) investigated the PHX performance when the delta T of heat source fluid was about 7 °C and LMTD was 4.7K. Claesson (2004) evaluated the PHX as an evaporator for the domestic heat pump. Heat source fluid had 5 to 15K of temperature difference. Buyukalaca (2003) investigated the PHX performance for a water source heat pump system, which had 4K of heat source fluid temperature difference. A very limited experimental research has been conducted for the performance of the PHX used in the LTLHP application.

Fig. 1.4 shows the commercial PHX, which has a chevron angle (corrugated) on the plate. Two plates form complex flow channels. Fig. 1.5 shows the flow directions in the PHX. Plates are stamped and easily stacked together. PHX can be easily disassembled, maintenance such as cleaning and replacement of the parts are effortless. Therefore, it is relatively easy to manufacture and to regulate the heat exchanger capacity.



Fig. 1.4: Plate heat exchanger

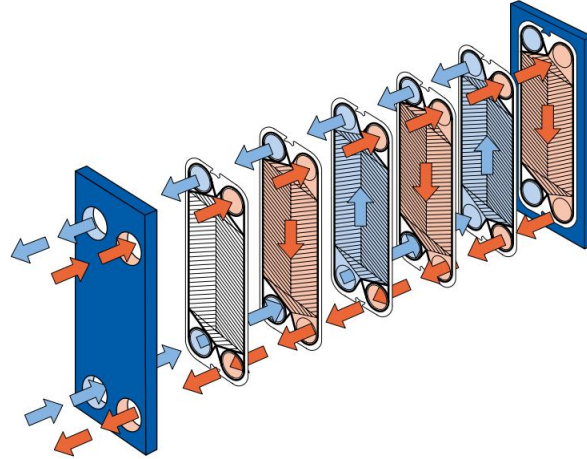


Fig. 1.5: Flow principle of a plate heat exchanger (Courtesy of Alfa Laval)

1.2.2 Single-phase heat transfer and pressure drop in plate heat exchanger

Extensive amount of studies have been investigated for the heat transfer coefficient and pressure drop in the PHX. Among them, several meaningful correlations were introduced, which considered geometrical parameters such as a chevron angle (β) or enlargement factor (ϕ). Geometric parameters of the plate are shown in Fig. 1.6.

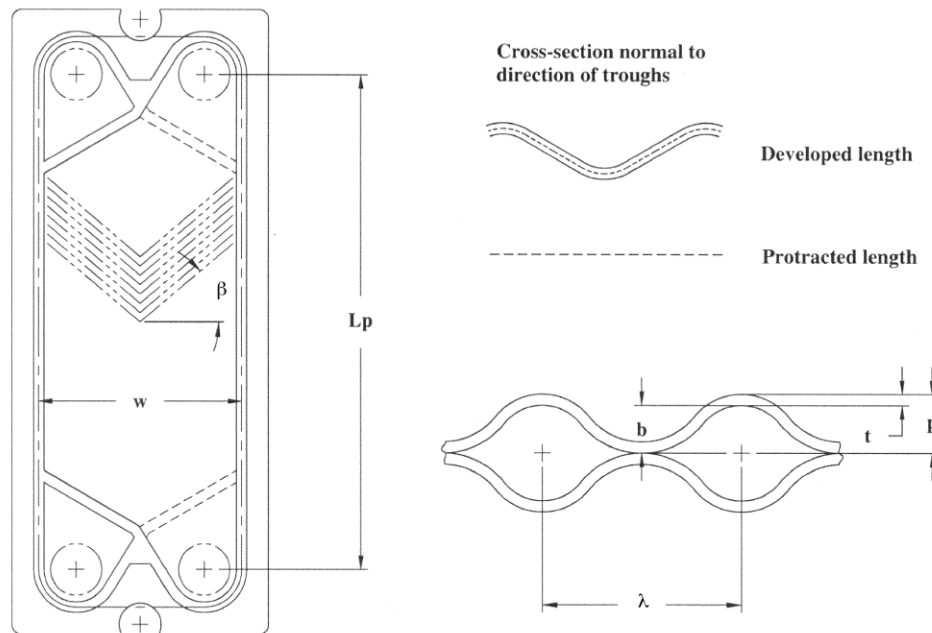


Fig. 1.6: Parameters of plate (Ayub, Zahid H., 2003)

- **Muley and Manglik (1999)**

Experimental heat transfer and pressure drop data for single-phase flows in a PHX with chevron plates were presented by Muley and Manglik (1999). The Nusselt number (Nu) is defined with a chevron angle, enlargement factor, Re , Prandtl number (Pr), and viscosity ratios. Through the increase of either a chevron angle or the enlargement factor, the heat transfer coefficient was increased. The results showed that at constant pumping power, and depending upon Re_e , β , and ϕ , the heat transfer could be enhanced by up to 2.8 times, as compared to that in an equivalent flat plate channel. Correlations of Nu and friction factor (f) are described as following Eqs. for $Re_e > 1000$, $30 < \beta < 60$, $1 < \phi < 1.5$:

$$Nu = [0.2668 - 0.006967 \cdot (90 - \beta) + 7.244 \times 10^{-5} \cdot (90 - \beta)^2] \times [20.78 - 50.94\phi + 41.16\phi^2 - 10.51\phi^3] \times Re_e^{[0.728 + 0.0543 \sin[\frac{\pi(90-\beta)}{45} + 3.7]]} \times Pr^{1/3} \times \left(\frac{\mu}{\mu_s}\right)^{0.14} \quad (1.3)$$

$$f = [2.917 - 0.1277 \cdot (90 - \beta) + 2.016 \times 10^{-3} \cdot (90 - \beta)^2] \times [5.474 - 19.02\phi + 18.93\phi^2 - 5.341\phi^3] \times Re_e^{-[0.2 + 0.0577 \sin[\frac{\pi(90-\beta)}{45} + 2.1]]} \quad (1.4)$$

$$f = \frac{\rho \cdot \Delta p_{core} \cdot d_e}{2 \cdot G^2 \cdot L_p} \quad (1.5)$$

where L_p is indicating the length between port center and center.

- **Wanniarachchi et al. (1995)**

The effect of the chevron angle and enlargement factor on the heat transfer and pressure drop of the PHX was presented by Wanniarachchi et al. (1995). They correlated the data with an asymptotic correlation with two parts: laminar and turbulent. This correlation covers all the three flow regions, including the transition. Correlations of Nu and f are expressed by Eqs. (1.6) through (1.14) for $1 < Re_e < 10,000$, $20 < \beta < 62$:

$$Nu = [Nu_l^3 + Nu_t^3]^{1/3} Pr^{1/3} (\mu/\mu_w)^{0.17} \quad (1.6)$$

$$Nu_l = 3.65\beta^{-0.455} \phi^{0.661} Re_e^{0.339} \quad (1.7)$$

$$Nu_t = 12.6\beta^{-1.142} \phi^{1-m} Re_e^m \quad (1.8)$$

$$m = 0.646 + 0.0011\beta \quad (1.9)$$

$$f = [f_l^3 + f_t^3]^{1/3} \quad (1.10)$$

$$f_l = 1774\beta^{-1.026} \phi^2 Re_e^{-1} \quad (1.11)$$

$$f_t = 46.6\beta^{-1.08} \phi^{1+p} Re_e^p \quad (1.12)$$

$$p = 0.00423\beta + 0.0000223\beta^2 \quad (1.13)$$

$$f = \frac{\rho \cdot \Delta p \cdot d_e}{2 \cdot G^2 \cdot L} \cdot \left(\frac{\mu}{\mu_s} \right)^{0.17} \quad (1.14)$$

where L is defined as A/W (flow length)

- **Chisholm & Wanniarachchi (1992)**

Unlike the two correlations described above, Chisholm and Wanniarachchi (1992) did not consider the Prandtl number and viscosity effect in their correlations. Their correlations are shown in Eqs. (1.15) and (1.16):

$$Nu = 0.72 \cdot Re_e^{0.59} \cdot \phi^{0.41} [(90 - \beta)/30]^{0.66} \quad (1.15)$$

$$f = 0.8 \cdot Re_e^{-0.25} \cdot \phi^{1.25} [(90 - \beta)/30]^{3.6} \quad (1.16)$$

for $1000 < Re_e < 40,000$, $30 < \beta < 80$

- **Martin (1996)**

Martin investigated the single-phase heat transfer coefficient and pressure drop of a PHX. He developed a heat transfer correlation including the friction factor with a hydraulic diameter for $400 < Re_h < 10000$, shown in Eqs. (1.17) through (1.18):

$$Nu = 0.122 \cdot Pr^{1/3} \cdot (\mu / \mu_w)^{1/6} (f Re_h^2 \cdot \sin 2\beta)^{0.374} \quad (1.17)$$

$$\frac{1}{\sqrt{f}} = \frac{\cos \beta}{(0.18 \tan \beta + 0.36 \sin \beta + c_1 / \cos \beta) 1/2} + \frac{1 - \cos \beta}{\sqrt{3.8 c_2}} \quad (1.18)$$

$$f = \frac{2 \cdot \Delta p \cdot d_h}{\rho \cdot G^2 \cdot L_p} \quad (1.19)$$

The summary of distinguishing features of each correlation is shown in Table 1.2. It should be noted that only Martin used a hydraulic diameter to calculate heat transfer coefficient and pressure drop correlation, while other authors used an equivalent diameter. Wanniarachchi et al. formulated the heat transfer coefficient and pressure drop correlation including laminar flow. For β range, Martin used widest range between 0 and 80.

Table 1.2: Summary of distinguishing features of each correlation

Investigator	Diameter	Reynolds number	β	Comments
Muley and Manglik (1999)	Equivalent diameter	$Re > 1,000$	$30 < \beta < 60$	$1 < \Phi < 1.5$
Wanniarachchi et al. (1995)	Equivalent diameter	$1 < Re < 10,000$	$20 < \beta < 62$ $\beta > 62 = 62$	-
Chisholm and Wanniarachchi (1992)	Equivalent diameter	$1,000 < Re < 40,000$	$30 < \beta < 80$	$Pr = 5$
Martin (1996)	Hydraulic diameter	$400 < Re < 10,000$	$0 < \beta < 80$	-

1.2.3 Two-phase heat transfer and pressure drop in plate heat exchanger

- **Yan and Lin (1999)**

The boiling heat transfer and pressure drop of R134a in the PHX were investigated experimentally. They found that the evaporation heat transfer coefficient in the PHX is much higher than that in circular pipes. When Re_{eq} are between 2,000 and 10,000, the heat transfer coefficient can be expressed in Eqs. (1.20) through (1.24).

$$\left(\frac{h_{tp}D_h}{\lambda_f}\right) Pr_f^{-1/3} Re^{0.5} Bo_{eq}^{-0.3} = 1.926 Re_{eq} \quad (1.20)$$

$$Re_{eq} = \frac{G_{eq}D_h}{\mu_f} \quad (1.21)$$

$$Bo_{eq} = \frac{q_w''}{G_{eq}i_{fg}} \quad (1.22)$$

$$G_{eq} = G[1 - x + x(\rho_f/\rho_g)^{1/2}] \quad (1.23)$$

$$Nu = 1.926 Pr_f^{1/3} Bo_{eq}^{-0.3} Re_{eq}^{0.5} \left[(1 - x) + \left(\frac{\rho_f}{\rho_g}\right)^{0.5} \right] \quad (1.24)$$

- **Arima et al. (2000)**

The correlation for local boiling heat transfer in the PHX was proposed. The equation was correlated where the mass flux ranged from 7.5 to 15 kg·m⁻²·s⁻¹, the heat flux ranged from 15 to 25 kW m⁻², and the vapor quality ranged from 0.1 to 0.4. With these operating conditions, the calculated heat transfer coefficient values agree with measured data within ±25% of accuracy. Heat transfer coefficient correlations are shown in Eqs. (1.25) to (1.27).

$$\frac{h_{tp}}{h_l} = 16.4 \left(\frac{1}{x_{tt}}\right)^{1.08} \quad (1.25)$$

$$X_{tt} = \left(\frac{1-x}{x}\right)^{0.9} \left(\frac{\rho_g}{\rho_f}\right)^{0.5} \left(\frac{\eta_f}{\eta_g}\right)^{0.1} \quad (\text{Turbulent – Turbulent}) \quad (1.26)$$

$$X_{tt} = \left(\frac{1-x}{x}\right)^{0.9} \left(\frac{\rho_g}{\rho_f}\right)^{0.5} \left(\frac{\eta_f}{\eta_g}\right)^{0.1} \quad (\text{Laminar – Laminar}) \quad (1.27)$$

- **Han et al. (2003)**

Blazed PHX was used with R410A and R22 as its working fluids. It is found that the heat transfer coefficients of R410A are greater than those of R22 and the pressure drops of R410A are less than those of R22. $Ge_1, Ge_2, Ge_3,$ and Ge_4 are non-dimensional geometric parameters that involve a corrugation pitch, an hydraulic diameter and a chevron angle. Correlations of Nu and f are described in Eqs. (1.28) through (1.33).

$$Nu = Ge_1 Re_{eq}^{Ge_2} Bo_{eq}^{0.3} Pr^{0.4} \quad (1.28)$$

$$Ge_1 = 2.81 \left(\frac{p_{co}}{D_h}\right)^{-0.041} \left(\frac{\pi}{2} - \beta\right)^{-2.83} \quad (1.29)$$

$$Ge_2 = 0.746 \left(\frac{p_{co}}{D_h}\right)^{-0.082} \left(\frac{\pi}{2} - \beta\right)^{-0.61} \quad (1.30)$$

$$f = Ge_3 Re_{eq}^{Ge_4} \quad (1.31)$$

$$Ge_3 = 64710 \left(\frac{p_{co}}{D_h}\right)^{-5.27} \left(\frac{\pi}{2} - \beta\right)^{-3.03} \quad (1.32)$$

$$Ge_4 = -1.314 \left(\frac{p_{co}}{D_h}\right)^{-0.62} \left(\frac{\pi}{2} - \beta\right)^{-0.47} \quad (1.33)$$

- **Ayub (2003)**

Two-phase heat transfer coefficient correlation for $30 < \beta < 65$ and R22 and ammonia as its working fluids was proposed in US units. Heat transfer coefficient and friction factor correlations are shown in Eqs. (1.34) through (1.37).

$$h_{tp} = C \left(\frac{k_l}{d_e} \right) \left[\frac{Re_l^2 h_{fg}}{L_p} \right]^{0.4124} \left(\frac{p}{p_{cr}} \right)^{0.12} (65/\beta)^{0.35} \quad (1.34)$$

C=0.1121 for flooded and thermo-syphon

C=0.0675 for direct expansion

$$f = \left(\frac{n}{Re^m} \right) (-1.89 + 6.56R - 3.69R^2) \quad (1.35)$$

$$R = \beta/30 \quad (1.36)$$

m=0.137 n=2.99 for Re < 4,000

m=0.172 n=2.99 for 4,000 < Re < 8,000

m=0.161 n=3.15 for 8,000 < Re < 16,000

m=0.195 n=2.99 for Re > 16,000

$$\Delta p_{port} = 0.0076 \rho V^2 / 2g \quad (1.37)$$

1.2.4 In-tube flow boiling heat transfer

1.2.4.1 Introduction

It is pivotal to understand the mechanism of flow boiling heat transfer, since it could be the first step to investigate the heat exchanger in this thesis. The correlations for the flow boiling heat transfer coefficient can be divided in two groups according to the size of the flow channel: macrochannel, and minichannel. Correlations of boiling heat transfer coefficient for macrochannels are pretty well established. It can predict the heat transfer performance within $\pm 20\%$ of deviation. The reason is that numerous studies have been conducted during many decades so that there were enough data to create generalized correlations. In contrast, that of minichannels has not been clearly established yet. Most of the studies tried to develop a specific correlation for their specific test case. Therefore,

the prediction of minichannel heat transfer could occasionally deviate more than 100%. In order to reasonably predict the boiling heat transfer coefficient of the novel heat exchanger that is developed in this study, literature review was conducted carefully.

Two main mechanisms of the flow boiling heat transfer are (1) nucleate boiling heat transfer and (2) convective boiling heat transfer. The main driving force of nucleate boiling heat transfer is the temperature difference between fluid and wall. Moreover, the bubbles generated from the wall helps quickly and efficiently transfer heat. In the convective boiling heat transfer, heat is transferred one place to another by movement of fluids.

1.2.4.2 Classification of boiling heat transfer correlations

Papers about the flow boiling heat transfer correlations were reviewed and categorized into four types, according to the formation of correlations: a superposition model, dominant mode selection model, asymptotic model, and product method model.

Firstly, the superposition model correlation is the addition of two contributions, nucleate boiling and convective boiling heat transfer. Most of the correlations derived from this correlation type, such as Gungor and Winterton (1986), Jung and Radermacher (1989), Kandlikar (1990), Zhang et al. (2004), Saitoh et al. (2007), Choi et al. (2007), and so on. Secondly, the dominant mode selection model correlation selects the dominant component from two components. Thirdly, the asymptotic model correlation used power additive model. Lastly, the product method model correlation formulates the equation based on the assumption that nucleate boiling is dominant.

Defining the transition criteria from macro tube scale to micro tube scale is important, since heat transfer mechanism could be different depending upon tube scale.

For example, heat transfer in macrochannels is usually dominated by both convective and nucleate boiling heat transfer. In contrast, heat transfer in minichannels is known to be more dominated by nucleate boiling heat transfer. There are several suggestions about how to define the criteria as follows:

Mehendal et al. (2000) proposed that microchannels are from 1 to 100 μm , mesochannels are from 100 μm to 1 mm, macrochannels are from 1 to 6 mm, and conventional channels are larger than 6 mm. Kandlikar (2002) suggested that microchannels are between 10 and 200 μm , mini channels are from 200 μm to 3 mm, and conventional channels are larger than 3 mm. Kew and Cornwell (1997) defined the threshold diameter (D_{th}) based on the confinement of growing bubble within channel as described in Eq. (1.38). If the threshold diameter is larger than the hydraulic diameter, then it is classified into microchannel, otherwise, macrochannel. For example, the criteria are 5 mm for water at low pressure, and 1 mm for CO_2 at high pressure, respectively.

$$D_{th} = \left(\frac{4\sigma}{g(\rho_f - \rho_g)} \right)^{1/2} \quad (1.38)$$

In this dissertation, correlations are divided into two groups: macrochannel when the hydraulic diameter is larger than 3 mm, and minichannel when the hydraulic diameter is smaller than 3 mm according to Kandlikar (2002).

1.2.4.3 Boiling heat transfer correlation for macrochannels

- **Chen (1966)**

Generalized additive form of correlation was firstly proposed. Two-phase heat transfer coefficient was correlated with the form of the summation of macro and micro convective heat transfer. Macroconvective heat transfer represents convective heat

transfer, and microconvective heat transfer symbolizes nucleate heat transfer coefficient. For the convective heat transfer term, it is the multiplication of F factor and liquid-phase heat transfer coefficient. For the nucleate boiling heat transfer term, it is the multiplication of S factor and nucleate boiling heat transfer coefficient. F is an enhancement factor which is usually larger than 1. Bubble helps the heat transfer by generating turbulence. Correlations are shown in Eqs. (1.39) to (1.44).

$$h_{tp} = h_{mac} + h_{mic} = Fh_l + Sh_{nb} \quad (1.39)$$

$$h_l = 0.023(Re_l)^{0.8}(Pr_l)^{0.4}(k_l/D) \quad (1.40)$$

$$F = (Re/Re_l)^{0.8} \quad (1.41)$$

$$h_{nb} = 0.00122 \left(\frac{k_L^{0.79} C_{pL}^{0.45} \rho_L^{0.49} g_c^{0.25}}{\sigma^{0.5} \mu_L^{0.29} \lambda^{0.24} \rho_v^{0.24}} \right) (\Delta T)^{0.24} (\Delta P)^{0.75} \quad (1.42)$$

$$S = (\Delta T_e/\Delta T)^{0.24} (\Delta P_e/\Delta P)^{0.75} \quad (1.43)$$

$$Re_l = \frac{G(1-x)D}{\mu_l} \quad (1.44)$$

- **Shah (1976, 1982)**

In 1976, Shah reported a chart correlation, which is the graphical method of solution. Then, in 1982, he developed the equation type of correlation. Instead of adding the two contributions together, the larger of the two calculated heat transfer coefficients is chosen. The heat transfer coefficient correlations are shown in Eqs. (1.45) to (1.57).

$$\frac{h_{tp}}{h_l} = \psi \quad (1.45)$$

$$h_L = 0.023 \left(\frac{G(1-x)D}{\mu_L} \right)^{0.8} (Pr_L)^{0.4} (k_L/D) \quad (1.46)$$

$$Fr_L = \frac{G^2}{\rho_L^2 g D}, \text{ Froude number assuming the fluid to be flowing as liquid phase only}$$

Vertical tube, horizontal tube with $Fr_L \geq 0.04$

$$N > 1.0$$

$$Bo > 0.3 \times 10^{-4}, \psi_{nb} = 230 Bo^{0.5} \quad (1.47)$$

$$Bo < 0.3 \times 10^{-4}, \psi_{nb} = 1 + 46 Bo^{0.5} \quad (1.48)$$

$$\psi_{cb} = 1.8/Co^{0.8} \quad (1.49)$$

$$\psi = \text{Max} (\psi_{nb}, \psi_{cb}) \quad (1.50)$$

$$0.1 \leq N \leq 1.0$$

$$\psi_{bs} = FBo^{0.5} \exp(2.74Co^{-0.1}) \quad (1.51)$$

$$\psi = \text{Max} (\psi_{bs}, \psi_{cb}) \quad (1.52)$$

$$N \leq 0.1$$

$$\psi_{bs} = FBo^{0.5} \exp(2.47Co^{-0.15}) \quad (1.53)$$

$$\psi = \text{Max} (\psi_{bs}, \psi_{cb}) \quad (1.54)$$

$$F=14.7, Bo \geq 11 \times 10^{-4} \quad (1.55)$$

$$F=15.43, Bo < 11 \times 10^{-4} \quad (1.56)$$

Horizontal tube with $Fr_L \leq 0.04$

$$N = 0.38Fr_L^{-0.3}Co \quad (1.57)$$

- **Gungor and Winterton (1986)**

Chen type correlation was developed with E and S factors. E is defined as an enhancement factor and S is defined as a suppression factor. The factor f ($f > 1$) reflects the much higher velocities and hence forced convection heat transfer in the two-phase flow compared to liquid only flow. The factor s ($s < 1$) reflects the lower effective superheat available in forced convection as opposed to pool boiling due to the thinner

boundary layer. The correlations for the heat transfer coefficient are shown in Eqs. (1.58) to (1.66).

$$h_{tp} = Eh_l + Sh_{pool} \quad (1.58)$$

$$h_l = 0.023 Re_l^{0.8} Pr_l^{0.4} (k_l/D) \quad (1.59)$$

$$X_{tt} = \left(\frac{1-x}{x}\right)^{0.9} \left(\frac{\rho_v}{\rho_l}\right)^{0.5} \left(\frac{\mu_L}{\mu_v}\right)^{0.1} \quad (1.60)$$

$$E = f(X_{tt}, Bo) \quad (1.61)$$

Vertical, horizontal $Fr > 0.05$

$$E = 1 + 24,000Bo^{1.16} + 1.37(1/X_{tt})^{0.86} \quad (1.62)$$

$$S = \frac{1}{1 + 1.15 \times 10^{-6} E^2 Re_l^{1.17}} \quad (1.63)$$

$$h_{pool} = 55P_r^{0.12} (-\log_{10} P_r)^{-0.55} M^{-0.5} q^{0.67} \quad (1.64)$$

P_r : reduced pressure, M : molecular weight, q : heat flux

Horizontal $Fr < 0.05$

$$E_2 = E * Fr^{(0.1-2*Fr)} \quad (1.65)$$

$$S_2 = S \times \sqrt{Fr} \quad (1.66)$$

- **Jung and Radermacher (1989)**

Chen's correlation was supported and developed by Jung and Radermacher (1989). As the quality of working fluid was increased in annular flow, the effective wall superheat decreased due to a thinner liquid film, which means less thermal resistance and enhanced convection caused by high vapor velocity. Under the suppression of nucleate boiling, it was shown that h_{tp} is directly proportional to $G^{0.8}$. The correlations for the heat transfer coefficient are shown in Eqs. (1.67) to (1.81).

i. For pure refrigerants

$$h_{tp} = h_{nbc} + h_{cec} = Nh_{SA} + F_p h_{lo} \quad (1.67)$$

$$N = 4048 X_{tt}^{1.22} Bo^{1.13} \text{ for } X_{tt} < 1 \quad (1.68)$$

$$h_{SA} = 207 \frac{k_L}{bd} \left(\frac{qbd}{k_L T_{sat}} \right)^{0.745} \left(\frac{\rho_v}{\rho_L} \right)^{0.581} Pr_L^{0.533} \quad (1.69)$$

$$F_p = 2.37 \left(0.29 + \frac{1}{X_{tt}} \right)^{0.85} \quad (1.70)$$

$$h_{mac} = 0.023 \left(\frac{G(1-x)D}{\mu_L} \right)^{0.8} (Pr_L)^{0.4} (k_L/D) \quad (1.71)$$

$$Pr_L = \frac{C_{pl}\mu_L}{k_l} \quad (1.72)$$

$$bd = 0.0146\beta [2\sigma/(g(\rho_l - \rho_v))]^{0.5} \quad (1.73)$$

ii. For mixtures

$$h_{tp} = \frac{N}{C_{UN}} h_{SA} + C_{me} F_p h_{lo} \quad (1.74)$$

$$F_m = F_p C_{me} \quad (1.75)$$

$$C_{me} = 1 - 0.35|Y - X|^{1.56}, \text{ Y-X composition difference in two-phase} \quad (1.76)$$

$$C_{UN} = [1 + (b_2 + b_3)(1 + b_4)](1 + b_5) \quad (1.77)$$

$$b_2 = (1 - X) \ln \left(\frac{1.01 - X}{1.01 - Y} \right) + X \ln \left(\frac{X}{Y} \right) + |Y - X|^{1.5} \quad (1.78)$$

$$b_3 = 0, \text{ for } X > 0.01 \quad (1.79)$$

$$b_3 = (Y/X)^{0.1} - 1 \quad (1.80)$$

$$b_4 = 152(p/p_{cmvc})^{3.9} \quad (1.81)$$

- **Kandlikar (1990)**

Kandlikar correlation is based on a model utilizing the contributions due to nucleate boiling and convective boiling mechanisms. It incorporated a fluid-dependent parameter F_{fl} in the nucleate boiling terms. h_{tp} is the two-phase flow boiling heat transfer coefficient and h_l is the heat transfer coefficient only considering the liquid phase flow in the channel. The correlations for the heat transfer coefficient are shown in Eqs. (1.82) to (1.84).

$$\frac{h_{tp}}{h_l} = C_1 Co^{C_2} (25 Fr_{l0})^{C_5} + C_3 Bo^{C_4} F_{fl} \quad (1.82)$$

$$h_l = 0.023 Re_l^{0.8} Pr_l^{0.4} (k_l/D) \quad (1.83)$$

$$Fr_{l0} = \frac{G^2}{\rho_l^2 g D}, \text{ all flow as liquid phase} \quad (1.84)$$

(a) Case 1, Convective boiling region ($Co < 0.65$): $C_1=1.136$, $C_2=-0.9$, $C_3=667.2$, $C_4=0.7$, $C_5=0.3$

(b) Case 2, Nucleate boiling region ($Co > 0.65$): $C_1=0.6683$, $C_2=-0.2$, $C_3=1058$, $C_4=0.7$, $C_5=0.3$

($C_5 = 0$ for vertical tubes, and for horizontal tube with $Fr_l > 0.04$)

$F_{fl} = 0.7$ for the ammonia

- **Liu and Winterton (1990)**

An asymptotic type model suggested by Kutateladze (1961) was developed by Liu and Winterton (1999). They pointed out that the boiling heat transfer coefficient cannot be linear like Chen type superposition correlation. Since the superposition correlation considerably over-predicted the heat transfer coefficient in the high quality region and under-predicted in the low quality region, the asymptotic type model was proposed.

The same data bank used by Gungor and Winterton (1986) was utilized in this paper. Goal was to reduce the number of physical properties required in the correlations and to extend the range of applicability. Concept was the combination of Gungor and Winterton (1986) and Kutateladze (1961). The correlations for the heat transfer coefficient are shown in Eqs. (1.85) to (1.91).

i. Vertical, horizontal $Fr > 0.05$

$$h_{TP} = \sqrt{(Fh_l)^2 + (Sh_{pool})^2} \quad (1.85)$$

$$h_L = 0.023 \left(\frac{G(1-x)D}{\mu_L} \right)^{0.8} (Pr_L)^{0.4} (k_L/D) \quad (1.86)$$

$$h_{pool} = 55Pr^{0.12} (-\log_{10} Pr)^{-0.55} M^{-0.5} q^{0.67} \quad (1.87)$$

$$F = \left[1 + x Pr_l \left(\frac{\rho_l}{\rho_v} - 1 \right) \right]^{0.35} \quad (1.88)$$

$$S = (1 + 0.055F^{0.1} Re_l^{0.16})^{-1} \quad (1.89)$$

ii. Horizontal $Fr < 0.05$

$$E_2 = E * Fr^{(0.1-2*Fr)} \quad (1.90)$$

$$S_2 = S \times \sqrt{Fr} \quad (1.91)$$

1.2.4.4 Flow boiling heat transfer correlation for minichannels

- **Lazarek and Black (1981)**

The originality of this study was the investigation about small diameter tube (< 1 cm), and short tubes for fluorocarbon refrigerants. Since it was extremely short tube, the contribution of convective boiling heat transfer was small. The correlations for the heat transfer coefficient are shown in Eqs. (1.92) and (1.93).

$$h_{tp} = 30Re^{0.857}Bo^{0.714} \frac{k_l}{D_h} \quad (1.92)$$

$$Re = \frac{GD_h}{\mu_L} \quad (1.93)$$

- **Tran et al. (1996)**

Main variables of Tran's correlation are the heat flux, mass flux, and quality. At the lowest wall superheats, heat transfer was found to be dependent on heat flux and not on mass flux. Nucleation mechanism dominated over the convection mechanism in small channel evaporators over the full range of qualities which is contrary to situations in larger channels where the convection mechanism dominates at qualities typically > 0.2 . Nucleation was more dominant so that Re was replaced with Weber number (We) to eliminate viscous effect in favor of surface tension. Convective boiling heat transfer dominated at sufficiently low value of heat flux and $\Delta T < 2.75$ °C. Nucleate boiling heat transfer dominated at $\Delta T > 2.75$ °C. The correlations for the heat transfer coefficient are shown in Eqs. (1.94) and (1.95).

$$h = (8.4 \times 10^{-5})(Bo^2We_l)^{0.3} \left(\frac{\rho_l}{\rho_v}\right)^{-0.4} (W \cdot m^{-2} \cdot K^{-1}) \quad (1.94)$$

$$We_l = \frac{G^2 d}{\rho_l \sigma} \quad (1.95)$$

- **Kew and Cornwell (1997)**

For small tubes, simple pool boiling heat transfer correlation, such as Cooper's correlation best predicted the data. Therefore, the correlation was developed based on the pool boiling correlation as shown in Eq. (1.96).

$$h_{tp} = 30Re^{0.857}Bo^{0.714} \frac{k_l}{D_h} (1 - x)^{-0.143} \quad (1.96)$$

- **Zhang et al. (2004)**

The author presented that common feature of flow boiling heat transfer in many mini-channels is liquid-laminar and gas-turbulent flow, however all existing correlations were developed for liquid turbulent and gas turbulent flow conditions. Therefore, this flow pattern was taken into account. The correlations for the heat transfer coefficient are shown in Eqs. (1.97) to (1.113).

$$\text{Re}_f = \frac{G(1-x)D_h}{\mu_L} \quad (1.97)$$

$$\text{Re}_g = \frac{G(x)D_h}{\mu_g} \quad (1.98)$$

$$h_{tp} = Sh_{nb} + Fh_{sp} \quad (1.99)$$

$$S = 1/(1 + 2.53 \times 10^{-6} \text{Re}_f^{1.17}) \quad (1.100)$$

$$h_{nb} = 0.00122 \left(\frac{k_L^{0.79} C_{pL}^{0.45} \rho_L^{0.49}}{\sigma^{0.5} \mu_L^{0.29} h_{fg}^{0.24} \rho_v^{0.24}} \right) (\Delta T)^{0.24} (\Delta P)^{0.75} \quad (1.101)$$

$$F = \text{MAX}(F', 1), F' = 0.64 \phi_f, \phi_f^2 = 1 + \frac{C}{X} + \frac{1}{X^2} \quad (1.102)$$

For $\text{Re}_f < 1000$ and $\text{Re}_g < 1,000$, $X = X_{vv}$, $C = 5$

For $\text{Re}_f > 2000$ and $\text{Re}_g < 1,000$, $X = X_{tv}$, $C = 10$

For $\text{Re}_f < 1000$ and $\text{Re}_g > 2,000$, $X = X_{vt}$, $C = 12$

For $\text{Re}_f > 2000$ and $\text{Re}_g > 2,000$, $X = X_{tt}$, $C = 20$

For other regions of Re_k , ($k=f$ or g), interpolate the above values of C

$$X = \left(\frac{f_f}{f_g} \right)^{0.5} \left(\frac{1 - x_{eq}}{x_{eq}} \right) \left(\frac{\rho_g}{\rho_f} \right)^{0.5} \quad (1.103)$$

For circular channel and $Re_k < 1,000$

$$f_k = 16/Re_k \quad (1.104)$$

For $Re_k < 1,000$ in rectangular channel;

$$f_k = 24/Re_k(1 - 3.55\beta + 1.947\beta^2 - 1.701\beta^3 + 0.956\beta^4 - 0.254\beta^5) \quad (1.105)$$

For $Re_k > 2,000$

$$f_k = 0.046Re_k^{-0.2}, \quad (1.106)$$

For h_{sp} calculation,

$$Nu'_{sp,v} = 4.36 \text{ for circular channel;} \quad (1.107)$$

$$Nu_{sp,t} = 0.023(Re_L)^{0.8}(Pr_L)^{0.4} \quad (1.108)$$

$$Nu'_{sp,v} = 8.235(1 - 2.042\beta + 3.085\beta^2 - 2.4765\beta^3 + 1.058\beta^4 - 0.186\beta^5) \text{ for rectangular channel;} \quad (1.109)$$

$$Nu_{colier} = 0.17(Re_L)^{0.33}(Pr_L)^{0.43} \left(\frac{Pr_f}{Pr_w} \right)^{0.25} \left\{ \frac{g \cdot \beta \cdot \rho_f^2 \cdot D_h^3 \cdot (T_w - T_f)}{\mu_L^2} \right\}^{0.1} \quad (1.110)$$

$$h_{sp} = \frac{k_f}{D_h} \text{MAX}(Nu'_{sp,v}, Nu_{colier}), \text{ if } Re_f \leq 2,000 \text{ for vertical flow;} \quad (1.111)$$

$$h_{sp} = \frac{k_f}{D_h} \text{MAX}(Nu'_{sp,v}, Nu_{sp,t}), \text{ if } Re_f < 2,300 \text{ for horizontal flow;} \quad (1.112)$$

$$h_{sp} = \frac{k_f}{D_h} Nu_{sp,t}, \text{ if } Re_f \geq 2,300 \text{ for both vertical and horizontal flows;} \quad (1.113)$$

For vertical flow at $2,000 < Re_f < 2,300$,
interpolate the values of h_{sp} for vertical flow at $Re_f = 2,000$ and $Re_f = 2,300$

- **Saitoh et al. (2007)**

Saitoh et al. (2007) developed a boiling heat transfer coefficient correlation based on the Chen type superposition correlation. Tube diameter effect was characterized by the

We , and it was considered in F factor. The fluid flow conditions more strongly affect forced convective evaporation. The correlations for the heat transfer coefficient are shown in Eqs. (1.114) through (1.121).

$$h_{tp} = Fh_l + Sh_{SA} \quad (1.114)$$

$$F = 1 + \frac{\left(\frac{1}{\bar{X}}\right)^1}{1 + We_g^m} \quad (1.115)$$

$$S = \frac{1}{1 + a(Re_{TP} \times 10^{-4})^n} \quad (1.116)$$

$$Re_{TP} = Re_l F^{1.25} \quad (1.117)$$

$$h_{pool} = 207 \frac{\lambda_L}{d_b} \left(\frac{qd_b}{\lambda_L T_1}\right)^{0.745} \left(\frac{\rho_v}{\rho_L}\right)^{0.581} Pr_L^{0.533} \quad (1.118)$$

$$d_b = 0.51 \left[\frac{2\sigma}{g(\rho_L - \rho_v)} \right]^{0.5} \quad (1.119)$$

$$h_l = 0.023 \left(\frac{G(1-x)D}{\mu_L} \right)^{0.8} (Pr_L)^{0.4} (k_L/D) \quad (1.120)$$

$$Pr_L = \frac{C_{pl}\mu_L}{k_l} \quad (1.121)$$

- **Sun and Mishima (2009)**

Collected database from the literature was used to develop the new correlation. For the mini channel, Lazarek and Black correlation (1981) and Kew and Cornwell correlation (1997) showed the best results. It was found that heat transfer coefficient was much more dependent on the We than the vapor quality. Sun and Mishima (2009) developed a new correlation based upon the Lazarek and Black correlation. The correlations for the heat transfer coefficient are shown in Eqs. (1.122) through (1.123).

$$h_{tp} = \frac{6Re_{lo}^{1.05} Bo^{0.54} \lambda_l}{We_1^{0.191} \left(\frac{\rho_L}{\rho_g}\right)^{0.142} d_h} \quad (1.122)$$

$$We_1 = \frac{G^2 d}{\rho_l \sigma} \quad (1.123)$$

1.2.4.5 Description of the flow boiling heat transfer database

In order to predict the boiling heat transfer coefficient for minichannels used in this study, a new correlation was developed for minichannels in this thesis. Table 1.3 shows the summary of flow boiling heat transfer database for minichannels. Ten different working fluids were used and hydraulic diameters ranged between 0.5 and 3.1 mm. 1,688 data points were extracted from ten published papers, and a new correlation was proposed.

Table 1.3: Summary of boiling heat transfer database for minichannels

Author	Working fluid	Tube hydraulic diameter (mm)	Tube material	Data points
Lie et al. (2006)	R134a, R407C	2, 0.83	Copper	309
Bao et al. (2000)	R11, R123	1.95	Copper	158
Choi et al. (2008)	R22, R134a, CO ₂	1.5, 3	SS	308
Tran et al. (1996)	R12	2.46	Brass	79
Yan and Lin (1998)	R134a	2	Copper	140
Saisorn et al. (2010)	R134a	1.75	SS	55
Pamitran et al. (2007)	R410A	1.5, 3	SS	146
Lie et al. (2006)	R134a	2.01	SS	191
Bao et al. (2000)	R134a, R245fa	2.3	SS	155
Choi et al. (2008)	R134a	0.51, 1.12, 3.1	SUS304	147

Table 1.4 shows the comparison of the heat transfer correlations against the database. Gungor and Winterton (1986) correlation shows relatively good agreement, even though this correlation was developed for macrochannel. Lazarek and Black (1981), Kew and Cornwell (1990), and Sun and Mishima (2009) correlations show 36 to 38% of mean absolute deviation (MAD), respectively.

Table 1.4: Comparison of the heat transfer correlations against the database

Correlations	MAD (%)
Shah (1982)	55.17
Gungor and Winterton (1986)	39.96
Kandlikar (1990)	51.02
Lazarek and Black (1981)	37.99
Kew and Cornwell (1997)	37.78
Zhang et al. (2004)	60.04
Liu and Winterton (1990)	57.79
Tran et al. (1996)	43.93
Yun et al. (2006)	72.76
Sun and Mishima (2009)	36.65

In order to improve the MAD, the new correlation was proposed by considering the convective number and reduced pressure as shown in Eq. (1.124). New correlation showed 26.9 % of MAD against the database.

$$h_{tp} = \frac{0.538 Re_{10}^{1.21} Bo^{0.497} Co^{0.083} (Pr)^{0.186} \lambda_l}{We_l^{0.294}} \frac{\lambda_l}{d_h} \quad (1.124)$$

1.2.5 In-tube flow boiling pressure drop

There are plentiful correlations on pressure drop in two-phase flows in the literature. The most important contributions are briefly discussed. Many studies have developed pressure drop correlations based on the Chisholm (1972) and Friedel (1979) correlations, which uses separated flow models. The basic equations for the separated flow model are not dependent on the particular flow configuration adopted. It is assumed that the velocities of each phase are constant, in any given cross-section, within the zone occupied by the phase.

- **Chisholm (1972)**

A theoretical basis with the Lockhart-Martinelli correlation was proposed for two-phase flow pressure drop. The correlations are described in Eqs. (1.125) through (1.133).

$$\frac{\Delta P_{TP}}{\Delta P_{l0}} = \Phi_{l0}^2 \quad (1.125)$$

$$\frac{\Delta P_{TP}}{\Delta P_{l0}} = 1 + (X^2 - 1)[Bx^{0.875}(1 - x)^{0.875} + x^{1.75}] \quad (1.126)$$

$$X^2 = \frac{\left(\frac{dp}{dl}\right)_{go}}{\left(\frac{dp}{dl}\right)_{lo}}, \text{ go and lo denote that the whole mixture flows as vapor phase only or liquid phase only} \quad (1.127)$$

If $0 < X < 9.5$,

$$B = \frac{55}{G^{0.5}} \text{ for } G \geq 1,900 \quad (1.128)$$

$$B = \frac{2400}{G} \text{ for } 500 \leq G \leq 1,900 \quad (1.129)$$

$$B = 4.8 \text{ for } G \leq 500 \quad (1.130)$$

If $9.5 < X < 28$,

$$B = \frac{520}{XG^{0.5}} \text{ for } G \leq 600 \quad (1.131)$$

$$B = \frac{21}{X} \text{ for } G > 600 \quad (1.132)$$

If $X > 28$,

$$B = \frac{15000}{X^2 G^{0.5}} \quad (1.133)$$

- **Friedel (1979)**

A correlation was optimized for the two-phase frictional multiplier (ϕ_{10}^2). The correlations are described in Eqs. (1.134) through (1.140).

$$\left(\frac{dp}{dl}\right)_{TP} = \left(\frac{dp}{dl}\right)_{10} \phi_{10}^2 \quad (1.134)$$

$$\phi_{10}^2 = E + \frac{3.24FX}{F_r^{0.045} We_1^{0.035}} \quad (1.135)$$

$$F_r = \frac{G^2}{gD\rho_{TP}^2} \quad (1.136)$$

$$F = x^{0.78}(1-x)^{0.224} \quad (1.137)$$

$$We_1 = \frac{G^2 d}{\rho_l \sigma} \quad (1.138)$$

$$X = \left(\frac{\mu_g}{\mu_l}\right)^{0.19} \left(1 - \frac{\mu_g}{\mu_l}\right)^{0.7} \left(\frac{\rho_l}{\rho_g}\right)^{0.91} \quad (1.139)$$

$$E = (1-x)^2 + x^2 \frac{\rho_l f_{go}}{\rho_g f_{10}} \quad (1.140)$$

- **Muller-Steinhagen and Heck (1986)**

A new correlation was proposed for the prediction of frictional pressure drop for two-phase flow in pipes, which is simpler and more convenient to use than other methods.

The correlations are described in Eqs. (1.141) and (1.142).

$$\left(\frac{dp}{dl}\right)_{TP} = F(1-x)^{1/3} + \left(\frac{dp}{dl}\right)_{10} x^3 \quad (1.141)$$

$$F = \left(\frac{dp}{dl}\right)_{lo} + 2 \left[\left(\frac{dp}{dl}\right)_{go} - \left(\frac{dp}{dl}\right)_{lo} \right] x \quad (1.142)$$

1.2.6 CFD simulation for heat exchangers

1.2.6.1 Recent CFD researches for the heat exchanger

Computational fluid dynamics (CFD) is a numerical solution methodology of governing equations for mass conservation, momentum, heat transfer and other transport processes (Sunden, 2007). CFD simulation applied for the heat exchangers can be categorized into two main groups: one is to model the entire heat exchanger or the heat transferring surface, and the other is to identify modules or group of modules that repeat themselves in a periodic or cyclic manner in the main flow direction. Table 1.5 shows the summary of recent CFD researches for the heat exchanger.

Table 1.5: Summary of CFD research for the heat exchanger

Author	Computational domain	Viscous model	Fluid	Heat exchanger	Experimental verification
Sunden (2007)	Unitary cell	RANS-based turbulent model	Air	Corrugated plate heat exchanger	Yes
Jain et al. (2007)	Entire plate	Realizable k- ε	Water	Corrugated plate heat exchanger	No
Freund and Kabelac (2010)	Unitary cell	RSM	Water	Corrugated plate heat exchanger	Yes
Galeazzo et al. (2006)	Entire HX	k- ε	Water	Flat plate heat exchanger	Yes
Ozden and Tari (2010)	Entire HX	k- ε standard, k- ε realizable, Spalart-Allmaras 2nd order	Water	Shell and tube heat exchanger	No
Zhang et al. (2009)	Entire HX	-	Water	Shell and tube heat exchanger	Yes
Kumar et al. (2006)	Part of HX	k- ε	Water	Tube in tube heat exchanger	Yes
Kho et al. (1999)	Plate with inlet and outlet port	k- ε	Water	Flat plate heat exchanger	Yes

1.2.6.2 Turbulent model

The flow is said to be turbulent when all the transport quantities (mass, momentum and energy) exhibit periodic, irregular fluctuations in time and space. Such conditions enhance mixing of these transport variables. Since these turbulent flows have the characteristic of high frequency and very small scale, it is hard to simulate directly in the calculation. Therefore, two alternative methods came up to be able to simulate turbulent flows in the calculation, namely Reynolds-averaging and filtering. (Fluent 6.1 documentation)

Reynolds averaging method defines the quantities in the Navier-Stokes equation as the summation of mean and fluctuating quantity. Therefore, the exact Navier-Stokes equation shown in Eq. (1.143) can be expressed as Eq. (1.144).

$$\nabla \cdot (\rho \mathbf{u} \mathbf{u}) = -\nabla P + \nabla \cdot \left[\mu \left(\nabla \mathbf{u} + \nabla \mathbf{u}^T - \frac{2}{3} \nabla \cdot \mathbf{u} \right) \right] \quad (1.143)$$

$$\nabla \cdot (\rho \bar{\mathbf{u}} \bar{\mathbf{u}}) = -\nabla P + \nabla \cdot \left[\mu \left(\nabla \bar{\mathbf{u}} + \nabla \bar{\mathbf{u}}^T - \frac{2}{3} \nabla \cdot \bar{\mathbf{u}} \right) \right] + \nabla \cdot (-\rho \mathbf{u}' \mathbf{u}') \quad (1.144)$$

The additional term, $(-\rho \mathbf{u}' \mathbf{u}')$ in Eq. (1.144) represents turbulent flow, which is called Reynolds stresses. This method includes Spalart-Allmaras model, Standard k- ϵ model, Renormalization-group (RNG) k- ϵ model, Realizable k- ϵ model, Standard k- ω model, and Shear-stress transport (SST) k- ω model (Fluent[®] 6.3.26).

A Filtering method defines that large eddies are directly solved, while small eddies are modeled. It assumes that momentum, mass, energy, and other passive scalars are transported mostly by large eddies.

The choice of turbulent model will depend on considerations such as the physics encompassed in the flow, the established practice for a specific class of problem, the level of accuracy required, the available computational resources, and the amount of time available for the simulation (Fluent Inc, 2006). Table 1.6 shows the summary of turbulent models in Fluent 6.3.2.

Table 1.6: Turbulent model in Fluent

Turbulent model	Description
Spalart-Allmaras Model	Relatively crude simulations on coarse meshes where accurate turbulent flow computations are not critical.
Standard $k - \epsilon$ model	Fully turbulent, and the effects of molecular viscosity are negligible.
Renormalization-group (RNG) $k - \epsilon$ model	Enhancing accuracy for swirling flows.
Realizable $k - \epsilon$ model	Flows involving rotation, boundary layers under strong adverse pressure gradients, separation, and recirculation.
Standard $k - \omega$ model	For low-Reynolds-number effects, compressibility, and shear flow spreading
Shear-stress transport (SST) $k - \omega$ model	Accurate and reliable for a wider class of flows (e.g., adverse pressure gradient flows, airfoils, transonic shock waves)
Reynolds stress model (RSM)	Suitable for the effects of streamline curvature, swirl, rotation, and rapid changes in strain rate in a more rigorous manner than one-equation and two-equation models. Accurate predictions for complex flows.
Large eddy simulation (LES) model	More appropriate in the turbulent modeling, but it requires a significant amount of computational resources, which is several orders of magnitudes higher than that of SST $k - \omega$

Successful computations of turbulent flows require some consideration during the mesh generation since turbulence plays a dominant role in the transport of mean momentum and other parameters (Fluent 6.3 document). A parameter called y^+ , which is a non-dimensional parameter, is used to check the near-wall mesh. This is defined in Eq. (1.145). Table 1.7 shows the guideline of the y^+ value for different wall treatment.

$$y^+ = \frac{\rho u_\tau y_p}{\mu} \quad (1.145)$$

where,

$u_\tau = \sqrt{\tau_w / \rho_w}$ is the friction velocity

y_p is the distance to the wall

Table 1.7: Guideline for the y^+ values

Treatment	y^+ value	Comments
Standard wall treatment	$30 < y^+ < 300$	A value close to 30 is most desirable.
Enhanced wall treatment	the order of $y^+=1$	A higher y^+ is acceptable as long as it is inside the viscous sub-layer. ($y^+ < 5$)

1.2.7 Heat exchanger design optimization

When the complete CFD simulation is performed to determine the optimum thermal and hydraulic performance of the heat exchanger, it may result in huge computational cost even though the periodic module of the heat exchanger was chosen for simulation. Moreover, the optimization algorithms require multiple evaluations of objectives and constraints. Therefore, approximation-assisted optimization (AAO) has been applied for optimization using numerical simulations. AAO techniques have been developed by the creation of meta-models or correlations that could represent the thermal-hydraulic performances of heat exchangers, thus using fewer numerical simulation runs. Two types of responses are identified in approximation techniques: true response and predicted response. The true response is the output from an experiment or simulation, while the predicted response is the output of a meta-model representing the experiment or the simulation (Abdelaziz, 2009). The meta-model can be referred to as a simpler analysis/simulation model that can replace the original simulation model with

acceptable estimation errors in their responses, but can be more computationally efficient when compared to the original experiments or simulation models. Numerous meta-model techniques have been developed and applied to engineering applications such as artificial neural networks (ANNs) (Fonseca et al., 2003), response surface models (RSM), the Kriging method, multivariate adaptive regression splines (MARS), and the radial basis function (RBF) (Park et al., 2006). Among them, Kriging meta-model techniques are most widely used for heat exchangers because of their flexibility and suitability (Simpson et al., 2001). Moreover, they are proven to work well with highly nonlinear functions, as well as for predicting uncertainty (Li et al., 2007, 2008). Table 1.8 shows the summary of recent heat exchanger optimization research with the AAO techniques. When the typical AAO technique was utilized to develop a reasonable meta-model in the optimized region, its process could require a large number of CFD runs. This obtained meta-model was globally accurate in given boundary conditions. However, when the objectives and constraints of the optimization problem were clearly defined, the process of building meta-model could be improved by updating the samples near the expected optimum region. It should be noted that this approach is only valid for the optimization problems with moderately non-linear behaviors such as a heat exchanger design optimization. After obtaining intermediate optimum solutions as calculated by the multi-objective genetic algorithm (MOGA), the optimum solutions can be filtered and the next set of samples can be selected to improve the meta-models' response in the expected optimum region. This AAO technique named as online approximation-assisted optimization (OAAO) was validated with an air-cooled heat exchanger design (Saleh et al., 2010). When the accuracy of the results was comparable with the typical AAO, the OAAO approach

resulted in a significant reduction of computational cost: the typical AAO required 300 samples, while the OAAO needed only 140 samples. The OAAO could save more than 60% of the computational time required to obtain similar results as the typical AAO.

Table 1.8: Summary of heat exchanger optimization research with AAO technique

Authors	Meta-model method	Data selection	Application	Objectives
Lee et al. (2001)	Curve fitting	-	Plate heat exchanger	Min: pressure loss Max: heat transfer
Park and Moon (2005)	3-Points Polynomial Interpolation	DOE	Micro heat exchanger	Min: pressure loss
Park et al. (2006)	Kriging	DOE – Space filling (Latin Hypercube)	Plate- fin heat sink	Min: pressure loss Max: heat transfer
Aute (2008)	Kriging	DOE – Space filling method	Air-cooled heat exchanger	Min: pressure loss Max: heat transfer
Abdelaziz (2009)	Kriging	Space filling method	Air-cooled heat exchanger	Min: pressure loss Max: heat transfer
Han et al. (2011)	Kriging	Space filling method	Plate heat exchanger	Min: pressure loss Max: heat transfer
Khaled et al. (2010)	Kriging	Space filling method	Air-cooled heat exchanger	Min: HX volume Min: pressure drop

While exploring and understanding the design space of the low temperature lift heat exchangers for the LTLHP application, literature survey suggests there are significant gaps as follows:

- There was very limited research about the heat exchanger performance for the low temperature lift heat pump application. Most of the studies were about the system performance investigations.

- It has not done before about the study of the plate heat exchanger performance under low refrigerant mass flux and low heat flux conditions.
- CFD simulation with different turbulent models for the plate heat exchanger was not conducted.
- There were very limited studies about the online approximation assisted optimization technique in the area of the heat exchanger optimization.

1.3 Objective

This dissertation focuses on the comprehensive understanding and investigation of the hydraulic and thermal performance of low temperature lift high performing heat exchangers for the low temperature lift heat pump applications. It has four main objectives: (1) investigate the performance of the current plate heat exchanger (PHX) experimentally and numerically to establish a baseline for the application of the LTLHP system, and explore and understand the design space for low temperature difference high performing heat exchangers, (2) based on the lessons from the PHX investigation, develop a novel LTLHX with new geometries which has improved thermal and hydraulic performance compared to the baseline, (3) optimize that geometry for the optimum performance of the LTLHP system, (4) validate the novel LTLHX performance with experimental test, and (5) apply the LTLHXs to a water source heat pump system.

Investigation of the PHX performance includes: (a) addressing the characteristics of the PHX performance under the LTLHP operating conditions, which requires unique operating conditions of small temperature difference between water inlet and outlet, and between heat source and refrigerant; (b) conducting experimental test with R22 and

ammonia; (c) conducting CFD simulation to explore the PHX performance; (d) addressing potentials and limitations of the PHX.

Investigation of the novel LTLHX designs encompass: (a) newly defining geometries of the novel LTLHX, such as a channel width, channel height, channel pitch, and plate gap; (b) conducting the CFD simulations and optimization to develop the optimum novel LTLHX; (c) conducting the experimental test to validate the CFD simulation; (d) exploring and understanding hydraulic and thermal characteristics of the novel LTLHX.

Optimization of the novel LTLHX is conducted based on the online approximation assisted optimization technique. It requires: (a) design of experiments (DOE) and sampling; (b) meta-model building; (c) meta-model evaluation; (d) optimization; (e) updating the meta-models using selected optimum designs based on a space filling filter; (f) verification of optimal design using CFD results.

Application of the LTLHX to the LTLHP system includes: (a) parametric study of the LTLHP system; and (b) comparison between the PHX and novel LTLHX.

1.4 Dissertation organization

This dissertation is organized that Chapter 1 contains the introduction of low temperature lift heat exchanger, and literature review including heat transfer and pressure drop of heat exchangers, CFD simulation, and optimization research. This supports the motivation of this thesis. Approaches about experimental test, CFD simulation, and optimization are presented in Chapter 2. Chapter 3 is dedicated to the study of PHX as a baseline, which is currently available as the best LTLHX in the market. Numerical simulation as well as experimental test is carried out with considering various parameters

and operating conditions. Chapter 4 presents the development of the novel LTLHX, which is designed to improve the performance of PHX. Its geometries were newly defined and optimized to maximize heat transfer coefficient and minimize pressure drop with approximation assisted optimization (AAO) techniques. Then the novel heat exchanger is investigated with numerically and experimentally with various parameters. In Chapter 5, the LTLHXs are applied to a water heat source heat pump system. The design guide line is suggested. The performance of the water heat source heat pump system is investigated, and optimized. Chapter 6 includes the summary and conclusions of the study. Finally, Chapter 7 concludes the thesis with contributions and future work.

CHAPTER 2. Research Approach

The approaches of the experimental test, Computational Fluid Dynamics (CFD) simulation and optimization are described in this chapter.

2.1 Experimental setup

2.1.1 Test facility

An experimental test facility was built to evaluate the thermal and hydraulic performance of the PHX. The heat transfer coefficient and pressure drop of the PHX was investigated as an evaporator. The experimental apparatus, which consists of the evaporator and condenser connected in series in a closed loop, is shown schematically in Fig. 2.1. Pre-heater and post-heater units were installed before and after the evaporator to regulate the test conditions. A variable speed pump was used to control the refrigerant flow rate, and the expansion valve was for the evaporation pressure control. For the water-side, cold water was supplied to the condenser and warm water was supplied to the evaporator. Water temperature was regulated with a chiller package and an electric heater, and the mass flow rate of the water was controlled with variable speed pumps.

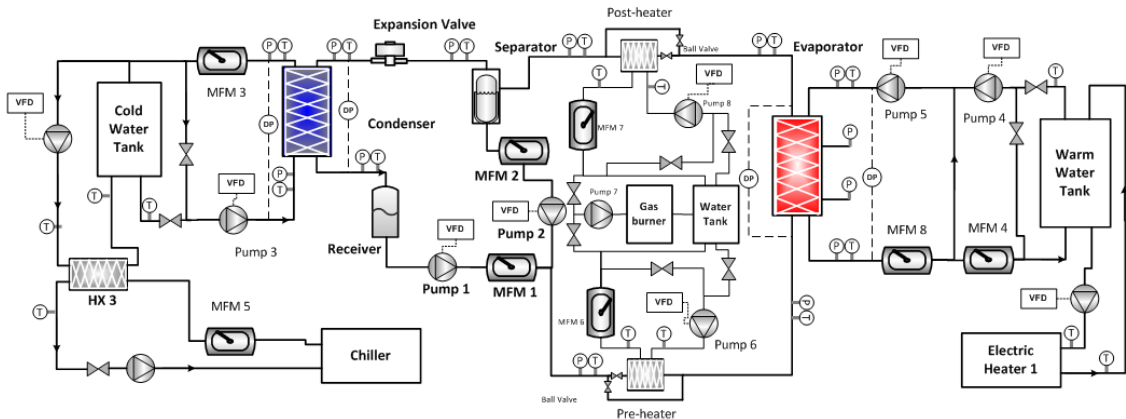


Fig. 2.1: Schematic of test facility

2.1.2 Instrumentation and DAQ system

Table 2.1 shows the instruments installed in the test facility. Coriolis type mass flow meters were installed in the working fluid and water side. For the measurement of temperatures, RTD sensors were installed instead of thermocouples to get a higher accuracy.

Table 2.1: Measurement instruments

Instrument	Type	Manufacturer	Model #	Range	Systematic Uncertainty
Mass Flow Meter	Coriolis	Micro Motion	CMF100H	0 ~ 3 kg/s	0.03%
Pressure Transducers	Strain	Wika	S-11	0 ~ 1,379 kPa	0.13%
Differential Pressure Transducer	Strain	Omega	PX-409	0 ~ 69 kPa	0.08%
RTD	Resistance	Omega	P-M-1/10-1	- 200 ~ 800 °C	0.03°C
Level sensor	Conductivity	Intempco	LTX-LP-BHS	0 ~ 100%	1%

24 National Instrument's compact field point modules were installed as the data acquisition (DAQ) system. In addition to receiving the data from the test facility, it can also provide signals to the system so that a proportional–integral–derivative (PID) control was possible. Fig. 2.2 shows the screenshot of Labview program, which was developed for controlling the system. All controls for temperatures, mass flow rates and pressures were performed through the Labview program. System control can be conducted with either PID or manual. For the PID control, 10 PID controllers were created.

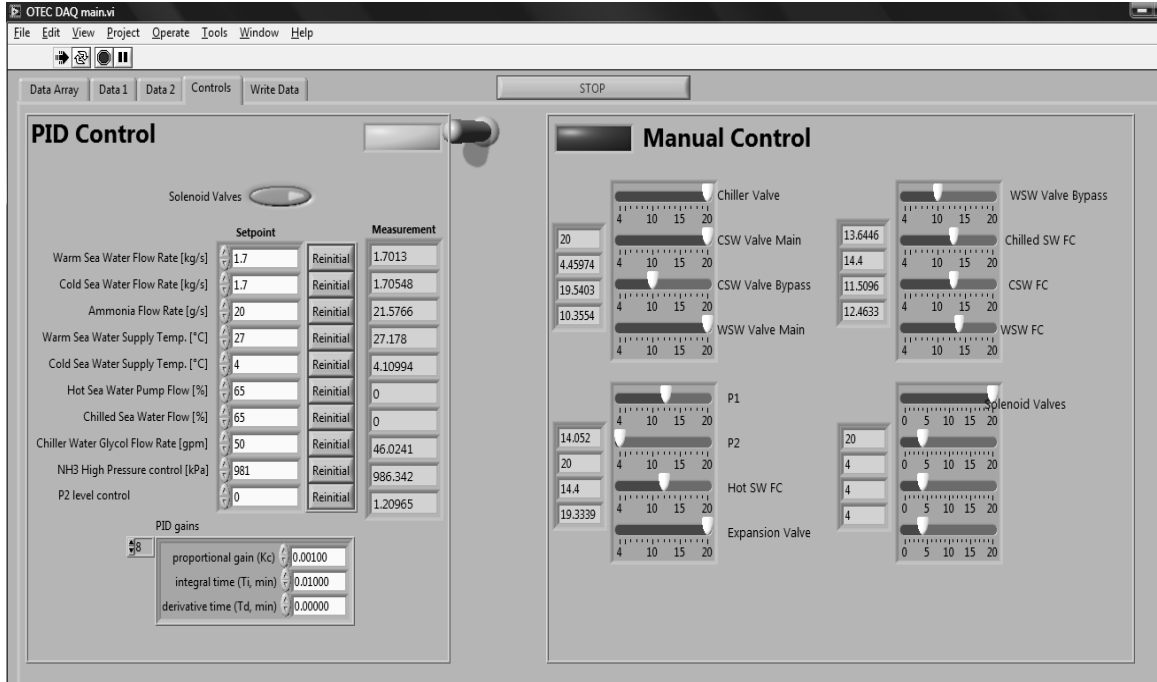


Fig. 2.2: Screenshot of Labview control program

2.1.3 Energy balance

The energy balance of the heat exchangers was checked out for each test. Heat transfer capacity of working fluid-side was calculated by the enthalpy method as shown in Eq. (2.1). It was compared with heat transfer capacity of water-side calculated by the enthalpy method. Energy balance of the heat exchangers is defined as the difference ratio of these two capacities as shown in Eq. (2.2).

$$\dot{Q} = \dot{m} \times \Delta h \quad (2.1)$$

$$\epsilon = \left(1 - \frac{\dot{Q}_{\text{Refrigerant}}}{\dot{Q}_{\text{Water}}} \right) \times 100 \quad (2.2)$$

2.1.4 Uncertainty analysis

Total uncertainty is the summation of systematic error and random error. Systematic error is caused by measurement itself. It is the difference between true value

and the value that instrument can measure. Random error is caused by predictable fluctuation in reading. Standard deviation is usually used as a random error.

The uncertainties of directly measured parameters such as temperatures, pressures, and mass flow rates are calculated by combining the absolute error and standard deviation which can be obtained during steady state condition. The uncertainty of calculated parameters such as an enthalpies, superheat and capacities are more complex to calculate. In these cases, the uncertainty is calculated by considering possible maximum and minimum cases. Pythagorean summation can be used for uncertainty propagation. For example, enthalpy is a function of pressure and temperature. The uncertainty of an enthalpy is calculated with Eqs. (2.3) through (2.7). Typical propagation of uncertainty for each measured property is summarized in Table 2.2.

$$\omega_h = \sqrt{\left(\frac{\delta h}{\delta P} \omega_p\right)^2 + \left(\frac{\delta h}{\delta T} \omega_T\right)^2} \quad (2.3)$$

$$\frac{\delta h}{\delta P} = \frac{h(P_{\max}) - h(P_{\min})}{P_{\max} - P_{\min}} \quad (2.4)$$

$$\frac{\delta h}{\delta T} = \frac{h(T_{\max}) - h(T_{\min})}{T_{\max} - T_{\min}} \quad (2.5)$$

$$P_{\max} = P_{\text{measured}} + \omega_{p,\text{combined}} \quad (2.6)$$

$$T_{\max} = T_{\text{measured}} + \omega_{T,\text{combined}} \quad (2.7)$$

Table 2.2: Typical propagation of uncertainty

Property	Unit	Value	Systematic error	Random error	Uncertainty
T Water in	°C	26.1	0.03	0.13	0.16
T Water out	°C	25.2	0.03	0.11	0.14
P Water in	kPa	102	0.34	0.08	0.08
P Water out	kPa	124	0.34	0.09	0.43
T ref in	°C	12.0	0.03	0.03	0.06
T ref out	°C	25.2	0.03	0.03	0.06
P ref in	kPa	877	0.34	4.66	5.0
P ref out	kPa	869	0.34	4.66	5.0
P evaporation	kPa	873	-	-	3.5
T evaporation	°C	20.6	-	-	0.13
LMTD	°C	5.05	-	-	0.17
MFR water	kg s ⁻¹	7.0	0.189	0.012	0.201
Q water	kW	27.8	-	-	6.19
MFR ref	g s ⁻¹	22.0	0.03	0.08	0.11
h ref in	kJ kg ⁻¹	399	-	-	0.28
h ref out	kJ kg ⁻¹	1638	-	-	0.42
Q ref	kW	27.2	-	-	0.14
Energy balance	%	-2.0	-	-	-
Uo	W·m ⁻² ·K ⁻¹	989	-	-	33
Heat flux	kW m ⁻²	5.00	-	-	0.03
Sub-cooling	K	8.6	-	-	0.1
Super-heating	K	4.6	-	-	0.1
DP water	kPa	6.2	0.02	0.1	0.1
DP refrigerant	kPa	7.7	-	-	7.1
h refrigerant	W·m ⁻² ·K ⁻¹	1989	-	-	65
G (mass flux)	kg·m ⁻² ·s ⁻¹	41.14	-	-	0.71
H _{fg}	kJ·kg ⁻¹	1184	-	-	0.09
Bo	-	0.00010258	-	-	0.000002
G water	kg·m ⁻² ·s ⁻¹	958.9	-	-	27.6
v	m·s ⁻¹	0.962	-	-	0.0277
density	kg·m ⁻³	996.9	-	-	0.0000
mu wall	kg·m ⁻¹ ·s ⁻¹	0.0009	-	-	0.000003
Wall temp	°C	23.1	-	-	0.08
Nu water	-	80.1	-	-	1.73
h water	W·m ⁻² ·K ⁻¹	3874	-	-	84

2.1.5 Data reduction

Convective heat transfer coefficient between the solid surface and moving fluid is calculated by Newton's law of cooling. The main difficulty of this methodology lies in the measurement of the surface temperature (Fernandez-Seara et al., 2007). The surface temperature varies from location to location along the flow, and sometimes the surface is not accessible for temperature measurement. The Wilson plot method is an alternative experimental method for calculating the convective heat transfer coefficient without measuring surface temperature. In this study, a modified Wilson plot method (Shah, 1990; Longo et al., 2004; Hayes and Jokar, 2009) was applied to calculate the heat transfer coefficient, which reflects the temperature change on both fluids.

In order to evaluate the performance of heat exchangers, it is essential to calculate the mean temperature difference between two fluids. Basically, there are two sections in the refrigerant-side: the single-phase section and the two-phase section. Since the single-phase section is much smaller than the two-phase section, the single-phase section was neglected and only the two-phase section was considered. Logarithmic mean temperature difference (*LMTD*) in the plate heat exchanger is defined as:

$$LMTD = \frac{(t_{w,in} - t_r) - (t_{w,out} - t_r)}{\ln\left[\frac{(t_{w,in} - t_r)}{(t_{w,out} - t_r)}\right]} \quad (2.8)$$

The overall heat transfer coefficient (U) is the ratio between heat transfer capacity (\dot{Q}) and the heat transfer area (A) and *LMTD*:

$$U = \frac{\dot{Q}}{A \cdot LMTD} \quad (2.9)$$

In the calculation of each heat transfer coefficient in the refrigerant-side and the water-side, the heat transfer coefficient of water-side (h_w) was calculated with correlations from the water-to-water test (obtained from modified Wilson plot). Then the heat transfer coefficient of the refrigerant-side (h_r) was calculated from U and h_w :

$$h_r = \frac{1}{\frac{1}{U} - \frac{1}{h_w} + \frac{t}{k}} \quad (2.10)$$

$$f = \frac{\rho \cdot (p_{in} - p_{out}) \cdot d_e}{2 \cdot L \cdot G^2} \quad (2.11)$$

For the water-side, all properties such as a density, conductivity, and viscosity were calculated based on the average temperature and pressure of the heat exchanger inlet and outlet. Friction factor (f) was calculated with Eqs. (2.20).

In this thesis, an equivalent diameter (d_e), was used in calculating the Re and f . It has the advantage of scaling the convection performance to that of plain parallel plates and isolating the effects of the area enlargement factor on the heat transfer enhancement, especially when the enlargement factor is unknown (Shah et al., 1988; Wang et al., 2007; Han et al., 2011).

2.2 CFD simulation

2.2.1 CFD simulation for heat exchanger

Fig. 2.3 shows the flow chart of the CFD simulation. In order to create the computational domain, Solidworks 2010 was used. For the meshing, Gambit 2.4.6 was utilized. This meshed object was solved with Fluent 6.3.26.

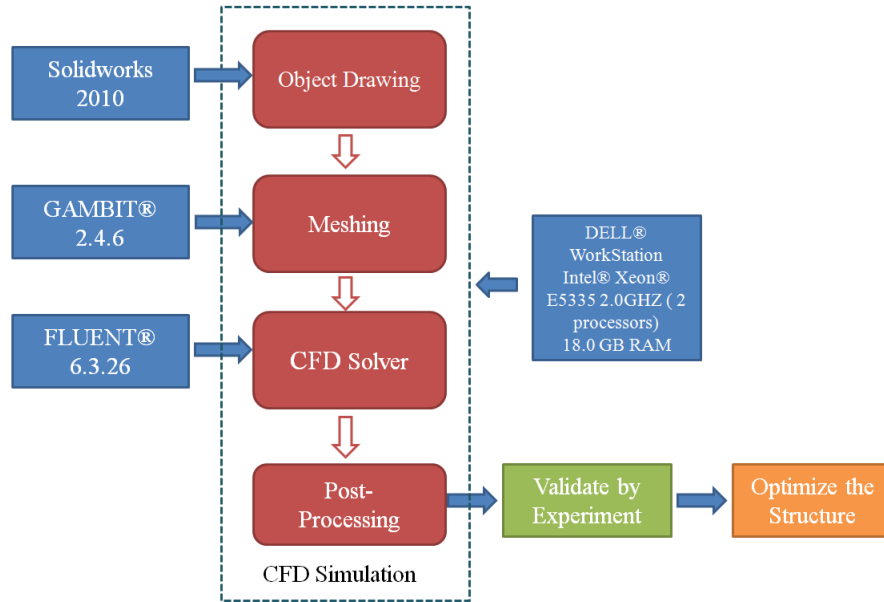


Fig. 2.3: Flow chart of CFD simulation

2.2.1.1 Turbulent model

In this thesis, several different turbulent models were selected from Fluent 6.3.26 and tested: Spalart-Allmaras model, standard $k-\epsilon$ model, realizable $k-\epsilon$ model, SST $k-\omega$ model, and Reynolds stress model. The simulation results of these turbulent models were compared with experimental results, and the best turbulent model is selected.

2.2.1.2 Model assumption and data reduction

The governing equations of continuity, momentum (Navier-Stokes) and energy listed as Eqs. (2.1) through (2.3) were solved in Cartesian coordinates based on the assumptions as follows:

- Three-dimensional, incompressible and steady state flow;
- Single phase flow, no gravity or any other body force involved;
- Constant wall temperature with water as the working fluid;
- No fouling of any kind exists in the computational domain;

- The computational domain is located in the central part of the heat exchanger, and the periodicity is established perpendicular to the flow direction;
- Viscous dissipation is negligible in the energy equations.

$$\nabla \cdot (\rho \bar{u}) = 0 \quad (2.12)$$

$$\nabla \cdot (\rho \bar{u} \bar{u}) = -\nabla p + \nabla \cdot \left[\mu \left(\nabla \bar{u} + \nabla \bar{u}^T - \frac{2}{3} \nabla \cdot \bar{u} \right) \right] \quad (2.13)$$

$$\nabla \cdot \left[\rho \bar{u} \left(h + \frac{u^2}{2} \right) \right] = \nabla \cdot (k \nabla T) \quad (2.14)$$

The Re and Nu are defined as follows:

$$Re = \frac{G \cdot d}{\mu} \quad (2.15)$$

$$Nu = \frac{h \cdot d}{k} \quad (2.16)$$

where h stands for the heat transfer coefficient; and μ and k are fluid dynamic viscosity and thermal conductivity, respectively.

In the numerical modeling, the thermal-hydraulic performances were evaluated in terms of heat transfer coefficient (h) and the pumping power (P/L), which were calculated using the following Eqs:

$$h = \frac{Q}{A \cdot \Delta T} = \frac{C_p \cdot \dot{m} \cdot (T_{out} - T_{in})}{A \cdot \frac{(T_{in} - T_w) - (T_{out} - T_w)}{\ln[(T_{in} - T_w)/(T_{out} - T_w)]}} \quad (2.17)$$

$$P/L = V \cdot (p_{in} - p_{out}) \quad (2.18)$$

where A is the total heat transfer area and ΔT between the fluid and wall was calculated using the logarithmic mean temperature difference (LMTD).

2.2.1.3 Post-processing

Temperatures and pressures of inlet and outlet sections were calculated based on the mass-weighted average method in the Fluent. The surface temperature of the wall was calculated with area-weighted average method. Mass weighted average method can be used when the average value on a flow boundary, such as average enthalpy at a velocity inlet needs to be found. Area-weighted average method can be used when the average value on a solid surface, such as the average heat flux on a heated wall with a specified temperature needs to be found.

2.2.2 PHX simulation

2.2.2.1 Geometrical parameters

A CFD simulation was conducted for a better understanding of the heat transfer and pressure drop characteristics of the PHX. Fig. 2.4 shows the geometry of the PHX used in the CFD simulation, which includes the flow gap (b), corrugation pitch (λ), chevron angle (β), and enlargement factor (ϕ).

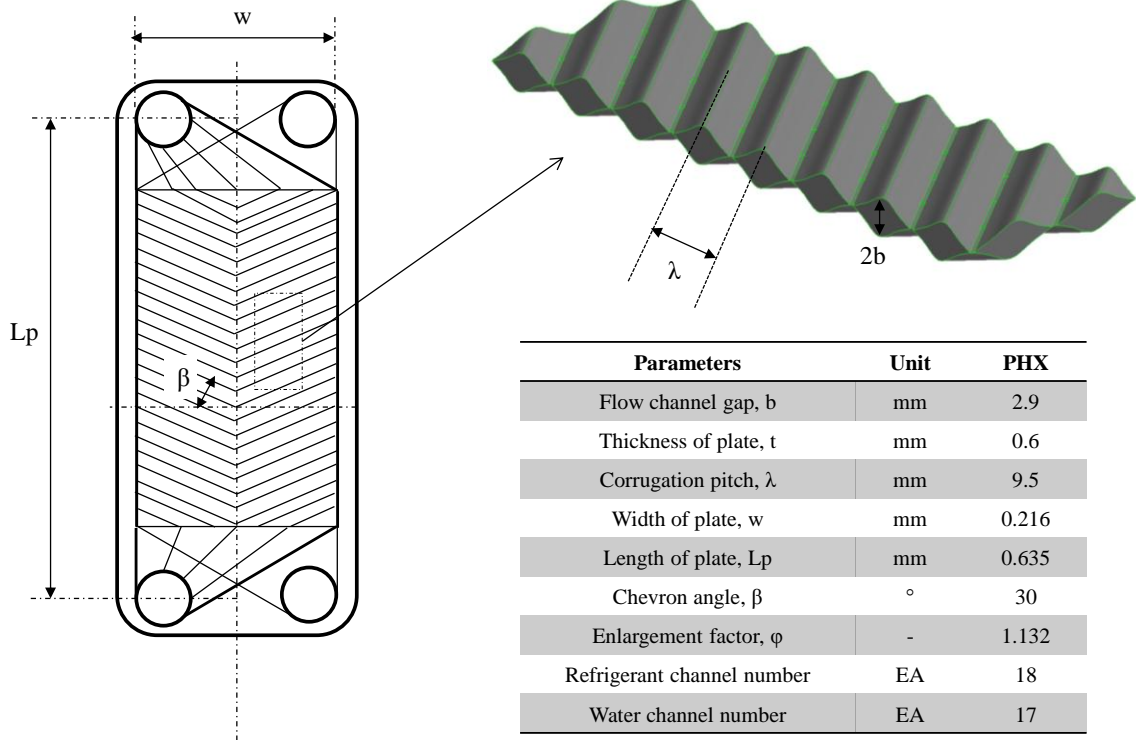


Fig. 2.4: Parameters of plate heat exchanger

PHX consists of chevron-type corrugations that have a sinusoidal shape, and the sinusoidal curve can be described as the Eq. (2.19).

$$f(x) = \frac{b}{2} \sin \left[\frac{2\pi}{P} \left(x - \frac{P}{4} \right) \right] + \frac{b}{2} \quad (2.19)$$

where, b is the corrugation depth (or corrugation amplitude) defined as the actual gap available for the flow and P is the corrugation pitch (or wavelength). The most influential geometrical parameters that will affect the thermal-hydraulic performances of the PHEs are corrugation angle β and enlargement factor ϕ . The corrugation angle β (some named inclination angle and defined as $\pi/2 - \beta$) defines the thermal-hydraulic softness and hardness while the enlargement factor ϕ is the ratio of the developed surface

area to the projected area depending on the corrugation depth b and corrugation pitch P , which could be approximately calculated using Eq. (2.20).

$$\phi = \frac{1}{6} \left[1 + \sqrt{1 + \left(\frac{\pi b}{P} \right)^2} + 4 \sqrt{1 + \left(\frac{\pi b}{P} \right)^2} / 2 \right] \quad (2.20)$$

2.2.2.2 Computational grid system

Due to the complexity of the inner geometry of plate heat exchanger, generating the object and meshing are the most challenging parts. Fig. 2.5 shows the calculation domain which simulates the part of PHX. Fig. 2.6 shows the calculation domain that simulates the role of the PHX. A rendering of the mesh system for the inner space of the PHX was generated using Gambit 2.4.6 (ANSYS FLUENT 12.0 Documentation, 2009). An unstructured mesh system with hexahedral and tetrahedral type of mesh is created. In an actual PHX, the two plates are in direct contact. Because of this, a contact point was required for the virtual PHX. However, a virtual contact point would cause too much skewing in the mesh rendering process, so a contact area was created in the virtual PHX. The contact area was designed to be less than 0.3 mm^2 . To create a small viscous sub-layer, the size function was used with 1.5 of growth factor.

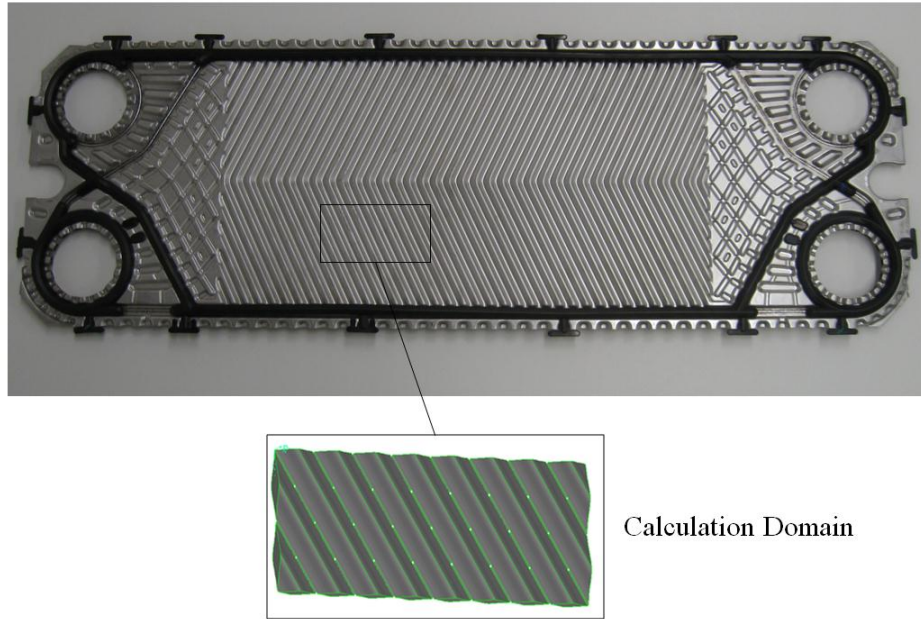


Fig. 2.5: Calculation domain for CFD simulation

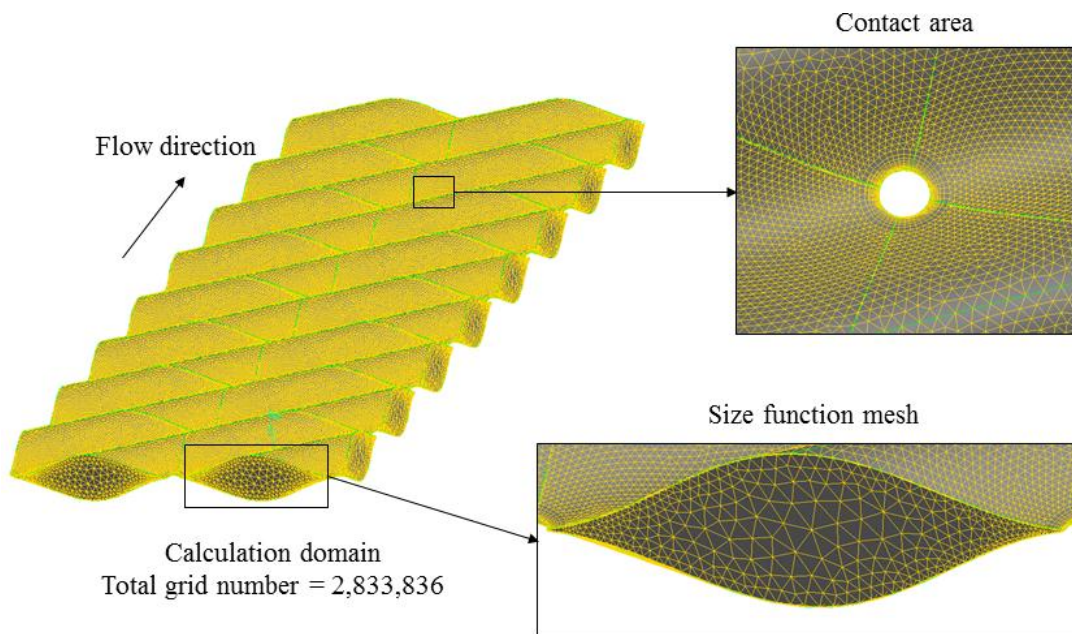


Fig. 2.6: Computational grid system

2.2.2.3 Numerical test matrix

Table 2.3 shows the test matrix of CFD simulation. Water velocity was varied from 0.15 to 0.55 m/s, with 0.05 of increments. Test set 1 is designed to investigate the effect of LMTD on the heat transfer and pressure drop characteristics. There is no clear

explanation about the selection of the turbulent models in the Fluent 6.3.26. Therefore, test set 2 is designed and the effect of the performance difference with different turbulent models will be investigated. Test set 3 are intended to study the effect of Re with laminar model and turbulence model.

Table 2.3: Test matrix of CFD simulation

Test set	Turbulent model	T water inlet (K)	T wall (K)	Water velocity (m/s)
1	SST k- ω model	294	287 to 292 with 1 step	0.14
2	S-A model Standard k-e model Realizable k-e model SST k-w model RSM model	294	292	0.1 to 0.2 with 0.02 step, 0.2 to 0.6 with 0.1 step
3	Laminar	294	292	0.1 to 0.2 with 0.02 step, 0.2 to 0.6 with 0.1 step

2.2.2.4 Near wall treatment

The near-wall modeling significantly impacts the fidelity of numerical solutions. The solution variables in the near-wall region have large gradients, and the momentum and other scalar transports occur most vigorously (Fluent 6.3 document). Since enhanced near-wall model approach is adopted in Fluent, which requires the dimensionless wall distance y^+ to be on the order of 1. Therefore small thickness of boundary layer is created near the wall to ensure that the value y^+ is less than 10. For each simulation, the y^+ value is checked to ensure the fidelity of the calculation as shown in Fig. 2.7. The average y^+ factor of the PHX was less than 3.

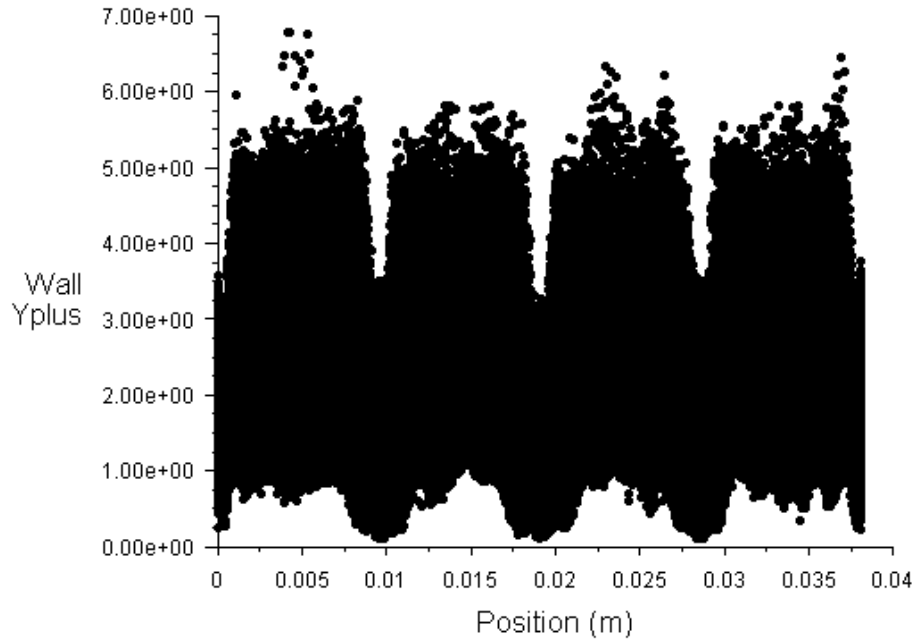


Fig. 2.7: Variation of wall y^+ with position

2.2.3 LTLHX simulation

2.2.3.1 Geometrical parameters

Table 2.4 shows the parameters of initial design and actual manufactured prototype. Since the current manufactured prototype has different dimensions from our initial design, these two dimensions are investigated numerically.

Table 2.4: Parameters of novel LTLHX

	Parameters	Initial design	Actual design
r	area ratio between horizontal and vertical areas	7.55	7.55
a	channel width (mm)	13.5	16.485
b	bonding space (mm)	6	3.519
w	plate width (mm)	350	350
L	plate length (mm)	1,536	1,536
N	channel number (EA)	76	76
c	summit width (mm)	1.5	6.697
h	channel height (mm)	2	1.651
d	gap between the plates (mm)	4, 5, 6	4, 5, 6
t	plate thickness (mm)	1.1	1.1

2.2.3.2 Computational grid system

Fig. 2.8 and Fig. 2.9 show the water flow computational domain of initial design between the horizontal and vertical ammonia channels, respectively. Fig. 2.10 and Fig. 2.11 show the water flow computational domain of current prototype between the horizontal and vertical ammonia channels, respectively. The mesh of the plate and inner space are generated using Gambit 2.4.6. An unstructured mesh system with a tetrahedral type-mesh was created for the inner space, and a structured mesh system with hex type-mesh was created for the wall space. To create a small viscous sub-layer, a boundary layer function was used with a 1.26 growth factor.

Initial design

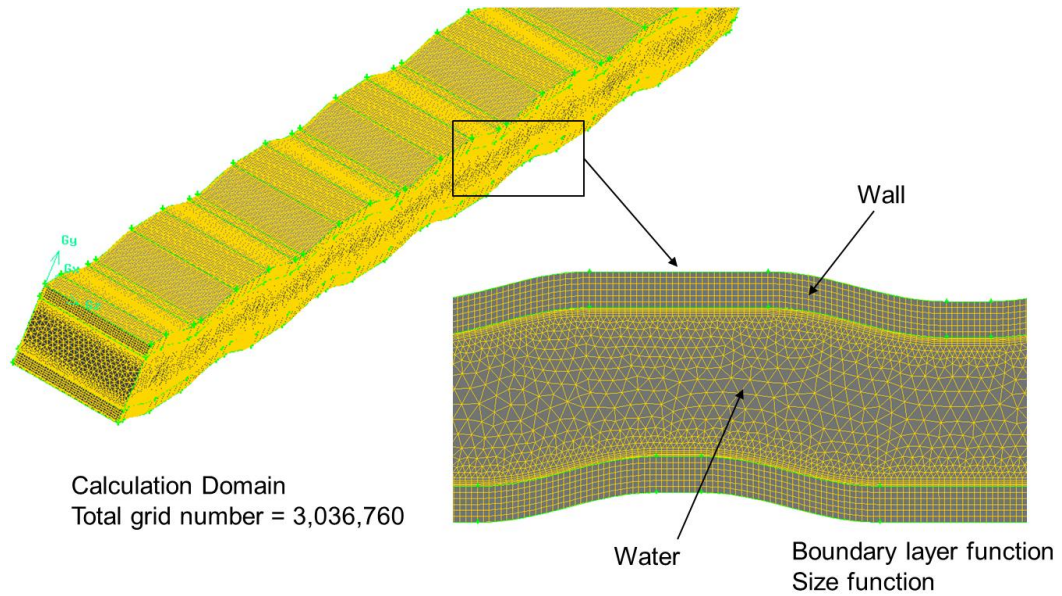


Fig. 2.8: Water flow computational domain of initial design between horizontal ammonia channels

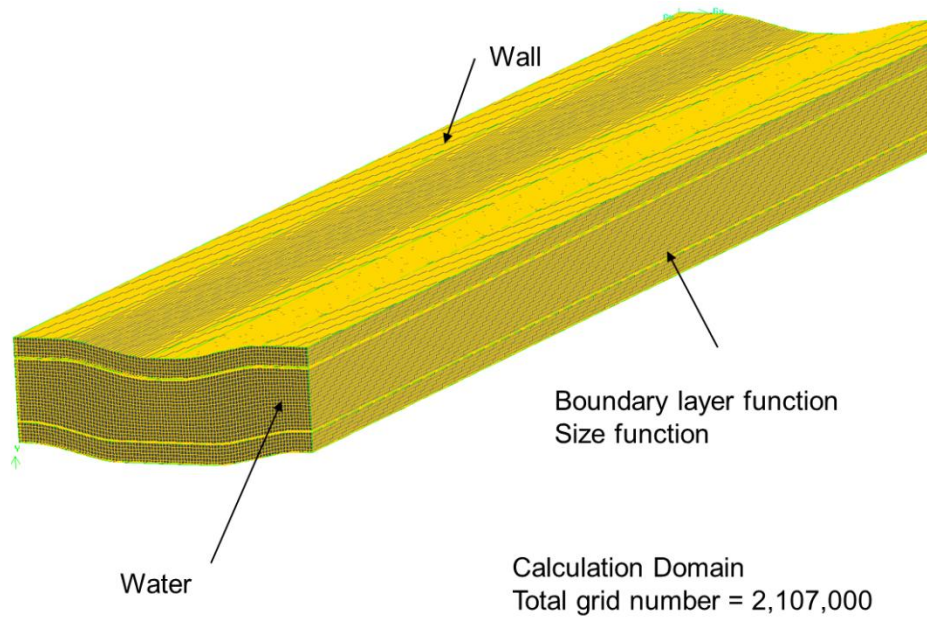


Fig. 2.9: Water flow computational domain of initial design between vertical ammonia channels

Current prototype

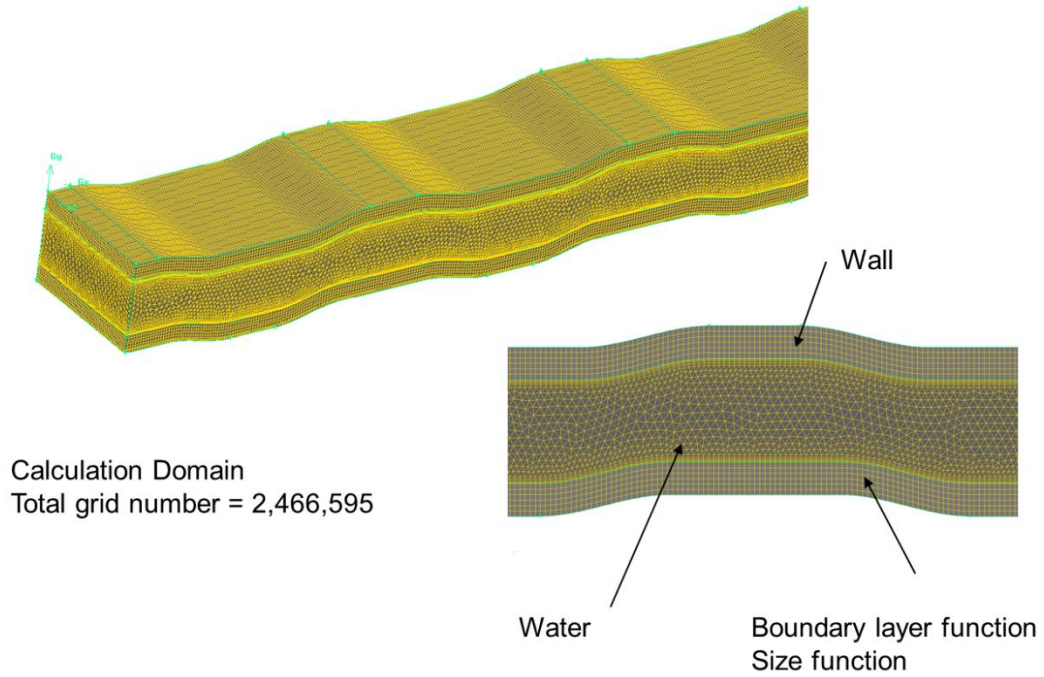


Fig. 2.10: Water flow computational domain of current prototype between horizontal ammonia channels

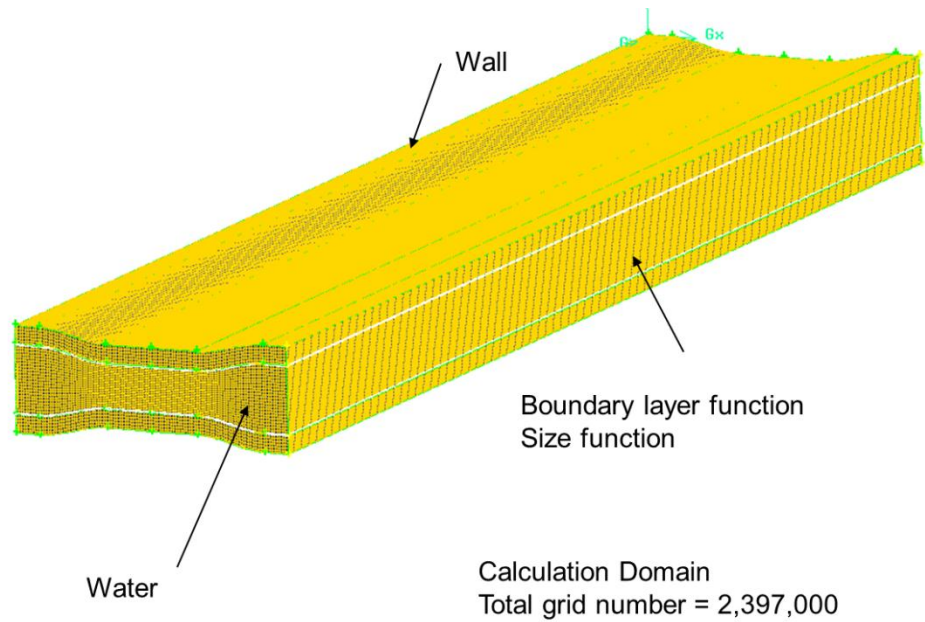


Fig. 2.11: Water flow computational domain of current prototype between vertical ammonia channels

2.2.3.3 Parameter matrix

Table 2.5 shows the parameter matrix of the CFD simulation. Water velocity was varied from 1.0 to 2.0 m/s with 0.2 m/s increment. First, the effects of the logarithmic mean temperature difference (LMTD) on the water-side heat transfer and pressure drop characteristics was investigated. Then, the CFD simulation was carried out for geometries of initial design and current prototype.

Table 2.5: Parameter matrix of CFD simulation

Domain	Case	$T_{\text{water inlet}}$ (K)	T_{wall} (K)	Water velocity (m/s)	Plate gap (mm)
			292		5
			291		5
Initial design	Effect of LMTD	294	290	1.4	5
			289		5
			288		5
			287		5
Initial design	Horizontal flow	294	292		4/5/6
	Vertical flow	294	292	1 to 2.0 with 0.2 step	4/5/6
Current prototype	Horizontal flow	294	292		4/5/6
	Vertical flow	294	292		4/5/6

2.2.3.4 Near wall treatment

The SST $k-\omega$ model was used in Fluent, so that the near-wall model approach is adopted in Fluent, which requires the dimensionless wall distance y^+ to be on the order of 1. Therefore small thickness of boundary layer is created near the wall to ensure that the value y^+ is less than 10. For each simulation, the y^+ value is checked to ensure the fidelity of the calculation as shown in Fig. 2.12. The average y^+ factor of novel heat exchanger was less than 1.

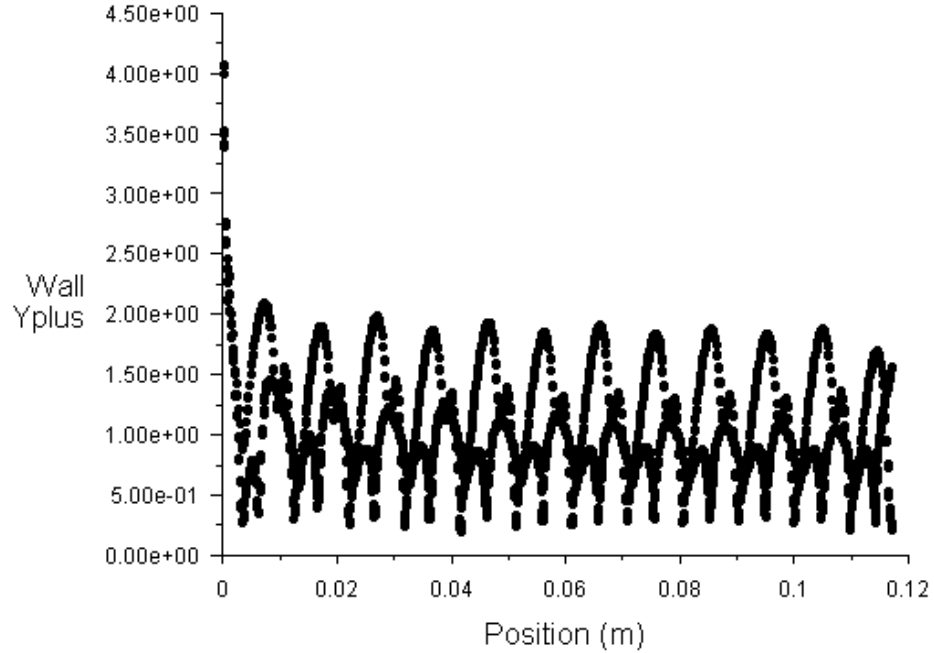


Fig. 2.12: Variation of wall y^+ with position

2.3 Optimization

As described previously, the AAO is an optimization technique that can replace the time-consuming function evaluation with a meta-model or surrogate model. Furthermore, online approximation-assisted optimization (OAAO) updates the meta-models to improve the accuracy of the meta-models in the expected optimum region (Saleh et al, 2010). In this dissertation, the CFD simulation was carried out using a parallel parameterized computational fluid dynamics (PPCFD) simulation, which was proposed by Abdelaziz (2009). This tool automatically generates mesh and CFD journal files, runs the files, and performs post processing to summarize the results. The detailed steps applied in OAAO with PPCFD simulations can be identified as follows: 1) Design of Experiments (DOE) and sampling; 2) meta-model building; 3) meta-model evaluation; 4) optimization; 5) updating the meta-models using selected optimum designs based on a

space filling filter; and 6) verification of optimal design using CFD results. Fig. 2.13 shows the flow chart of optimization of the novel heat exchanger. In order to select the next set of samples to update the meta-models, the space-filling filter was applied to avoid the clustering in the design space (Aute, 2008; Han et al., 2011). The space-filling metric was based on the Euclidean distance in the design space. For all recommended samples, the minimum non-zero distances between each sample and all the pre-existing samples in the design space were calculated. For example, for n points, there are n non-zero distances. Then, a threshold equal to one-half of the maximum of these distances is used as the space filling metric and no more samples are added within this distance. This approach ensures that the new sample points will not be placed close to existing points in the design. Accordingly, the space-filling filter is helpful for reducing the computational cost.

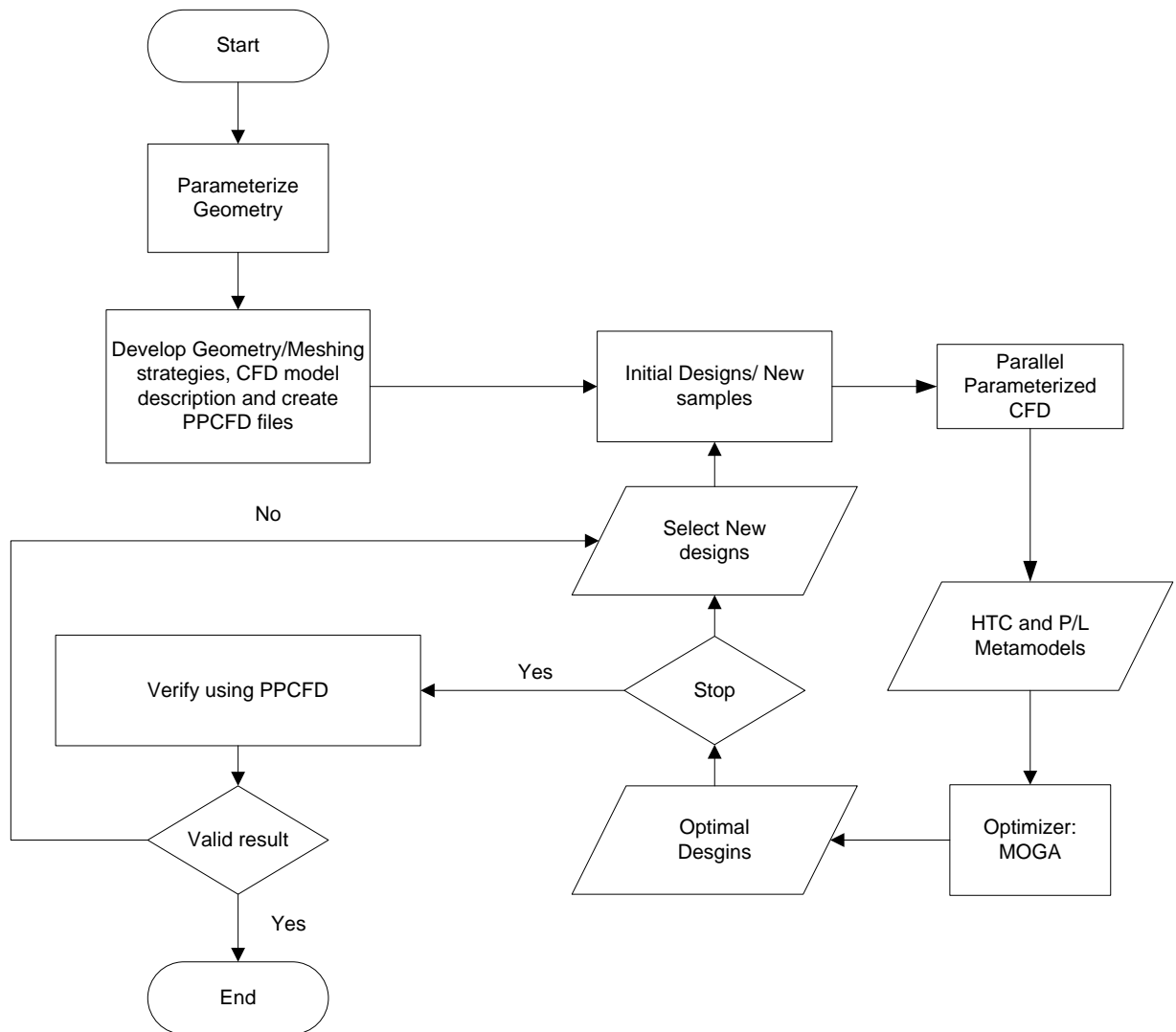


Fig. 2.13. Flow chart of the optimization of novel heat exchanger

The optimization work presented in this study was conducted based on a MOGA. Conventional MATLAB® MOGA was used with 100 individuals in the population in each generation of MOGA. The total number of generations used is 200, with a mutation probability of 0.05, a crossover probability of 0.85, and a 10% individuals' replacement at each generation. This method has many advantages over the conventional gradient-based approach, such as being able to obtain the discrete and global optimum solutions (Deb, 2001).

CHAPTER 3. Baseline Test with Plate Heat Exchanger

Thermal and hydraulic performance of a sinusoidal corrugated plate heat exchanger (PHX) was investigated for the application of a low temperature lift heat pump (LTLHP). The water-side heat transfer coefficient and pressure drop of the PHX were obtained through experimental test. The refrigerant-side heat transfer performance was investigated experimentally by varying several parameters. CFD simulation of the PHX is conducted to explore the potentials of the PHX.

3.1 Experimental test with water-to-water

Convective heat transfer coefficient between the solid surface and moving fluid is calculated by Newton's law of cooling. The main difficulty of this methodology lies in the measurement of the surface temperature. The surface temperature varies from point to point along the flow and sometimes the surface is not accessible to measure temperature. Wilson plot method is an alternative experimental method to calculate convective heat transfer coefficient without measuring surface temperature. Preliminary experimental test is intended to calculate the individual heat transfer coefficients of water-side and refrigerant-side.

3.1.1 Test conditions and test matrix

Table 3.1 shows the experimental test matrix. The test set #1 is designed for the heat transfer calculation of warm water. The test set #2 is designed for achieving same goals for the cold water.

Table 3.1: Test matrix of water-to-water test

Test set	Heat source temperature (°C)	Heat sink temperature (°C)	Heat source MFR (kg-s ⁻¹)	Heat sink MFR (kg-s ⁻¹)	Test
1	25	17	1.0 to 3.0 with 0.1 step	2.50	16

3.1.2 Test procedure

Fig. 3.1 shows the schematic of the water-to-water test facility. Temperature of cold water and warm water was regulated by the chiller package and electric heater, respectively. Water mass flow rates were controlled by the variable speed pump. Water mass flow rate was varied with a certain amount of increments to apply Wilson plot method as shown in Table 4.1. Once the water-side heat transfer coefficient correlation can be calculated, the refrigerant-side heat transfer coefficient correlation can be obtained.

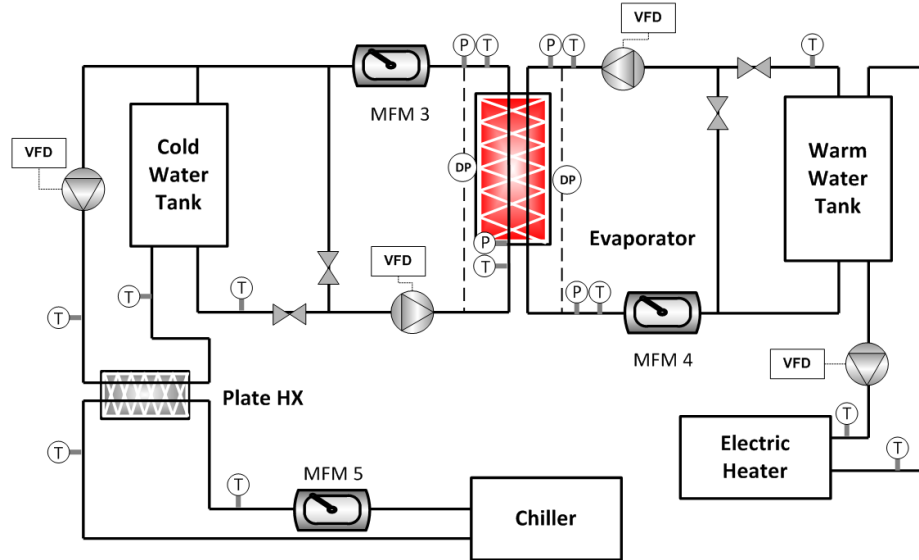


Fig. 3.1: Schematic of the water-to-water test facility

Water-side heat transfer coefficient can be obtained experimentally with several different ways. First is well known original Wilson plot method. When warm water mass

flow rate is varied while cold water mass flow rate is remained constant, the change in the overall heat transfer coefficient is assumed that it is due to the change in warm water mass flow rate. Therefore, the cold water-side heat transfer coefficient is assumed to be constant. Second is modified Wilson plot method. The main difference from the original Wilson plot is that cold water-side heat transfer coefficient is not any more constant. Moreover, temperature changes could be reflected. Third is a direct calculation of heat transfer coefficient without using the Wilson plot. Nusselt numbers of each side are defined as Eqs. (3.1) and (3.2). Constants of both warm and cold water sides are assumed to be identical.

$$Nu_w = C_1 Re_w^{c_2} Pr_w^{c_3} \quad (3.1)$$

$$Nu_c = C_1 Re_c^{c_2} Pr_c^{c_3} \quad (3.2)$$

Heat exchanger used in the test facility is installed vertically, and its height is larger than 0.6 m, so that the correlation can be different between upstream and downstream flows. Therefore, the third approach was excluded from the consideration. Instead, original Wilson plot and modified Wilson plot were used.

3.1.3 Test results of water-side heat transfer coefficient

Test set # 1 was considered to apply Wilson plot in this test, warm water mass flow rate was varied while cold water mass flow rate was maintained at constant. Fig. 3.2 shows the results of the original Wilson plot. A term “v” in X Axis indicates the velocity of warm water in the heat exchanger. Regression fit was 0.9983 and intercept was 0.0001.

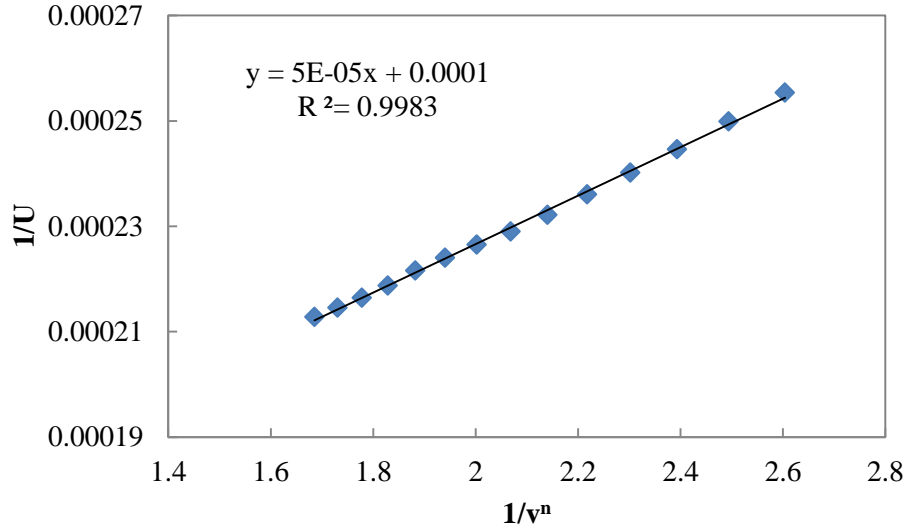


Fig. 3.2: Original Wilson Plot

For water-side heat transfer coefficient (h_w), calibration equations were established from data obtained with a modified Wilson plot technique. This modification of the classical Wilson plot method incorporates variable fluid property effects. Fig. 3.3 shows the water-to-water heat transfer coefficient data plotted on the X-Y graph with the following parameters:

$$\text{X axis: } \frac{\frac{k_{f1}}{D_h} \cdot \text{Re}_{f1}^n \cdot \text{Pr}_{f1}^{1/3} \cdot \left(\frac{\mu_{f1}}{\mu_s}\right)^{0.14}}{\frac{k_{f2}}{D_h} \cdot \text{Re}_{f2}^n \cdot \text{Pr}_{f2}^{1/3} \cdot \left(\frac{\mu_{f2}}{\mu_s}\right)^{0.14}} \quad (3.3)$$

$$\text{Y axis: } \left(\frac{1}{U} - \frac{t}{k}\right) \frac{k_{f1}}{D_h} \cdot \text{Re}_{f1}^n \cdot \text{Pr}_{f1}^{1/3} \cdot \left(\frac{\mu_{f1}}{\mu_s}\right)^{0.14} \quad (3.4)$$

The slope of the plot gives the constant of the calibration correlation, which is a power-law type, for the heat transfer coefficients on the water-side. The calibration correlation for the water-side Nusselt number is:

$$Nu = 0.2083 \cdot Re_e^{0.7} \cdot Pr^{1/3} \cdot \left(\frac{\mu_{f1}}{\mu_s} \right)^{0.14} \quad (3.5)$$

for $600 < Re < 2700$, $6.4 < Pr < 6.8$

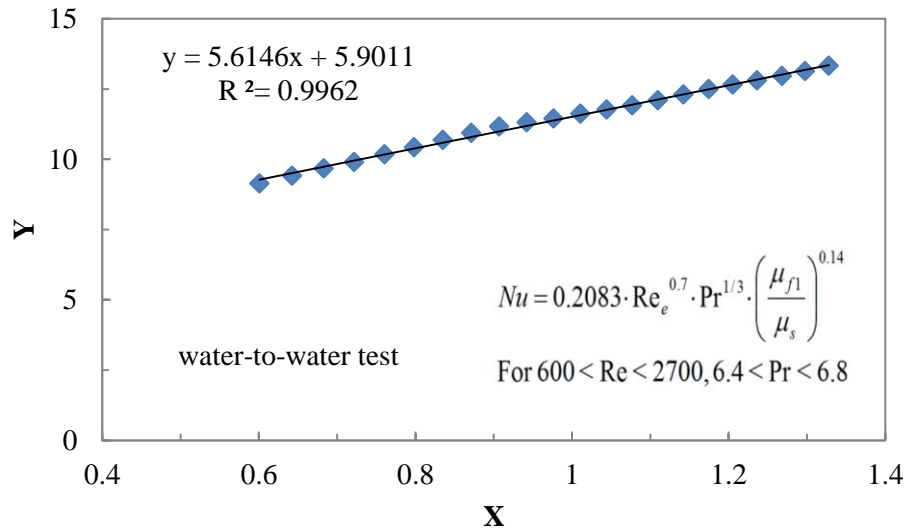


Fig. 3.3: Modified Wilson plot for calibration of water-side heat transfer coefficient (X and Y are defined in Eqs. (3.3) and (3.4), respectively)

3.1.4 Test results of water-side pressure drop

Friction factor was correlated with Reynolds number since friction factor is the function of the Reynolds number as shown in Fig. 3.4. Eq. (3.6) shows the pressure drop correlation of the plate heat exchanger.

$$f = \frac{6.592 \times 10^{-5} \cdot Re_e^{1.734} \cdot \rho \cdot d_e}{2 \cdot G^2} \quad (3.6)$$

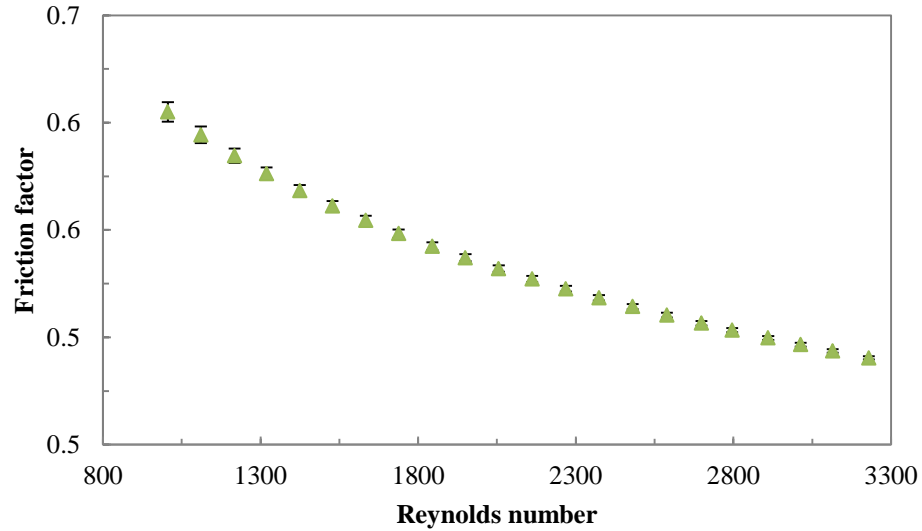


Fig. 3.4: Variation of pressure drop per length with Reynolds number

3.2 Experimental test results with R22

In this chapter, the PHX performance was investigated as an evaporator; water was used as a heat source fluid and R22 as a working fluid. For the refrigerant-side, there were single phase region and two phase region. For the further investigation, the area of each region was needed, however it was not possible. Therefore, it should be noted that the heat transfer coefficient of the refrigerant-side includes not only two-phase region, but also single-phase region, such as subcooled region and superheated region.

3.2.1 Test conditions and test matrix

The experimental test matrix is shown in Table 3.2. The temperature of water, the MFR of water, the MFR of R22, and the evaporation pressure were selected as design variables.

Table 3.2: Test matrix of PHX with R22

Test	Heat source temperature (°C)	Heat source MFR (kg·s ⁻¹)	Heat sink MFR (kg·s ⁻¹)	R22 MFR (g·s ⁻¹)	Saturation pressure (kPa)
Variation of water flow	26 (inlet)	1.0 to 2.8 with 0.2 step	2.0	40	-
Variation of water flow	24 (outlet)	1.0 to 2.8 with 0.2 step	2.0	40	-
Variation of water flow	24 (outlet)	1.0 to 2.8 with 0.2 step	2.0	60	-
Variation of R22 flow	26 (inlet)	2.0	2.0	60 to 64 with 1 step	-
Variation of evaporation pressure	26 (inlet)	2.0	2.0	30	948 to 1,019

3.2.2 Variation of water MFR with fixed water outlet temperature

The MFR of refrigerant was maintained at constant, and the temperature of the water outlet was fixed at 24 °C. The MFR of water was varied from 1.0 to 2.8 kg s⁻¹ with 0.2 kg s⁻¹ of step. The degrees of subcooling and superheating were kept constant. Fig. 3.5 shows the variation of the heat transfer capacity, pressure drop per unit length (DP/L) and $LMTD$ with the water-side Reynolds number. As the water-side Reynolds number was increased, the heat transfer capacity of the heat exchanger did not change, the DP/L increased, and the $LMTD$ decreased. The constant heat transfer capacity was due to the constant degrees of subcooling and superheating, and the fixed refrigerant MFR. The DP/L of the water-side ranged from 2 to 31 kPa m⁻¹. As the water flow rate was increased, the temperature difference between water inlet and outlet decreased while the evaporation temperature slightly increased. This resulted in a decrease of the $LMTD$.

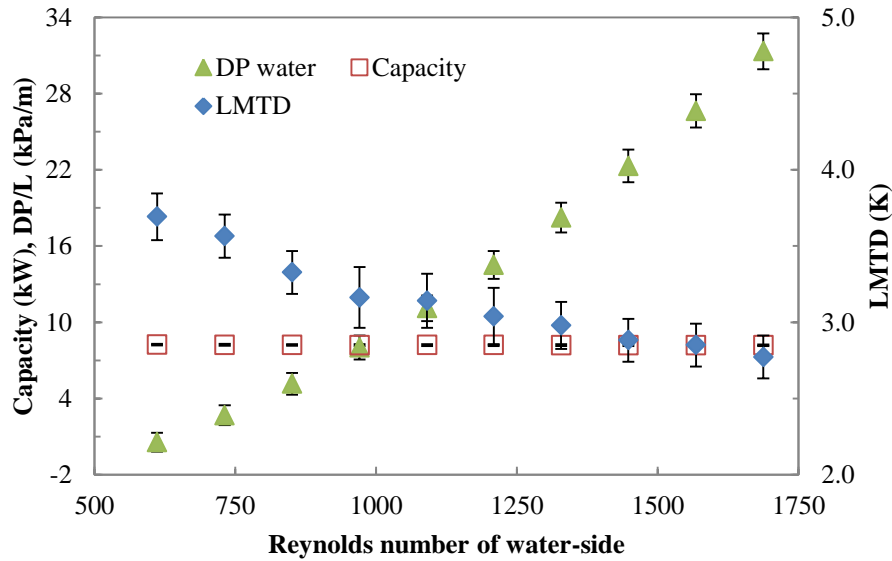


Fig. 3.5: Variation of capacity and LMTD with Reynolds number of water-side

Fig. 3.6 shows the variation of heat transfer coefficients with water-side Reynolds number. It shows that the water-side heat transfer coefficient increased as the water-side Reynolds number was increased. This is obvious because the water-side heat transfer coefficient is directly proportional to the Reynolds number. However, the refrigerant-side heat transfer coefficient increased as well, even though the entire heat flux and mass flow rate of refrigerant were maintained at constant over the test conditions. The change in the refrigerant-side heat transfer coefficient can be addressed with a two-phase heat transfer mechanism. Boiling heat transfer coefficient is governed by two mechanisms: nucleate boiling heat transfer and convective boiling heat transfer. Nucleate boiling heat transfer is mainly dominated by a heat flux, and convective boiling heat transfer is dominated by a quality and mass flux. For the application of the LTLHP, the PHX needed to have a large flow area for the water-side in order to reduce the heat-source side pressure drop. The DP/L of the PHX for the LTLHP application was aimed at less than 10 kPa/m, while the DP/L in the PHX usually is less than 100 kPa/m (Wang et al., 2007). This resulted in the

low mass flux of the refrigerant-side. Low refrigerant mass flux caused the boiling heat transfer mechanism to be dominated by nucleate boiling heat transfer. Fig. 3.7 shows the experimental data of Bo number with criterion of Thonon et al. (1995). It is shown that flow boiling heat transfer under the test conditions was mainly dominated by the nucleate boiling heat transfer.

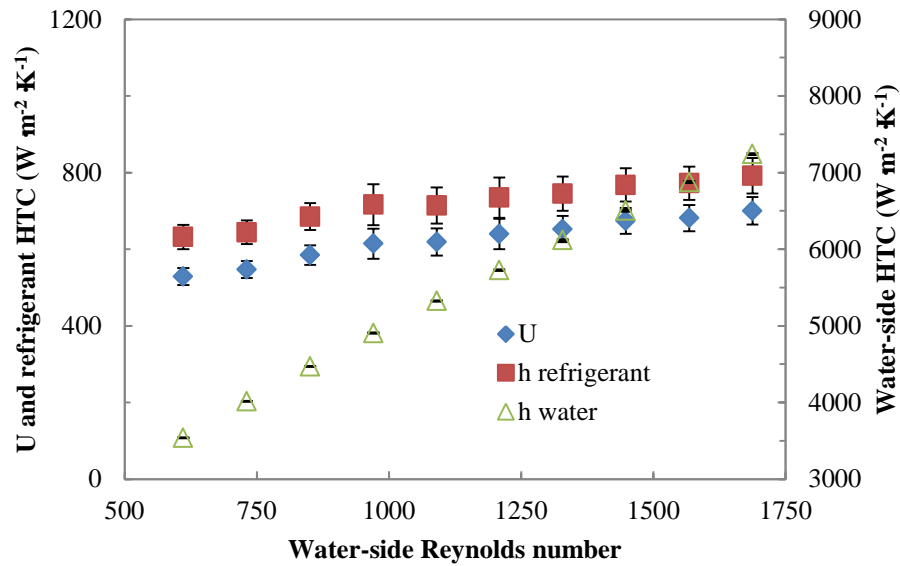


Fig. 3.6: Variation of heat transfer coefficients with Reynolds number of water-side

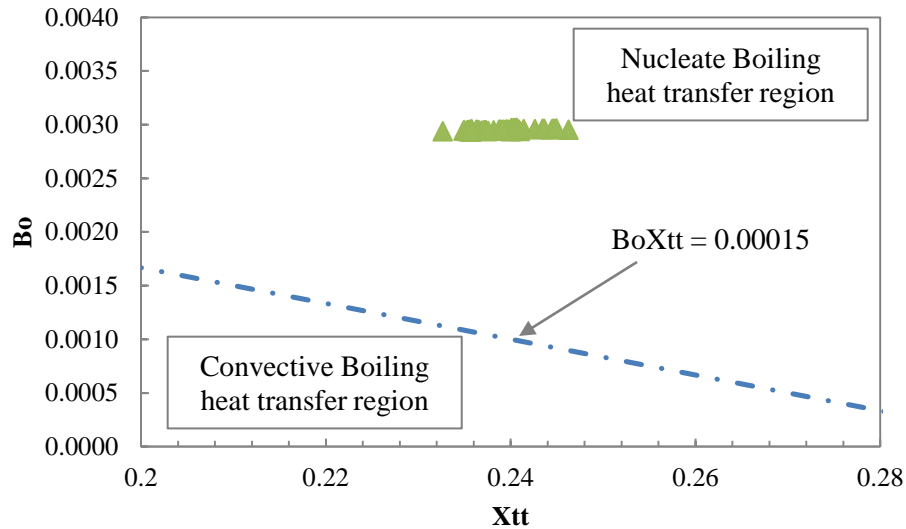


Fig. 3.7: Experimental data with criterion of Thonon et al. (1995)

Fig. 3.8 shows the temperature profile with low and high water-side Reynolds number. As the water-side Reynolds number was increased, the water inlet temperature decreased, and the saturation temperature increase. It is obvious that the water inlet temperature decreased as the water flow rate was increased, because the heat transfer capacity was constant. As the water flow rate was increased, the water temperature profile over the heat exchanger was changed. Under the fixed heat transfer capacity, the changed temperature profile redistributed the local heat flux over the heat exchanger; the local heat flux on the high quality region (marked as B in Fig. 3.8) decreased, and the local heat flux on the low quality region (marked as A in Fig. 3.8) increased. Eventually, an increased heat flux on the low quality region enhanced the boiling heat transfer coefficient as the low quality region is more affected by the heat flux.

For the flow boiling heat transfer, in general, as the quality is increased from 0 to 1, the flow pattern changed with following steps: (1) bubbly flow, (2) slug flow, (3) annular flow, and (4) dispersed mist flow. Especially bubbly flow and slug flow regions are dominated by nucleate boiling heat transfer, and the annular flow region is dominated

by forced convective heat transfer. Even though it is not clearly defined about the flow pattern in the PHX, it can be assumed that the dominant heat transfer mechanism with quality would be similar. Therefore, for the PHX, the increased heat flux on the low quality region increased the total boiling heat transfer coefficient. Furthermore, dry-out would occur at a higher quality region. Therefore, the decreased heat flux on the high quality region would be advantageous in terms of reducing dry-out region where heat transfer coefficient would suddenly drop.

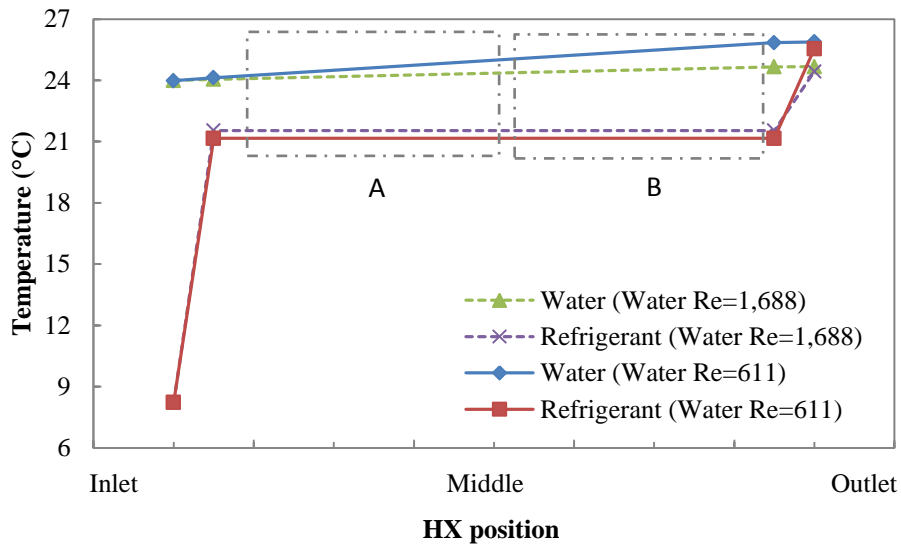


Fig. 3.8: Temperature profile with low and high water Reynolds numbers

3.2.3 Variation of water MFR with fixed water inlet temperature

The MFR of the refrigerant was maintained at constant, and the temperature of the water inlet was fixed at 26 °C. The MFR of water was varied from 1.0 to 2.8 kg s⁻¹ with 0.2 kg s⁻¹ of step. The degrees of subcooling and superheating were kept constant. The heat transfer capacity did not change with the water-side Reynolds number increase. As the water-side Reynolds number was increased, the water-side heat transfer coefficient

increased, however, the refrigerant-side heat transfer coefficient decreased as shown in Fig. 3.9. Fig. 3.10 shows the variation of the temperature profile along the heat exchanger as the water-side Reynolds number was increased from 612 to 1,740. As the water-side Reynolds number was increased, the water outlet temperature increased. Since the total heat transfer capacity was constant, a changed temperature profile resulted in an increase of the local heat flux on the high quality region and a decrease of the local heat flux on the low quality region. The decreased boiling heat transfer can be explained with two main aspects: (1) the redistributed heat flux over the heat exchanger, and (2) dry-out. The decreased heat flux on the low quality region made the boiling heat transfer coefficient decrease, and the increased local heat flux caused the dry-out to occur earlier. Hence, the refrigerant-side heat transfer coefficient decreased as the water-side Reynolds number was increased.

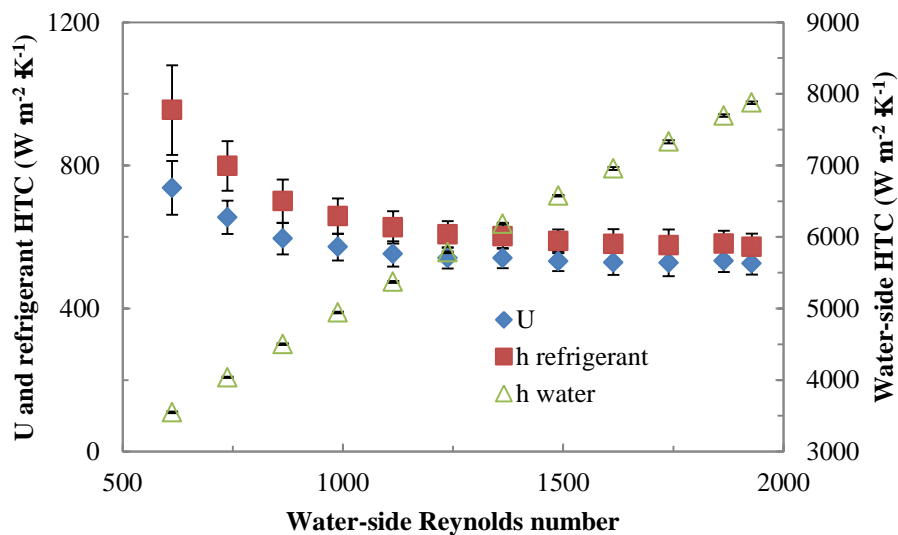


Fig. 3.9: Variation of heat transfer coefficients with Reynolds number of water-side

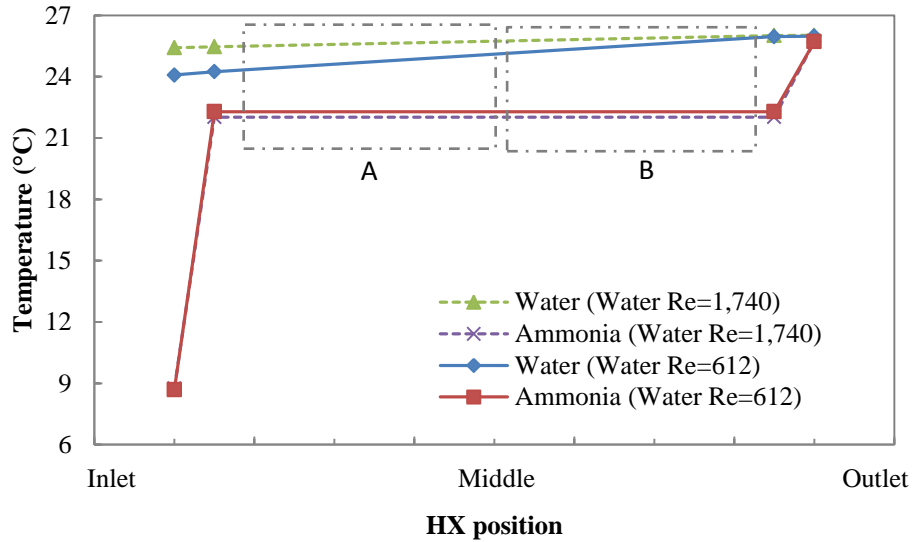


Fig. 3.10: Variation of temperature profiles with different water Reynolds numbers

3.2.4 Effect of the heat flux on the refrigerant-side heat transfer

Two different heat flux cases were compared to investigate the effect of the heat flux on refrigerant-side heat transfer. The heat flux was regulated to 1.95, and 2.93 kW m^{-2} . For both cases, the temperature of the water inlet was fixed at 26 $^{\circ}\text{C}$, and the MFR of water was varied from 1.0 to 2.8 kg s^{-1} with 0.2 kg s^{-1} of step. The degrees of subcooling and superheating were kept constant. For the fair comparison, the evaporation temperatures of both cases were maintained at constant.

The effect of the heat flux on the refrigerant-side heat transfer coefficient with water-side Reynolds number is shown in Fig. 3.11. For the low heat flux test, as the water-side Reynolds number was increased from 610 to 1,740, the boiling heat transfer coefficient increased by 25.3%. In contrast, for the high heat flux test, the boiling heat transfer coefficient increased by 9.3%. It was found that the boiling heat transfer coefficient with the low heat flux was more sensitive to the water flow rate.

As the refrigerant flow rate was increased, both the refrigerant mass flux and heat flux increased. An increased mass flux enhanced the convective heat transfer, and an increased heat flux increased nucleate boiling heat transfer over the entire heat exchanger. These two factors mainly caused boiling heat transfer to be less sensitive to the local heat flux change. Therefore, as the total heat flux became larger, the change of local heat flux on the low quality region affected less on the boiling heat transfer.

In addition, the experimental data was compared with a Cooper's pool boiling heat transfer coefficient correlation (1984) because boiling heat transfer coefficient correlations developed for the PHX (Yan and Lin, 1999; Hsieh and Lin, 2002; Han et al., 2003) had a large deviation from the experimental results due to the different operating conditions. The experimental data was higher than Coopers' correlation as shown in Fig. 3.11. However, overall, the Coopers' correlation predicted very well because the refrigerant mass flux tested in the experimental test was relatively small. As shown in Fig. 3.11, the deviation between experimental data and Cooper's correlation increased due to an increased local heat flux on the low quality region as the water-side Reynolds number was increased.

It should be noted that the heat transfer coefficient of the refrigerant-side included not only two-phase region but also single-phase region such as superheated vapor region and subcooled liquid region. Even though the heat transfer was mostly happened in the two-phase region, for the fair comparison with the correlation, only two-phase region should be considered. Then either the heat transfer area of the two-phase region or the correlation for the single-phase region is required. However, since the Reynolds number of refrigerant was extremely small, there were no appropriate correlations for the single-

phase heat transfer coefficient in the literature. Moreover, to measure the heat transfer area of the two-phase region, the temperature profile of the refrigerant-side along the flow is needed.

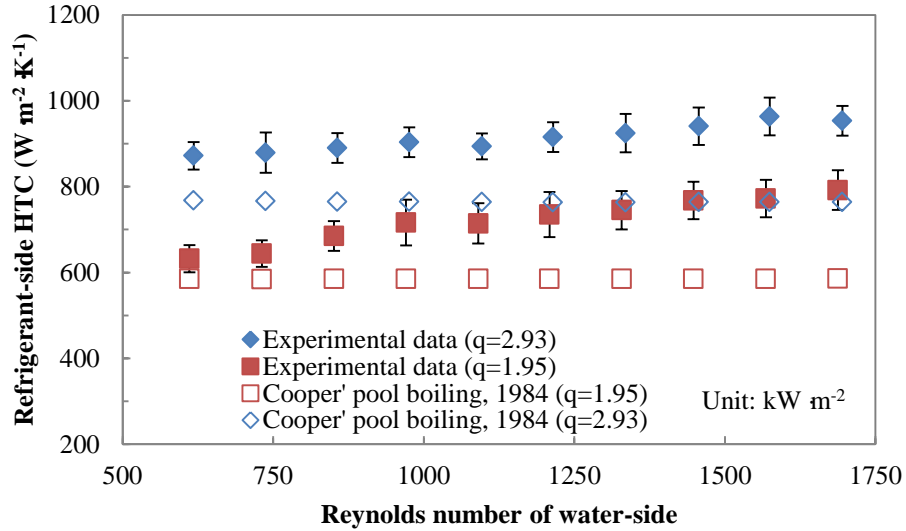


Fig. 3.11: Effect of heat flux on boiling heat transfer coefficient with water Reynolds number

3.2.5 Effect of refrigerant property

Fig. 3.12 shows the variation of heat transfer coefficients with the liquid refrigerant Reynolds number. The MFR of water was maintained at constant, and the temperature of the water inlet was fixed at 26 °C. The MFR of refrigerant was varied from 60 to 64 g s⁻¹ with 1 g s⁻¹ of step. The degrees of subcooling and superheating were both kept constant, respectively. In addition, the expansion opening was maintained at constant. As the liquid refrigerant Reynolds number was increased, the heat transfer capacity of the heat exchanger increased, while the *LMTD* decreased. This caused *U* value to increase. The refrigerant-side heat transfer coefficient increased as liquid refrigerant Reynolds number was increased. This can be addressed with two main factors. First, the convective heat transfer improved by the increased refrigerant mass flux.

Second, as the refrigerant flow rate was increased, the total heat flux on the heat exchanger increased. An increased heat flux enhanced the nucleate boiling heat transfer as well. Therefore, the increased refrigerant flow rate enhanced the boiling heat transfer coefficient.

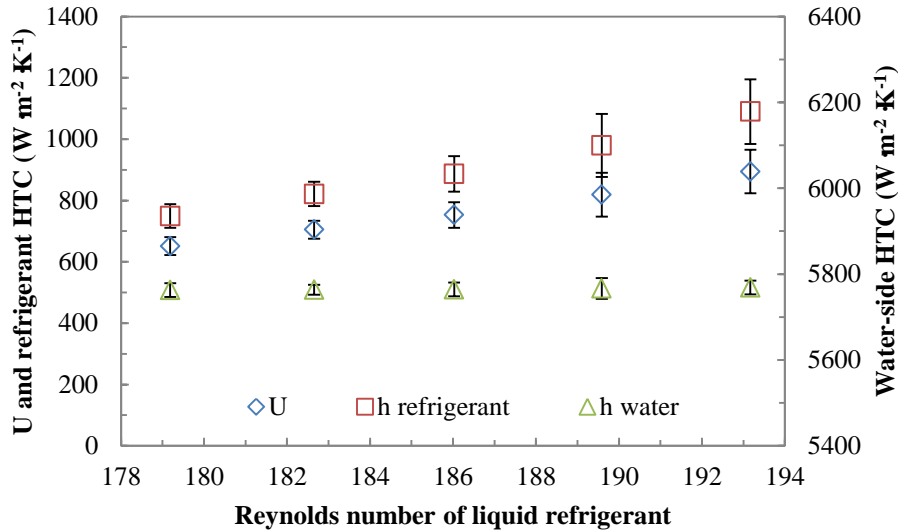


Fig. 3.12: Variation of heat transfer coefficients with R22 flow rate

Fig. 3.13 shows the variation of heat transfer coefficients with evaporation temperature. The MFR of water was maintained at constant, and the temperature of the water inlet was fixed at 26 °C. The MFR of refrigerant was kept at 60 g s⁻¹. The expansion opening was regulated to vary the evaporating temperature. As the evaporation temperature was increased, the heat transfer capacity did not change much due to a fixed refrigerant flow rate, but the *LMTD* decreased because of increased evaporation temperature. As the evaporation temperature was increased, the *U* value increased due to a reduced *LMTD*, and the water-side heat transfer coefficient was constant due to a maintained water flow rate. An increased refrigerant-side heat transfer coefficient by

increasing the evaporation temperature can be explained with three main aspects. First, the surface tension decreases as the evaporation temperature is increased. A lower surface tension enhances nucleate boiling heat transfer. Second, an increased vapor density and a decreased liquid density at the low quality region increase the flow velocity, which enhances the convective boiling heat transfer. Third, a liquid film thickness becomes thinner due to a large liquid droplet entrainment. This reduces the thermal resistance, and then enhances the heat transfer (Yun, 2002). Therefore, an increased evaporation temperature enhances both nucleate boiling and convective heat transfer mechanisms. It should be noted that at the high quality region, the boiling heat transfer coefficient reduces as the evaporation pressure is increased, because the dry-out occurs earlier, and the reduced pressure causes the convective heat transfer lower. Under the given test condition, an increased heat transfer on the low quality region was larger than a decreased heat transfer coefficient on the high quality region. Therefore, the boiling heat transfer coefficient over the heat exchanger improved.

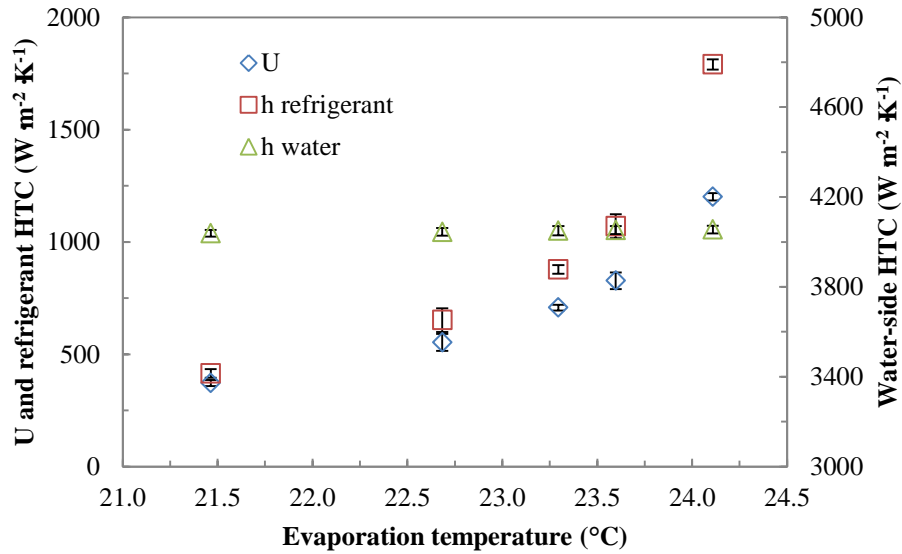


Fig. 3.13: Variation of heat transfer coefficients with evaporation temperature

3.3 Experimental test results with ammonia

3.3.1 Test conditions and test matrix

The test matrix is shown in Table 3.3. The temperature of water, the MFR of water, the MFR of ammonia, and the evaporation pressure were selected as design variables.

Table 3.3: Test matrix of PHX with ammonia

Test	Heat source temperature (°C)	Heat source MFR (kg·s ⁻¹)	Heat sink MFR (kg·s ⁻¹)	Ammonia MFR (g·s ⁻¹)	Saturation pressure (kPa)
Variation of water flow	26 (inlet)	1.0 to 2.8 with 0.2 step	2.0	16	-
Variation of water flow	24 (outlet)	1.0 to 2.8 with 0.4 step	2.0	16	-
Variation of water flow	26 (inlet)	1.0 to 2.8 with 0.2 step	2.0	7	-
Variation of evaporation pressure	26 (inlet)	1.8	2.0	7	822 to 962

3.3.2 Variation of water mass flow rate

The MFR of refrigerant was maintained at constant, and the temperature of the water inlet was fixed at 26 °C. The MFR of water was varied from 1.0 to 2.8 kg s⁻¹ with 0.2 kg s⁻¹ of step. The degrees of subcooling and superheating were both kept constant. Fig. 3.14 shows the variation of the heat transfer capacity and *LMTD* with the water-side Reynolds number. As the water-side Reynolds number was increased, the heat transfer capacity of the heat exchanger did not change much, and the *LMTD* increased. The constant heat transfer capacity was due to the constant degrees of subcooling and superheating as shown in Fig. 3.15, and the fixed refrigerant MFR. As the water-side Reynolds number was increased, the temperature of the water outlet increased while the refrigerant evaporation temperature was kept constant as shown in Fig. 3.16. This resulted in an increase of the *LMTD*. The pressure drop per length of the water-side ranged from 2 to 13 kPa m⁻¹.

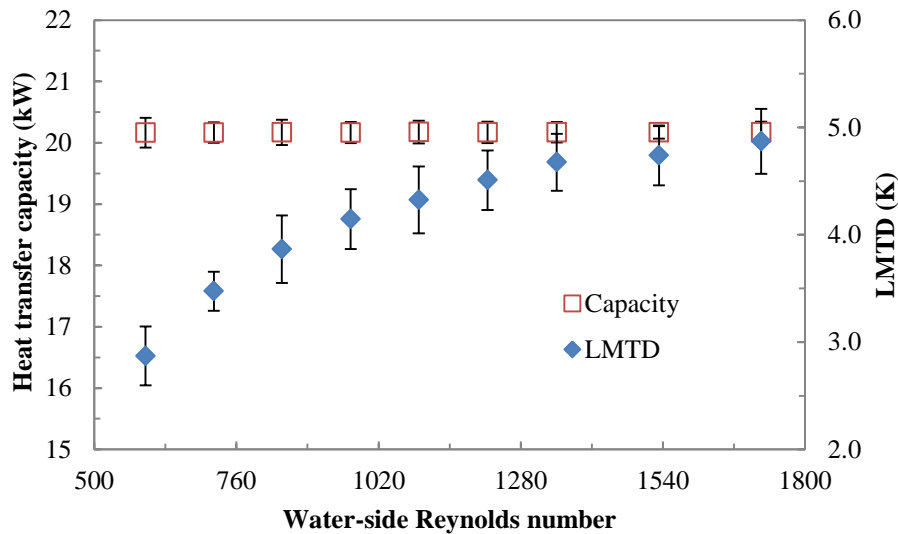


Fig. 3.14: Variation of capacity and LMTD with water-side Reynolds number

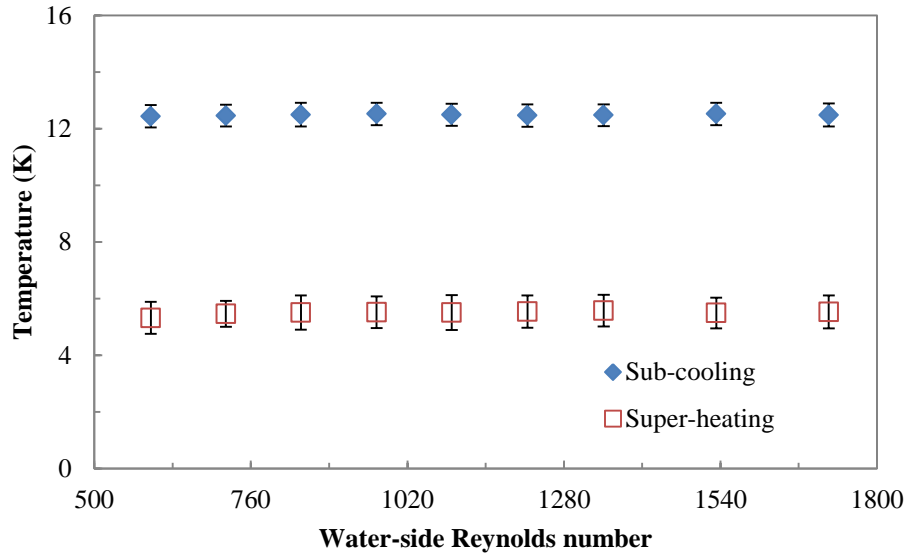


Fig. 3.15: Variation of subcooling and superheating with water-side Reynolds number

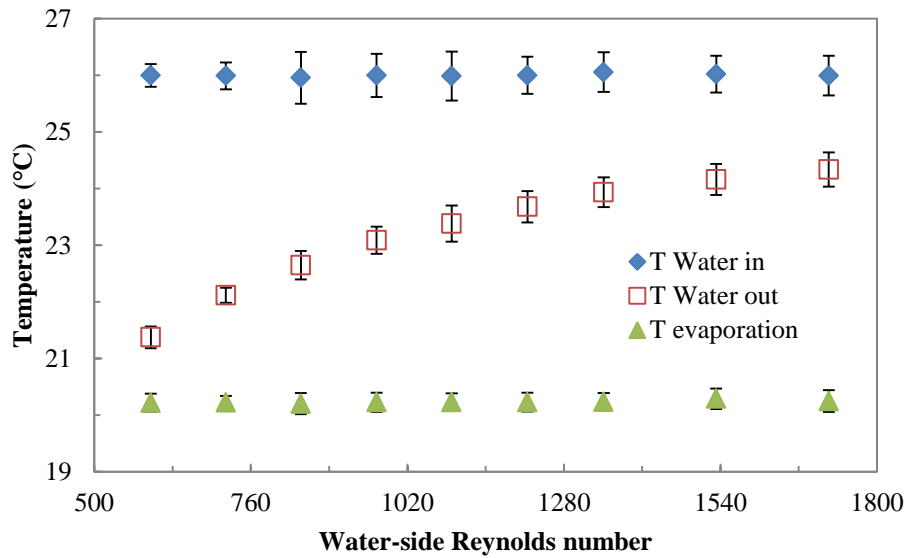


Fig. 3.16: Variation of temperatures with water-side Reynolds number

Fig. 3.17 shows the variation of the heat transfer coefficients with water-side Reynolds number. U value decreased as the water-side Reynolds number was increased. This was due to the increased $LMTD$. As the water-side Reynolds number was increased, the water-side heat transfer coefficient increased, since the water-side heat transfer

coefficient is the function of the water-side Reynolds number. However, the refrigerant-side heat transfer coefficient decreased with water-side Reynolds number. In order to understand this result while there was no change in the refrigerant-side (such as flow rate or heat transfer capacity), the heat transfer mechanism of the refrigerant-side was investigated.

Fig. 3.18 shows the experimental data of Bo number with criterion of Thonon et al. (1995). It is shown that flow boiling heat transfer under the test conditions was mainly dominated by nucleate boiling heat transfer.

Fig. 3.19 shows the variation of the water and refrigerant temperature profiles with the water-side Reynolds number. As the water-side Reynolds number was increased, the water outlet temperature increased. Since the total heat transfer capacity was constant, a changed water temperature profile resulted in an increase of the local heat flux on the high quality region and a decrease of the local heat flux on the low quality region. The decreased boiling heat transfer can be explained with two main aspects: (1) the redistributed heat flux over the heat exchanger, and (2) dry-out. The decreased heat flux on the low quality region made the boiling heat transfer coefficient decrease, and the increased local heat flux caused the dry-out to occur earlier.

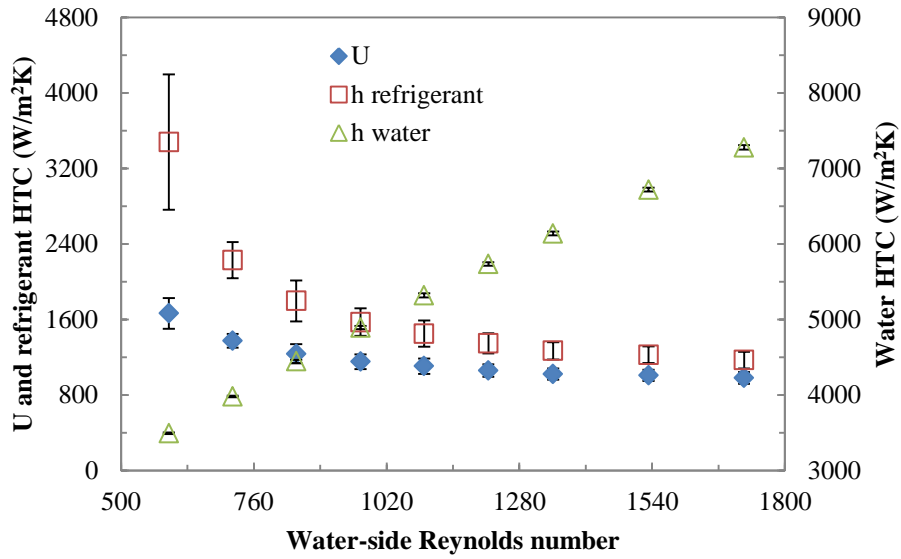


Fig. 3.17: Variation of heat transfer coefficients with water flow rate

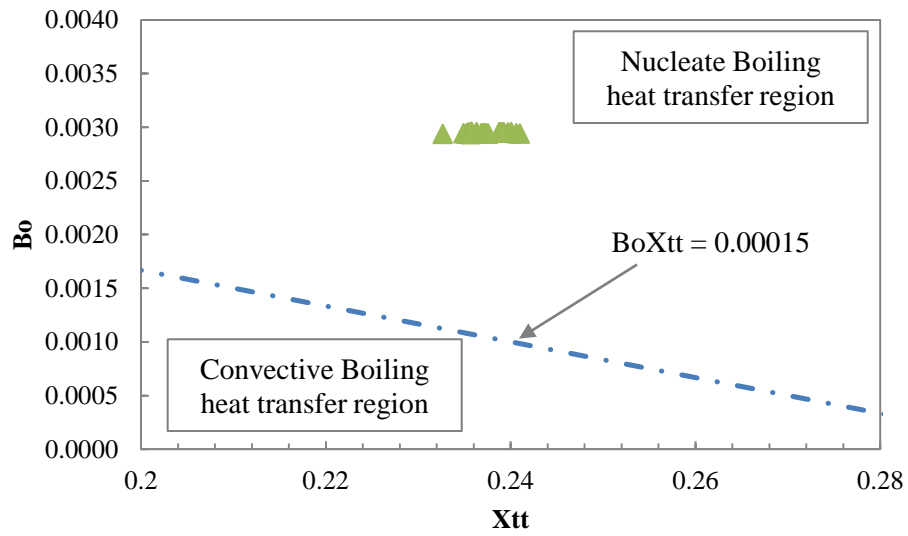


Fig. 3.18: Experimental data of boiling number with criterion of Thonon et al. (1995)

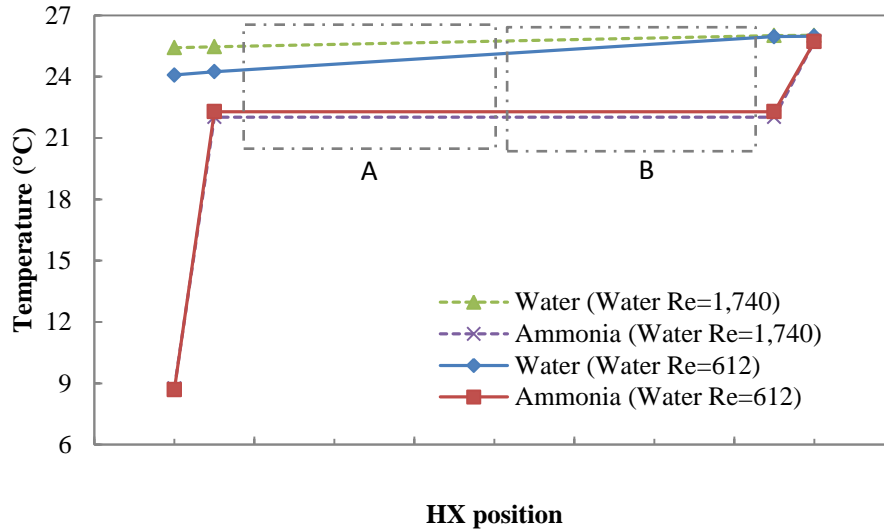


Fig. 3.19: Refrigerant and water temperature profiles with low and high water Reynolds numbers for fixed water outlet temperature

3.3.3 Variation of refrigerant mass flow rate

The MFR of water was maintained at constant, and the temperature of the water inlet was fixed at 26 °C. The MFR of refrigerant was varied from 7 to 20 g s⁻¹. The degrees of subcooling and superheating were both kept constant. As the refrigerant mass flux was increased, the heat transfer capacity of the heat exchanger increased and the *LMTD* decreased as shown in Fig. 3.20. These increased heat transfer capacity and decreased *LMTD* resulted in an increase of *U* value. The refrigerant-side heat transfer coefficient increased as refrigerant mass flux was increased as shown in Fig. 3.21. This can be addressed with two main factors. First, the convective heat transfer improved by increasing the refrigerant mass flux. Second, as the refrigerant mass flux was increased, the total heat flux on the heat exchanger increased. An increased heat flux enhanced the nucleate boiling heat transfer as well. Therefore, the increased refrigerant flow rate enhanced the refrigerant-side heat transfer coefficient.

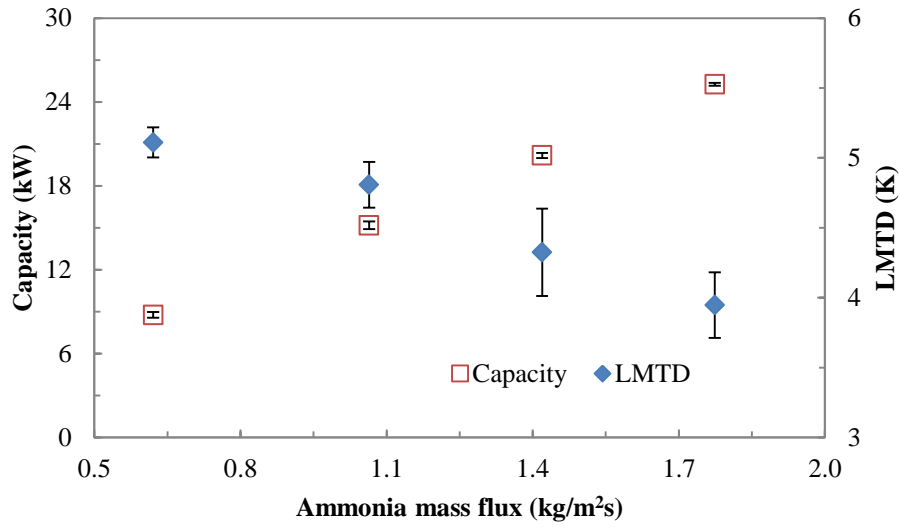


Fig. 3.20: Variation of the capacity and LMTD with ammonia mass flux

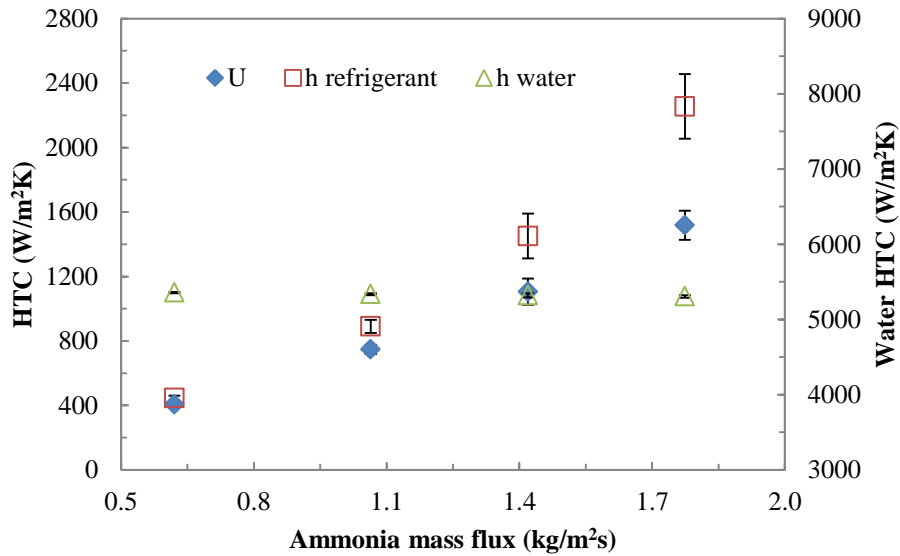


Fig. 3.21: Variation of the heat transfer coefficient with ammonia mass flux

3.3.4 Discussion

The PHX performance for the application of LTLHP was investigated when the PHX works as the evaporator. When the DP/L of the water-side was between 2 and 31 kPa m⁻¹, the water-side heat transfer coefficient ranged from 3,538 to 7,876 W·m⁻²·K⁻¹,

and the refrigerant-side heat transfer coefficient ranged from 415 to $1,790 \text{ W}\cdot\text{m}^{-2}\cdot\text{K}^{-1}$. The two heat transfer coefficients were not balanced due to the limitation in the refrigerant-side heat transfer. Moreover, there was a large pressure drop on the water-side. In order to solve this issue, the heat exchanger constraints must be solved. In general, the heat exchanger design requires reducing the water-side pressure drop, and increasing the heat transfer performance by adjusting the flow area of each fluid.

3.4 PHX performance comparison between R22 and ammonia

The PHX performance was experimentally investigated under LTLHP test conditions with R22 and ammonia, and their performance was compared

3.4.1 Comparison between R22 and ammonia for the PHX

The PHX heat transfer performance with R22 was compared to that with ammonia. Two cases were compared while water-side Reynolds number was varied. The heat transfer capacity of the ammonia case was greater than that of R22 case by 66% as shown in Fig. 3.22. This is due to the higher latent heat of the ammonia vaporization and higher thermal conductivity of ammonia. Fig. 3.23 shows the variation of U value with water-side Reynolds number. U value of the ammonia case was higher than that of R22 case by 52%. The heat transfer coefficient of the water-side was identical for both cases, so that the higher U value was caused by the higher refrigerant-heat transfer coefficient.

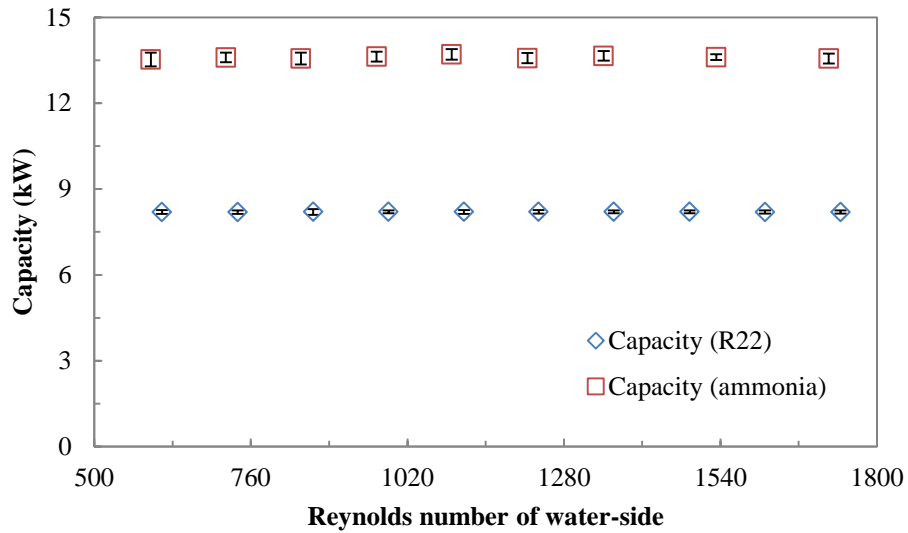


Fig. 3.22: Variation of capacity with water-side Reynolds number

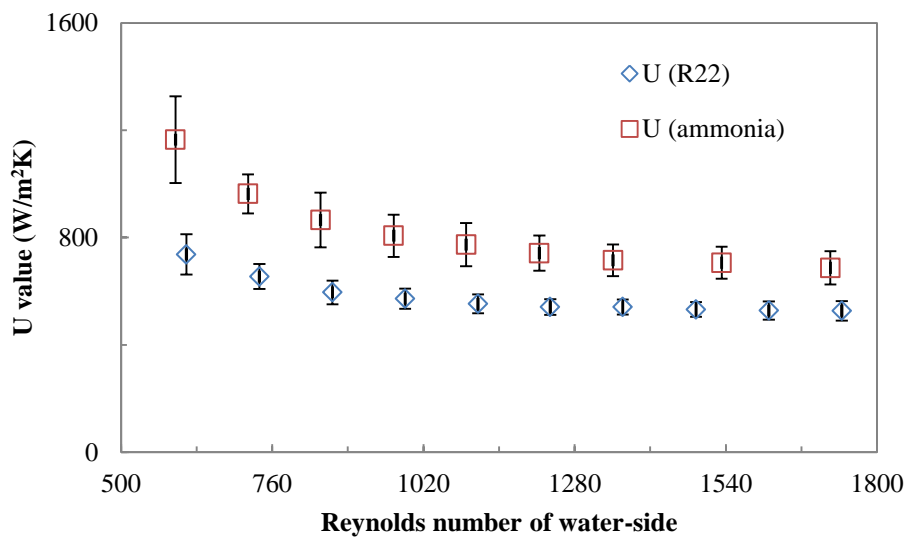


Fig. 3.23: Variation of U value with water-side Reynolds number

Fig. 3.24 shows the variation of refrigerant-side heat transfer coefficient with water-side Reynolds number for the ammonia and R22 cases. Refrigerant-side heat transfer coefficients of both ammonia and R22 cases were decreased as the water-side Reynolds number was increased. The change in the ammonia heat transfer coefficient with water-side Reynolds number was greater than that of R22. This was due to the larger

heat transfer capacity of ammonia. Since the heat transfer capacity of ammonia was larger than that of R22, the water temperature profile change was larger for ammonia than that of R22. Furthermore, the refrigerant-side heat transfer coefficient was larger for the ammonia case than that of R22 case by 83%.

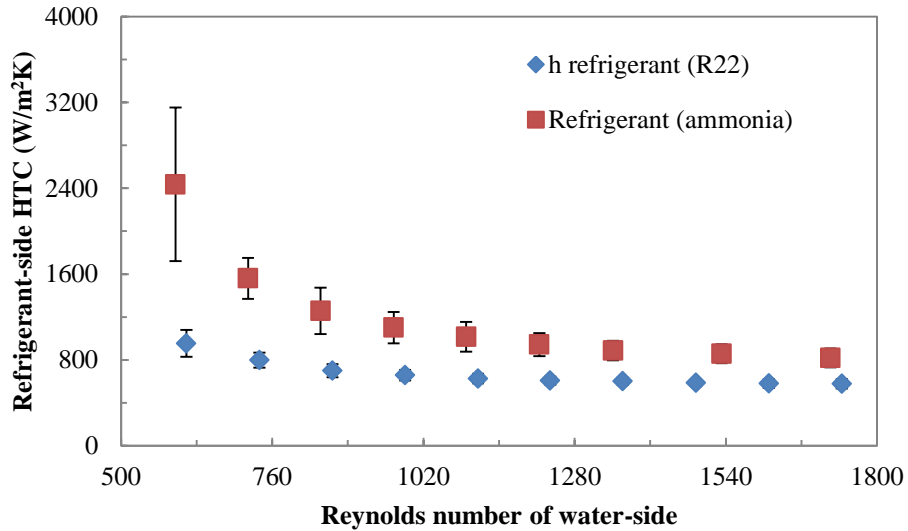


Fig. 3.24: Variation of refrigerant-side HTC with water Reynolds number

3.4.2 Comparison with fixed heat transfer capacity

Table 3.4 shows the thermal property comparison between ammonia and R22. In this table, thermal properties were compared when the evaporation temperature and heat transfer capacity of the heat exchanger were maintained at constant for both fluids. First of all, the latent heat of the vaporization of ammonia was greater than that of R22 by 6.3 times. For the heat pump system, when the heat transfer capacity of the heat exchanger is fixed, the latent heat of the vaporization decides the mass flow rate of the system. Larger latent heat of the vaporization results in less refrigerant flow rate. Since the mass flow rate of ammonia was smaller than that of R22, the convection number of ammonia was smaller than that of R22.

Table 3.4: Comparison between ammonia and R22

Property	Unit	Ammonia	R22	Ratio of ammonia to R22 property
Evaporation temp.	°C	22	22	1
Heat transfer capacity	kW	8.2	8.2	1
k liquid	W m ⁻¹ K ⁻¹	0.4943	0.08485	5.8
k vapor	W m ⁻¹ K ⁻¹	0.02577	0.01165	2.2
H _{fg}	kJ kg ⁻¹	1,178	186	6.3
μ liquid	kg s ⁻¹ m ⁻¹	0.000136	0.000170	0.8
μ vapor	kg s ⁻¹ m ⁻¹	0.0000097	0.0000124	0.8
ρ liquid	kg m ⁻³	607	1,202	0.5
ρ vapor	kg m ⁻³	7.1	40.8	0.2
c _p liquid	kJ kg ⁻¹ K ⁻¹	4.8	1.2	3.8
c _p vapor	kJ kg ⁻¹ K ⁻¹	3.1	0.9	3.6
G (mass flux)	kg m ⁻² s ⁻¹	0.6	3.5	0.17
Bo	-	0.003	0.003	1.0
Co	-	0.108	0.184	0.6

The operating conditions of the water-side were maintained at constant, and the heat capacities of the both cases were set to be equivalent. Fixed water-side condition decided the heat transfer capacity, water temperature profile, and water-side heat transfer coefficient. In addition, fixed refrigerant evaporation temperature, superheating and subcooling decided the refrigerant temperature profile. Heat transfer capacity (\dot{Q}), heat transfer area (A), and $LMTD$ were identical for the R22 and ammonia test. Therefore, U values of R22 and ammonia test were equal to each other. Since water flow rate was same for both cases, water-side heat transfer coefficient was same. This resulted in the identical refrigerant-side heat transfer coefficient for the R22 and ammonia test.

In the experimental test, the equivalent PHX was used for the two different refrigerant tests. However, since there is significant difference in the thermal property

between R22 and ammonia, the heat exchanger has to be designed differently for the each refrigerant. Heat transfer coefficient of the ammonia was calculated to be higher than that of R22 by 67%. This resulted that the heat transfer area of the ammonia system could be smaller than that of R22 system by 26%.

In the test results, the refrigerant-side heat transfer coefficients of R22 and ammonia were same under the test conditions, although ammonia two-phase heat transfer coefficient is predicted to be higher than R22 two-phase heat transfer coefficient. This can be explained with different heat transfer areas in the refrigerant-side. In the evaporator, there were three refrigerant state sections: subcooled liquid section, two-phase section, and superheated vapor section. The refrigerant-side heat transfer coefficient includes the heat transfer coefficient of these three sections. Heat transfer coefficient of the single-phase section is known to be much smaller than that of two-phase section. Therefore, it can be thought that two phase region of the R22 was larger than that of ammonia. The superheated vapor section of ammonia would be larger than that of R22. For the ammonia test under the same capacity with the R22, the heat exchanger was oversized.

In order to address the difference between R22 and ammonia, boiling heat transfer coefficient needed to be compared. Then heat transfer area of each section should be calculated. However, because the mass flux of the refrigerant-side was very small (the flow was extremely laminar flow), it was hard to find the relevant correlation.

3.5 CFD simulation results

3.5.1 Contours of the PHX properties

The temperatures of the water inlet and the wall were set to 25 °C and 23 °C, respectively, while the inlet velocity was maintained at 0.2 m·s⁻¹. Contours of PHX properties were investigated. The vertical mid-section of the flow domain was chosen for contours. Fig. 3.25 shows the contours of static temperature and absolute pressure of the plates. Water flows along y-axis from bottom direction to top. A corrugated shape and contact area enhanced the heat transfer between wall and fluid. In the entrance region, high pressure developed in front of contact areas. The contact area caused a high pressure drop.

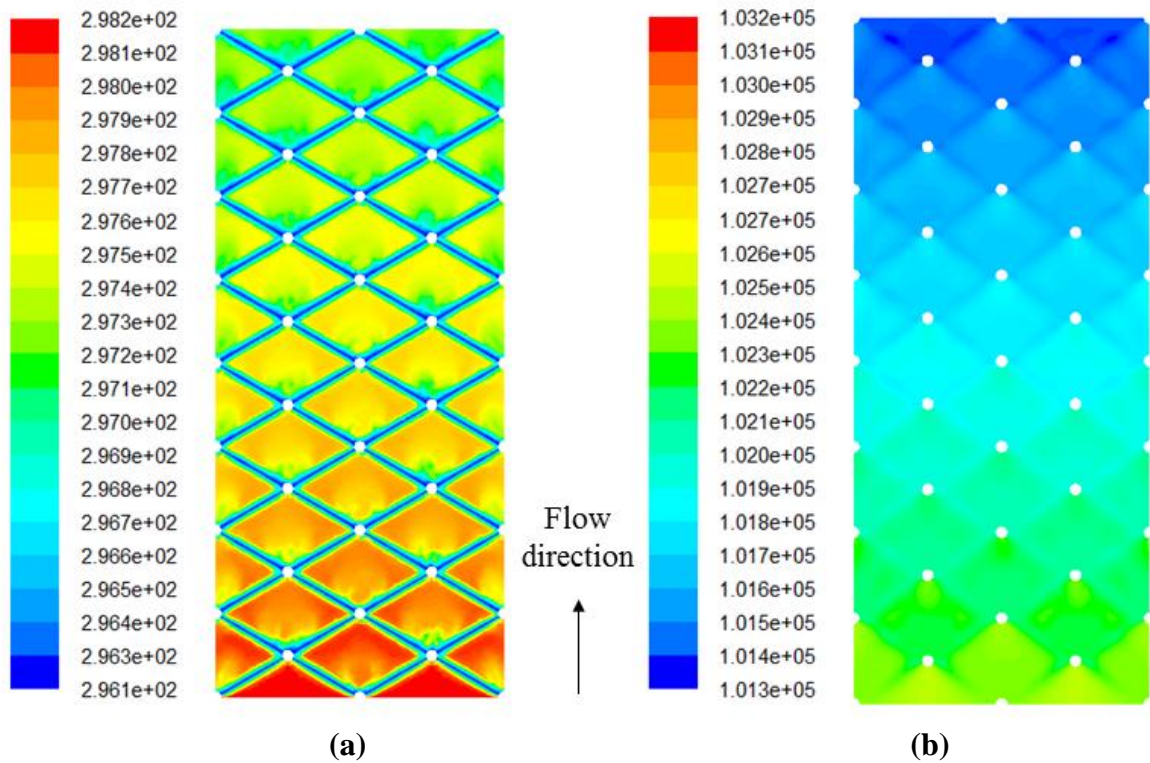


Fig. 3.25: Contours of (a) static temperature of the plate and (b) absolute pressure of the plate (Unit: K, Pa)

Fig. 3.26 shows the velocity vectors by velocity magnitude. Yellow colors are shown between contact areas. This results that main flows were developed in these regions. As water flows went through the contact areas, an unsteady wake region was developed behind the contact area. The main stream exhibited a zigzag flow pattern. The viscous effect increases as the Re decreases, so a wake region can be decreased through increasing the flow velocity.

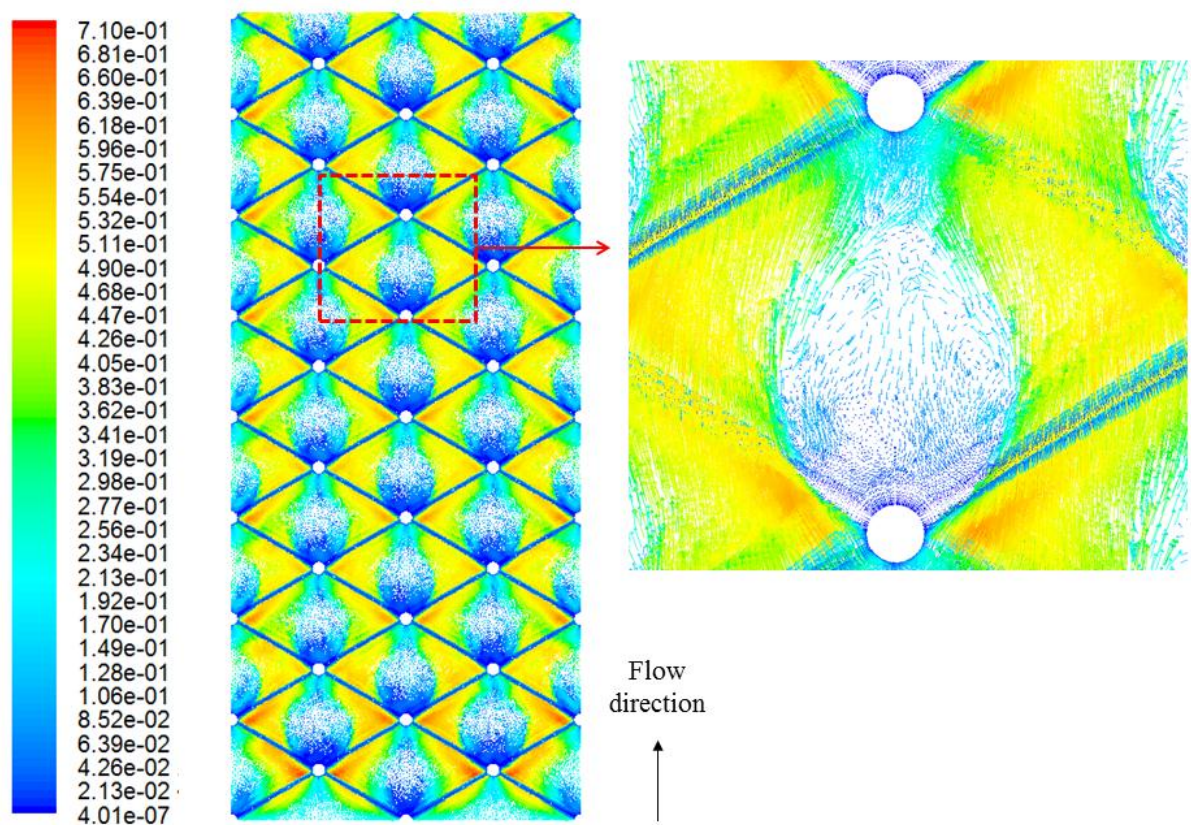


Fig. 3.26: Velocity vectors by velocity magnitude (unit: m/s)

3.5.2 Effect of LMTD on HTC and pressure drop

It is difficult to include the whole plate into the CFD calculation, so that only a part of the corrugation channel was designed as the CFD calculation domain. As the water flows through the plate channel, the temperature differences between the fluid and

wall are changing. Therefore, it is important to check if these temperature differences will affect the heat transfer coefficient of water-side.

Fig. 3.27 shows the CFD results of heat transfer coefficient and pressure drop per length with different *LMTDs*. The heat transfer coefficient and pressure drop were almost independent of temperature difference, which is reasonable because the water-side is single phase-flow. Therefore, it can be assumed that the local heat transfer coefficient obtained from the CFD results could be used as the “global” heat transfer coefficient.

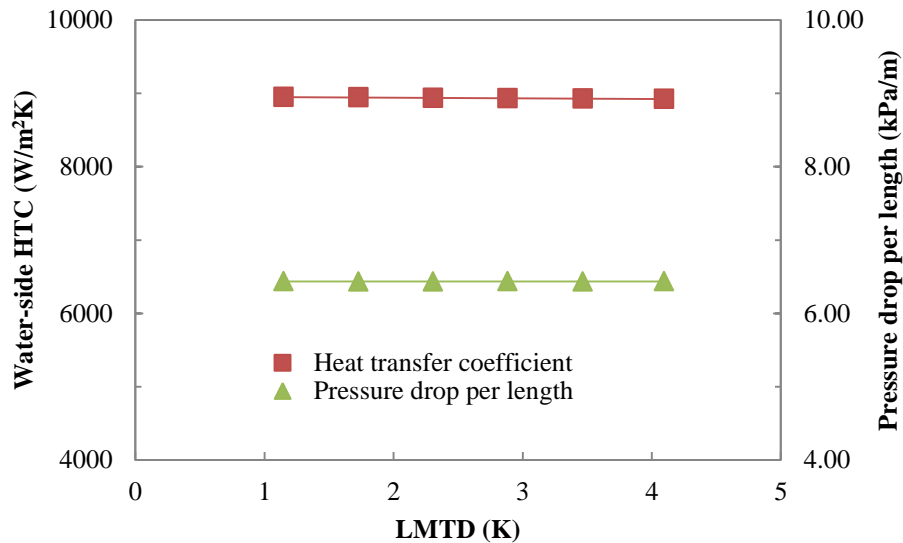


Fig. 3.27: Variation of HTC and pressure drop per length with LMTD

3.5.3 Effect of the turbulent models on the HX performance

Fig. 3.33 shows the variation of the HTC with the Reynolds number. Heat transfer coefficient of SST $k-\omega$ model was higher than any other models and that of S-A model was lower than any other models. S-A model, SST $k-\omega$ model and RSM showed that HTC increases gently with Re . In contrast, Standard $k-\epsilon$, Realizable $k-\epsilon$ models showed that HTC was more sensitive to the Reynolds number. HTC difference between each turbulent model showed less than 15%.

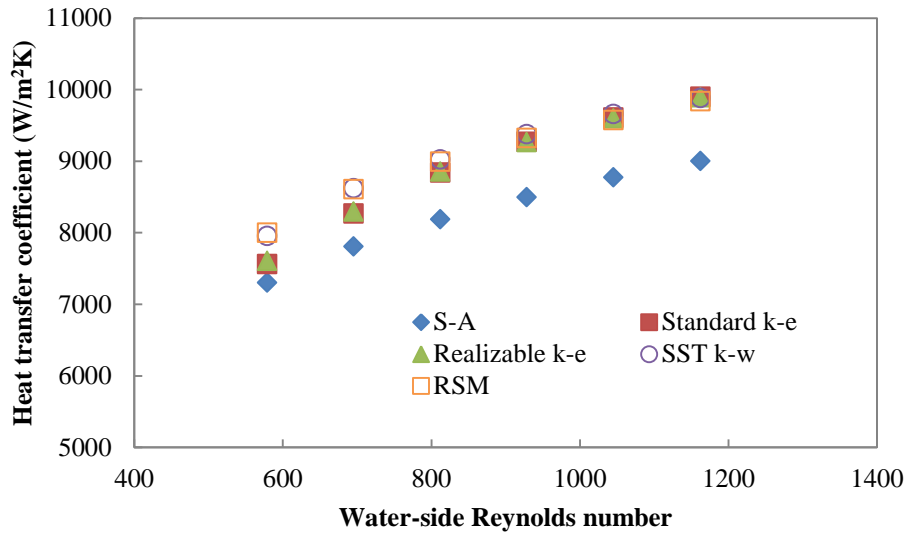


Fig. 3.28: Variation of HTC with Reynolds number and different turbulence models

Fig. 3.29 shows the variation of pressure drop per length with the Reynolds number. RSM predicted the highest pressure drop. Pressure drops of SST k- ω and S-A model were almost same. The pressure drop per length difference between models was very small at low Reynolds number range, but it was increased as the Reynolds number increased.

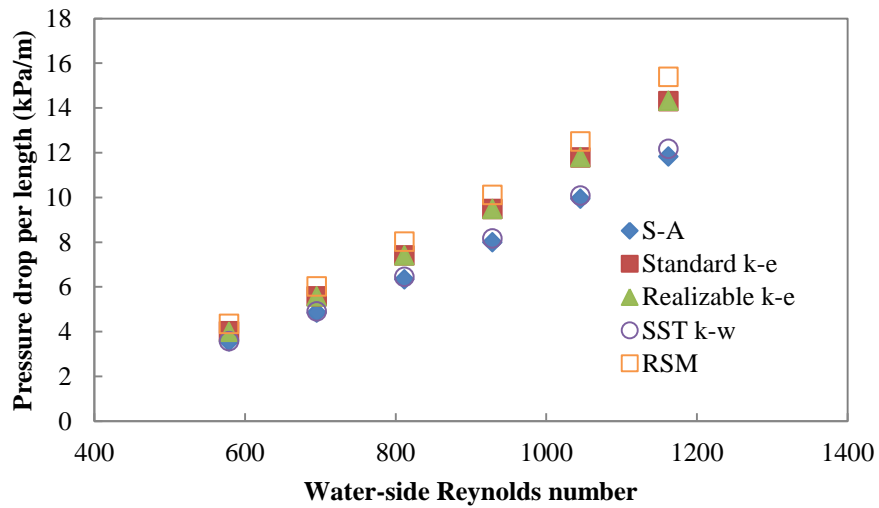


Fig. 3.29: Variation of pressure drop per length with Reynolds number

Except for the S-A model, the deviation between different turbulent models was very small. Therefore, SST k- ω model was selected as the turbulent model in this thesis hereafter, because of its robust and accurate formation in combining both the k- ω and k- ϵ models, which makes it more precise and reliable for a wider class of flows (ANSYS FLUENT 12.0 Documentation, 2009).

3.5.4 Comparison between turbulent and laminar flow models

The chevron corrugations produce early transition to turbulent flow due to its complicated flow. Various investigators have reported that critical Re values are ranging from 400 to 1,000 (Shah and Focke, 1988; Muley and Manglik, 1997, 1999). In order to validate the flow region, SST k- ω model which is one of the turbulent flow models was compared with laminar flow model. Fig. 3.30 shows the variation of Nu with Re . As water-side Reynolds number was increased, Nusselt number of both models increased. Nusselt number of SST k- ω model was higher than that of laminar flow model. As Reynolds number was increased, Nusselt number difference between turbulent model and laminar model became larger. When Re was about 3,000, the Nu difference between laminar model and SST k- ω model was 27%.

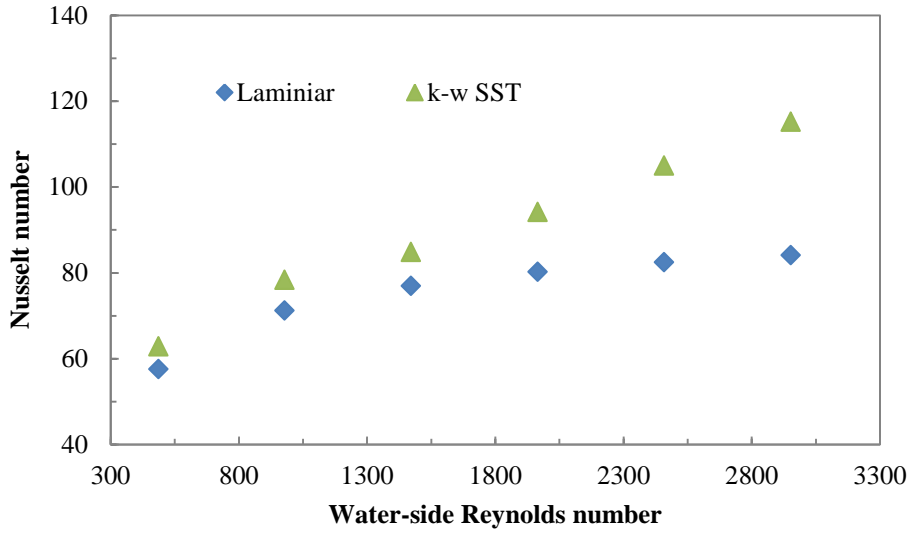


Fig. 3.30: Variation of Nusselt number with Reynolds number and different turbulence models

Fig. 3.31 shows the variation of friction factor with the water-side Reynolds number. At low Reynolds number range, the f difference between models was very small, but it increased as the Reynolds number was increased.

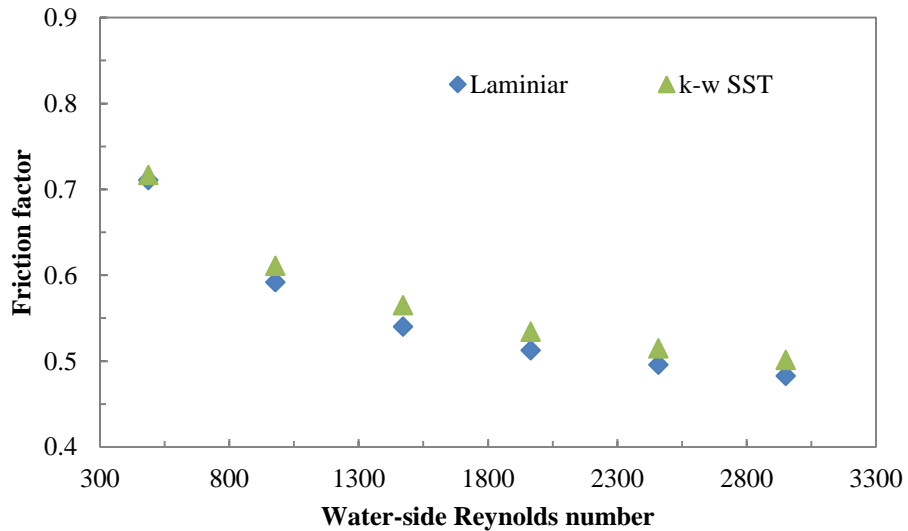


Fig. 3.31: Variation of pressure drop per length with Reynolds number

3.5.5 Comparison between CFD simulation and experimental results

The water-side Nusselt number calculated by the Wilson plot technique was compared with that of the CFD simulation result. Moreover, they were compared with several general correlations, as shown in Fig. 3.32. Among three correlations compared, the present experimental data are seen to be in best agreement with the results of Wanniarachchi et al. (1995). The disagreement could be from factors such as the geometrical differences in the chevron plate corrugations (corrugation depth, wave length, and enlargement factor), the flow distribution channel configurations, as well as different working conditions. The Nusselt number difference between the CFD simulation and experimental test results decreased as the Reynolds number increased. For a PHX, there are two regions: the corrugated region and the distribution region. Only the corrugation region of the PHX was considered in the CFD simulation, while both regions were considered in the experimental test. As the Reynolds number increased, turbulence in the distribution section increased, resulting in the reduction of the Nusselt number deviation between the CFD simulation and the experimental test.

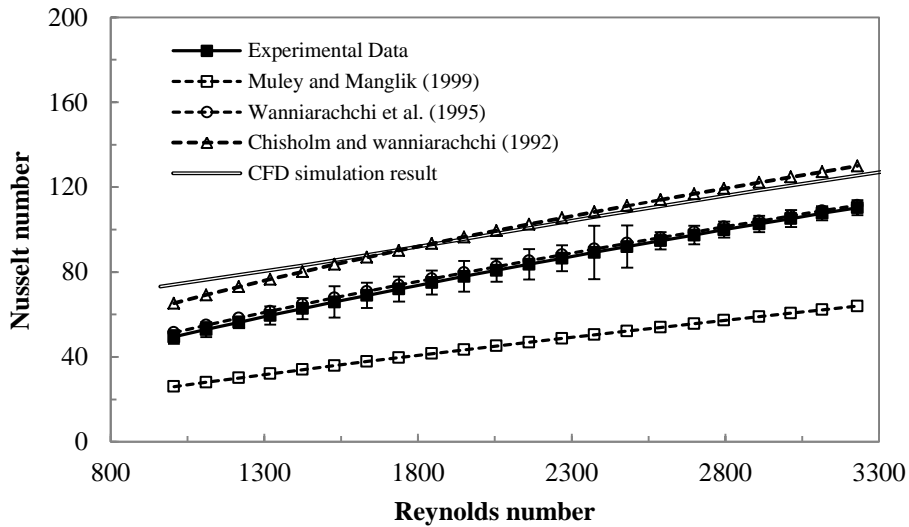


Fig. 3.32: Variation of heat transfer coefficient with water Reynolds number

In general, the heat transfer performance by CFD simulation was predicted as higher than that of the experimental results by 15%. This trend is also found in the literature (Sunden, 2007), and can be explained with three points. First, the active heat transfer area must be considered. The heat transfer coefficient was obtained based on the overall heat transfer coefficient, which was calculated with the total heat transfer area. Since heat transfer of the distribution area is smaller than that of the corrugated area, the total heat transfer coefficient can be smaller. The second point is in regards to the maldistribution of flow among plates. It would be almost impossible to create a perfectly even flow to the plates in the heat exchanger during experimental test. Typically, the fluid preferentially flows through a path with a small pressure drop. In the case of increased plate numbers, the mal-distribution issue will be coming more serious. The third point addresses the fouling issue. Even though clean water was used for the test facility, there could be small particles from the system or bio-fouling. Either could decrease the performance of heat transfer. Hence, the experimental result showed a lower heat transfer coefficient rather than the CFD simulation.

Friction factors calculated by the experimental test are also compared with the CFD simulation result, and two commonly used correlations as shown in Fig. 3.33. The experimental test results are closer to the value calculated by Wanniarachchi et al. (1995). The experimental result showed larger friction factor than the CFD simulation by 25% result due to maldistribution and fouling issues. For most of the Re range, Muley and Manglik (1995) predicted relatively low friction factors, as compared to the other data. This trend was also noted in Han et al. (2011), as well as by Hayes and Jokar (2009).

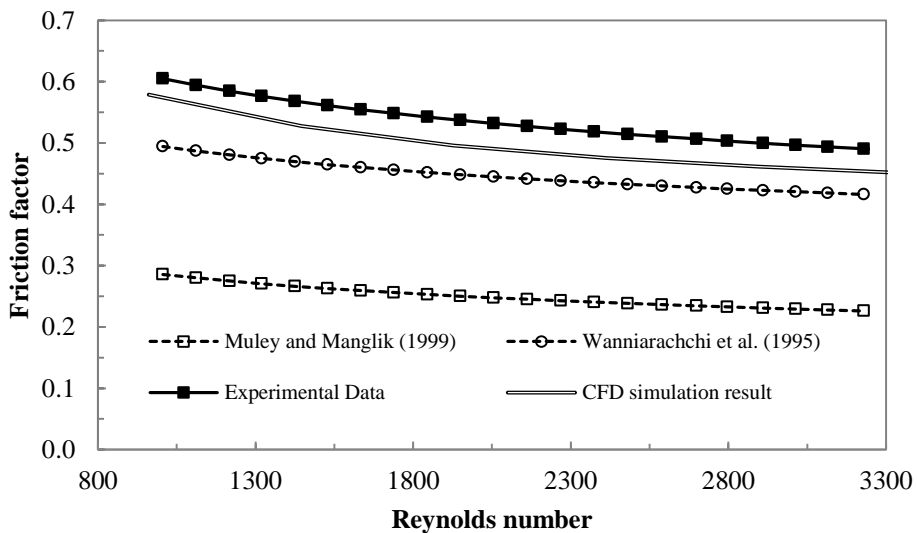


Fig. 3.33: Variation of friction factor with water Reynolds number

3.5.6 Discussion

The two heat transfer coefficients were not balanced due to the limitation of heat transfer of the refrigerant-side. Moreover, there was a large pressure drop on the water-side. In order to apply these results to the LTLHP, the PHX constraints must be solved. The PHX design requires reducing the water-side pressure drop, and increasing the heat transfer performance by adjusting the flow area of fluids. Therefore, established CFD simulation technique was applied to improve the PHX performance. The plate gap for the

water-side was increased instead of contacting each other as shown in Fig. 3.34. This design can be beneficial for not only reducing the pressure drop of water-side but regulating the flow area of fluids. However, under LTLHP operating conditions, the flow area ratio between water-side and refrigerant-side was calculated as larger than 10. However, the current design of the PHX had the limitation to increase the plate for the water-side. Therefore, a new concept of the heat exchanger was required to improve the PHX.

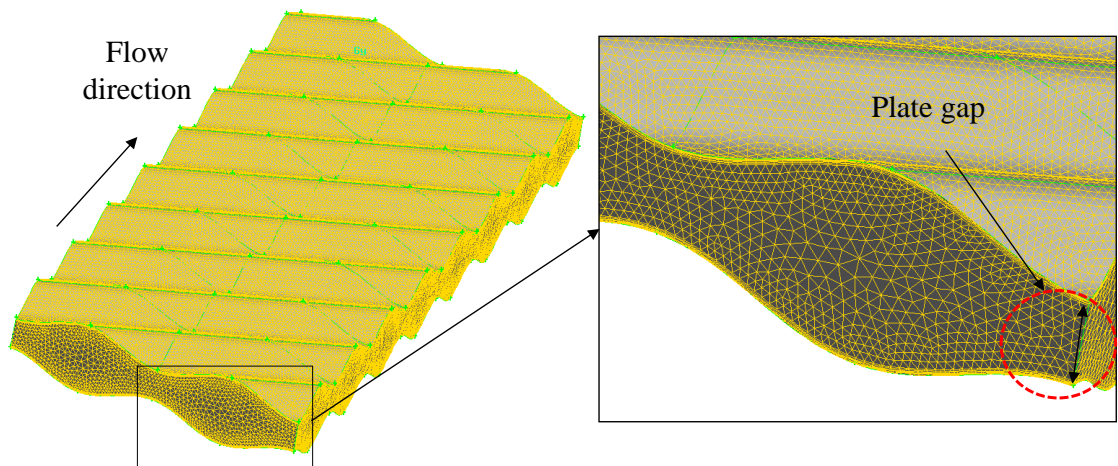


Fig. 3.34: Computational domain of the wide gap PHX

3.6 Conclusions of the chapter 3

The sinusoidal corrugated plate heat exchanger performance was investigated for the application of the LTLHP, which requires unique operating conditions of small temperature difference between water inlet and outlet, and between heat source and refrigerant. The PHX needed to have a large heat source-side flow area in order to reduce the heat source-side pressure drop. Moreover, the PHX has to have an identical flow area of both fluids so that it caused a low mass flux of the refrigerant-side. This resulted that the refrigerant-side heat transfer was dominated by nucleate boiling heat transfer rather than convective boiling heat transfer. In the experimental test, although the refrigerant flow rate and total heat flux over the PHX were maintained at constant, the heat transfer coefficient of the refrigerant-side changed with the water-side Reynolds number. As the water flow rate was changed, the temperature profile on the heat exchanger changed. This resulted in the redistribution of local heat transfer in the heat exchanger. An increased local heat flux on the low quality region increased the total boiling heat transfer, and decreased local heat flux on low quality region decrease the total boiling heat transfer. Moreover, a changed local heat flux on the high quality region affected on the dry-out. As the refrigerant flow rate was increased, the boiling heat transfer coefficient increased due to the increased heat flux and mass flux. This enhanced both nucleate and convective boiling heat transfer mechanisms. In addition, boiling heat transfer improved as the evaporation temperature was increased. An increase in the evaporation temperature decreased the surface tension, increased convective heat transfer, and reduced the liquid film thickness. The PHX performance with R22 was compared to that with ammonia. The U value of the ammonia case was higher than that of R22 case by 52%. This was due

to the larger heat transfer coefficient of the refrigerant-side. It was larger for the ammonia case than that of R22 case by 84%. This was due to high thermal conductivity of the ammonia. The CFD simulation was carried out to investigate the design space for improving the current PHX. Its hydraulic and thermal performance was validated with experimental tests. The deviation between CFD simulation and experimental results was due to the possible factors of distribution section, water mal-distribution, and fouling issue. From the current study, it is concluded that the conventional PHX applied for the LTLHP application is limited by two main factors: a large pressure drop on the water-side due to corrugated shape, and a low heat transfer performance due to the low refrigerant-side heat transfer performance. In order to address these drawbacks, the PHX constrains must be solved by regulating the flow area ratio, however, there was a limitation in the PHX design.

The major conclusions of the PHX performance test for the LTLHP application were summarized as follows:

- The performance of the PHX was investigated experimentally under the unique LTLHP conditions, small temperature difference between water inlet and outlet, and small LMTD
- The refrigerant-side heat transfer was dominated by nucleate boiling heat transfer rather than convective heat transfer due to low mass flux.
- The refrigerant-side heat transfer coefficient was affected by the water-side Reynolds number. The changed water temperature profile resulted in the redistribution of the heat flux and the change of dry-out location in the heat exchanger.

- Under LTLHP operating conditions, U value of the PHX was very small (500 to $900 \text{ W m}^{-2} \text{ K}^{-1}$), and water-side pressure drop was large (between 2 to 31 kPa/m).
- The limitation of the PHX for the LTLHP application was a large pressure drop on the water-side due to corrugated shape, and a low heat transfer performance due to the low refrigerant-side heat transfer performance.
- In order to address these problems, the heat exchanger design must be improved by optimizing its geometry and flow area asymmetrically for each fluid.

CHAPTER 4. Novel Low Temperature Lift Heat Exchanger

4.1 Introduction

For the application of LTLHP, the PHX performance was poor because of two main factors: one was a large pressure drop on the water-side due to corrugated shape, and the other was low heat transfer performance due to the low refrigerant-side heat transfer performance. In order to apply these results to the LTLHP, a novel heat exchanger with new geometries has been developed. The geometries of the novel LTLHX were optimized with approximation assisted optimization technique. The heat transfer and pressure drop performance of the novel LTLHX were investigated numerically and experimentally.

4.2 Development of novel heat exchanger concept

In order to solve the limitations of the conventional PHXs, the flow area ratio needs to be regulated and plates should be offset, which can balance the heat transfer and pressure drop in both fluid sides. These strategies were applied to a novel heat exchanger, and its performance was validated. Two heat-transferring fluids are used: refrigerant and water. The refrigerant undergoes phase change, while the water undergoes temperature change only in single-phase. The single-phase water-side is designed to have a wavy curve configuration in order to decrease the water-side pressure drop. In addition, heat transfer performance design enhancement was achieved by balancing the heat transfer coefficients of the two fluids, through regulating the flow area ratio between single-phase water flow and two-phase refrigerant flow. The overall schematic of the novel heat exchanger is shown in Fig. 4.1. Working fluid (refrigerant) flows are shown in red colored arrows as shown in Fig. 4.2. Water flows over the outside of the plates, and

refrigerant flows through the inside of the plates, perpendicular to the water flow, as shown with arrows in the figure. The refrigerant-side inlet and outlet ports are connected to the header.

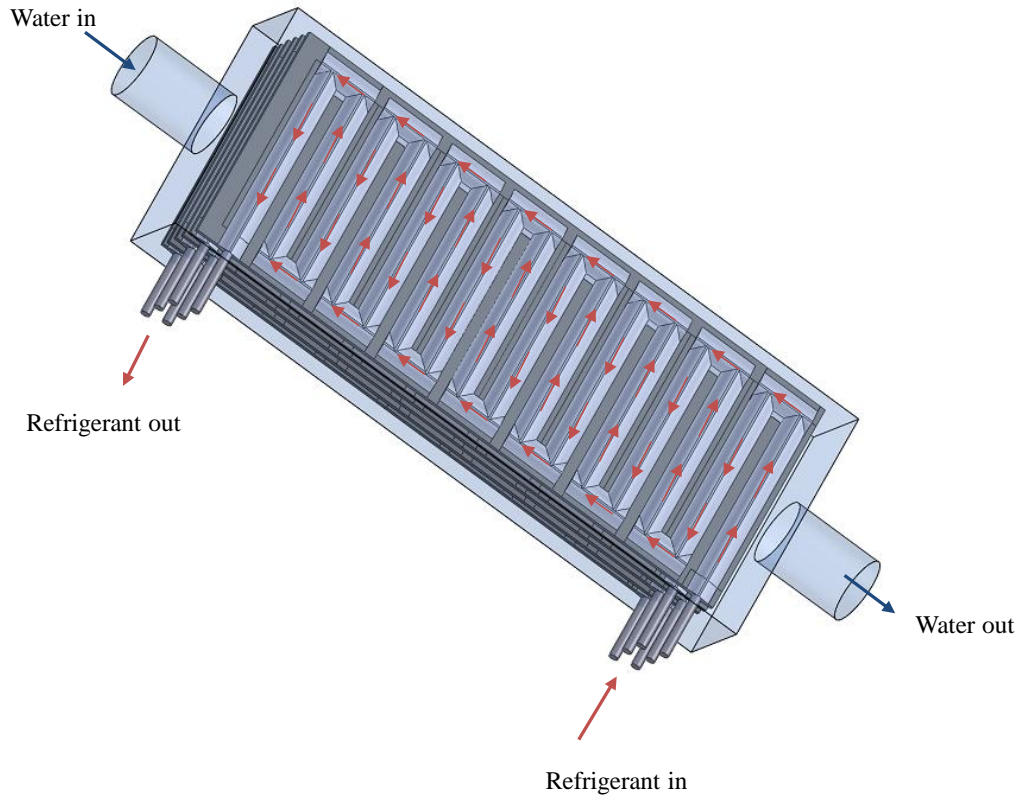


Fig. 4.1: Schematic of novel heat exchanger

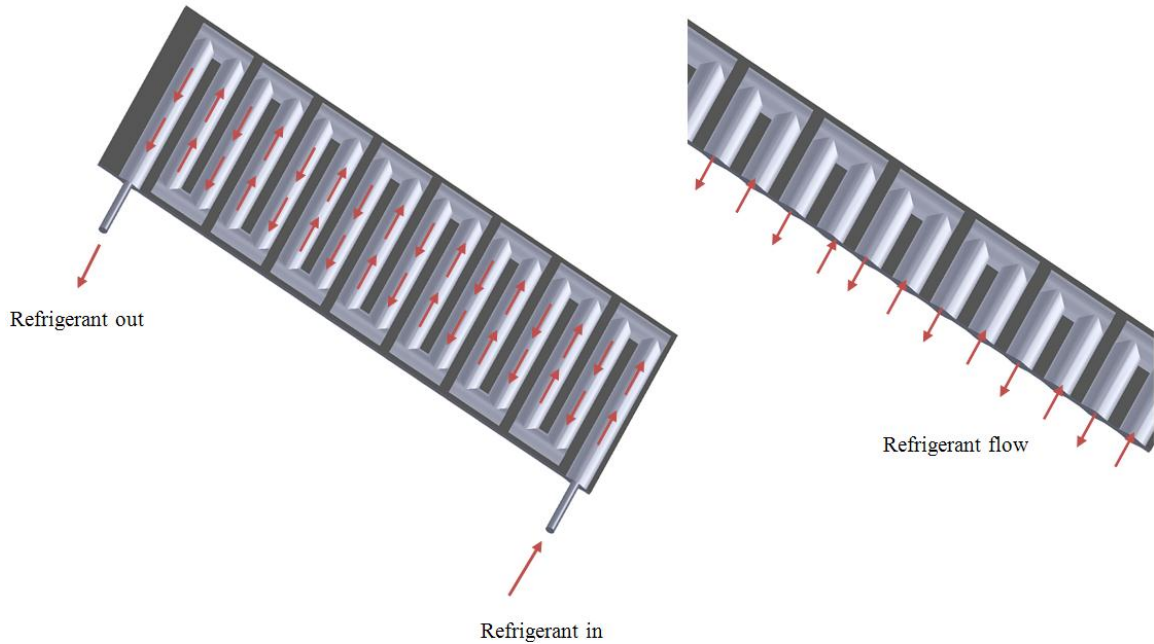


Fig. 4.2: Schematic of a single plate of novel LTLHX

Fig. 4.3 shows the side cut view of the novel LTLHX. Single-phase side flow is designed to be a wavy curve by offsetting the refrigerant flow channel to single-phase flow direction, thus reducing the pressure drop of water-side. By adjusting the gap between the plates and the channel width or height, the flow area ratio of two fluids can be regulated. Design parameters of the novel heat exchanger channel are defined. A channel width (a), channel distance (b), plate width, plate length, channel number, summit width (c), channel height (h), plate gap (d), and thickness of plate (t) are defined in the novel heat exchanger.

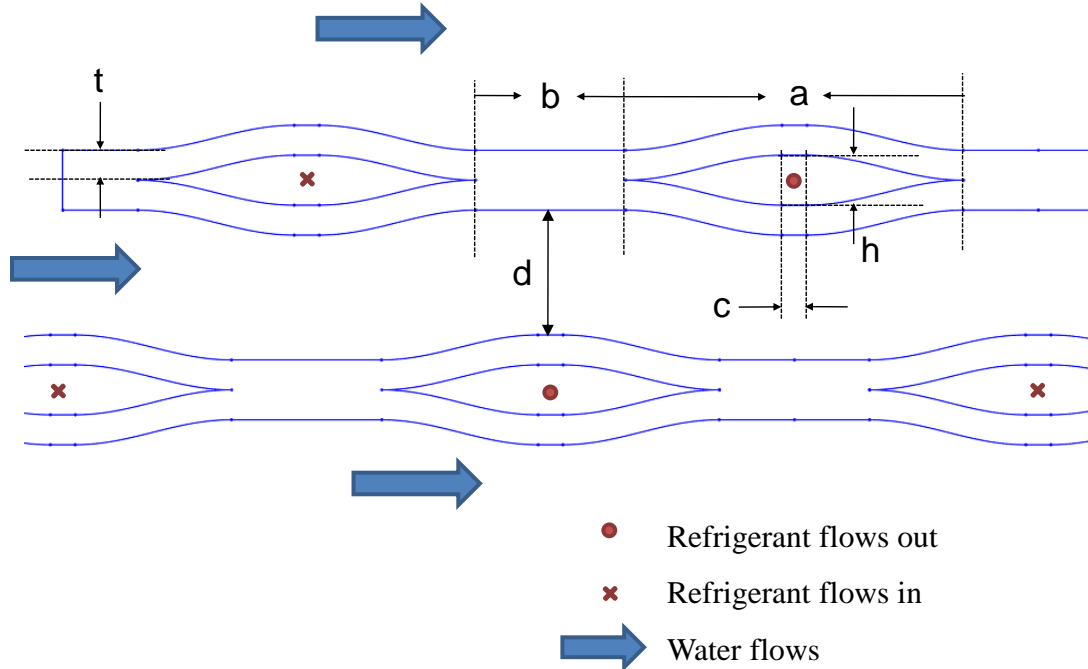


Fig. 4.3: Side cut view of novel LTLHX

4.3 Optimization of novel LTLHX

4.3.1 Overview of OAAO

For the novel heat exchanger optimization design, the objectives are to maximize the heat transfer coefficient (h) while minimizing the pumping power per unit length (P/L , along the HX flow direction). Since the CFD simulation was conducted on a section of the heat exchanger, a pumping power per unit length (P/L) was used instead of pumping power. The final formulation of the optimization problem can be written as:

- Maximize : h
 - Minimize : P/L
 - Subject to: $h \geq 8,000 \text{ W} \cdot \text{m}^{-2} \cdot \text{K}^{-1}$
 - $2 \text{ kPa} \cdot \text{m}^{-1} \leq DP/L \leq 10 \text{ kPa} \cdot \text{m}^{-1}$
- (5.8)

4.3.2 DOE and meta-model building

In this study, the maximum entropy design (MED) proposed by Shewry and Wynn (Shewry and Wynn, 1987) was used to generate the DOE points. The design variables used in the optimization are the plate gap, channel height, channel width, summit width, and fluid inlet velocity. The normalized lower and upper boundaries of these variables are listed in Table 4.1. The current DOE contains a total of 150 designs generated by the MED method. The geometric design variables can be seen in Fig. 4.4. The responses of h and P/L are obtained from these 150 numerical simulation runs, and then correlated into the meta-model using the Kriging meta-model techniques (Li, 2007; Lee et al., 2001). This process could be regarded as a method to find a predictor that is able to estimate the h and P/L based on the given designs. In the current study, the meta-model was generated using Kriging with different meta-model building methods. After obtaining some intermediate optimum solutions that were calculated by the MOGA, the OAAO method was applied to filter some of the optimum solutions and to select the next set of samples to improve the meta-models.

Table 4.1. Normalized boundary conditions for design variables

Variables	Lower limit	Upper limit
x1(d), gap between the plates	0	1
x2(h), channel height	0	1
x3(a), channel width	0	1
x4(c), summit width	0	1
x5(v), water velocity	0	1

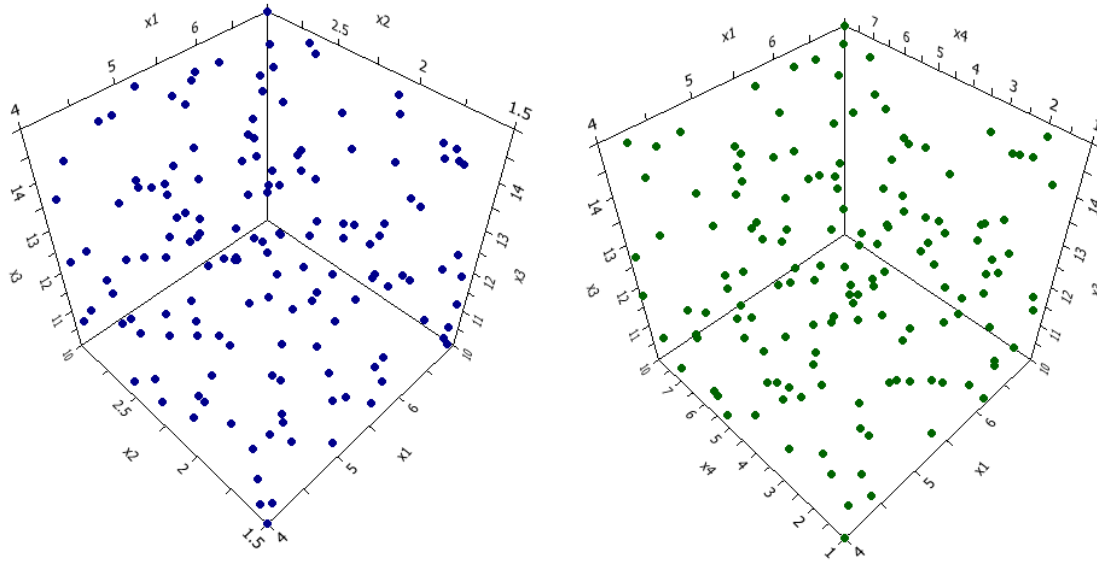


Fig. 4.4. Geometrical parameters distribution in DOE points [gap between the plates (x1), channel height (x2), channel width (x3), and summit width (x4)]

4.3.3 The verification of meta-models

The meta-models have been built based on the 250 cases of CFD simulation with the OAAO method. These h and P/L meta-models needed to be verified in advance of application to the optimization work. 20 random samples within the design boundaries were selected and simulated using CFD simulation. These results were compared with the numerical prediction that was calculated by the meta-model. The detailed validation of various building methods is shown in Table 4.2. It can be seen that the first order polynomial Gauss model has the best accuracy among these methods. The detailed comparisons of h and P/L between the CFD and meta-model are shown in Table 4.2. The relative root mean squared error (RRMSE) between the CFD simulation results and current meta-model prediction results was 1.15% for the heat transfer coefficient and 4.24% for the pumping power per unit length, which is good enough for further optimization. Fig. 4.5 shows the heat transfer coefficient comparison between the meta-model

prediction and CFD simulation for the 20 random samples. The heat transfer coefficient meta-model predicts random samples within $\pm 3\%$ of error bounds. The *P/L* meta-model had results within $\pm 8\%$ of the error bands as shown in Fig. 4.6.

Table 4.2: Validation of different meta-model building methods

Correlation functions	Regression models	RMSE*		RRMSE** (%)	
		HTC (W m ⁻² K ⁻¹)	<i>P/L</i> (W m ⁻¹)	HTC	<i>P/L</i>
Gauss	Poly0	138.85	0.03	1.38	5.29
	Poly1	120.58	0.03	1.15	4.24
	Poly2	105.46	0.05	1.02	10.49
Exponential	Poly0	142.04	0.07	1.38	9.51
	Poly1	105.32	0.06	1.09	12.41
	Poly2	112.05	0.07	1.26	29.91

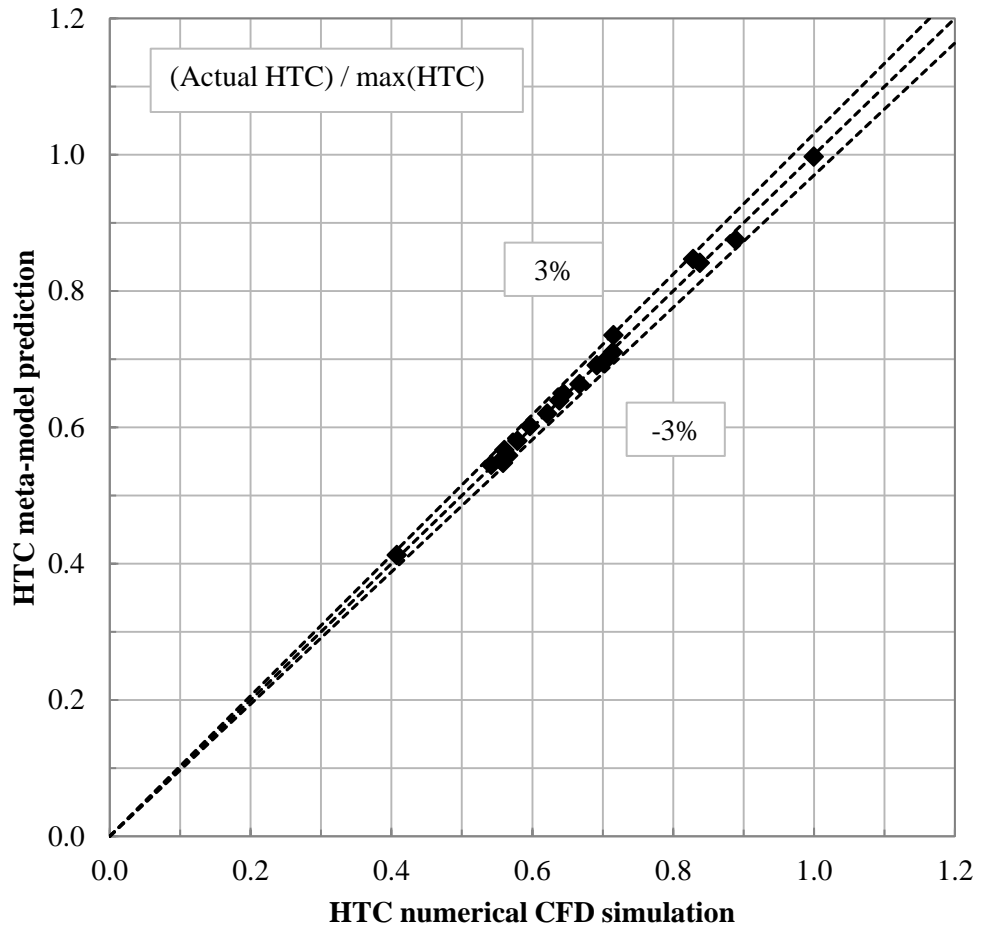


Fig. 4.5. HTC deviation between meta-model prediction and CFD simulation result

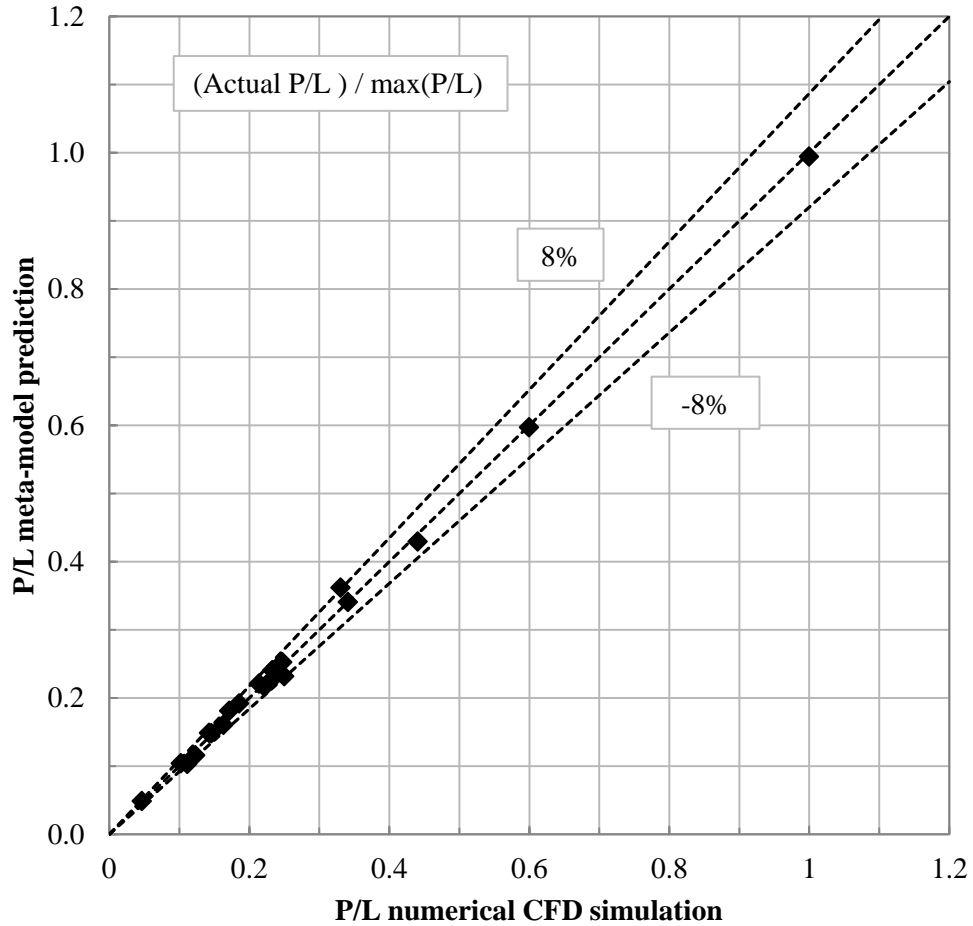


Fig. 4.6. P/L deviation between meta-model prediction and CFD simulation result

4.3.4 Pareto solutions and verifications

The Pareto set solutions were obtained from three different runs of MOGA. Fig. 4.7 shows the Pareto solutions (solid diamond symbol) as well as the DOE samples (hollow rectangle symbol). There was a tradeoff between maximizing the h and minimizing the P/L . The Pareto solutions were not obtained in the highlighted region A, because the pressure drop per unit length (DP/L) exceeded the upper bound allowed for this particular optimization problem, i.e., the constraints would have been violated at all points in region A. The optimum designs selected from the Pareto solution set are shown in Table 4.3. Design variables in the optimum design are well distributed, except for

summit width (x4) and channel width (x3). A large summit width increased both h and P/L . The effect of increased h was higher than that of an increased P/L , so the optimum designs were developed at a relatively large summit width that ranged from 0.552 to 0.942. Furthermore, it can be seen that the channel width (x3) exhibited low value ranges in optimum designs. A small channel width creates more periodic wavy curves per unit length. This can increase the turbulence in the water flow, and eventually increases both h and P/L . Therefore, the h increased faster than the P/L , thus optimum designs were obtained in the regions of small channel width.

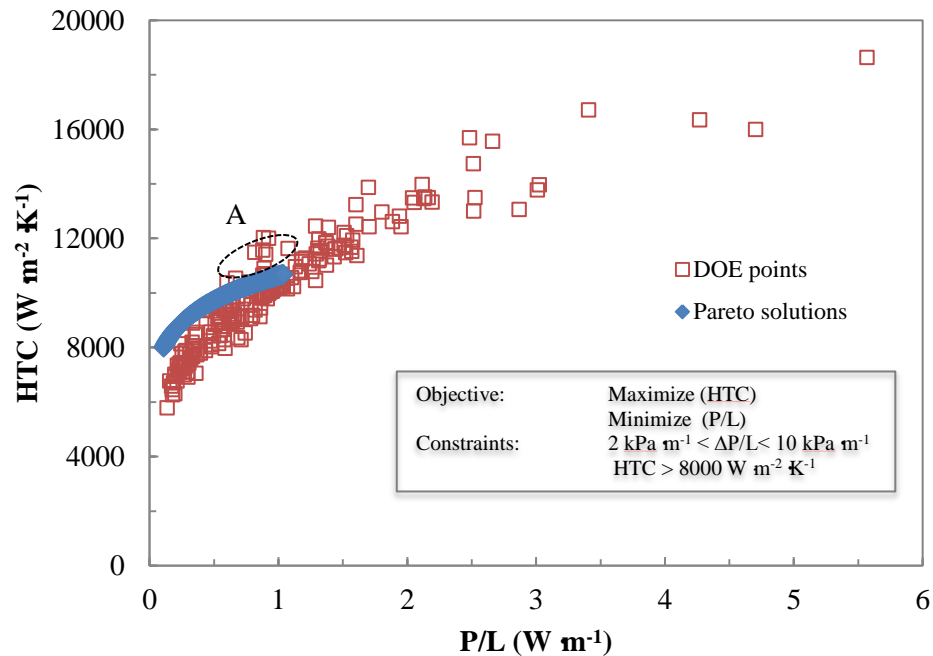


Fig. 4.7. Variation of water-side HTC with pump power per unit length

Design number 7 shows the highest h as well as largest P/L . In this case, channel height (x2) was near minimum limits, leading to relatively high water velocity. In contrast, design number 14 shows the lowest h and P/L , so the water velocity (x5) was almost at the minimum limit.

Typical objectives of the HX optimization study are to maximize the h and minimize pressure drop (DP/L). However, in this thesis, pumping power per unit length (P/L) was selected instead of DP/L for the following reason: Design numbers 2 and 11 have almost identical DP/L . However, the h of design number 2 was higher than that of design number 11 by 14%, while the P/L of design number 11 was only 45% of design number 2. Therefore, it can be seen that pumping power is a better representation than the pressure drop, in terms of the hydraulic characteristics of the heat exchanger. The h and P/L are correlated to the initial and maintenance costs of the system, so the relevant design can be chosen based upon the applications and goals.

Optimum designs in Table 4.3 were verified with the results obtained directly from the CFD simulation. The RRMSE between the meta-model prediction and CFD simulation are 0.82% for the h and 16.15% for the P/L . This indicates that the optimum results obtained from the OAAO are acceptable, given the number of samples.

Table 4.3: Optimum designs selected from Pareto solution set

OAAO Design	x1	x2	x3	x4	x5	HTC ($W\ m^{-2}\ K^{-1}$)	P/L ($W\ m^{-1}$)	DP/L ($kPa\ m^{-1}$)
1	0.399	0.120	0.323	0.662	0.508	9958	0.696	8.87
2	0.728	0.021	0.474	0.943	0.674	10618	0.962	9.28
3	0.291	0.022	0.361	0.645	0.674	10204	0.787	9.64
4	0.020	0.173	0.296	0.934	0.000	9139	0.345	8.49
5	0.078	0.008	0.098	0.853	0.195	9937	0.492	9.71
6	0.001	0.278	0.390	0.920	0.000	9152	0.353	8.81
7	0.660	0.171	0.780	0.733	0.981	10826	1.193	10.00
8	0.509	0.106	0.249	0.709	0.527	10357	0.789	9.35
9	0.503	0.575	0.808	0.701	0.527	9965	0.812	9.65
10	0.260	0.024	0.169	0.885	0.250	9908	0.542	9.06
11	0.007	0.351	0.431	0.749	0.167	9321	0.432	9.20
12	0.006	0.376	0.711	0.771	0.190	8671	0.378	7.90
13	0.221	0.637	0.027	0.552	0.038	9842	0.460	9.50
14	0.000	0.014	0.320	0.918	0.000	8356	0.271	6.76

4.3.5 Conclusions for optimization

In this chapter, design variables of the novel heat exchanger have been optimized with multi-scale approaches. First, the maximum entropy design method was utilized to build a meta-model for obtaining the heat transfer coefficient of the heat transfer fluid side, as well as the pumping power per unit length (P/L) from the parameterized CFD runs. After obtaining intermediate optimum solutions as calculated by the multi-objective genetic algorithm, the online approximation-assisted optimization approach was applied to filter the optimum solutions and select the next set of samples as a means to improve the meta-models' response in the expected optimum region. Finally, the Pareto optimal designs produced by the multi-objective genetic algorithm were validated by comparing them to the values that were directly obtained from numerical simulations. When the pressure drop per length of the heat exchanger was between 2 and 10 $\text{kPa}\cdot\text{m}^{-1}$, the water-side heat transfer coefficient ranged from 8,300 to 11,000 $\text{W}\cdot\text{K}^{-1}\cdot\text{m}^{-1}$ and P/L was between 0.271 and 1.193 $\text{W}\cdot\text{m}^{-1}$.

4.4 CFD simulation results

4.4.1 Contours of the LTLHX properties

Water inlet temperature and wall temperature were set to 294 K (20.85°C) and 292 K (18.85°C), respectively, while inlet velocity was maintained at 1.6 m/s. Contours of LTLHX properties were investigated. The vertical mid-section of the flow was taken for contours.

Fig. 4.8 shows the contours of static temperature of water flow in the LTLHX. Water flows along x axis from left to right side. Wavy shape made an enhancement of heat transfer between wall and fluid. Fig. 4.9 shows the contours of static temperature of wall in the LTLHX. The temperature was given at only refrigerant channels. The bonding area contributed the heat transfer as a fin.

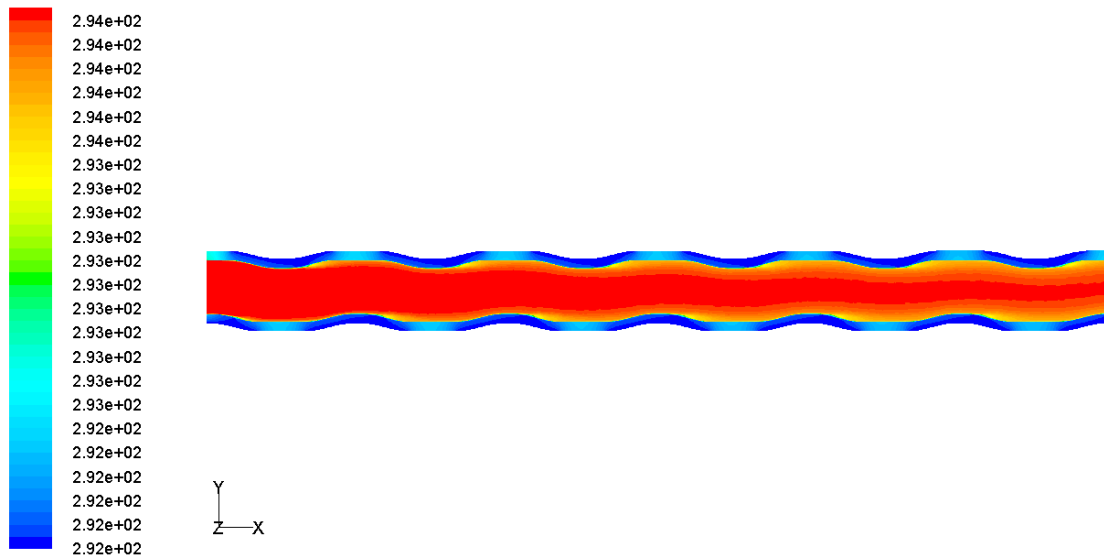


Fig. 4.8: Contours of static temperature of water flow in LTLHX

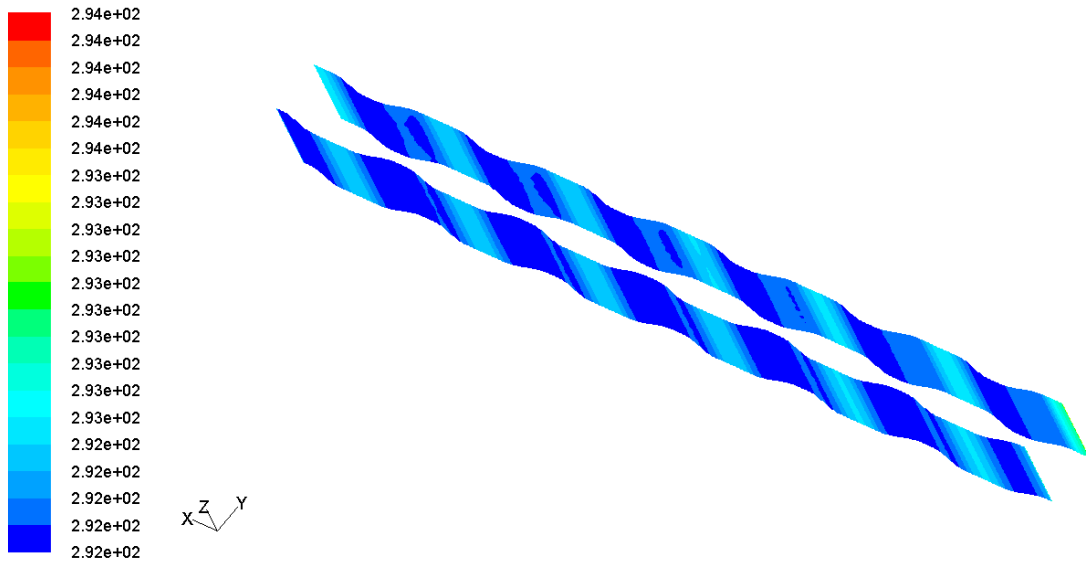


Fig. 4.9: Contours of static temperature of wall in LTLHX

Fig. 4.10 shows the contours of absolute pressure in the LTLHX. A high pressure was developed in refrigerant channels. Fig. 4.11 and Fig. 4.12 show the contours of velocity magnitude. It can be found that high velocity developed near refrigerant channels. The wave shaped pattern enhanced the heat transfer between the wall and the fluid.

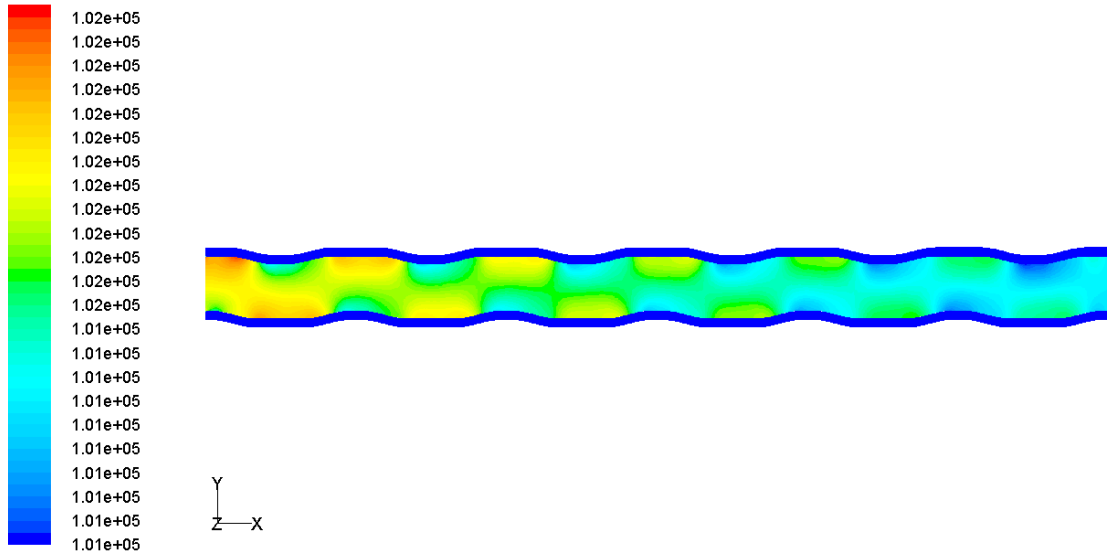


Fig. 4.10: Contours of absolute pressure of water flow in LTLHX

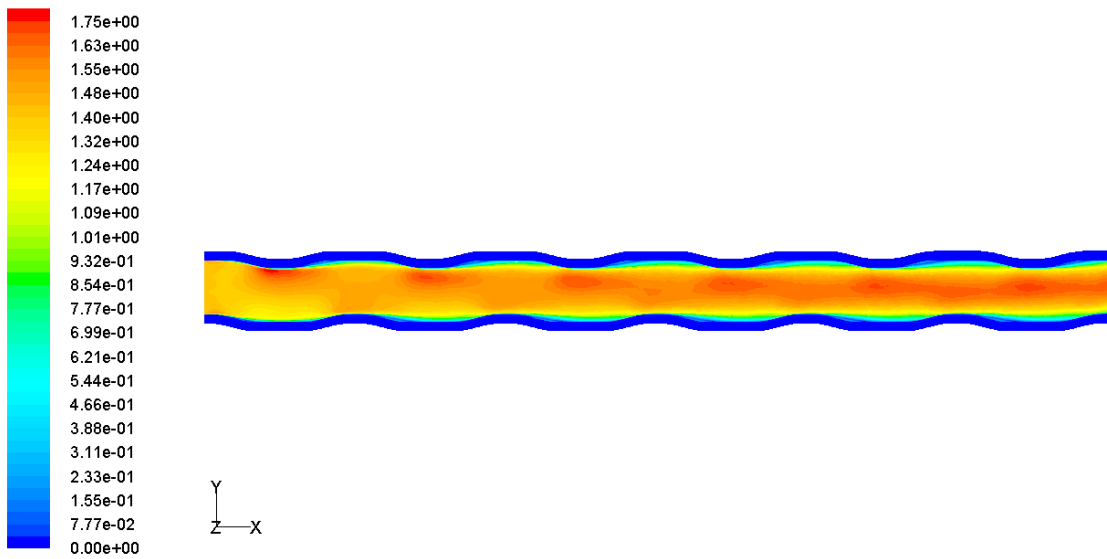


Fig. 4.11: Velocity vectors colored by velocity magnitude of water flow in LTLHX

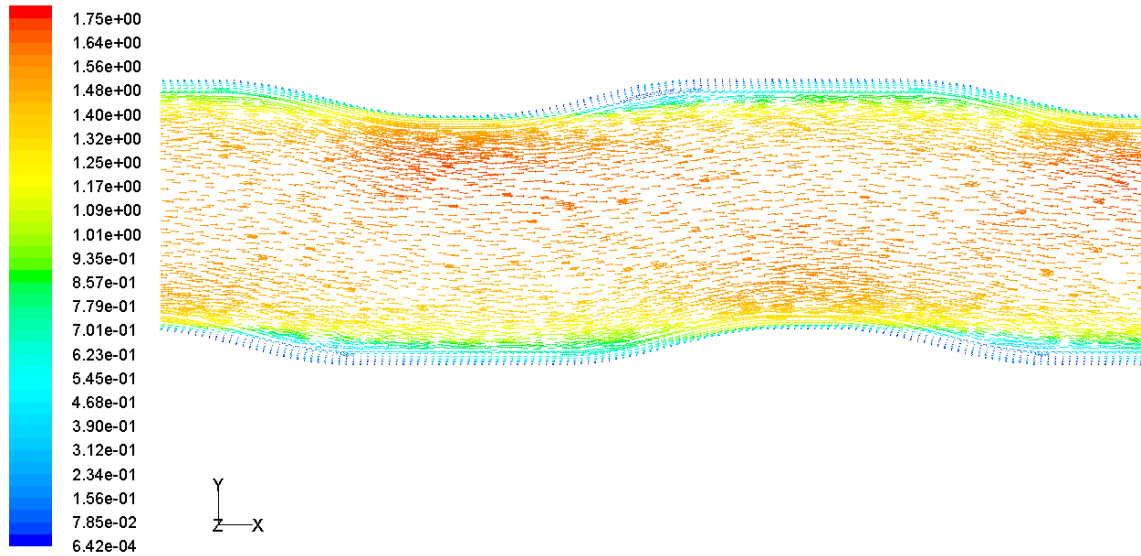


Fig. 4.12: Velocity vectors colored by velocity magnitude of water flow in LTLHX (Enlarged figure from Fig. 4.12)

4.4.2 Effect of LMTD on HTC and pressure drop

As water flows through the heat exchanger, the temperature difference between the fluid and wall is changing along the flow. This temperature difference was checked whether it will affect the heat transfer coefficient and pressure drop.

Fig. 4.13 shows the CFD results of heat transfer coefficient and pressure drop per length based on different *LMTD*. The heat transfer coefficient and pressure drop were almost independent of temperature difference. Therefore, heat transfer coefficient and pressure drop calculated from our domain can represent the global performance of the novel LTLHX.

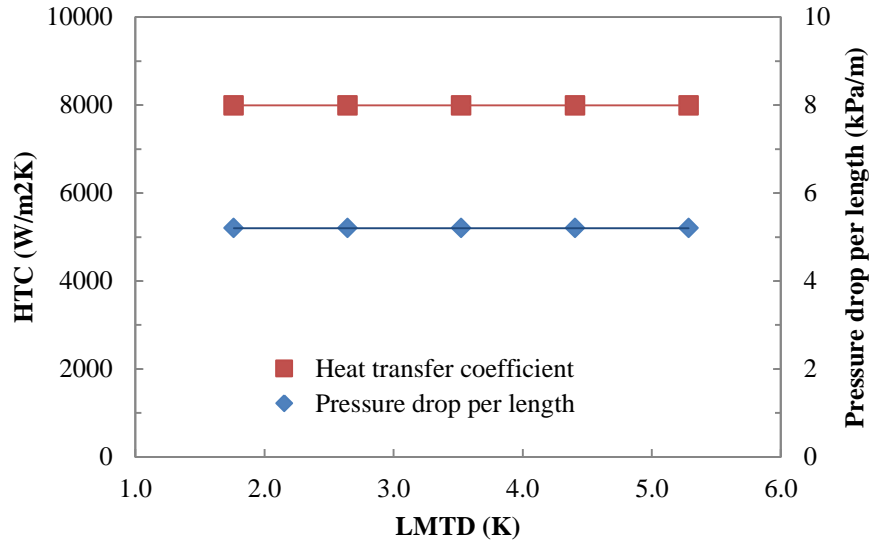


Fig. 4.13: Variation of HTC and pressure drop per length with LMTD

4.4.3 Prediction of novel LTLHX performance

CFD simulation was conducted for 108 cases, and the pressure drop per length and heat transfer coefficient results are shown in Table 4.4 for water flows over both horizontal channels and vertical channels. The ratio between horizontal channel and vertical channel section was 7.55.

Table 4.4: CFD simulation results (water-side)

	Properties	unit	Current design						Initial design					
	v	m/s	1.00	1.20	1.40	1.60	1.80	2.00	1.00	1.20	1.40	1.60	1.80	2.00
Horizontal flow	Pressure drop per length (4 mm)	kPa/m	4.45	5.95	7.61	9.46	11.45	13.57	3.57	4.77	6.08	7.53	9.10	10.78
	Heat transfer coefficient (4 mm)	W/m²K	6434	7258	8029	8802	9550	10286	6167	6913	7600	8275	8931	9567
	Pressure drop per length (5 mm)	kPa/m	3.45	4.63	5.93	7.37	8.95	10.61	2.99	4.05	5.24	6.53	7.94	9.45
	Heat transfer coefficient (5 mm)	W/m²K	6351	7151	7894	8636	9364	10068	5980	6754	7488	8207	8900	9582
	Pressure drop per length (6 mm)	kPa/m	2.91	3.92	5.03	6.26	7.61	9.06	2.64	3.60	4.67	5.82	7.06	8.40
	Heat transfer coefficient (6 mm)	W/m²K	6275	7061	7783	8504	9211	9801	5836	6610	7355	8058	8735	9381
Vertical flow	Pressure drop per length (4 mm)	kPa/m	3.04	4.04	5.16	6.41	7.78	9.24	2.73	0.00	4.70	5.84	7.10	8.45
	Heat transfer coefficient (4 mm)	W/m²K	4928	5661	6482	7337	8166	8949	4861	5761	6707	7581	8406	9182
	Pressure drop per length (5 mm)	kPa/m	2.37	3.14	4.03	5.01	6.08	7.23	2.18	2.92	3.76	4.67	5.68	6.76
	Heat transfer coefficient (5 mm)	W/m²K	4781	5503	6321	7175	7991	8769	4752	5622	6544	7404	8214	8980
	Pressure drop per length (6 mm)	kPa/m	1.94	2.58	3.31	4.12	5.00	5.95	1.81	2.43	3.13	3.90	4.73	5.64
	Heat transfer coefficient (6 mm)	W/m²K	4683	5398	6221	7070	7880	8653	4677	5526	6440	7285	8085	8846
Total	Pressure drop per length (4 mm)	kPa/m	4.28	5.73	7.32	9.10	11.02	13.06	3.47	4.21	5.92	7.34	8.87	10.51
	Heat transfer coefficient (4 mm)	W/m²K	6258	7071	7848	8631	9388	10130	6014	6778	7495	8194	8869	9522
	Pressure drop per length (5 mm)	kPa/m	3.32	4.46	5.71	7.09	8.61	10.22	2.89	3.92	5.07	6.31	7.67	9.13
	Heat transfer coefficient (5 mm)	W/m²K	6167	6958	7710	8465	9203	9916	5836	6622	7377	8113	8819	9511
	Pressure drop per length (6 mm)	kPa/m	2.79	3.76	4.83	6.01	7.30	8.69	2.54	3.47	4.49	5.59	6.79	8.08
	Heat transfer coefficient (6 mm)	W/m²K	6089	6866	7600	8336	9055	9666	5701	6483	7248	7967	8659	9318

Fig. 4.14 shows the variation of DP/L with water velocity and plate gap for the

initial design and current prototype. As the water velocity was increased, DP/L increased. As the plate gap was decreased, DP/L increased. At the same water velocity and plate gap, DP/L of the current prototype was 26% higher than that of initial design.

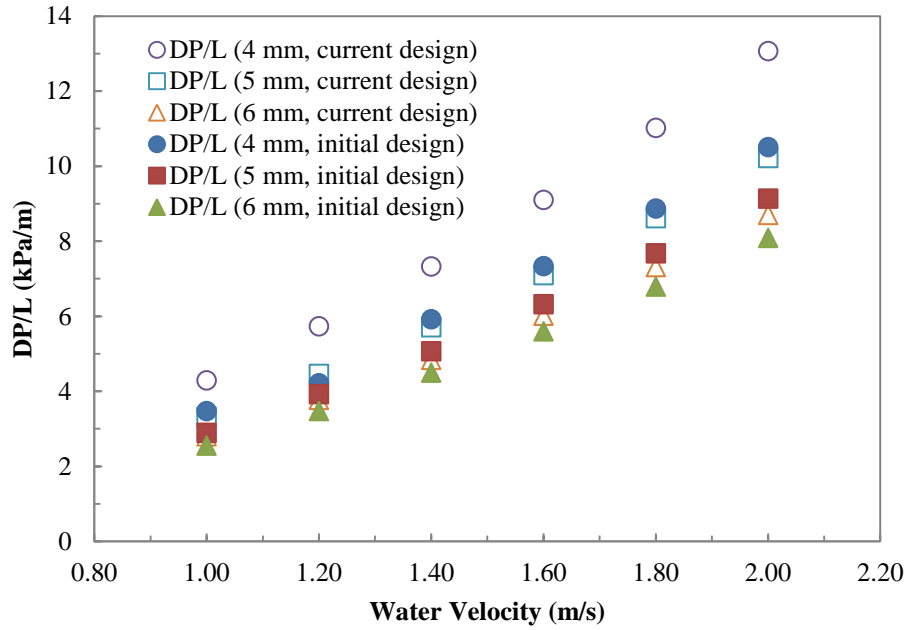


Fig. 4.14: Variation of DP/L with water velocity and plate gap

Fig. 4.15 shows the variation of water HTC with water velocity and plate gap for the initial design and current prototypes. As water velocity was increased, the water HTC increased. When the plate gap was decreased, the water HTC increased. For the same water velocity and the plate gap, the water-side HTC of current prototype was 6.6% higher than that of initial design.

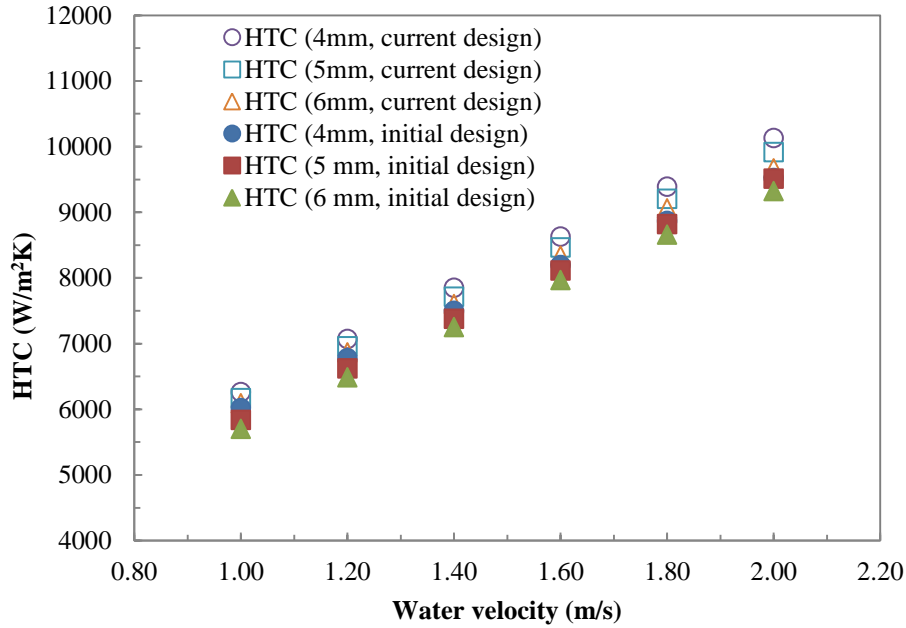


Fig. 4.15: Variation of water-side HTC with water velocity and plate gap

4.5 Experimental test with water to water

4.5.1 Test conditions and matrix

Table 4.5 shows the test matrix. The test is designed for calculation of the heat transfer coefficient and pressure drop of water-side. Test procedure is same as the water-to-water test of the plate heat exchanger.

Table 4.5: Test matrix of water-to-water test

Flow gap (mm)	Heat source temperature (°C)	Heat sink temperature (°C)	Heat source MFR (kg·s ⁻¹)	Heat sink MFR (kg·s ⁻¹)	Test
6.35	25	5.6	6.0 to 13.0 with 0.5 step	0.4	16
4	25	5.6	6.0 to 13.0 with 0.5 step	0.4	16

The convective heat transfer coefficient between the solid surface and moving fluid was calculated using Newton’s law of cooling. The main difficulty of using this

methodology lies in the measurement of the surface temperature (Fernandez-Seara et al., 2007). The surface temperature varies from location to location along the flow, and sometimes the surface is not accessible for temperature measurement. The Wilson plot method is an alternative experimental method to find the convective heat transfer coefficient without measuring the surface temperature. In this study, the original Wilson plot method was applied to indirectly measure the water-side heat transfer coefficient. It should be noted that in order to apply modified Wilson Plot, the Reynolds number of the refrigerant-side is required. However, in the novel heat exchanger design, it is intended to vary for the refrigerant flow area. Therefore, the original Wilson plot method was applied instead of the modified Wilson plot.

4.5.2 Test results of water-side heat transfer coefficient

In order to calculate the ammonia-side heat transfer coefficient, the water-side heat transfer coefficient (h_w) must be determined. For h_w , calibration equations were established from data obtained by the Wilson plot method. The slope of the plot provides the constant of the calibration correlation, a power-law relationship, for the water-side heat transfer coefficients. Fig. 4.16 shows the Wilson plot for the water-side HTC of the novel heat exchanger.

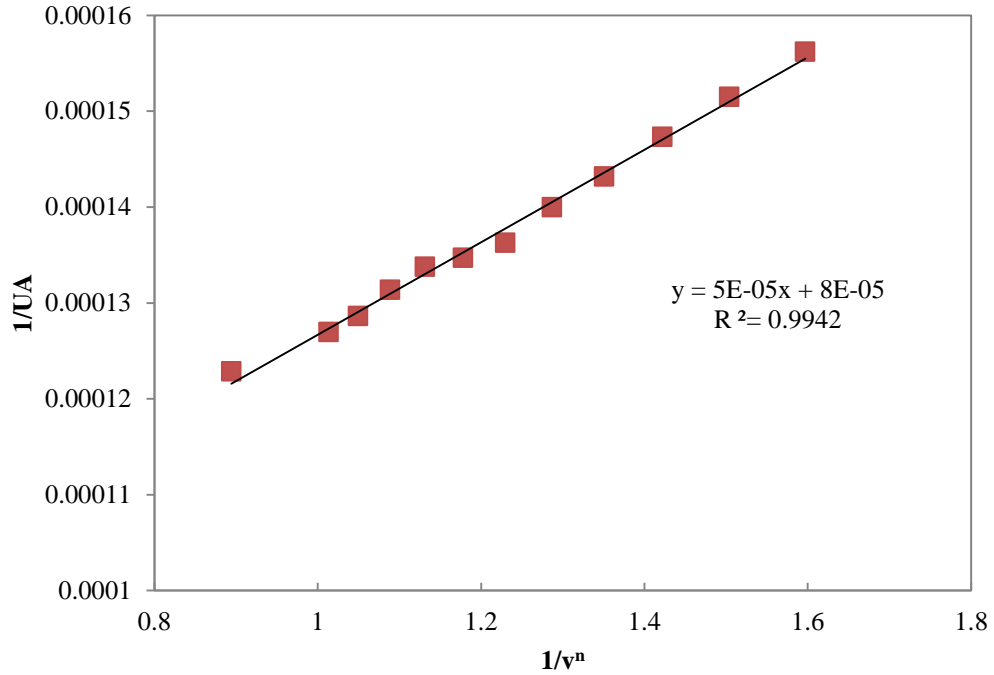


Fig. 4.16: Wilson Plot of novel heat exchanger

Fin efficiency was calculated to be 95% due to the large edge space. The calibration correlation for the water-side Nusselt number is calculated provided in Eq. (4.1).

$$Nu = 0.034944 \cdot Re^{0.75} \cdot Pr^{1/3} \cdot \left(\frac{\mu}{\mu_s} \right)^{0.14} \quad (4.1)$$

For $6,000 < Re < 22,000$

4.5.3 Test results of water-side pressure drop

Pressure drop was correlated with Reynolds number since the friction factor is the function of the Reynolds number as show in Fig. 4.17. Eq. (4.2) shows the pressure drop correlation of the novel heat exchanger.

$$f = \frac{8.1739 \times 10^{-8} \cdot Re^{1.764} \rho \cdot d}{2G^2} \quad (4.2)$$

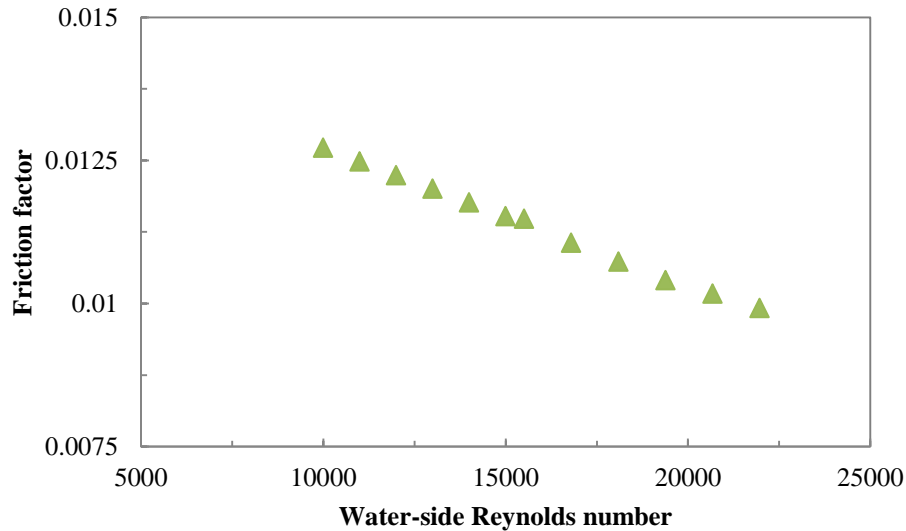


Fig. 4.17: Variation of the friction factor with water-side Reynolds number

4.5.4 Comparison between CFD simulation and experimental results

Fig. 4.18 shows the Nusselt number comparison between CFD simulation results and experimental results. Nusselt number of CFD simulation results was 37% higher than that of experimental results. Fig. 4.19 shows the friction factor comparison between CFD simulation results and experimental results. Friction factor of CFD simulation results was 22% higher than that of experimental results. There were three main reasons for this deviation. First, the novel LTLHX tested had manufacturing and installation limitations. There was gap between heat exchanger housing and plates, which caused bypass of the water. Moreover, the heat exchanger housing expanded when the pressure of the water-side was increased. Therefore, the actual flow rate to the heat exchanger could be lower than what it has to be. Second, the maldistribution of the water could happen. The heat exchanger flow gap of the header side was larger than other side. This can decrease the heat transfer in the header side. Third, the CFD simulation assumed that there is no

fouling of any kind exists in the computational domain. However, there was some fouling at the heat exchanger surface.

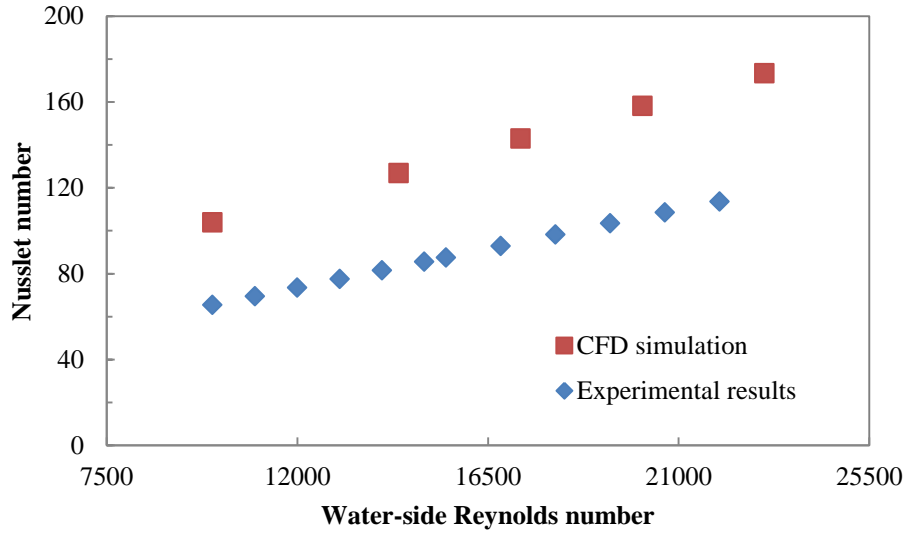


Fig. 4.18: Nusselt number comparison between CFD simulation and experimental results

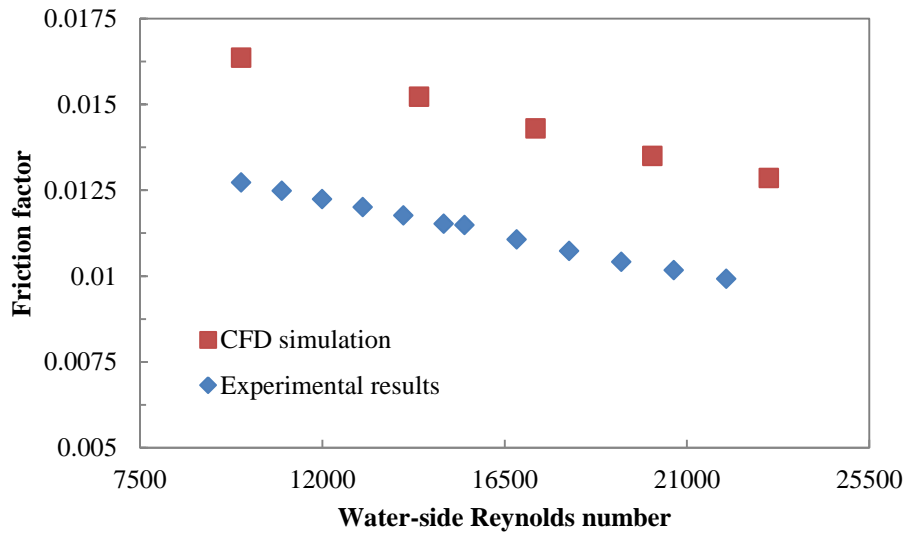


Fig. 4.19: Friction factor comparison between CFD simulation and experimental results

4.6 Experimental test results with R22

4.6.1 Test conditions and test matrix

The test matrix is shown in Table 4.6. The temperature of water, the MFR of water, the MFR of R22, and the evaporation pressure were selected as design variables. The novel heat exchanger was made of aluminum.

Table 4.6: Test matrix of novel heat exchanger

Test	Heat source temperature (°C)	Heat source MFR (kg·s ⁻¹)	Heat sink MFR (kg·s ⁻¹)	R22 MFR (g·s ⁻¹)	Saturation pressure (kPa)
Variation of water flow	26	10 to 14 with 1 step	2.0	70	-
Variation of R22	26	10	2.0	45 to 60 with 5 step	-
Variation of evaporation pressure	26	10	2.0	73	894 to 930

4.6.2 Data reduction

The U value (overall heat transfer coefficient) was calculated with $LMTD$ (Logarithmic Mean Temperature Difference) method with the active heat transfer area of the heat exchanger. Two different heat transfer areas can be calculated in terms of water and refrigerant flow. U_i was calculated based on the refrigerant-side heat transfer area considering only ammonia channel areas. On the other hands, U_o was calculated by the water-side heat transfer area considering both refrigerant channel areas and bonding areas as shown in Eq. (4.1). Water-side heat transfer coefficient was calculated from the Wilson plot method as described in the chapter 4.4. The refrigerant-side heat transfer coefficient was obtained from Eq. (4.2). Since the thermal resistance of the wall (R_w) was relatively small, it was neglected.

$$\frac{1}{U_o \cdot A_o} = \frac{1}{h_w \cdot A_o} + \frac{1}{h_r \cdot A_i} + R_w \quad (4.3)$$

$$h_r = \frac{1}{A_i \cdot \left(\frac{1}{U_o \cdot A_o} - \frac{1}{h_w \cdot A_o} \right)} \quad (4.4)$$

4.6.3 Variation of water-side Reynolds number

The MFR of refrigerant was maintained at constant, and the temperature of the water inlet was fixed at 26 °C. The MFR of water was varied from 10 to 14 kg s⁻¹ with 1 kg s⁻¹ of step. The degree of subcooling and superheating were both kept constant. Fig. 4.20 shows the variation of the heat transfer capacity and the *LMTD* with the water-side Reynolds number. As the water-side Reynolds number was increased, the heat transfer capacity of the heat exchanger increased slightly while the *LMTD* decreased. As the water-side Reynolds number was increased, the temperature of the water inlet increased while the evaporation temperature was kept constant. An increased capacity and decreased *LMTD* resulted in an increase of overall heat transfer coefficient as shown in Fig. 4.21.

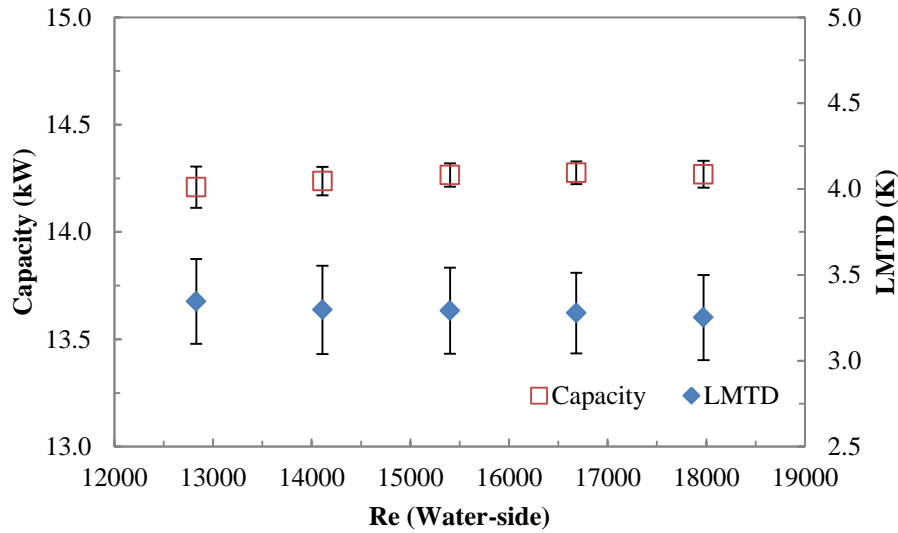


Fig. 4.20: Variation of capacity and LMTD with water-side Reynolds number

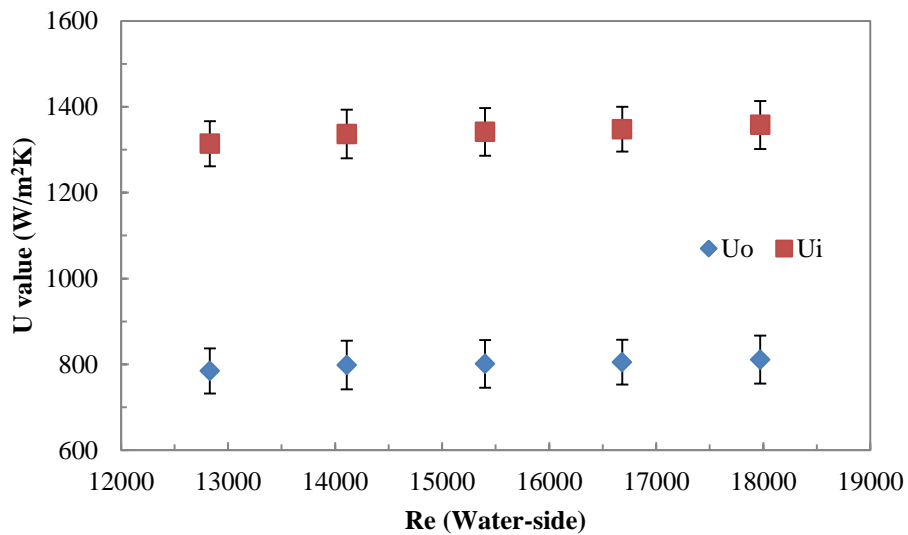


Fig. 4.21: Variation of U values with water-side Reynolds number

Fig. 4.22 shows the variation of heat transfer coefficients with water-side Reynolds number. As the water Reynolds number was increased, the water-side heat transfer coefficient increased, while the refrigerant-side heat transfer coefficient was shown to be almost constant. In the previous chapter, the PHX was tested under the same test conditions. As the water-side Reynolds number was increased, the refrigerant-side heat transfer coefficient changed due to the change of the local heat transfer. The main

reason was that the flow boiling heat transfer mechanism was on the nucleate boiling heat transfer region. However, the flow boiling heat transfer coefficient of the novel heat exchanger was not dependent on the water-side Reynolds number.

The Bo number of the experimental data was plotted with criterion of Thonon et al. as shown in Fig. 4.23. The experimental data was on the convective boiling heat transfer region rather than the nucleate boiling heat transfer region.

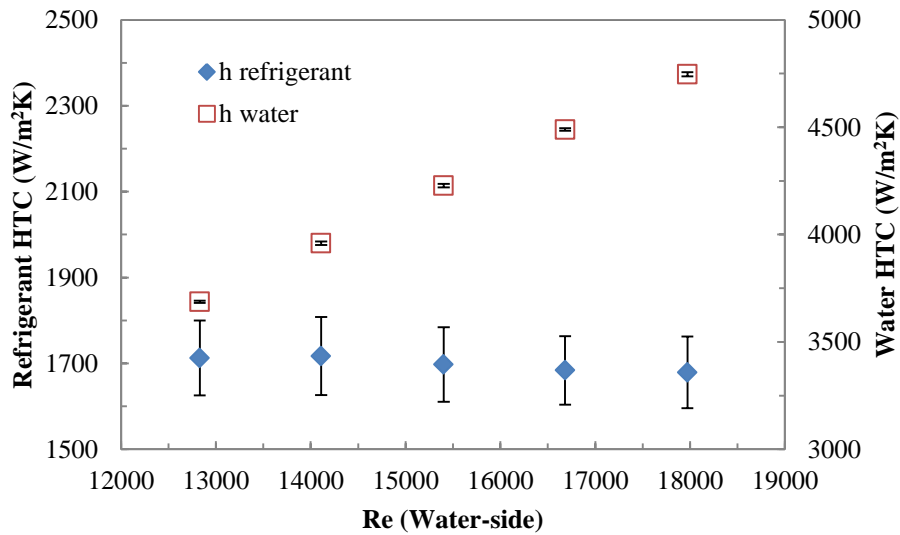


Fig. 4.22: Variation of heat transfer coefficients with water-side Reynolds number

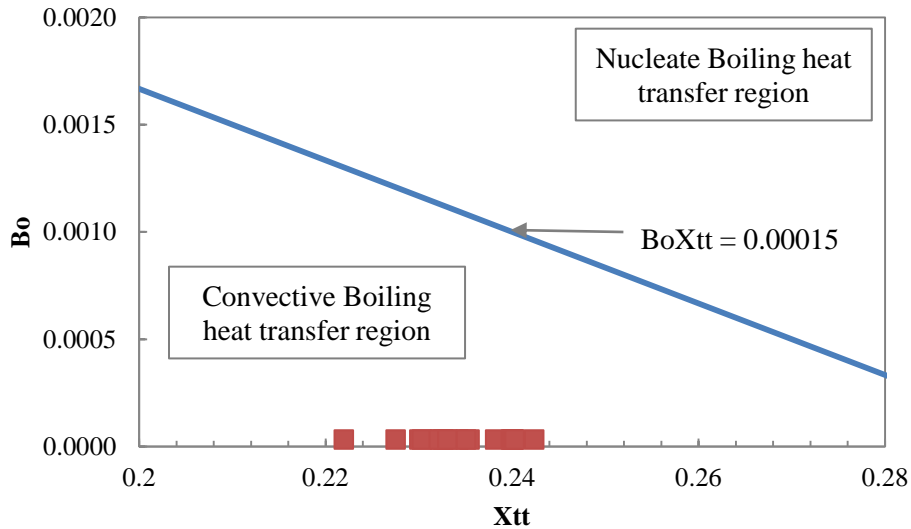


Fig. 4.23: Experimental data of boiling number with criterion of Thonon et al.

4.6.4 Variation of R22 liquid Reynolds number

The MFR of water was maintained at constant, and the temperature of the water inlet was fixed at 26 °C. The MFR of refrigerant was varied from 45 to 60 g s⁻¹ with 5 g s⁻¹ of step, while the expansion valve opening was fixed constant. Fig. 4.24 shows the variation of the heat transfer capacity and *LMTD* with Reynolds number of liquid refrigerant. As Reynolds number of liquid refrigerant was increased, the heat transfer capacity of the heat exchanger increased and the *LMTD* decreased. An increased heat transfer capacity was mainly due to an increased refrigerant flow rate. As Reynolds number of liquid refrigerant was increased, since the expansion valve opening was fixed, the evaporation temperature increased as shown in Fig. 4.25. An increased evaporation temperature caused the *LMTD* to decrease.

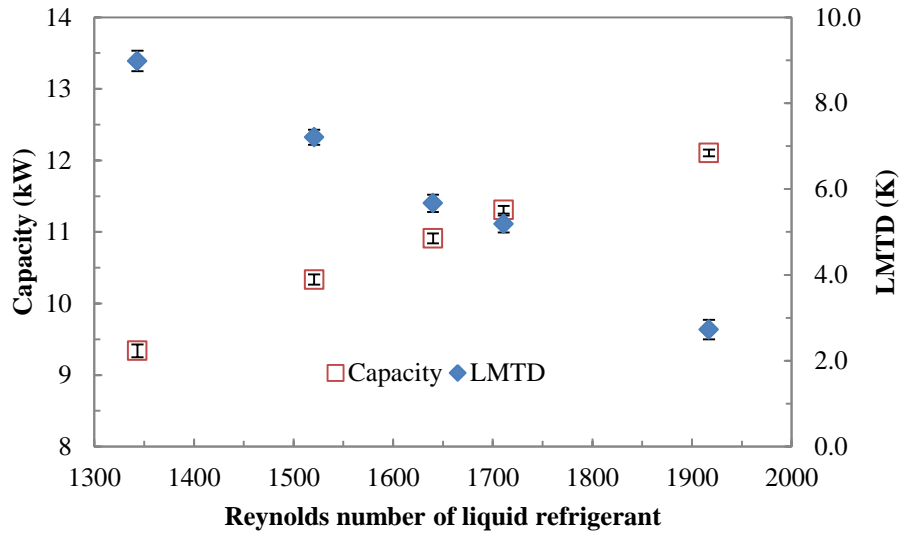


Fig. 4.24: Variation of capacity and LMTD with Reynolds number of liquid refrigerant

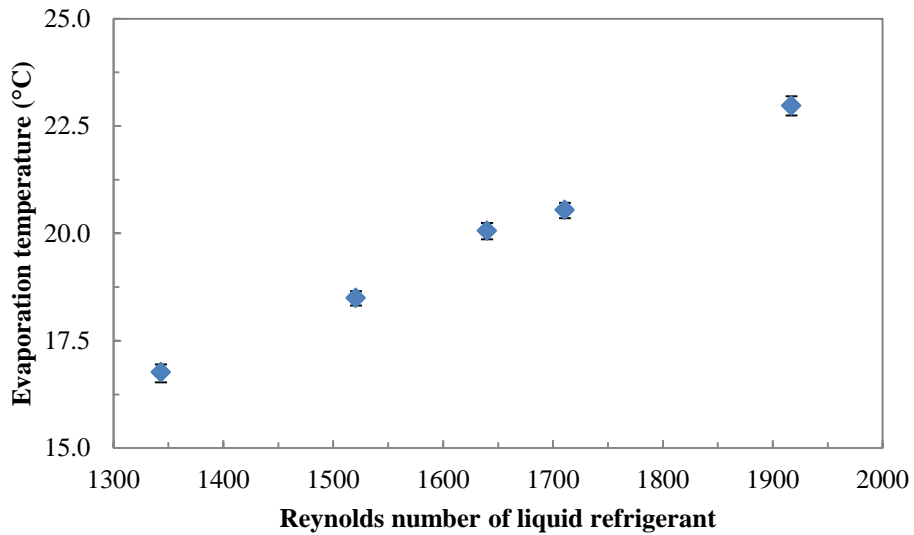


Fig. 4.25: Variation of evaporation temperature with Reynolds number of liquid refrigerant

Fig. 4.26 shows the variation of U value with Reynolds number of liquid refrigerant. As Reynolds number of liquid refrigerant was increased, U value increased due to an increased heat transfer capacity and a decreased $LMTD$.

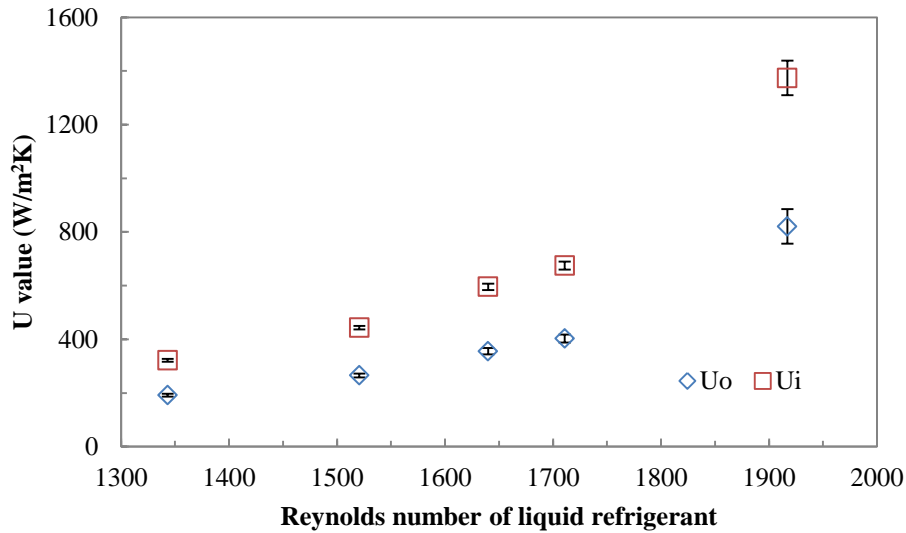


Fig. 4.26: Variation of U values with Reynolds number of liquid refrigerant

Fig. 4.27 shows the variation of water-side heat transfer coefficient and refrigerant-side heat transfer coefficient with Reynolds number of liquid refrigerant. It is clear that even though Reynolds number of liquid refrigerant was increased, it does not affect the water-side heat transfer coefficient because single-phase heat transfer is independent on the temperature change. An increased refrigerant MFR enhanced the refrigerant-side heat transfer coefficient. It can be explained with two main factors; enhanced convective number and increased Pr (reduced pressure) as shown in Fig. 4.28. First, as the refrigerant flow rate was increased, the heat transfer capacity and mass flux increased. An increased heat flux enhanced nucleate boiling heat transfer in the refrigerant-side heat transfer. Moreover, an increased mass flux enhanced convective boiling heat transfer. Second, an increased evaporation temperature increased the Pr .

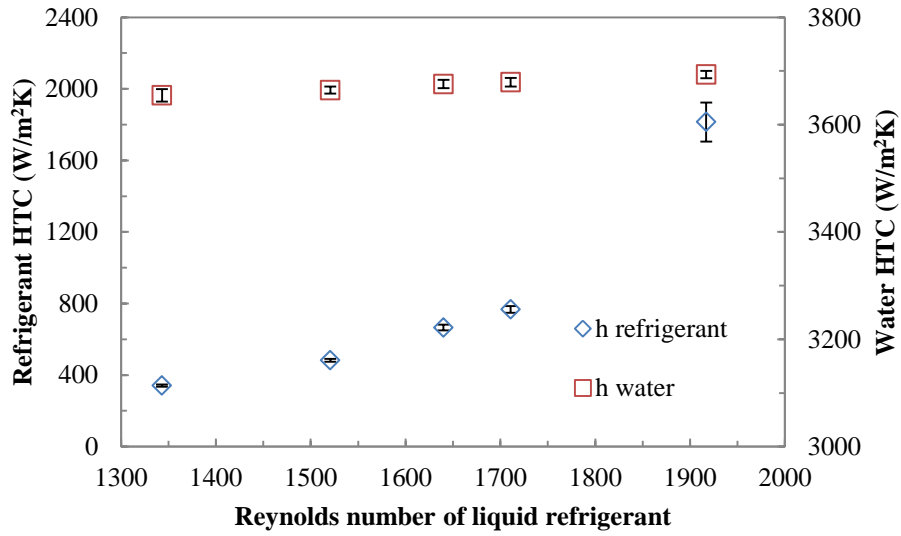


Fig. 4.27: Variation of heat transfer coefficients with Reynolds number of liquid refrigerant

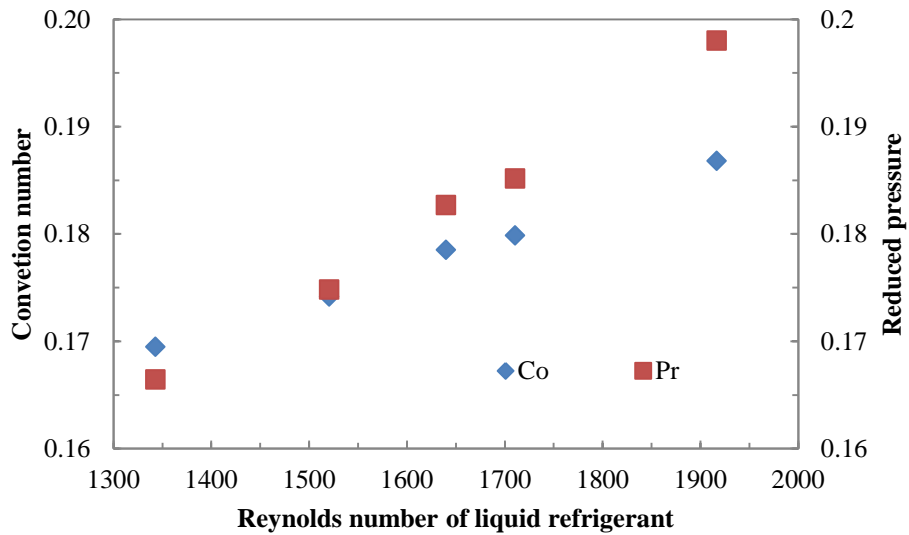


Fig. 4.28: Variation of convective number and reduced pressure with Reynolds number of liquid refrigerant

4.6.5 Variation of evaporation pressure

The MFR of water and the temperature of the water inlet were maintained at constant. The MFR of refrigerant was kept constant. The expansion valve opening was controlled to vary the evaporation pressure. Fig. 4.29 shows the variation of heat transfer capacity and $LMTD$ with evaporation pressure. As the evaporation pressure was increased from 894 to 930 kPa, U value increased by 29% as shown in Fig. 4.30. This was mostly due to the decreased $LMTD$.

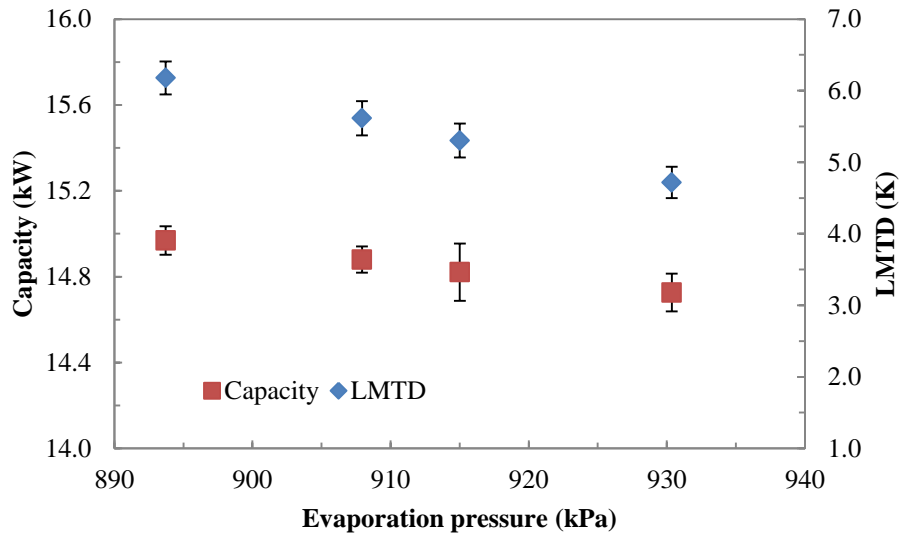


Fig. 4.29: Variation of degrees of capacity and LMTD with evaporation pressure

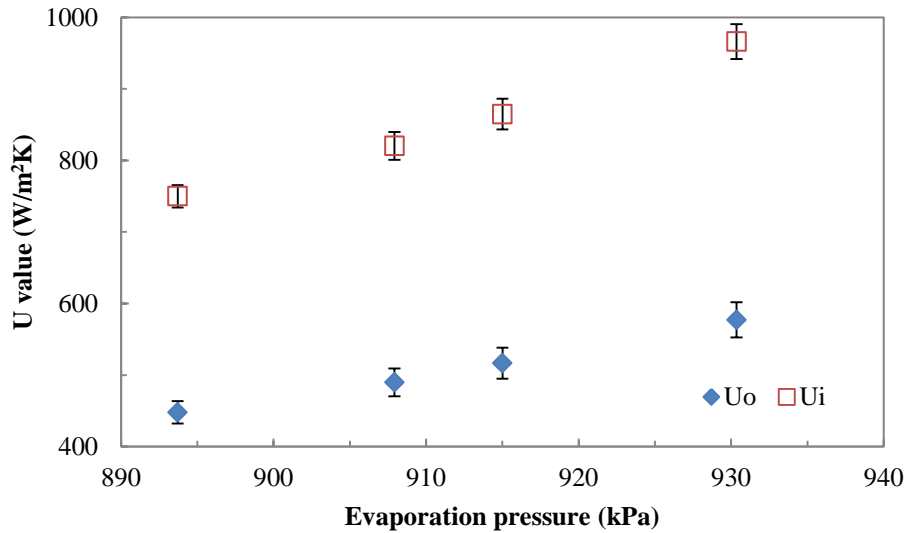


Fig. 4.30: Variation of U values with evaporation pressure

Fig. 4.31 shows the variation of water-side heat transfer coefficient and refrigerant-side heat transfer coefficient with the evaporation pressure. As the evaporation pressure was increased, refrigerant-side heat transfer coefficient increased, while water-side heat transfer coefficient was constant. As the evaporation pressure was increased from 894 to 930 kPa, the refrigerant-side heat transfer coefficient increased by 35%. An increased refrigerant-side heat transfer coefficient by increasing the evaporation pressure can be explained with 4 main aspects. First, the surface tension decreased as the evaporation temperature was increased. A lower surface tension enhanced nucleate boiling heat transfer. Second, the convection number increased and reduced pressure increased as shown in Fig. 4.32. An increased vapor density and decreased liquid density at low quality region increased the flow velocity, which enhanced the convective boiling heat transfer. Third, a liquid film thickness becomes thinner due to a large liquid droplet entrainment. This reduces the thermal resistance, and then enhanced the heat transfer (Yun, 2002). Last, the superheating and subcooling regions were reduced as shown in Fig. 4.33. In the heat exchanger, reduced vapor and liquid sections mean an increase of two-

phase region. This increased the refrigerant-side heat transfer coefficient. Therefore, an increased evaporation temperature enhanced both nucleate boiling and convective heat transfer mechanisms.

It should be noted that at the high quality region, the boiling heat transfer coefficient reduces as the evaporation pressure is increased, because the dry-out occurs earlier, and the reduced pressure causes the convective heat transfer lower. Under the given test condition, an increased heat transfer coefficient in the low quality region was greater than a decreased heat transfer coefficient in the high quality region. Therefore, the boiling heat transfer coefficient over the heat exchanger was improved.

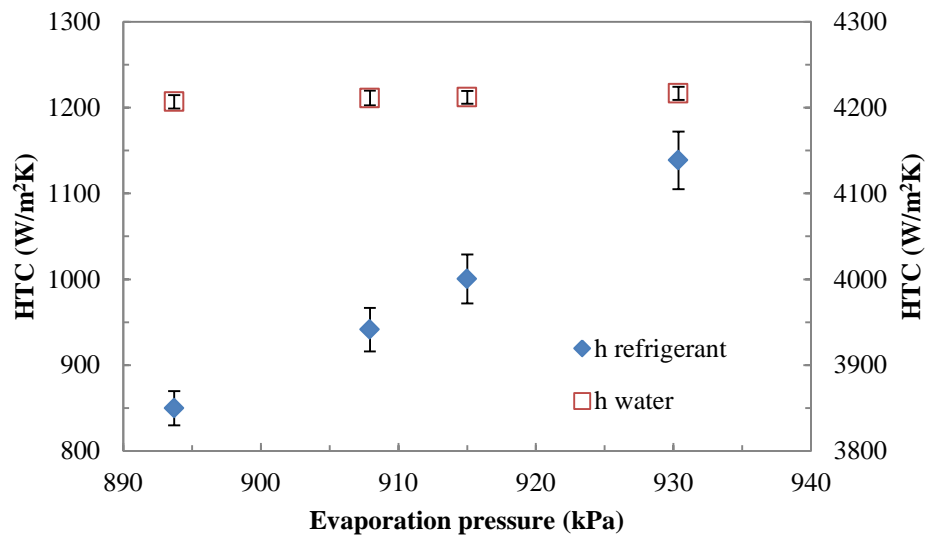


Fig. 4.31: Variation of heat transfer coefficients with evaporation pressure

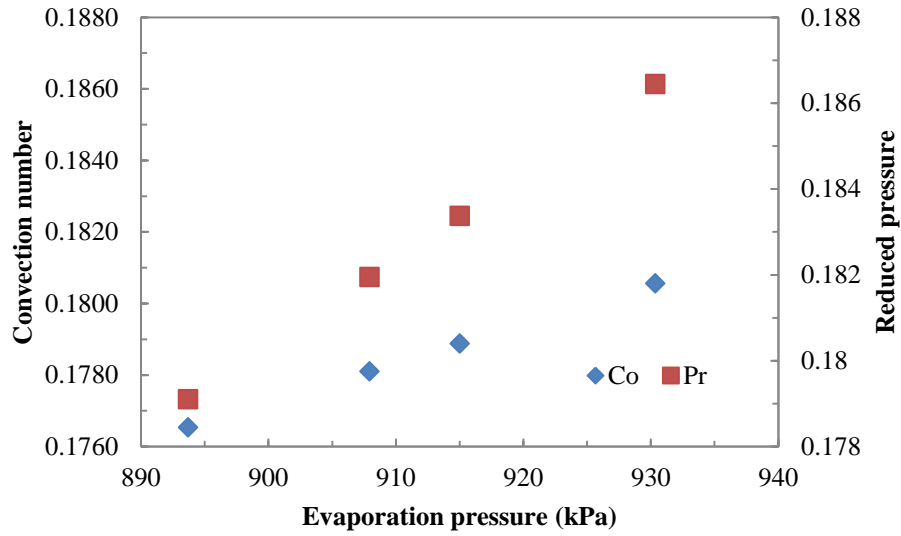


Fig. 4.32: Variation of convection number and reduced pressure with evaporation pressure

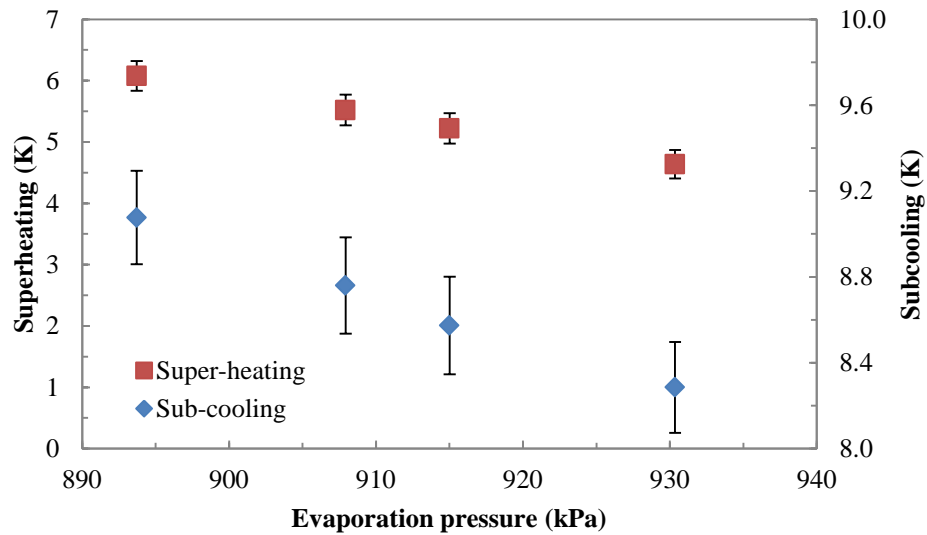


Fig. 4.33: Variation of degrees of superheating and subcooling with evaporation pressure

4.6.6 Performance comparison between PHX and novel LTLHX with R22

The performance of the novel LTLHX was compared with that of the PHX. Geometrical comparison between the PHX and novel LTLHX was shown in Table 4.7. The cross sectional flow area ratio between the water and refrigerant-side was 0.94 for the PHX, and it was 13.9 for the novel heat exchanger.

Table 4.7: Geometrical comparison between PHX and novel LTLHX

Property	Unit	Plate heat exchanger	Novel LTLHX
Heat transfer area	m ²	4.22	5.41/3.23 (Water-side/refrigerant-side)
Water channel number	EA	17	5
Refrigerant channel number	EA	18	5
Water flow area	mm ²	10,649	11,200
Refrigerant flow area	mm ²	11,275	808
Flow area ratio (Water to refrigerant)	-	0.94	13.9

To compare the novel heat exchanger with the PHX, the cases which have the same *LMTD* were chosen. Moreover, the water temperature change between the water inlet and outlet was same for both the PHX and novel heat exchanger cases. Fig. 4.34 shows the comparison of *U* values between the PHX and novel heat exchanger. *U* value of the PHX was 573 W·m⁻²·K⁻¹, and *U_o* and *U_i* of the novel heat exchanger were 785 and 1,314 W·m⁻²·K⁻¹, respectively. These were 37, and 130% higher than *U* value of the PHX.

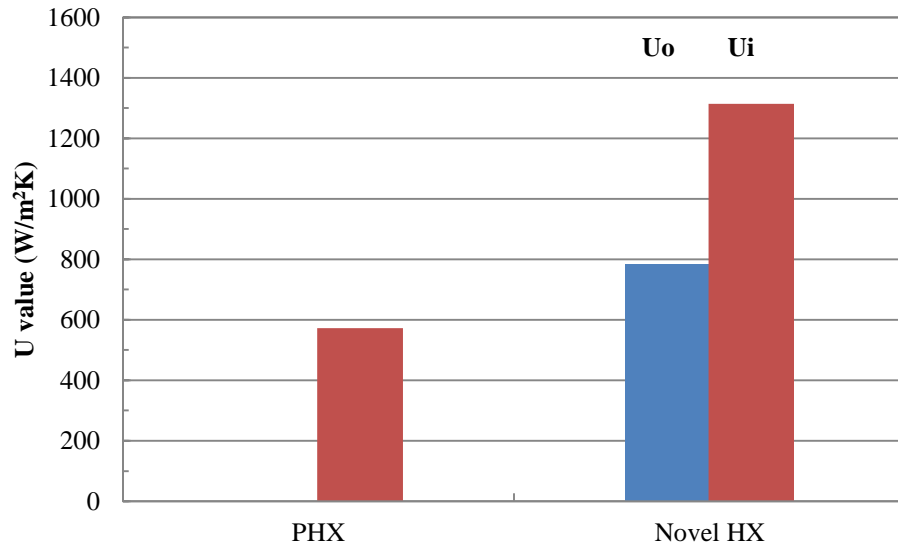


Fig. 4.34: Comparison of U values

Fig. 4.35 shows the pressure drop per length (DP/L) of the PHX and novel heat exchanger. DP/L of the PHX was 37.5 kPa/m, and that of the novel heat exchanger was 2.2 kPa/m. The water pressure drop of the PHX was higher than that of the novel heat exchanger. To reduce the water pressure drop, the PHX needs more plates, but this will increase the heat transfer area, and reduce refrigerant mass flux. Eventually, this will decrease the heat transfer performance. Even though the water MFR of the novel heat exchanger was higher than that of the PHX by 220%, the pressure drop of the novel heat exchanger was 17 times smaller so that pumping power of the novel heat exchanger was much smaller than that of the PHX.

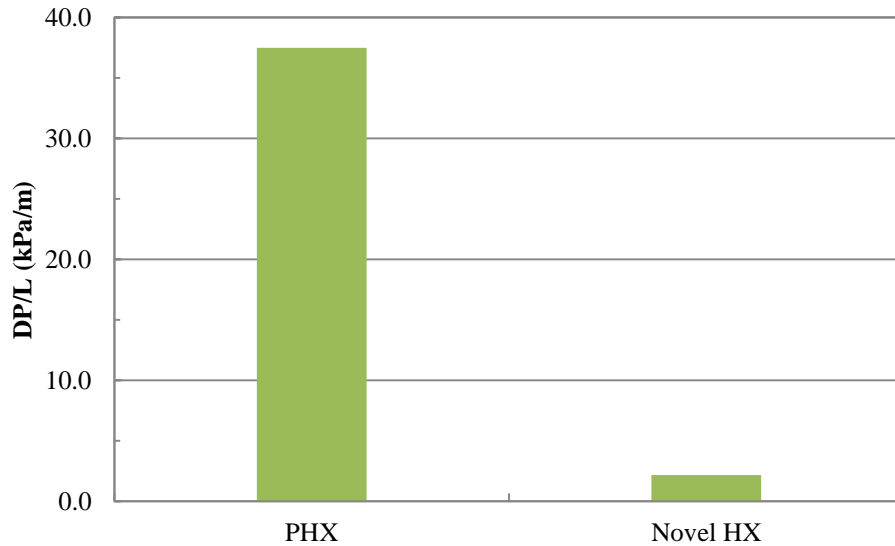


Fig. 4.35: Comparison of DP/L

The water-side heat transfer coefficient of the PHX was much higher than that of the novel heat exchanger as shown in Fig. 4.36. However, the refrigerant-side heat transfer coefficient of the novel heat exchanger was greater than that of the PHX as shown in Fig. 4.37. For the PHX, the refrigerant-side heat transfer coefficient was much smaller than water-side heat transfer coefficient. The limitation of the heat transfer was on the refrigerant side. In contrast, for the novel heat exchanger, the refrigerant-side heat transfer coefficient improved by adjusting the flow area ratio of water and refrigerant. Therefore, the total heat transfer performance of the novel heat exchanger was higher than that of PHX with a reduced pumping power.

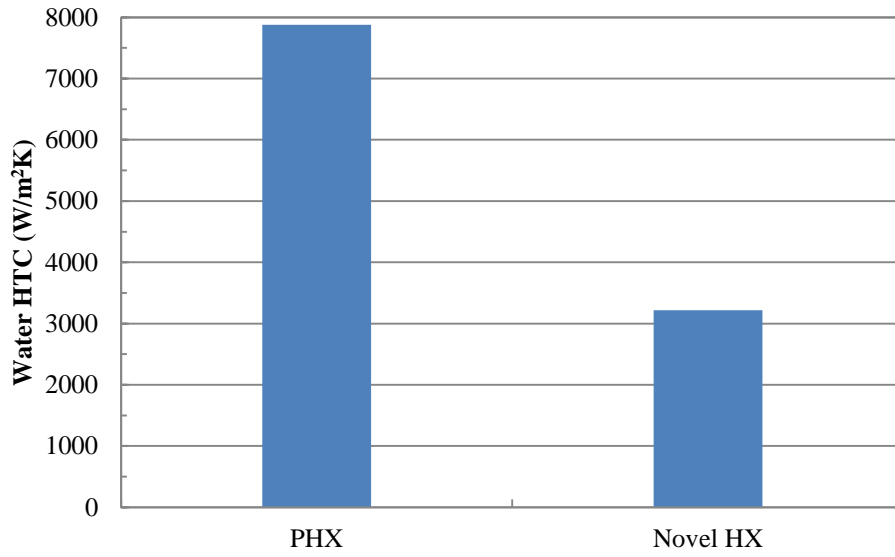


Fig. 4.36: Comparison of water-side heat transfer coefficient

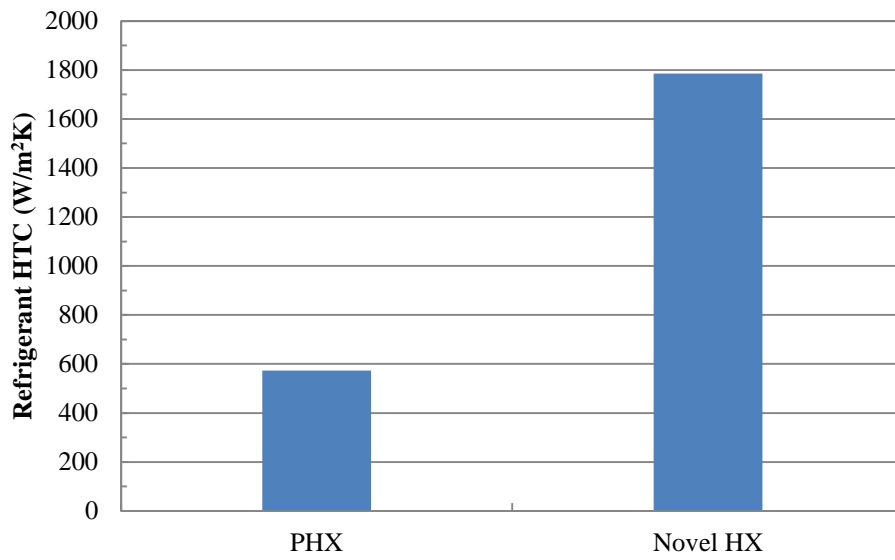


Fig. 4.37: Comparison of the refrigerant-side heat transfer coefficient

4.7 Experimental test results with ammonia

4.7.1 Test conditions and test matrix

The test matrix is shown in Table 4.8. The temperature of water, the MFR of water, the MFR of ammonia, and the evaporation pressure were selected as design variables. The novel heat exchanger was made of aluminum.

Table 4.8: Test matrix of novel heat exchanger

Test	Heat source temperature (°C)	Heat source MFR (kg·s ⁻¹)	Heat sink MFR (kg·s ⁻¹)	Ammonia MFR (g·s ⁻¹)	Saturation pressure (kPa)
Variation of water flow	26	7 to 11 with 1 step	2.0	28	-
Variation of ammonia	26	8	2.0	18 to 22 with 1 step	-
Variation of evaporation pressure	26	7	2.0	22	839 to 926

4.7.2 Variation of water-side Reynolds number

The MFR of refrigerant was maintained at constant, and the temperature of the water inlet was fixed at 26 °C. The MFR of water was varied from 7 to 11 kg s⁻¹ with 1 kg s⁻¹ of step. The degree of subcooling and superheating were both kept constant. Fig. 4.38 shows the variation of the heat transfer capacity and *LMTD* with the water-side Reynolds number. As the water-side Reynolds number was increased, the heat transfer capacity of the heat exchanger did not change much and *LMTD* decreased. As the water-side Reynolds number was increased, the temperature of the water outlet increased while the evaporation temperature was increased. A decreased *LMTD* resulted in an increase of the overall heat transfer coefficient as show in Fig. 4.39.

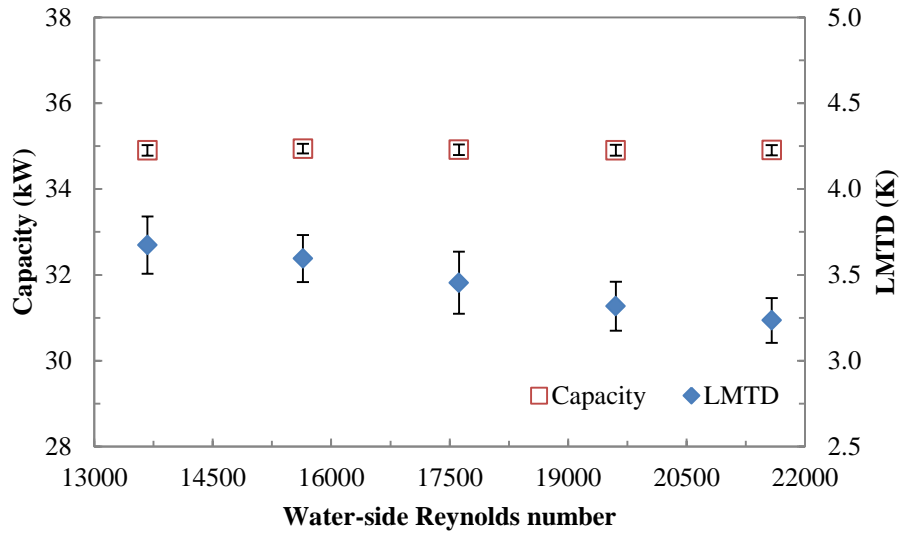


Fig. 4.38: Variation of capacity and LMTD with Water-side Reynolds number

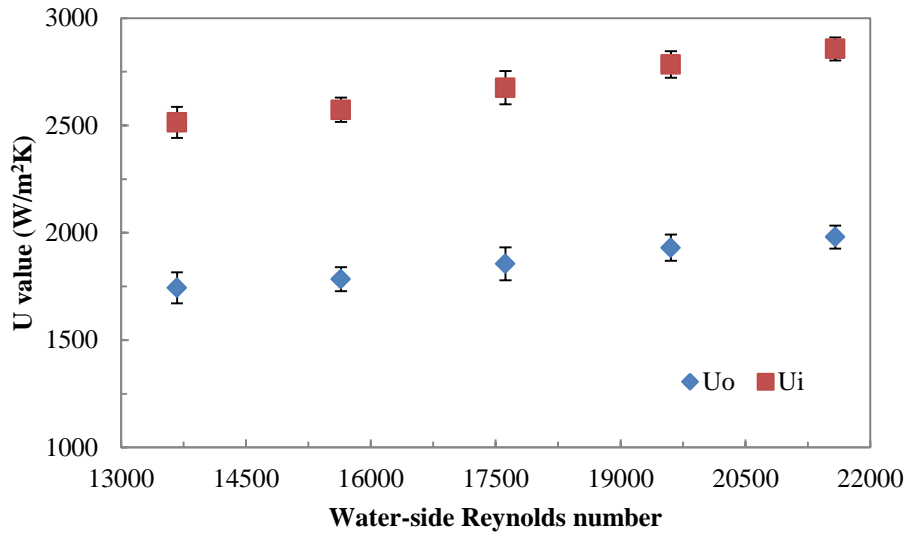


Fig. 4.39: Variation of U value with Water-side Reynolds number

Fig. 4.40 shows the variation of refrigerant-side heat transfer coefficient and water-side heat transfer coefficient with water-side Reynolds number. As water-side Reynolds number was increased, the water-side heat transfer coefficient was increased, and refrigerant-side heat transfer was almost constant. As discussed in section 4.6.3, the

dominant heat transfer contribution in the novel LTLHX was convective heat transfer, therefore, refrigerant-side heat transfer coefficient was not affected by water-side.

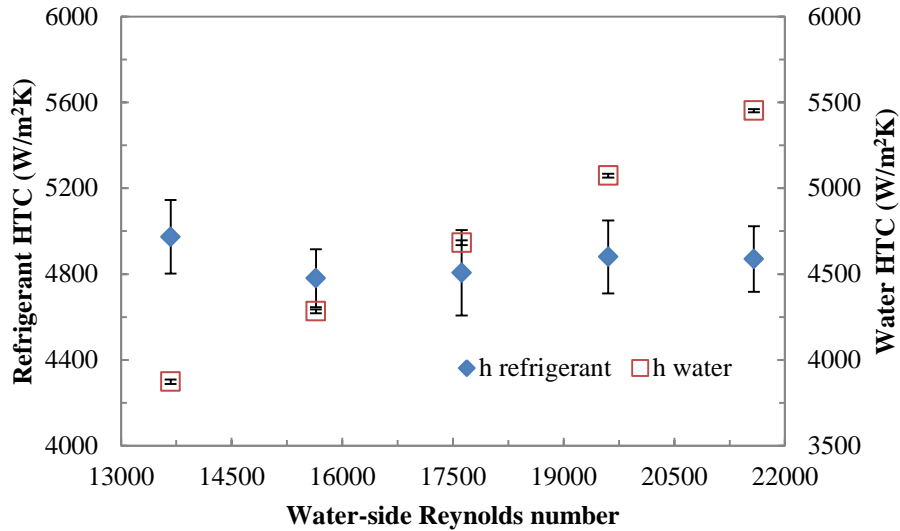


Fig. 4.40: Variation of heat transfer coefficient with Water-side Reynolds number

4.7.3 Variation of ammonia liquid Reynolds number

The MFR of water was maintained at constant, and the temperature of the water inlet was fixed at 26 °C. The MFR of refrigerant was varied from 18 to 22 g s⁻¹ with 1 g s⁻¹ of step, while the expansion valve opening was fixed constant. Fig. 4.24 shows the variation of the heat transfer capacity and *LMTD* with ammonia liquid Reynolds number. The heat transfer capacity of the heat exchanger increased and the *LMTD* decreased with ammonia liquid Reynolds number incensement. An increased heat transfer capacity was mainly due to an increased refrigerant flow rate. As ammonia liquid Reynolds number was increased, since the expansion valve opening was fixed, the evaporation temperature increased as shown in Fig. 4.25. An increased evaporation temperature caused the *LMTD*

to decrease. An increased heat transfer capacity and decreased $LMTD$ resulted in the increase of U values as shown in Fig. 4.42.

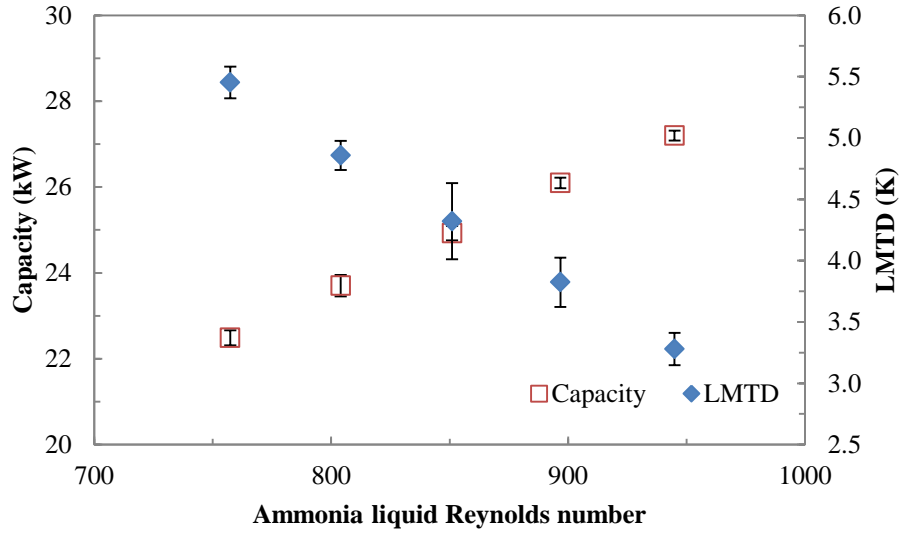


Fig. 4.41: Variation of capacity and LMTD with ammonia liquid Reynolds number

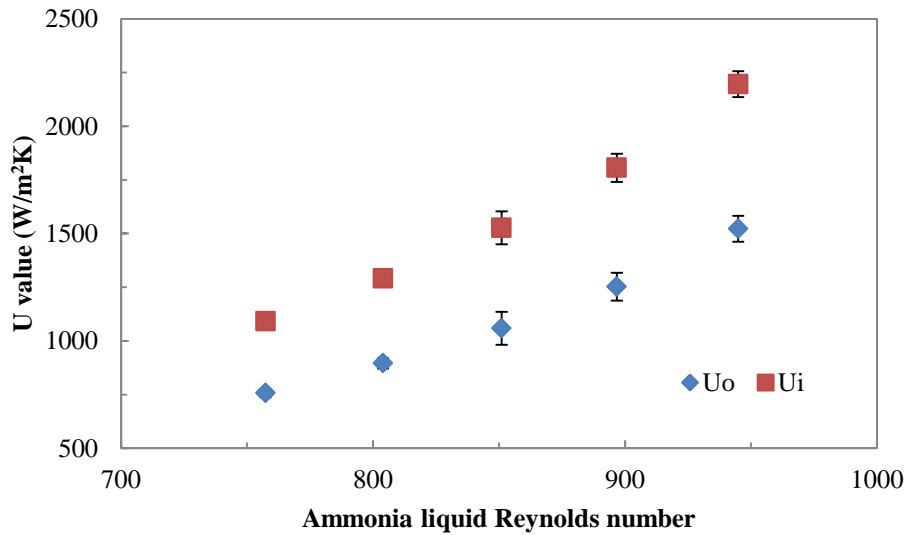


Fig. 4.42: Variation of U value with ammonia liquid Reynolds number

Fig. 4.43 shows the variation of the heat transfer coefficient with ammonia liquid Reynolds number. The water-side heat transfer coefficient did not change. The ammonia-side heat transfer coefficient increased with ammonia liquid Reynolds number. It is

because of increased mass flow rate resulted in the increase of both heat flux and mass flux. These enhanced nucleate boiling heat transfer and convective boiling heat transfer contributions.

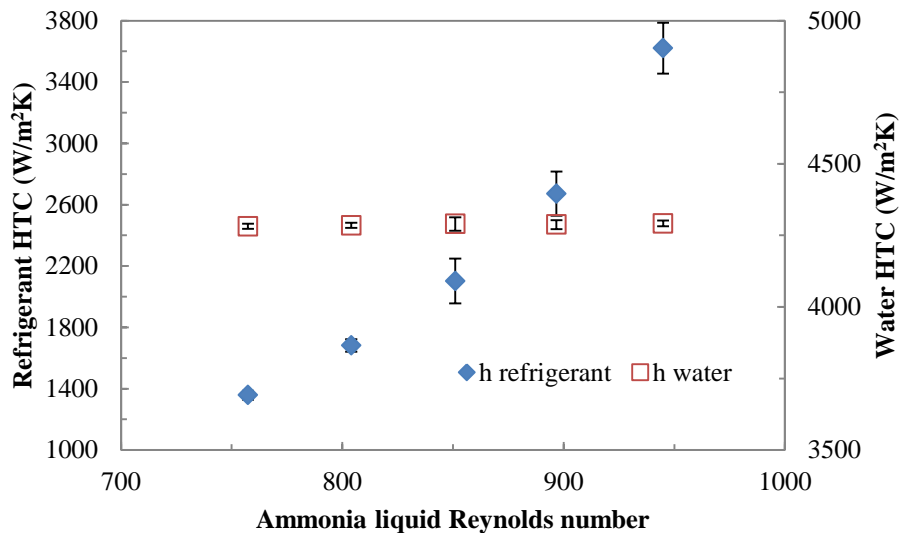


Fig. 4.43: Variation of heat transfer coefficient with ammonia liquid Reynolds number

4.7.4 Variation of evaporation pressure

The MFR of water and the temperature of the water inlet were maintained at constant, respectively. The MFR of the refrigerant-side was kept constant. The expansion valve opening was varied to change the evaporation pressure. As the evaporation pressure was increased, refrigerant-side heat transfer coefficient increased, while water-side heat transfer coefficient was constant as shown in Fig. 4.44. An increased refrigerant-side heat transfer coefficient by increasing the evaporation pressure can be explained with 4 main aspects: decreased surface tension, increased convection number, reduced liquid film thickness, and reduced superheated vapor and subcooled liquid region in the heat exchanger as discussed in section 4.6.5.

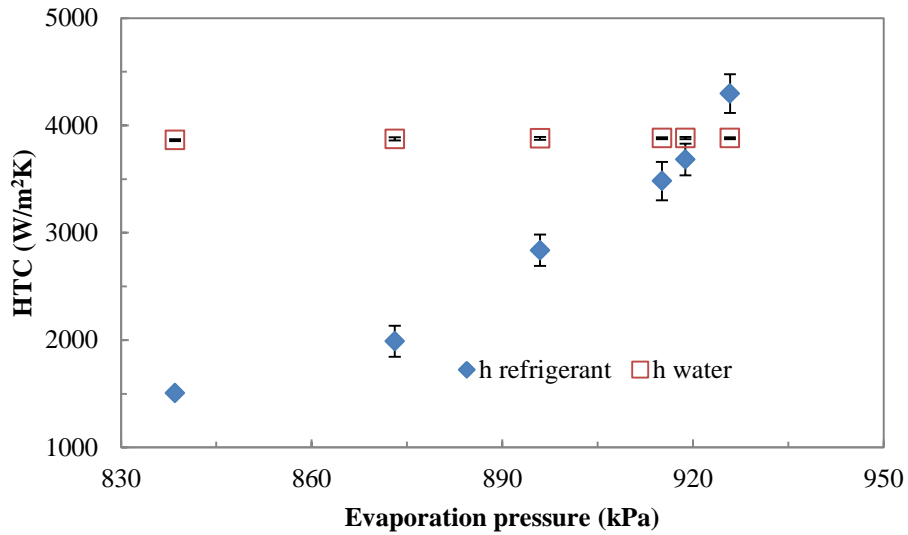


Fig. 4.44: Variation of heat transfer coefficient with evaporation pressure

4.7.5 Performance comparison between PHX and novel LTLHX with ammonia

The performance of novel LTLHX was compared with the PHX. Geometrical comparison between the PHX and novel LTLHX was shown in Table 4.7. To compare the novel LTLHX with the PHX, the cases which have the same *LMTD* were chosen. Moreover, the delta T between the water inlet and outlet was same for both the PHX and novel heat exchanger cases. Fig. 4.45 shows the comparison of *U* values between the PHX and novel heat exchanger. U_o and U_i of the novel heat exchanger were 1,455 and 2,105 $W \cdot m^{-2} \cdot K^{-1}$, respectively. These were 94, and 181% higher than *U* value of the PHX.

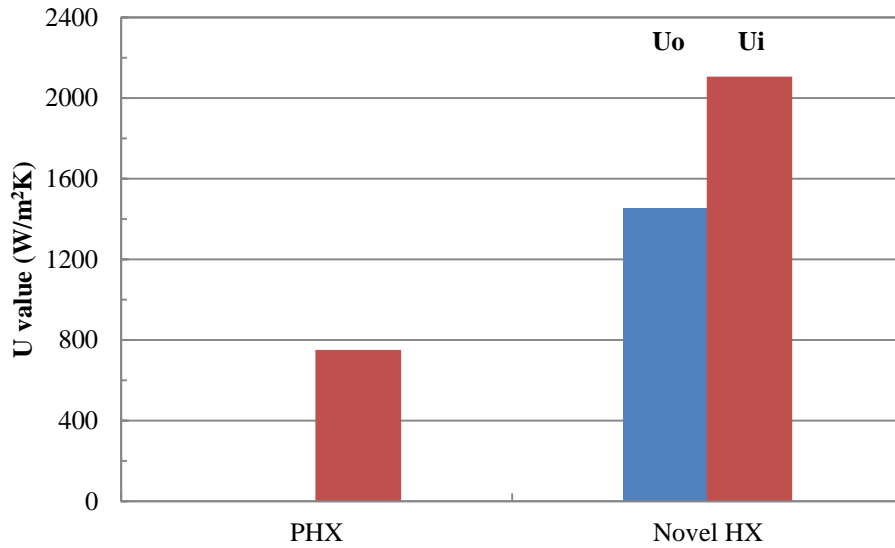


Fig. 4.45: Comparison of U value

Fig. 4.46 shows the pressure drop per length (DP/L) of the PHX and novel heat exchanger. DP/L of the PHX was 25.7 kPa/m, and that of the novel heat exchanger was 8.2 kPa/m. The water pressure drop of the PHX was higher than that of the novel heat exchanger. To reduce the water pressure drop, the PHX needs more plates, but this will increase the heat transfer area, and refrigerant mass flux. Eventually, this will decrease the heat transfer performance.

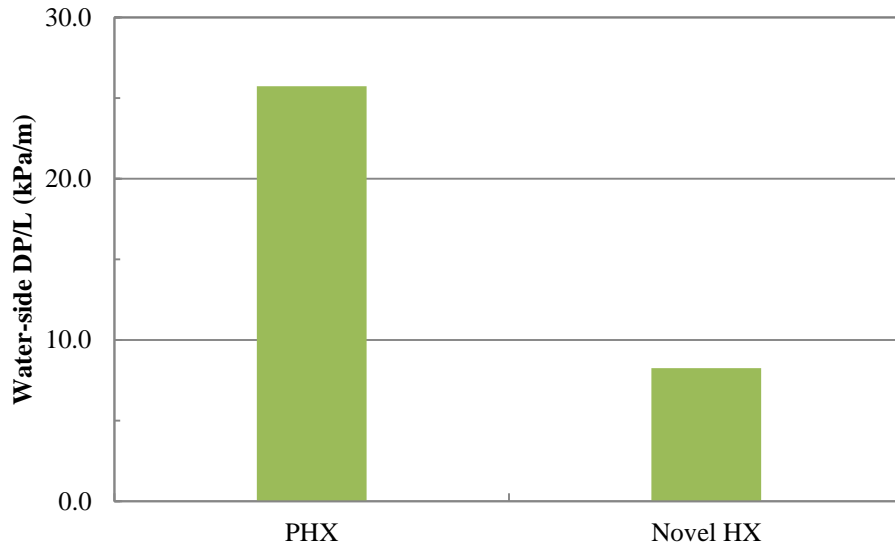


Fig. 4.46: Comparison of DP/L

Fig. 4.47 shows the heat transfer coefficient of the water-side and refrigerant-side in the PHX and novel LTLHX. For the PHX, the heat transfer was unbalanced due to low ammonia-side heat transfer. In contrast, for the novel LTLHX, even though water-side heat transfer coefficient decreased as compared to the PHX, ammonia-side heat transfer coefficient increased significantly. Therefore, the overall heat transfer performance of the novel LTLHX was greater than that of the PHX.

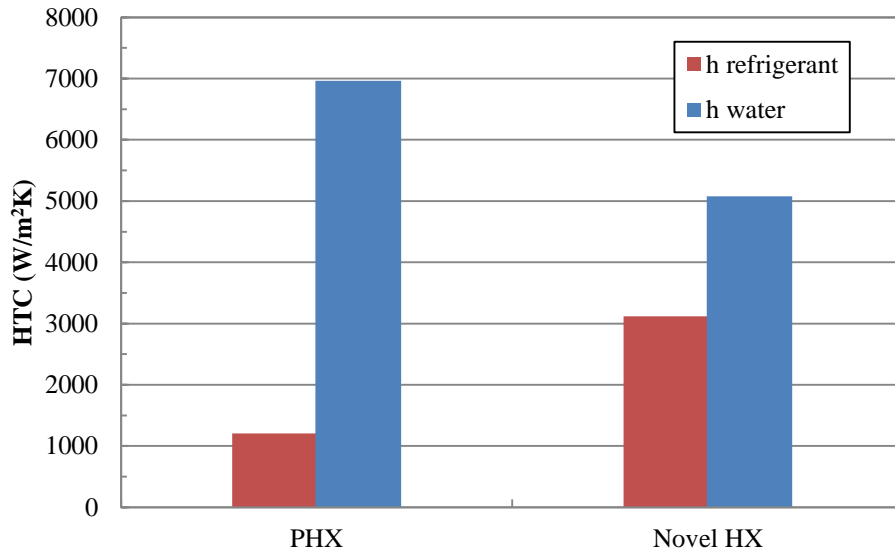


Fig. 4.47: Comparison of heat transfer coefficient

4.8 Flow boiling heat transfer and pressure drop of novel LTLHX

In this thesis, the refrigerant-side heat transfer coefficient in the novel LTLHX includes a subcooled liquid heat transfer coefficient, two-phase boiling heat transfer coefficient, and superheated vapor heat transfer coefficient. However, in this chapter, only two-phase boiling heat transfer coefficient in the novel LTLHX was calculated experimentally and its correlation was formulated. Moreover, the pressure drop correlation was developed as well.

Fig. 4.48 shows the variation of the boiling heat transfer coefficient with the liquid refrigerant Reynolds number. There was a large deviation between experimental results and correlation results. The average absolute deviation was between 32 and 44%. It is because the correlations were formulated for the round tube, while the channel in the novel LTLHX was a flat oval shape. In addition, the heat flux of the novel LTLHX was smaller than that of the round tube type, because there was an inactive heat transfer area

(a bonding space) in the heat exchanger. Therefore, a new correlation was developed for the novel LTLHX.

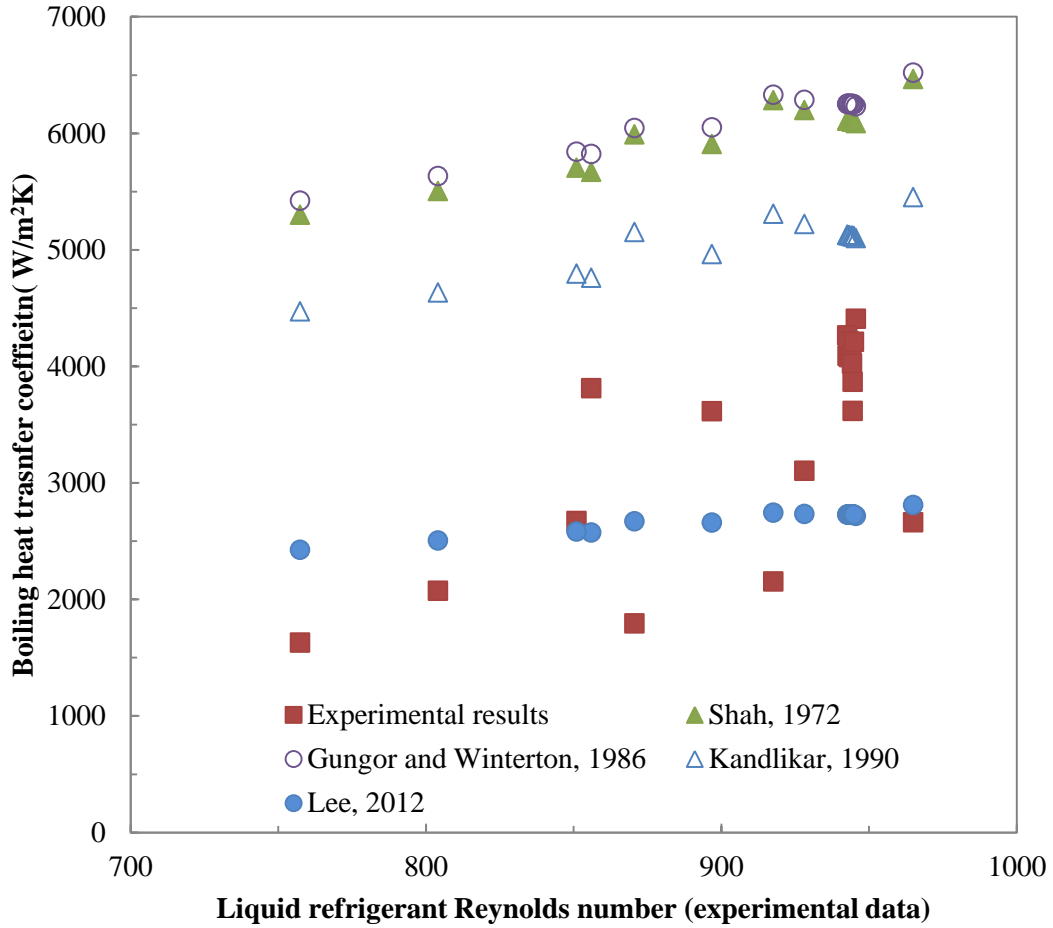


Fig. 4.48: Variation of boiling heat transfer coefficient with liquid refrigerant Reynolds number

The two-phase boiling heat transfer coefficient (h_{tp}) in the novel LTLHX was correlated with convection number (Co), liquid Reynolds number (Re_{lo}), and Weber number (We_l) as shown in Eq. (4.5).

$$h_{tp} = \frac{c_1 Re_{lo}^{c_2} Bo^{c_3} Co^{c_4} (Pr)^{c_5} \lambda_l}{We_l^{c_6} d_h} \quad (4.5)$$

For R22, $c_1=19.854$, $c_2=2.57$, $c_3=1.349$, $c_4=1.194$, $c_5=1.25$, and $c_6=0.446$

For ammonia, $c_1=47.476$, $c_2=2.133$, $c_3=0.842$, $c_4=1.727$, $c_5=0.3$, and $c_6=0.186$

Fig. 4.49 shows the h_{tp} comparison between ones calculated by the correlation and experimental data. The h_{tp} calculated by the correlation agreed with experimental data within $\pm 25\%$ deviation. Its averaged absolute deviation was 9.9% for ammonia, and 16.4% for R22.

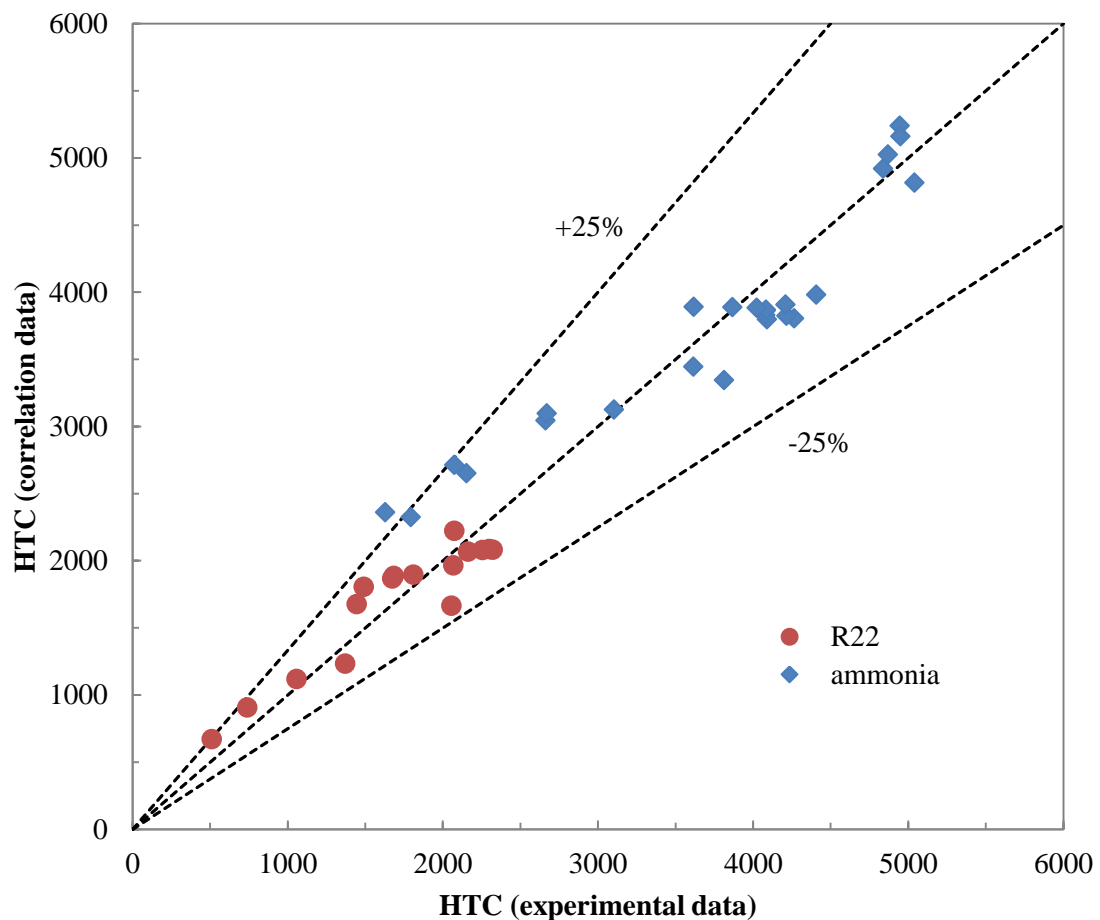


Fig. 4.49: HTC comparison between correlation results and experimental data with ammonia and R22

Fig. 4.50 shows the variation of pressure drop with liquid refrigerant Reynolds number, and correlations and experimental results. The experimental results agreed well

with Friedel correlation (1980) with 16.5% of the averaged absolute deviation. The deviation between correlations and experimental data

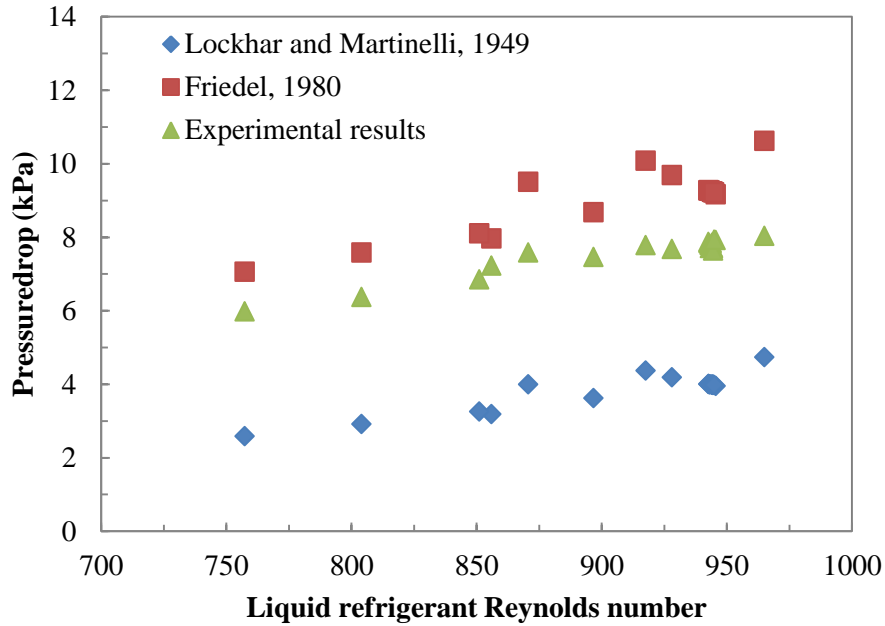


Fig. 4.50: Variation of pressure drop with liquid refrigerant Reynolds number

The two-phase boiling pressure drop correlation was formulated with a homogenous model instead of a liquid-vapor separated model because of limited operating conditions. The pressure drop correlation includes a two-phase Reynolds number (Re_{tp}), two-phase density (ρ_{tp}).

$$DP/L = \frac{c1 Re_{tp}^{c2} G^2}{d_e \rho_{tp}} \quad (4.6)$$

For R22, $c1=0.00411$ and $c2=0.48$

For ammonia, $c1=0.52$ and $c2=1.0126$

Fig. 4.51 shows the DP/L comparison between ones calculated by the correlation and experimental data. The correlation results predicted the f factor within $\pm 5\%$ deviation.

The averaged absolute deviation between experimental and correlation results were 1.8% for ammonia, and 3.1% for R22. It should be noted that heat transfer coefficient correlations and pressure drop correlations were obtained with the novel LTLHX geometries under given conditions.

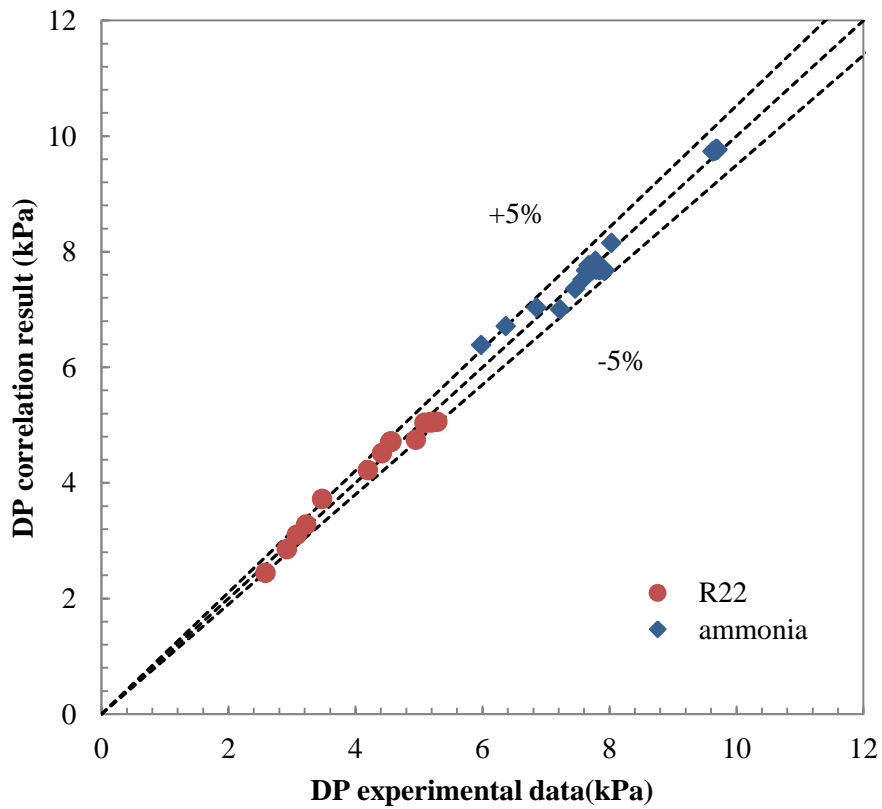


Fig. 4.51: DP comparison between correlation results and experimental data

4.9 Conclusions of the chapter 4

A novel LTLHX has been developed based on the lessons from the PHX investigation for the application to the LTLHP. Geometries are newly defined such as a channel width, channel height, channel pitch, and plate flow gap. Two design strategies were applied to the novel heat exchanger, which are regulating the flow area ratio between water-side and refrigerant-side and offsetting the plates to generate the wavy flow. These design parameters were optimized with multi-scale approaches. First, the maximum entropy design method was utilized to build a meta-model for obtaining the heat transfer coefficient of the heat transfer fluid side, as well as the pumping power per unit length (P/L) from the parameterized CFD runs. After obtaining intermediate optimum solutions as calculated by the multi-objective genetic algorithm, the online approximation-assisted optimization approach was applied to filter the optimum solutions and select the next set of samples as a means to improve the meta-models' response in the expected optimum region. Finally, the Pareto optimal designs produced by the multi-objective genetic algorithm were validated by comparing them to the values that were directly obtained from numerical simulations.

Optimized novel LTLHX was investigated experimentally and numerically with various parameters and operating conditions. The heat transfer coefficient correlation and friction factor correlation of the water-side were formulated for the novel LTLHX experimentally. And Two-phase boiling heat transfer coefficient correlation, and friction factor correlation was newly developed for the novel LTLHX. The U value of the novel LTLHX with ammonia ranged 1,300 to 2,000 $W \cdot K^{-1} \cdot m^{-1}$ when DP/L of the water-side was between 4 and 10 kPa/m. The refrigerant heat transfer coefficient ranged from 2,900

to $5,000 \text{ W}\cdot\text{K}^{-1}\cdot\text{m}^{-1}$, and water-side heat transfer coefficient ranged from 3,900 to 5,100 $\text{W}\cdot\text{K}^{-1}\cdot\text{m}^{-1}$. The U value was significantly improved with lower DP/L as compared to the PHX. It was due to the balanced hydraulic and thermal performance of the heat exchanger.

The major conclusions of the novel LTLHX performance test for the LTLHP application were summarized as follows:

- The novel LTLHX has been developed with new geometries based on the lessons learned from the PHX investigation
- Two design strategies were applied to the novel heat exchanger development: the flow area ratio was regulated, and plates were offset.
- Geometries of the novel LTLHX was optimized with online approximation assisted optimization. A maximum entropy design method was applied to build the meta-models, and its models were verified. These meta-models were used to optimize the novel LTLHX geometries. Finally, the Pareto optimal designs were verified against the values that were directly obtained from numerical simulations.
- Hydraulic and thermal performance of novel LTLHX was investigated with various parameters and operating conditions.
- Heat transfer coefficient correlations and pressure drop correlations were developed for the water-side and refrigerant-side experimentally.
- The U value of the novel LTLHX was calculated to 1,300 to 2,000 $\text{W}\cdot\text{K}^{-1}\cdot\text{m}^{-1}$, when DP/L of the water-side was between 4 and 10 kPa/m. The refrigerant heat transfer coefficient ranged from 2,900 to 5,000 $\text{W}\cdot\text{K}^{-1}\cdot\text{m}^{-1}$, and water-side heat transfer coefficient ranged from 3,900 to 5,100 $\text{W}\cdot\text{K}^{-1}\cdot\text{m}^{-1}$.

CHAPTER 5. Water Source Pump System

5.1 Introduction

In this chapter, as one of low temperature lift heat pump (LTLHP) systems, the water source heat pump (WSHP) system was selected and investigated. The heat pump system model was created and numerically investigated. First of all, the WSHP was compared with air-source heat pump (ASHP) to see the effect of the LTLHP compared to the typical high temperature lift heat pump system. Then, the parametric study of the WSHP was conducted, and the low temperature lift heat exchangers were applied and investigated.

5.2 Cycle simulation of WSHP

5.2.1 Modeling approach

A vapor compression cycles was modeled for the WSHP and ASHP. Fig. 5.1 shows the schematic diagram of the ASHP. This cycle mainly consists of a compressor, condenser, expansion device and evaporator. The cycle is operated as a heating mode, so that the condenser is used for the indoor unit, and the evaporator is used for the outdoor unit. Fig. 5.2 shows the schematic diagram of the WSHP. This cycle mainly consists of a compressor, condenser, expansion device, evaporator, and water pump.

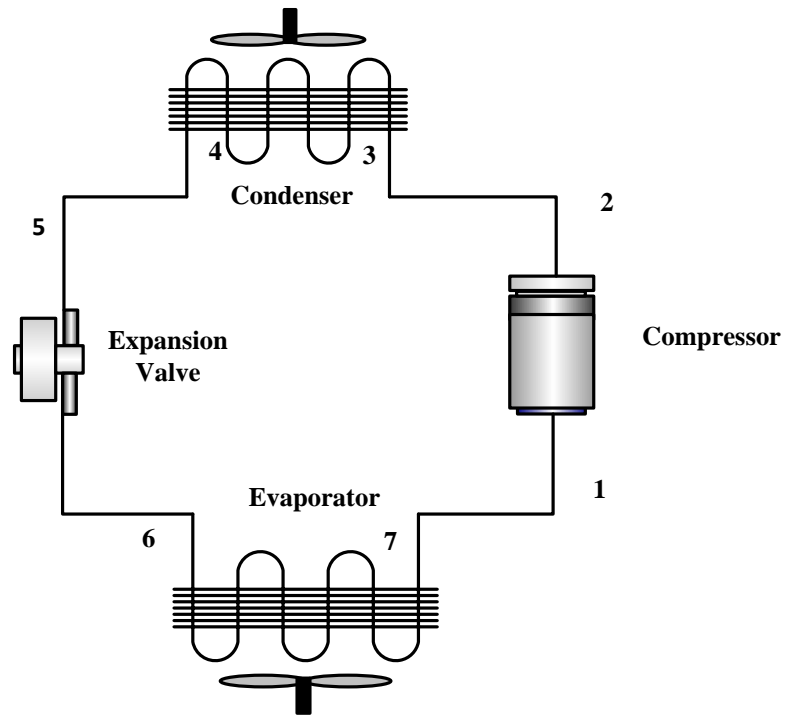


Fig. 5.1: Schematic diagram of ASHP

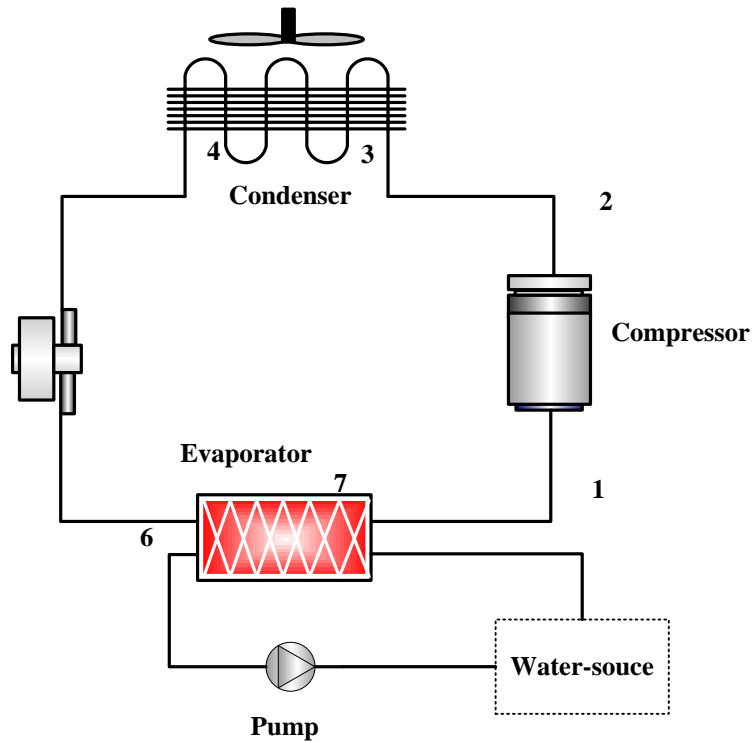


Fig. 5.2: Schematic diagram of WSHP

Summary of design conditions is shown in Table 5.1. The heating space was set to 27 °C of temperature, and 50 % of relative humidity. The heat from the evaporator for the ASHP was transferred by air, and that for the WSHP was done by water.

Table 5.1: Summary of design condition

Item	Property	Unit	Value
Space	Temperature	°C	21
	Relative humidity	%	50
	Rotational speed	RPM	3,500
Compressor	Isentropic efficiency	-	0.9-0.0467*PR
	Volumetric efficiency	-	1.00-0.04*PR
	Motor efficiency	%	95
Fan condenser	Airflow rate	m ³ /s/kW	0.054
	Power input	W/m ³ /s	775
Fan evaporator	Airflow rate	m ³ /s/kW	0.064
	Power input	W/m ³ /s	180
Water pump	Pump efficiency	-	0.5

The degree of subcooling was maintained at 5 K. For the WSHP, the temperature difference between the water outlet and evaporation temperature was set to 1.5 K. The pressure drops of the water pipe and the evaporator were designed to be 40 and 10 kPa, respectively. For the ASHP, the temperature difference of two fluids in the evaporator was fixed to 5 K.

Ambient air and ground-water temperature in Baltimore, MD was used for the cycle modeling, which was provided from National Oceanographic Data Center (NODC). Temperature data applied to the modeling was from 1/1/2010 to 2/28/2010 as shown in Fig. 5.3.

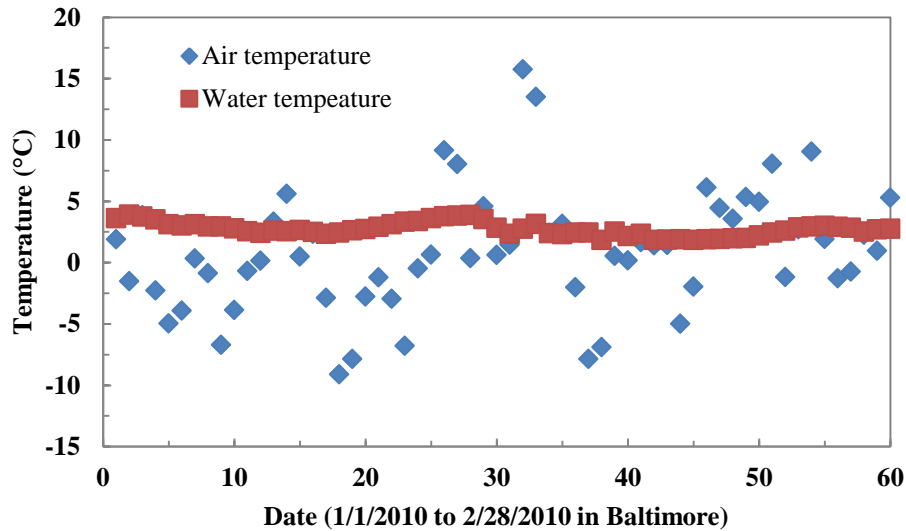


Fig. 5.3: Temperature of air and ground-water from 1/1/2010 to 2/28/2010

5.2.2 Modeling results

Fig. 5.4 shows the comparison of the evaporator capacity between the ASHP and WSHP. The condenser capacity was maintained at 4 MW. The evaporator capacity of the WSHP was larger than that of the ASHP. The WSHP had a higher evaporation temperature than the ASHP. As the evaporation temperature increased, the latent heat region increased. Therefore, the capacity of the WSHP was larger than that of ASHP

Fig. 5.5 shows the comparison of the power between the ASHP and WSHP. The power consumption of the ASHP was larger than that of the WSHP. Lower evaporation temperature of the ASHP as compared to the WSHP increased pressure ratio, which is related to the power consumption.

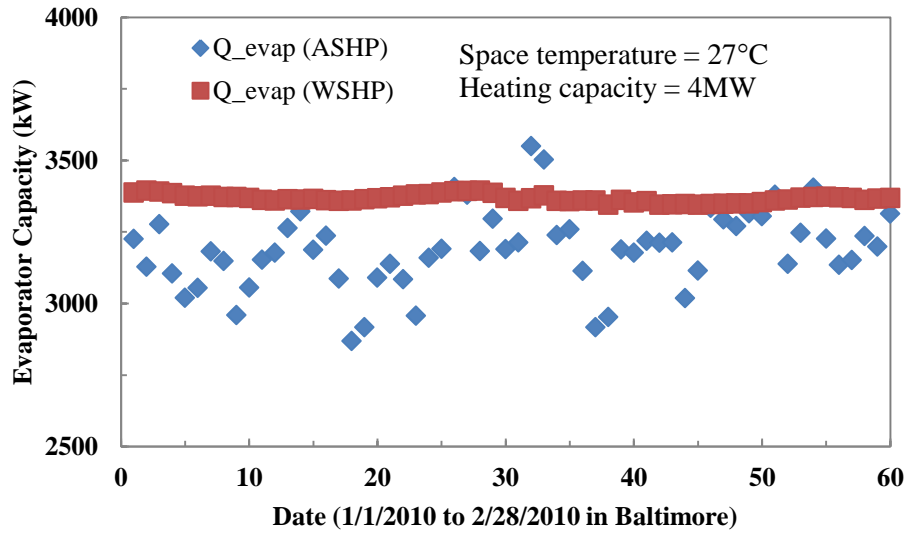


Fig. 5.4 Comparison of evaporator capacity between ASHP and WSHP

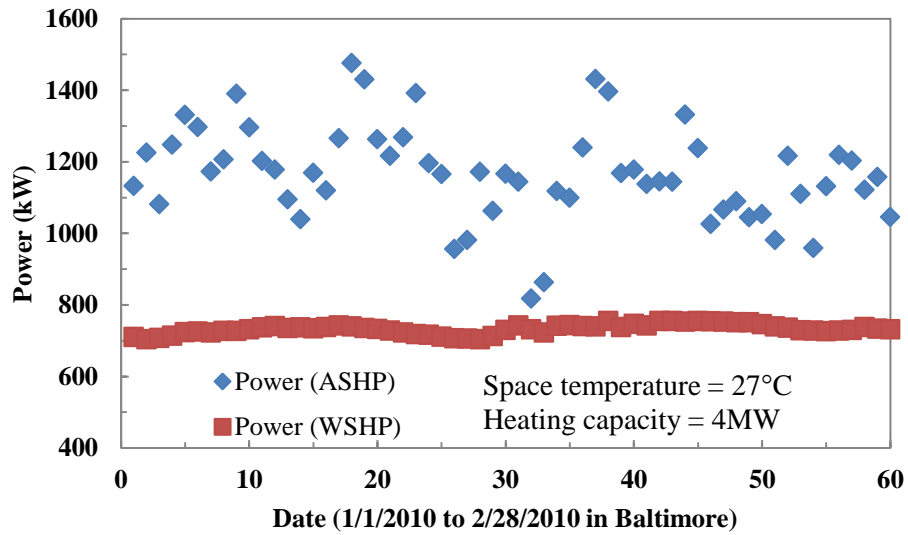


Fig. 5.5: Comparison of power between ASHP and WSHP

Fig. 5.6 shows the COP comparison between the ASHP and WSHP. A smaller power consumption of the WSHP caused COP to be larger, as compared to ASHP. COP of the WSHP was larger than that of ASHP by 57%.

Fig. 5.7 shows the comparison of UA value between the ASHP and WSHP. UA of the WSHP was about 1,093 kW/K, in contrast, that of ASHP ranged from 400 to 490 kW/K. UA was calculated with the evaporator capacity and *LMTD*. A higher *LMTD* of the ASHP resulted in a lower UA value compared to the WSHP. In terms of heat transfer area, since UA of the WSHP evaporator was larger than that of ASHP, the WSHP evaporator needed a smaller heat transfer area.

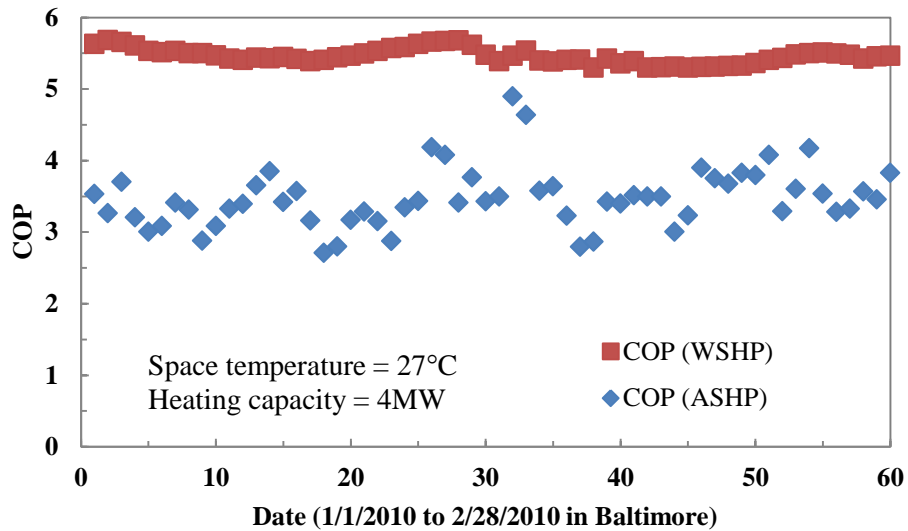


Fig. 5.6: Comparison of COP between ASHP and WSHP

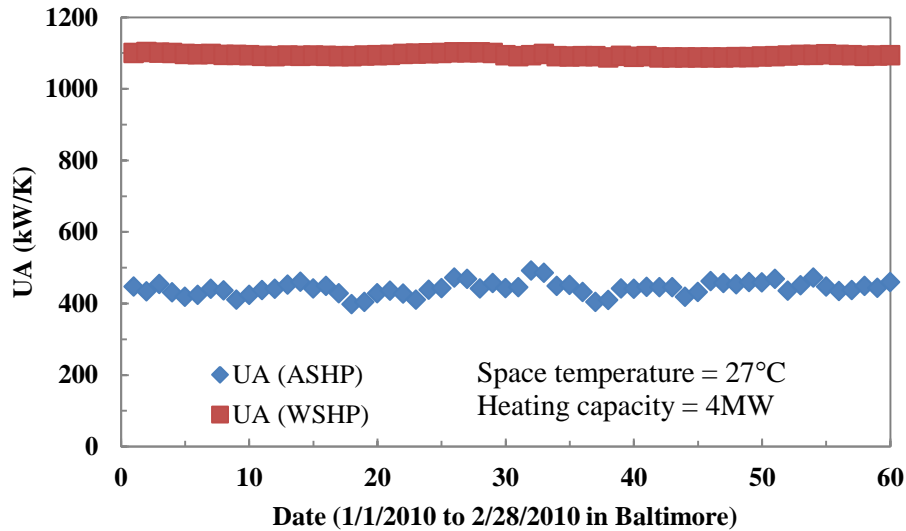


Fig. 5.7: Comparison of UA value between ASHP and WSHP

In this chapter, the performance of the WSHP was compared with that of the ASHP. The temperature data of water and ambient air in Baltimore, MD was selected from 1/1/2010 to 2/28/2010. WSHP performance was better than ASHP. First, for the WSHP, the heat source fluid temperature was higher. This resulted in a higher evaporation temperature. Second, the small temperature difference between heat source fluid and refrigerant increased the evaporation temperature. The increased evaporation temperature due to higher heat source fluid and small delta T reduced the pressure ratio, so that power consumption of the heat pump system decreased.

5.2.3 Parametric study with temperature difference

In this chapter, the effect of the water-side temperature difference between the water inlet and outlet on the WSHP performance was investigated. The system is modeled to be operated as a heating mode, and the heating capacity of the system is designed to be 4 MW. Heat source, water inlet temperature was fixed to 10 °C, and water outlet temperature was varied from 9 to 1 °C. System COP defined to include the pump

work, fan power and compressor power. And heat pump COP defined only to be considered the compressor power consumption. Fig. 5.8 shows the variation of COP with delta T between water inlet and outlet. As Delta T was increased, COP of the heat pump and system decreased. Reduced COP with delta T can be explained with the decreased power consumption since heating capacity was kept at constant.

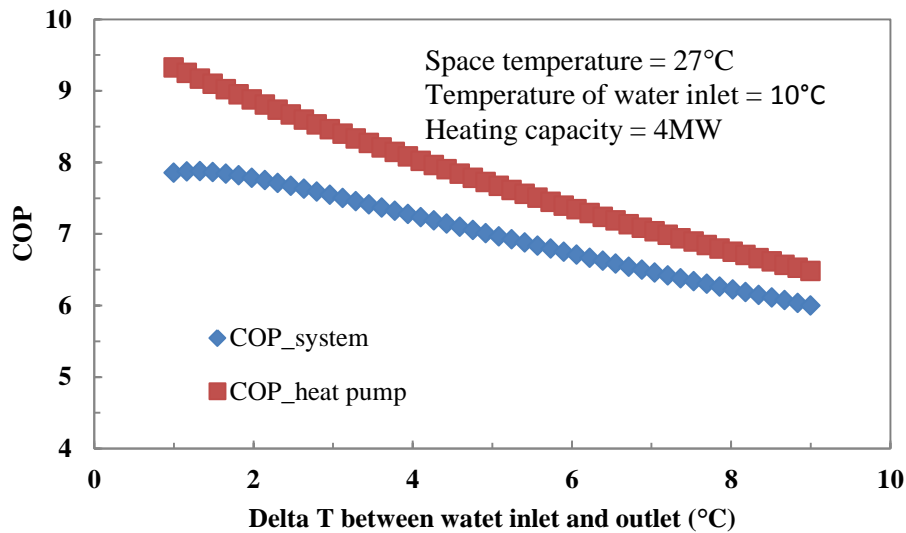


Fig. 5.8: Variation of COP with delta T between water inlet and outlet

Fig. 5.9 shows the variation of power consumption with delta T. As delta T was increased, the power consumption of the compressor increased, and that of the water pump reduced. Even though the power consumption of the water pump decreased with delta T, since an increase of the compressor work was larger than a decrease in the pump work, total power consumption increased.

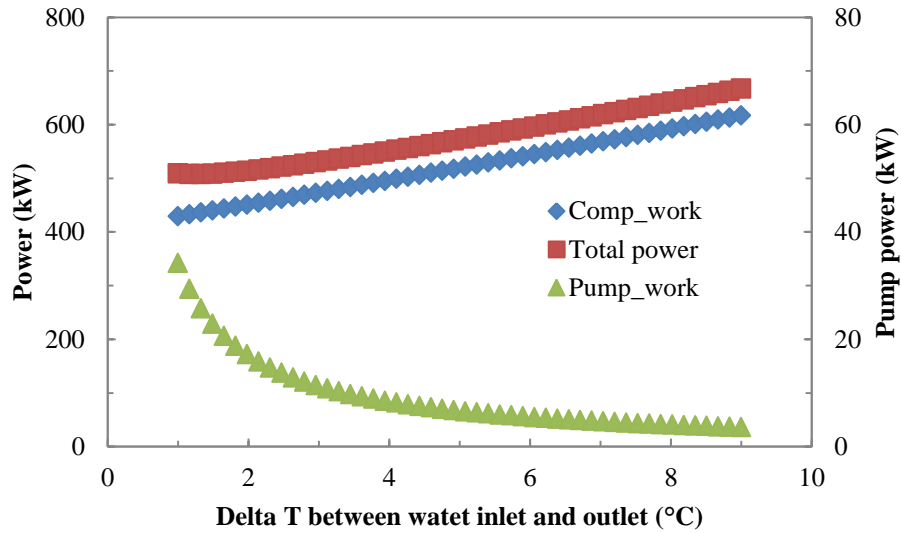


Fig. 5.9: Variation of power consumption with delta T between water inlet and outlet

Fig. 5.10 shows the variation of the evaporator capacity and *LMTD* with delta T. As delta T was increased, the capacity decreased and *LMTD* increased. The evaporation temperature decreased with delta T. This resulted in a decrease of the evaporator capacity. The temperature difference between water outlet and refrigerant-side was maintained at constant, so that the *LMTD* increased as delta T was increased.

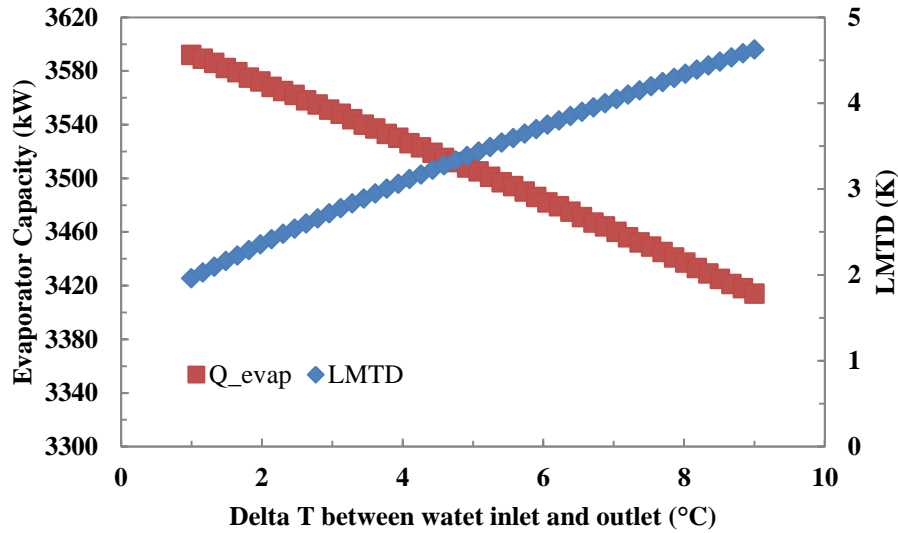


Fig. 5.10: Variation of capacity and LMTD with delta T between water inlet and outlet

UA value decreased as delta T was increased as shown in Fig. 5.11. As delta T was increased from 1 to 9 °C, UA decreased from 1,835 to 738 kW/K. The reason for the decrease in UA value was on the increased *LMTD* and decreased capacity.

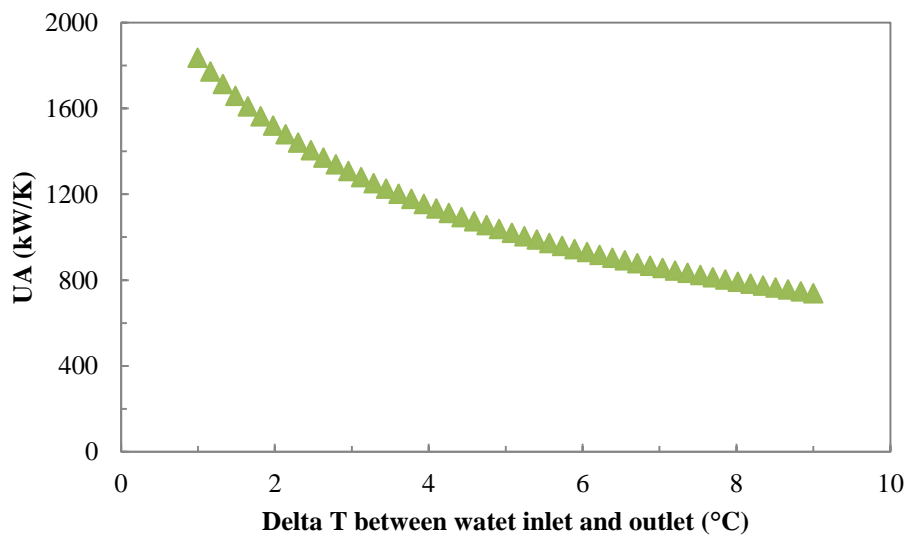


Fig. 5.11: Variation of UA value with delta T between water inlet and outlet

Fig. 5.12 shows the variation of MFR of the water-side and MFR of the refrigerant-side with delta T. As delta T was increased, both MFR of the water-side and

MFR of the refrigerant-side reduced. However, the decrease of water flow rate was larger than that of refrigerant flow rate. The ratio between water and refrigerant MFRs was changed from 40.4 to 4.6, as delta was increased. This is the critical to design the heat exchanger.

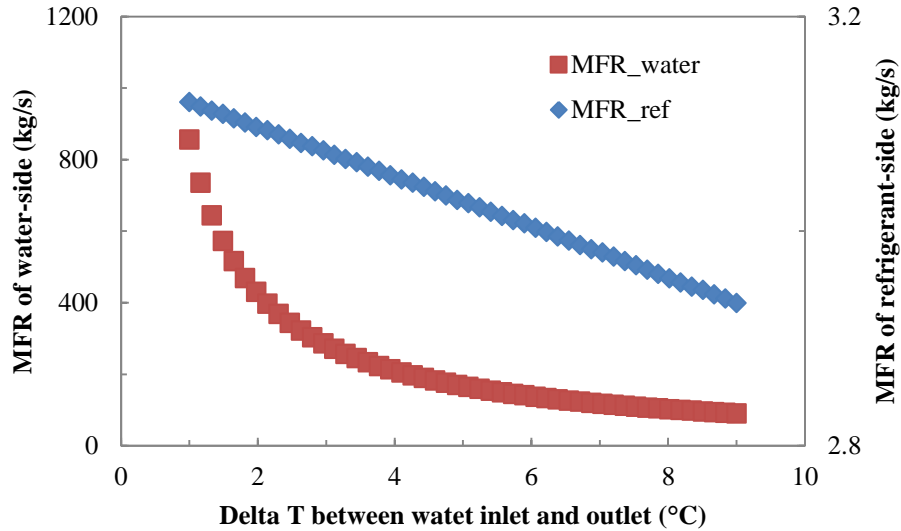


Fig. 5.12: Variation of MFR with delta T between water inlet and outlet

The performance of the WSHP was investigated as the delta T between water inlet and outlet of the evaporator was varied. When delta T was decreased, since the decrease of compressor work was larger than the increase of water pump work, COP of the system improved. UA of the evaporator increased as delta T was decreased. However, the MFR ratio between the water and refrigerant-side increased, which is critical to the heat exchanger design.

5.3 Cycle options for the WSHP

5.3.1 Modeling approach

In this chapter, 4 MW of heating capacity of the WSHP system is designed, and the heat exchanger performance was discussed. The design parameters are as follows:

- There are four buildings where need 1 MW of heating per each building
- The space temperature is 21 °C, and relative humidity is 50%
- Inlet and outlet temperature of water are 10 and 2 °C, respectively.
- Pressure drop of the water pipe is 250 Pa per kg/s

Two different WSHPs were suggested as shown in Fig. 5.13 and Fig. 5.14. The difference between WSHP 1 and WSHP 2 is the method how to provide the water to the evaporator. For WSHP 1, each heat pump system includes its own water pump system as shown in Fig. 5.13. For WSHP 2, the water is provided through one water loop.

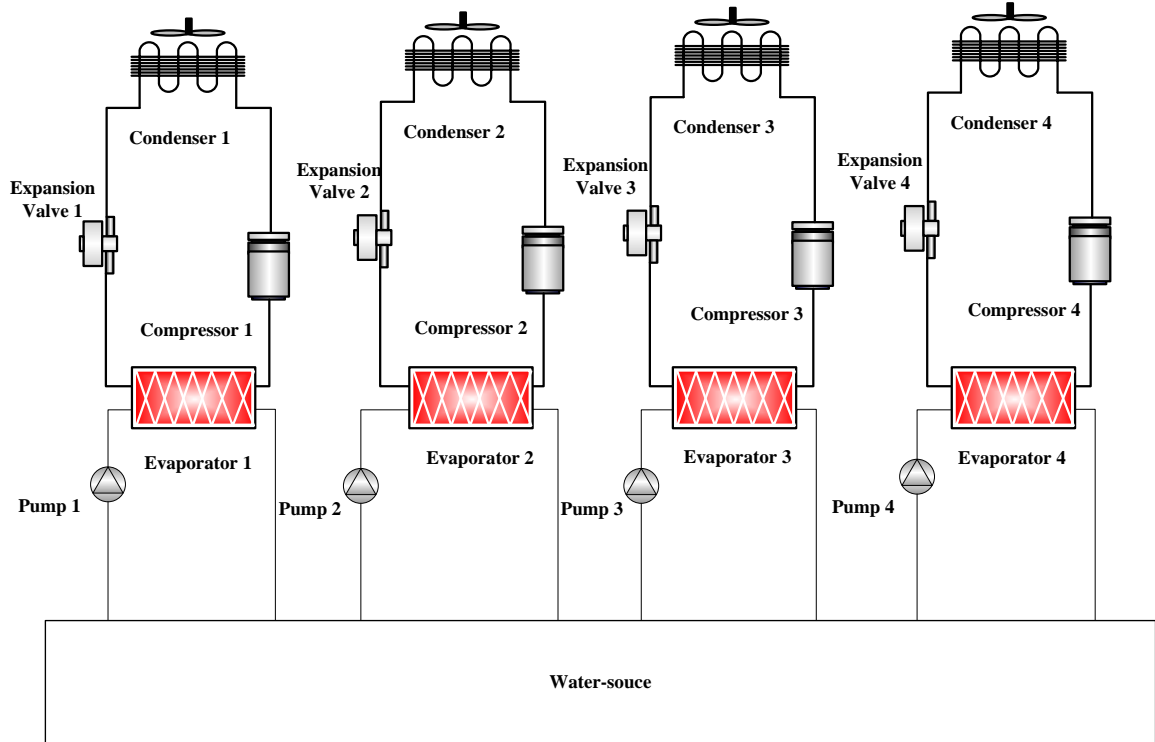


Fig. 5.13: Schematic diagram of WSHP1

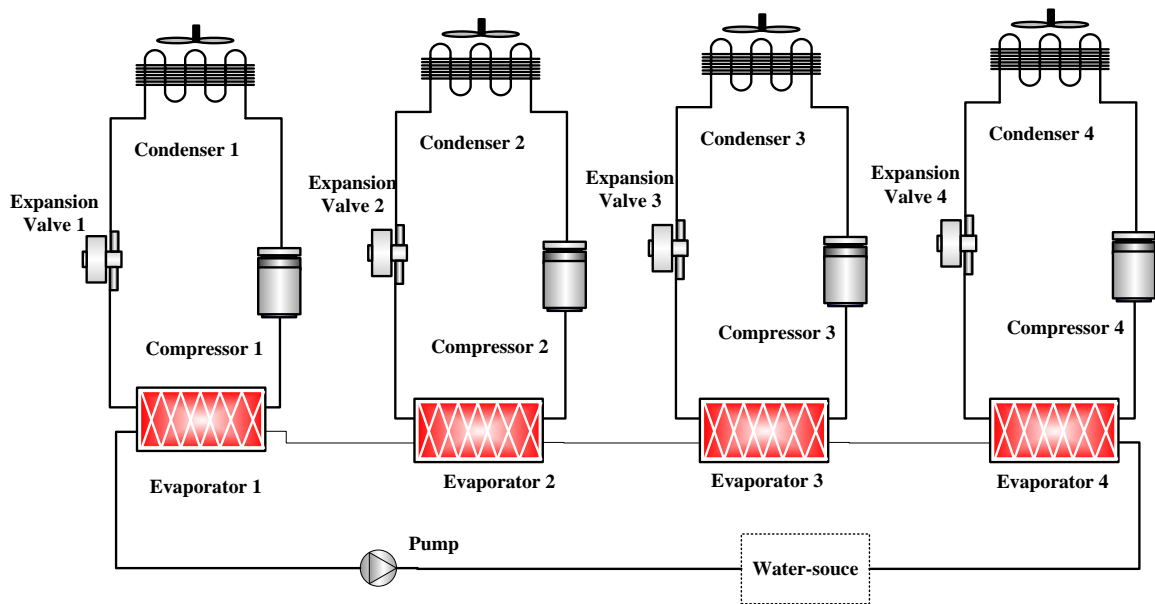


Fig. 5.14: Schematic diagram of WSHP2

5.3.2 Modeling results

When the heating capacity was designed to be 4 MW, WSHP1 and WSHP 2 were modeled. Fig. 5.15 shows the COP of WSHP1 and WSHP2. COP of WSHP 2 was higher than that of WSHP1 by 10.5%. For WSHP2, the temperature difference between the water inlet and outlet was much smaller than the WSHP1, and this increased the evaporation temperature. Since the condensing temperature was fixed, the power consumption of the compressor reduced. Hence, the performance of the WSHP2 was higher.

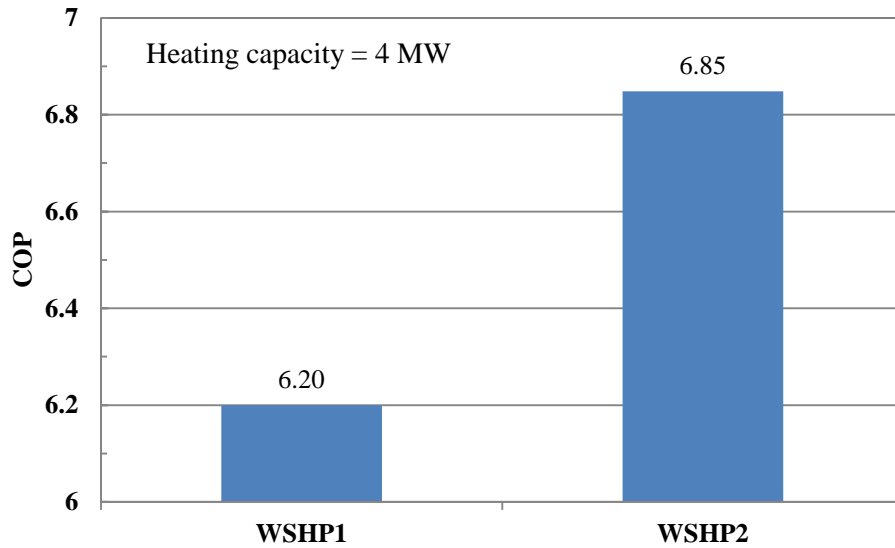


Fig. 5.15: COP of WSHP1 and WSHP2

Fig. 5.16 shows the averaged UA values of the evaporators of WSHP1 and WSHP2. For the WSHP2, the temperature difference between the water inlet and outlet of each evaporator was 2 °C. In addition, the averaged *LMTD* of the evaporator was 2.36K. In contrast, for the WSHP1, the temperature difference, and the averaged *LMTD* were 8 °C and 4.33K, respectively. The averaged *LMTD* of the WSHP2 was smaller than

that of the WSHP1 by 84%. This resulted that the averaged UA of the WSHP2 was larger than that of WSHP1 by 87%. If U values of the systems are designed to be same, the heat exchanger size of WSHP2 can be smaller than WSHP1.

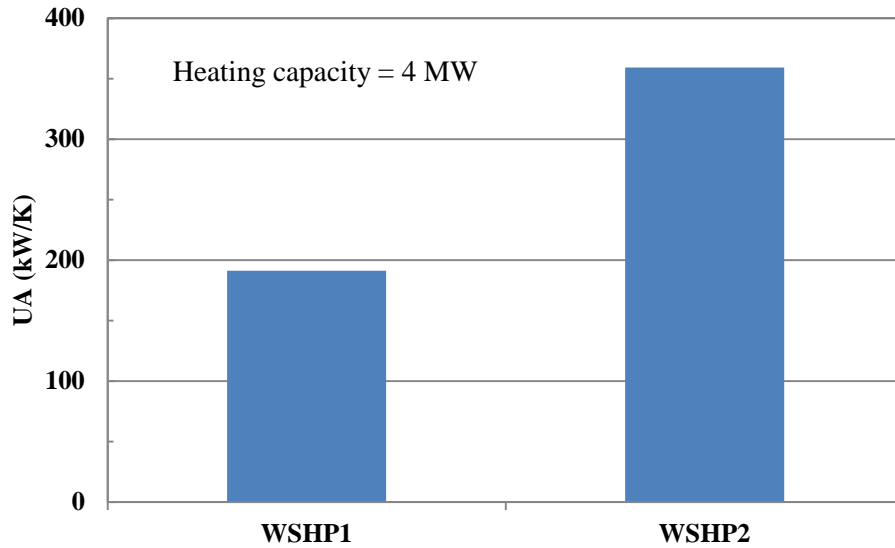


Fig. 5.16: UA of WSHP1 and WSHP2

Fig. 5.17 shows the mass flow rate of water and refrigerant of the evaporator. For WSHP1, the water MFR was 25.6 kg/s and refrigerant MFR was 0.73 kg/s. The ratio of water MFR to refrigerant MFR was 34.6. For WSHP2, the water and refrigerant MFRs were 104 kg/s and 0.76 kg/s, respectively. The ratio was 136.9. Since the evaporator capacities of the both systems were almost same, there was no difference of the refrigerant MFR. The ratio of water to refrigerant flow rate would be a critical factor to design a heat exchanger.

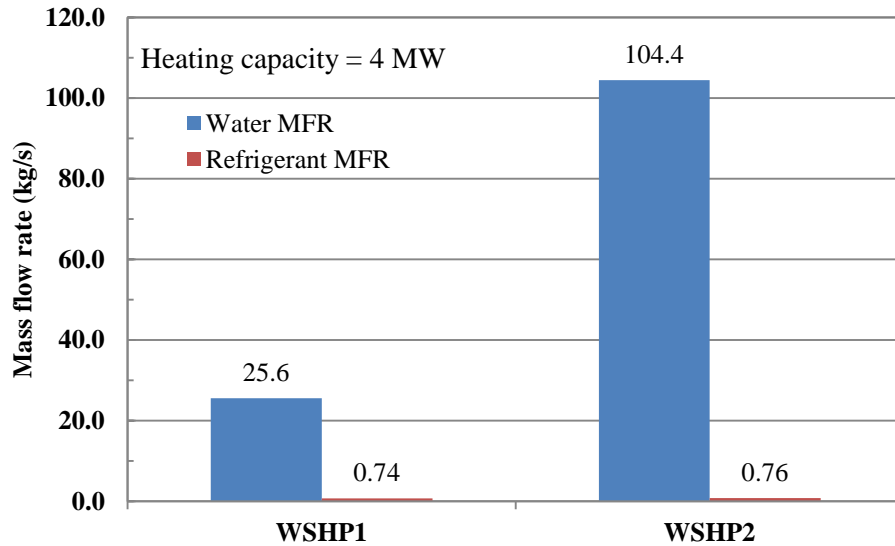


Fig. 5.17: Mass flow rates of water and refrigerant (ammonia)

5.4 Heat exchanger design

It was determined that the performance of the WSHP2 was higher than that of WSHP1, due to the decreased power consumption. The low temperature lift heat exchangers were applied to the WSHP2, and the performance of the heat exchangers were investigated and compared. The operating conditions are designed as follows:

- Evaporator capacity: 854 kW,
- UA: 362 kW/K
- Water inlet temperature: 8 °C
- Water outlet temperature: 6 °C
- Refrigerant inlet temperature: 4.5 °C
- Refrigerant outlet temperature: 7 °C
- Evaporation pressure: 575.2 kPa
- Water MFR: 101 kg/s
- Refrigerant MFR: 5.03 kg/s

- DP of the water-side: 10 kPa

Fig. 5.18 shows the flow chart of the heat exchanger design for the WSHP. First of all, design parameters of the heat exchangers are decided, such as flow channel gap, angle, and pitch. These design parameters will not be changed through the heat exchanger design. Then the second stage is to define initial design variables. At third stage, if the calculated DP/L of the water-side is smaller than the target DP/L , it goes to the next stage. If not, it goes back to the second stage. The heat transfer coefficients of the heat exchanger are calculated at the fourth stage. At fifth stage, if the calculated capacity is in the range of the target value, then the model ends. Otherwise, it goes back to the second stage.

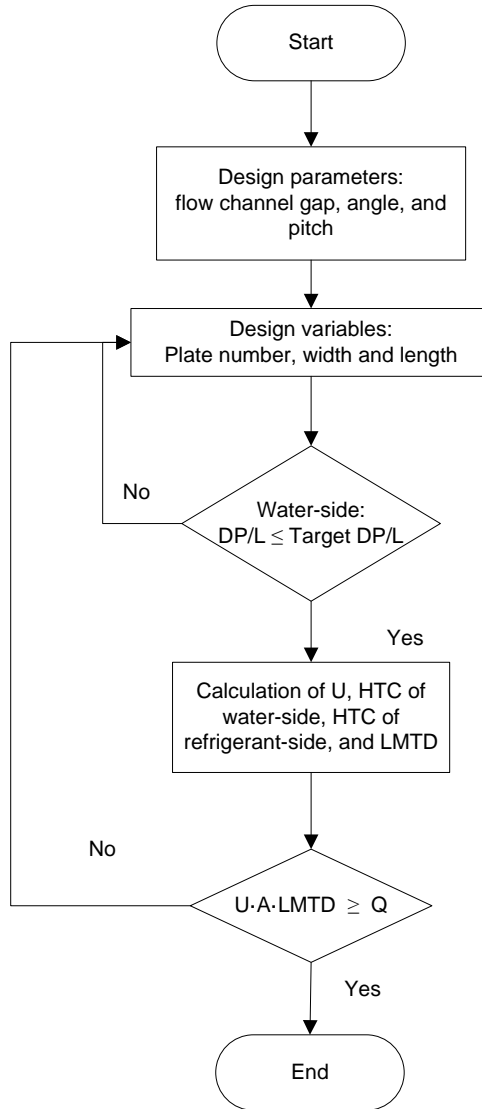


Fig. 5.18: Flow chart of the heat exchanger design for LTLHP application

5.4.1 PHX design

First of all, the PHX is applied to this application. Nusselt number and DP/L of the water-side shown in Eqs. (5.1) and (5.2) are obtained from the experimental tests in Chapter 3.2.

$$Nu = 0.2083 \cdot Re_e^{0.7} \cdot Pr^{1/3} \cdot \left(\frac{\mu_{f1}}{\mu_s} \right)^{0.14} \quad (6.1)$$

for $600 < Re < 2700$, $6.4 < Pr < 6.8$

$$f = \frac{6.592 \times 10^{-5} \cdot \text{Re}^{1.734} \cdot \rho \cdot d_e}{2G^2} \quad (6.2)$$

For the heat transfer coefficient of the refrigerant-side, Coopers' correlation was chosen as discussed in the Chapter 3. The simulation results of the PHX design are shown in Table 5.2 and

Table 5.3 for R22 and ammonia, respectively. The U value of the ammonia case was larger than that of R22 case by 209%. This resulted in about 60% decrease of total heat transfer area.

Table 5.2: Simulation results of the PHX design with R22

Property	Unit	Value
Plate number	EA	864
Plate width	m	0.5
Plate height	m	1
Total heat transfer area	m ²	864
Heat flux	W·m ⁻²	988
Water HTC	W·m ⁻² ·K ⁻¹	3,565
Refrigerant HTC	W·m ⁻² ·K ⁻¹	480
U value	W·m ⁻² ·K ⁻¹	419
Ratio of HTC	-	7.4

Table 5.3: Simulation results of the PHX design with ammonia

Property	Unit	Value
Plate number	EA	352
Plate width	m	0.5
Plate height	m	1
Total heat transfer area	m ²	352
Heat flux	W·m ⁻²	2,426
Water HTC	W·m ⁻² ·K ⁻¹	6,683
Refrigerant HTC	W·m ⁻² ·K ⁻¹	1,482
U value	W·m ⁻² ·K ⁻¹	1,180
Ratio of HTC	-	4.5

5.4.2 Novel LTLHX design

Nusselt number and friction factor of the water-side are shown in Eqs. (6.3) and (6.4), which are obtained from Chapter 4.4.

$$Nu = 0.034944 \cdot Re^{0.75} \cdot Pr^{1/3} \cdot \left(\frac{\mu}{\mu_s} \right)^{0.14} \quad (6.3)$$

For $6000 < Re < 22,000$

$$f = \frac{8.1739 \times 10^{-8} \cdot Re^{1.764} \rho \cdot d}{2G^2} \quad (6.4)$$

Table 5.4 shows the simulation results of the novel LTLHX design with ammonia. The heat transfer area was calculated to be 159 m² for the designed heat transfer. This is 45% of the heat transfer area for the PHX with ammonia. The U value of the novel heat exchanger was larger than that of the PHX by 93%. This was due to the balanced heat transfer coefficient of both fluids. Therefore, the system performance can be improved and the system cost can be reduced with novel LTLHX.

Table 5.4: Simulation results of the novel LTLHX design with ammonia

Property	Unit	Value
Plate number	EA	148
Plate width	m	0.35
Plate height	m	1.536
Total heat transfer area	m ²	159.1
Heat flux	W·m ⁻²	5,367
Water HTC	W·m ⁻² ·K ⁻¹	3,201
Refrigerant HTC	W·m ⁻² ·K ⁻¹	2,523
U value	W·m ⁻² ·K ⁻¹	2,277
Ratio of HTC	-	1.27

5.4.3 Guideline of novel heat exchanger design for the LTLHP application

Fig. 5.19 shows the design guideline of the novel exchanger for the LTLHP application. First step is to design the LTLHP system. When a LTLHP system is planned, its operating conditions can be decided to obtain the best system performance, for example, the heat transfer capacity, UA value, and temperature and pressure of working fluids. The second step is to decide the target U value. Once the target U value is fixed, the heat transfer area required to have the heat transfer capacity will be decided as well. The third step is to decide the plate width and length. This step depends on the heat exchanger design limit. After that, the next step is to design the channel dimensions which were considered in section 4.2. The water-side heat transfer coefficient can be calculated with OAAO technique discussed in section 4.3. It should be noted that when the design are flexible, and it needs to be globally accurate in given boundary conditions, then it is recommended to use offline AAO technique. The refrigerant channels need to be arranged to have optimum refrigerant mass flux. After that, the refrigerant heat transfer coefficient can be calculated with correlations. Then, U value can be calculated with the obtained heat transfer coefficients of the water and refrigerant-side. If this U value is smaller than the target U value, then it goes to step 4. If not, it goes to end.

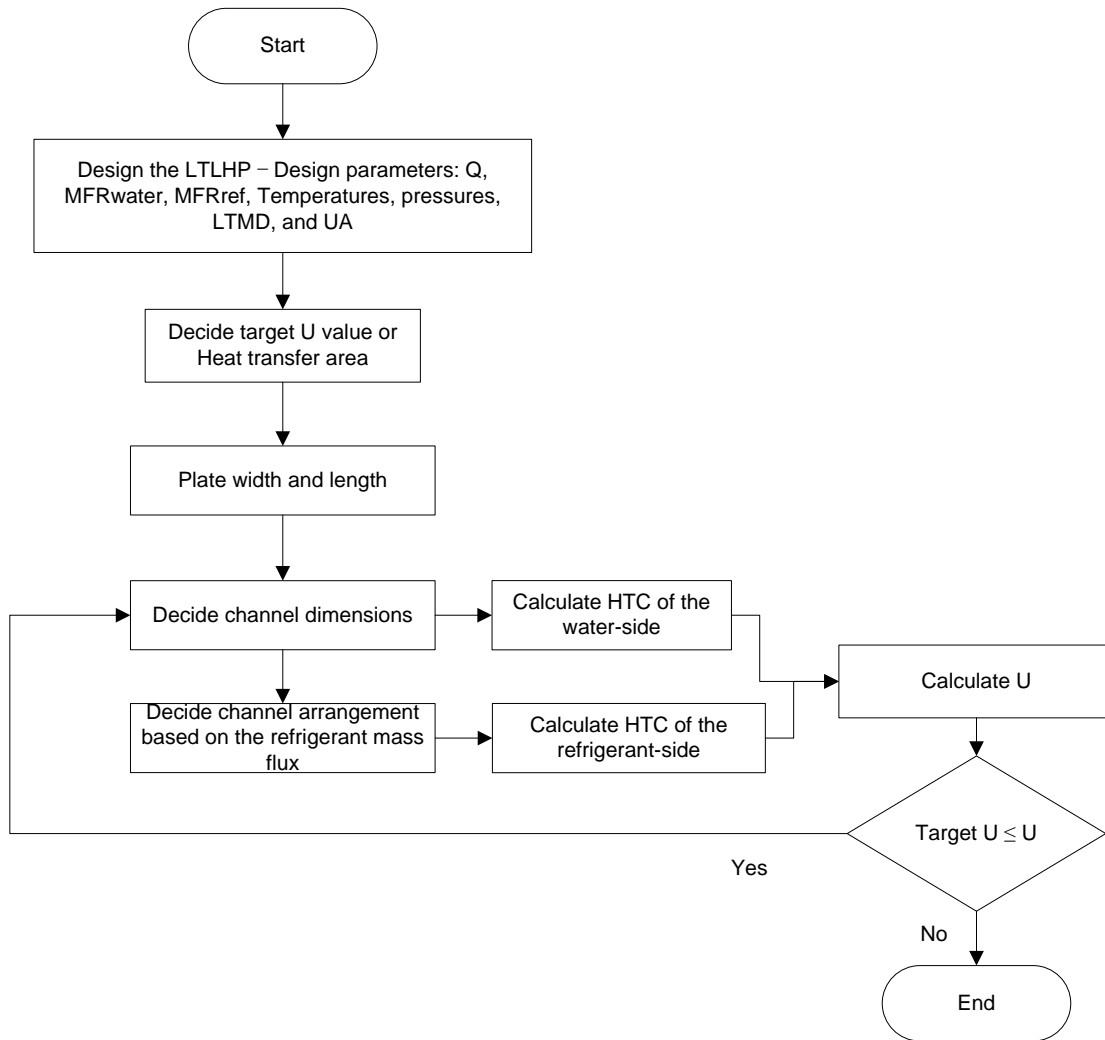


Fig. 5.19: Design guideline for novel heat exchanger for LTLHP application

5.5 Conclusions of the chapter 5

The low temperature lift heat pump (LTLHP) concept was applied to the water source heat pump (WSHP) system. Its model was created and numerically investigated. The performance of the WSHP was compared with that of the ASHP. The temperature data of water and ambient air in Baltimore, Maryland was selected from 1/1/2010 to 2/28/2010. The WSHP performance was better than the ASHP. First of all, for the WSHP, the heat source fluid temperature was higher. This resulted in a higher evaporation

temperature. Second, the small temperature difference between heat source fluid and refrigerant increased the evaporation temperature. The increased evaporation temperature due to higher heat source fluid and small delta T reduced the pressure ratio, so that power consumption of the heat pump system decreased.

Then, the parametric study of the WSHP was conducted by varying temperature difference (ΔT) between heat source inlet and outlet temperature. When ΔT was decreased, since the decrease of compressor work was larger than the increase of water pump work, COP of the system improved. UA of the evaporator increased as ΔT was decreased. However, the MFR ratio between the water and refrigerant-side increased, which is critical to the heat exchanger design.

The low temperature lift heat exchangers were applied and investigated. When the novel LTLHX was applied to the WSHP system, the heat transfer area of the novel LTLHX could be smaller than that of the PHX by 93%. This can significantly reduce the cost of the system.

The major conclusions of this chapter were summarized as follows:

- Water source heat pump (WSHP) model was created and numerically investigated.
- COP of the WSHP was greater than that of air source heat pump (ASHP) by 47% in Baltimore, Maryland from 1/1/2010 to 2/28/2010.
- When temperature difference between water inlet and outlet was decreased, COP of the system improved since the decrease of compressor work was larger than the increase of water pump work in WSHP modeling.
- When the PHX and novel LTLHX were applied to the WSHP application with ammonia as a working fluid, U value of the novel LTLHX was greater than that of

the PHX by 93%. This can increase the system performance and reduce the system cost.

- Design guideline of the novel heat exchanger for the LTLHP application was created. Channel geometries were decided with the automated process (PPCFD, and OAAO).

CHAPTER 6. Summary and Conclusions

The research about a low temperature lift heat pump (LTLHP) system becomes more important than ever, because there has been a huge demand for high efficient energy conversion systems due to dramatically growing energy demand and cost. Therefore, this dissertation focused on investigating and understanding the hydraulic and thermal design space and tradeoffs of low temperature lift high performing heat exchangers for the LTLHP system, which benefits from a small difference between the condensing and evaporating temperatures of a working fluid. The heat exchangers for the LTLHP application require a larger heat transfer area, a higher volume flow rate, and a higher temperature of heat source fluid, as compared to the typical high temperature lift heat pump system. Therefore, heat exchanger research is critical, and it needs to be balanced between the heat transfer and pressure drop performance of both fluids in the heat exchanger. Major insights and conclusions were summarized as follows:

- A plate heat exchanger (PHX) was selected to establish a baseline of a low temperature lift heat exchanger and was investigated experimentally.
 - The traditional PHX is designed to have the identical surface area and enhancements on both fluid sides for ease of production. However, fluid side heat transfer coefficients and heat capacities can be drastically different, for example, single-phase water versus two-phase refrigerant.
 - Moreover, the PHX needed to have a large cross sectional flow area in order to reduce the heat-source fluid-side pressure drop for the LTLHP application so that it caused a low mass flux of the refrigerant-side.

- The refrigerant-side heat transfer was mainly dominated by nucleate boiling heat transfer. In these operating conditions, the refrigerant-side heat transfer coefficient was affected by the water-side Reynolds number. The changed water temperature profile resulted in the redistribution of the heat flux and the change of the dry-out location in the heat exchanger geometries.
 - U value of the PHX ranged from 500 to 900 W m⁻² K⁻¹, when water-side pressure drop was between 2 to 31 kPa/m. U value was relatively small due to the low refrigerant-side mass flux.
 - The PHX performance with R22 was compared to that with ammonia. The *U* value of the ammonia case was higher than that of R22 case by 52% due to high thermal conductivity of ammonia.
 - The CFD simulation was carried out to further improve the potential of the PHX performance, and the design space was explored and investigated.
 - It was concluded that the PHX was restricted by two main factors: one was a large pressure drop on the heat source fluid-side due to corrugated shape, and the other was low overall heat transfer performance due to the unbalanced heat transfer performance between two fluids.
- A concept of the novel LTLHX has been developed based on the lessons learned from the PHX performance investigation for the application to the LTLHP.
 - Geometries of the novel LTLHX were newly defined such as a channel width, channel height, channel pitch, and plate flow gap.

- Two design strategies were applied to the novel heat exchanger development: the flow area ratio was regulated, and plates were offset, which can balance the heat transfer and pressure drop performance between two fluids.
- The design parameters of the novel heat exchanger were optimized with multi-scale approaches.
 - Online approximation-assisted optimization approach with PPCFD was applied to determine the optimum heat transfer and pressure drop performance of the novel LTLHX. This approach reduced huge computational cost.
 - A maximum entropy design method was applied to build the meta-models, and its models were validated. These meta-models were used to optimize the novel LTLHX geometries.
 - Finally, the Pareto optimal designs were verified against the values that were directly obtained from numerical simulations.
- The laboratory heat exchanger test facility and the prototype of the novel LTLHX were developed, and its performance was experimentally measured.
 - Hydraulic and thermal performance of the novel LTLHX was investigated with various parameters and operating conditions. Refrigerant-side heat transfer in the novel LTLHX was mainly dominated by the convective boiling heat transfer.
 - Heat transfer coefficient correlations and pressure drop correlations were developed for the water-side and refrigerant-side with experimental data.

- The U value of the novel LTLHX was calculated to 1,300 to 2,000 $\text{W}\cdot\text{K}^{-1}\cdot\text{m}^{-1}$, when DP/L of the water-side was between 4 and 10 kPa/m. U value of the novel heat exchanger was much greater than that of the PHX due to the balanced heat transfer performance of two-fluids. This can improve the system efficiency and reduce the system cost.
- Heat exchangers were applied to a water source heat pump system
 - Its performance was investigated with parametric studies: when temperature difference between water inlet and outlet was decreased, COP of the system improved since the decrease of compressor work was larger than the increase of water pump work in WSHP modeling
 - When the PHX and novel LTLHX were applied to the WSHP application, the heat transfer performance of the novel LTLHX was about doubled as compared to that of the PHX.
 - Design guideline of the novel heat exchanger for the LTLHP application was created by considering main design strategies. OAAO approach with PPCFD was applied to decide the geometries of the heat exchanger.

CHAPTER 7. List of Major Contributions and Future Work

7.1 List of major contributions

The contribution of this thesis is broken down into three main parts and summarized as follows:

- Investigation of the performance of the conventional PHX applied for Low Temperature Lift Heat Pump (LTLHP):
 - The PHX performance was investigated under the LTLHP conditions, which requires the unique operating conditions: a large heat source-fluid flow rate and small refrigerant flow rate
 - The characteristics of the PHX performance are addressed
 - Potentials and limitations of the PHX are addressed
 - Thermal and hydraulic PHX performance are compared between using R22 and ammonia for the application of LTLHP

- Novel low temperature lift heat exchanger design development with new geometry for the LTLHP application
 - Geometries of novel LTLHX are newly defined - a channel width, channel height, channel pitch, and plate gap
 - Concept development strategy is regulating a flow area ratio and offsetting plates in order to balance the heat transfer and pressure drop of water-side and refrigerant-side
 - The design guidelines was developed for low temperature lift heat pump system with the novel heat exchanger

- Investigation of heat transfer and pressure drop characteristics of the novel LTLHX with CFD simulation and experimental test
 - Generalized two-phase heat transfer coefficient of the minichannel with different working fluids, and channel size was proposed
 - Heat transfer coefficient correlations and pressure drop correlations of the novel LTLHX geometries were developed for single-phase and two-phase fluids.
 - The CFD simulation was experimentally verified
 - The hydraulic and thermal performance of the novel heat exchanger was investigated.

7.2 List of related publications

- Journal papers
 - Hoseong Lee, Yunho Hwang, Reinhard Radermacher, 2012, Experimental investigation of sinusoidal corrugated plate heat exchanger performance for low temperature lift heat pump, IJR, (on revision) – submitted 032612
 - Hoseong Lee, Khaled Saleh, Yunho Hwang, Reinhard Radermacher, 2012, Optimization of novel heat exchanger for the application to low temperature lift heat pump, Energy 42, 204-212.

- Invention disclosure
 - Ejector Compressor Cooling, 2009, invention disclosure
 - Rollbonded heat exchangers for low temperature lift energy conversion, 2010, invention disclosure

- Heat exchanger design optimized for low temperature lift energy conversion, 2011, invention disclosure
- Patent application (United States)
 - Heat exchanger plate, art unit= 2913; serial number = 29/399,462; Patent number= US D657,854 S, Date of Patent= 04/17/2012; US patent
 - Heat exchanger plate, art unit= 2913; serial number = 29/399,464; Patent number= US D657,855 S, Date of Patent= 04/17/2012; US patent
 - Transferring heat between fluids, 2011, art unit= 3748, serial number = 13/209,944, US patent (In progress)
 - Heat exchanger plate, art unit= 2913; serial number = 29/399,466; Patent number= US D657,856 S, Date of Patent= 04/17/2012; US patent
 - Heat exchanger plate, art unit= 2913; serial number = 29/399,468; Patent number= US D657,857 S, Date of Patent= 04/17/2012; US patent

7.3 Future work

In this dissertation, the typical PHX performance was investigated numerically and experimentally to establish the baseline. To overcome the limitations of the PHX, the novel LTLHX was proposed and developed with the approximation assisted optimization technique. Future work may be extended to encompass more details of the heat transfer mechanism of the heat exchangers for the LTLHP use. There are several recommended future works as follows:

The PHX was selected as a baseline of the low temperature lift heat exchanger. In this study, limited number of PHX configurations, which were expected to have the best

performance under the LTLHP operating condition, was evaluated under LTLHP application. If various configurations were evaluated such as chevron angle, distribution area, and ratio between length and width, the assessment of the PHX would be clearer.

The refrigerant side heat transfer coefficient of the PHX was investigated with various water-side Reynolds number. To deepen the knowledge of the PHX heat transfer, the refrigerant-side heat transfer needs to be broken down to three different heat transfer sections: subcooled liquid heat transfer, two-phase boiling heat transfer, and superheated vapor heat transfer. In order to know each heat transfer, either (1) the temperature profile of the working fluid or (2) heat transfer coefficient correlations of the subcooled liquid and superheated vapor is required. For the LTLHP application, the mass flux of the refrigerant side was extremely small, so that it was hard to implement method (2). Therefore, method (1) would be a realistic approach in the future.

In order to design the novel LTLHX, the boiling heat transfer coefficient correlation was created based on the data extracted from the literature. For the boiling heat transfer coefficient, the channel material and surface roughness are more important for the minichannel than the macro channel. Therefore, research about these aspects would clarify the boiling heat transfer mechanism of the minichannel. It is further recommended to include new findings in the correlation.

The correlations for the water-side heat transfer coefficient, and pressure drop of the novel LTLHX were created based on the fixed flow gap size. Flow gap size can be changed depending upon the design of the system or applications. If this variable can be included in the correlations, then it would be the best. Moreover, the two-phase refrigerant heat transfer coefficient and pressure drop correlation of the novel LTLHX

were obtained from the limited operating conditions. For the better correlations, a various operating conditions should be considered.

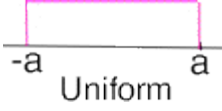


The heat exchanger performance of the low temperature lift system was investigated throughout the thesis, especially about the evaporator. One of the differences between the low temperature lift and large temperature lift systems was the mass flow rate ratio difference between heat source and working fluid. This was reflected on the novel heat exchanger concept development. This concept could be applied for both the evaporator and condenser. However, two-phase heat transfer and pressure drop characteristics of the condenser could be different with the evaporator. Therefore, the heat transfer study of the condenser is recommended.

Geometries of the novel LTLHX were determined to obtain the optimum heat transfer and pressure drop performance with OAAO with PPCFD. Then based on the results of the optimization, the novel LTLHX was fabricated. However, in real case, there was a tradeoff between the manufacturing cost and manufacturing accuracy. Therefore, it is recommended to investigate the effect of the sensitivity of design variables on the heat exchanger performance.

Appendix A. Uncertainty Analysis

Total uncertainty is the summation of systematic error and random error. Systematic error is caused by measurement itself. It is the difference between true value and the value that instrument can measure. Random error is caused by predictable fluctuation in reading. Random error can be decided based on the characteristics of the distribution as shown in Table A.1. In this thesis, the distributions were mostly normal as shown in Fig. A.1 and Fig. A.2. Therefore a standard deviation was used as a random error.

Table A.1. Random error with distributions (a = maximum value, -a = minimum value): reference: NIST Technical Note 1297 (1994)

Distribution		Random error
Uniform		$\frac{1}{\sqrt{3}}a$
Triangular		$\frac{1}{\sqrt{6}}a$
Normal		$\frac{1}{3}a$

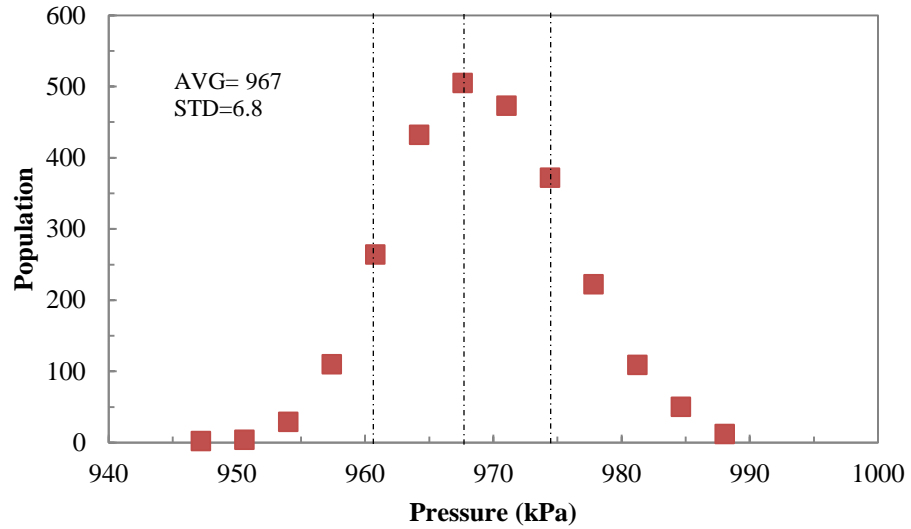


Fig. A.1: Standard deviation graph of pressure

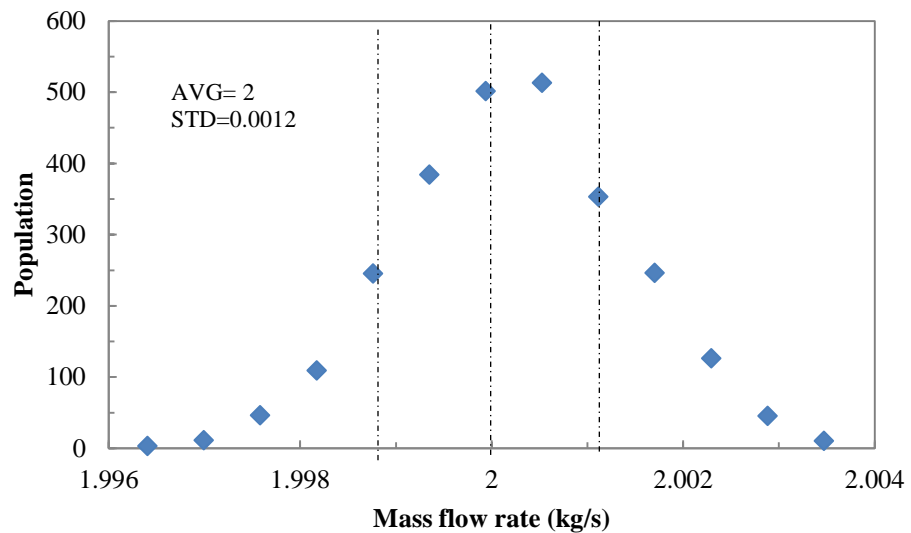


Fig. A.2: Standard deviation graph of mass flow rate

The uncertainties of directly measured parameters such as temperatures, pressures, and mass flow rates are calculated by combining the absolute error and standard deviation which can be obtained during steady state condition. The uncertainty of calculated parameters such as an enthalpies, superheat and capacities are more complex to calculate. In these cases, the uncertainty is calculated by considering possible

maximum and minimum cases. Pythagorean Summation can be used for uncertainty propagation.

The method for determining this uncertainty propagation is described in NIST Technical Note 1297 (Taylor B.N. and Kuyatt, C.E., Guidelines for Evaluating and Expressing the Uncertainty of NIST Measurement Results, National Institute of Standards and Technology Technical Note 1297, 1994). Assuming the individual measurements are uncorrelated and random, the uncertainty in the calculated quantity can be determined as:

$$w_Y = \sqrt{\sum_i \left(\frac{\partial Y}{\partial x_i}\right)^2 w_{x_i}^2} \quad (\text{A.1})$$

<Uncertainty calculation for the PHX>

The uncertainty of RTD sensor was calculated with the summation of systematic error and random error. For the RTD sensor used in the test, systematic error, ω_{sys} was 0.03 K, random error, ω_{ran} was 0.11 K. Therefore the uncertainty of the RTD was 0.14 K.

$$\omega_T = \omega_{\text{sys}} + \omega_{\text{ran}} \quad (\text{A.2})$$

When the uncertainty of *LMTD*, ω_{LMTD} is 0.187 K (0.8%), and the uncertainty of the heat transfer capacity, ω_Q is 0.07 kW (6.1%), the uncertainty of the overall heat transfer coefficient ω_U is calculated to 40 W·m⁻²·K⁻¹ (6.2%).

$$\omega_U = \sqrt{\left(\frac{\delta U}{\delta \text{LMTD}} \omega_{\text{LMTD}}\right)^2 + \left(\frac{\delta U}{\delta Q} \omega_Q\right)^2} \quad (\text{A.3})$$

Appendix B. Reproducibility experiments

Three tests were conducted under the same operating conditions, in order to investigate the reproducibility of the experiments. Fig. B.1 through Fig. B. 4 show the reproducibility results of important parameters. All parameters were agreed with each other within 3% range.

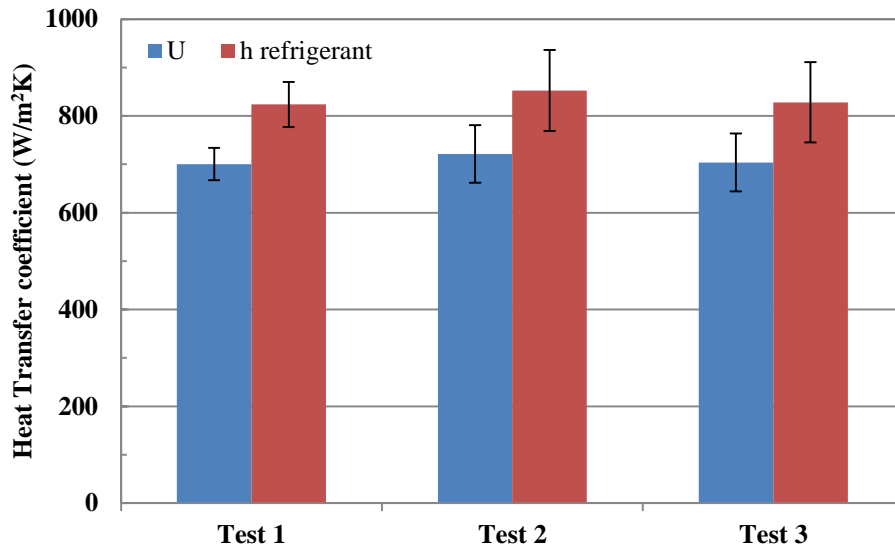


Fig. B.1: Reproducibility of refrigerant-side heat transfer coefficient

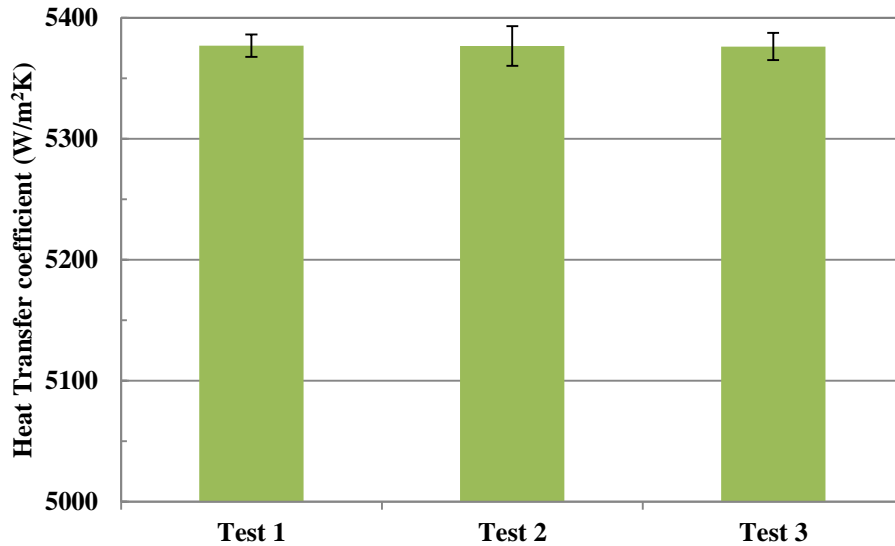


Fig. B.2: Reproducibility of water-side heat transfer coefficient

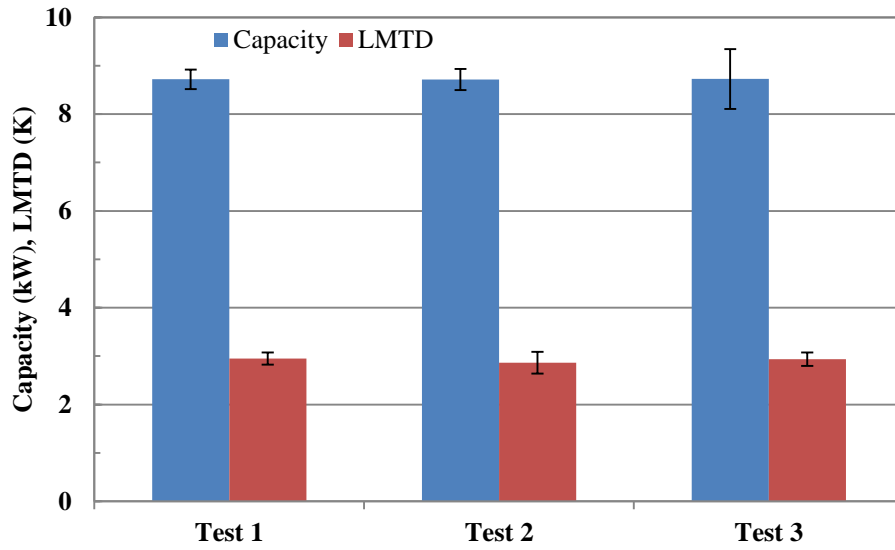


Fig. B.3: Reproducibility of capacity and LMTD

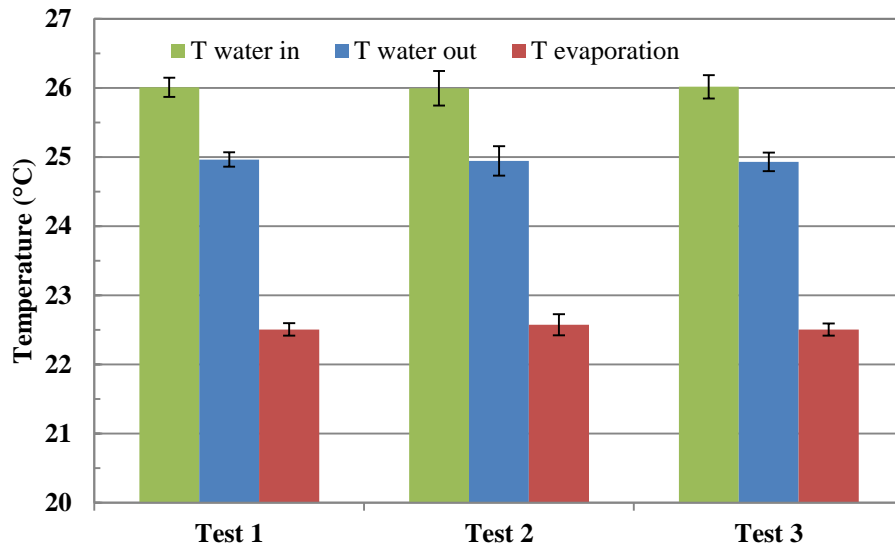


Fig. B.4: Reproducibility of temperatures

Reference

- [1] Abdelaziz, O. (2009). Development of Multi-scale, Multi-physics, Analysis Capability and its Application to Novel Heat Exchanger Design and Optimization. University of Maryland college park.
- [2] ANSYS Inc. ANSYS FLUENT 12.0 Documentation; 2009.
- [3] Arima H., Kim J.H., Okamoto A., Ikegami Y. (2010) Local boiling heat transfer characteristics of ammonia in a vertical plate evaporator. *International Journal of Refrigeration*, 33(2010), 359-370.
- [4] Aute, V. (2008) Single and Multi-response Adaptive Design of Experiments with Application to Design Optimization of Novel Heat Exchangers, Working Dissertation, University of Maryland, College Park, MD, June 20th 2008.
- [5] Ayub, Z. (2003). Plate Heat Exchanger Literature Survey and New Heat Transfer and Pressure Drop Correlations for Refrigerant Evaporators. *Heat Transfer Engineering*, 24(5), 3-16.
- [6] Baek N, Shin U, Yoon J. A study on the design and analysis of a heat pump heating system using wastewater as a heat source. *Solar Energy* 2005; 78(3):427-40.
- [7] Bao Z.Y., Fletcher D.F., Haynes B.S., (2000) Flow boiling heat transfer of Freon R11 and HCFC123 in narrow passages. *International Journal of Heat and Mass Transfer*, 43(2000), 3347-3358.
- [8] Bertsch, S., Groll, E., & Garimella, S. (2008). Refrigerant flow boiling heat transfer in parallel microchannels as a function of local vapor quality. *International Journal of Heat and Mass Transfer*, 51(19-20).
- [9] Buonopane, R.A., Troupe, R.A., Morgan, J.C., 1963. Heat transfer design methods for plate heat exchangers. *Chem. Eng. Prog.* 59(7), 57-61.
- [10] Büyükalaca O, Ekinçi F, Yılmaz T. Experimental investigation of Seyhan River and dam lake as heat source–sink for a heat pump. *Energy* 2003; 28:157-69.
- [11] Chisholm, D. (1967). A theoretical basis for the Lockhart-Martinelli correlation for two-phase flow. *International Journal of Heat and Mass Transfer*, 10, 1767-1778.
- [12] Chisholm, D., and Wanniarachchi, A. S., (1992) Maldistribution in Single-Pass Mixed-Channel Plate Heat Exchangers, *Compact Heat Exchangers for Power and Process Industries*, HTD-vol. 201, ASME, New York, pp. 95–99.
- [13] Cho Y, Yun R. A raw water source heat pump air-conditioning system. *Energy and Buildings* 2011; 43(11):3068-73.

- [14] Choi, K., Pamitran, a, Oh, C., & Oh, J. (2007). Boiling heat transfer of R-22, R-134a, and CO₂ in horizontal smooth minichannels. *International Journal of Refrigeration*, 30(8), 1336-1346.
- [15] Choi, K., Pamitran, a, Oh, C., & Oh, J. (2008). Two-phase pressure drop of R-410A in horizontal smooth minichannels. *International Journal of Refrigeration*, 31(1), 119-129.
- [16] Claesson, 2004. Thermal and hydraulic performance of compact brazed plate heat exchangers operating as evaporators in domestic heat pumps. Ph. D. Thesis. KTH Energy technology.
- [17] Cooper MG. Heat flow rates in saturated nucleate pool boiling e a wide-ranging examination using reduced properties. *Advances in Heat Transfer* 1984; 16: 157-239.
- [18] Crozier, R. D., Booth, J. R., Stewart, J. E., 1964. Heat transfer in plate and frame heat exchangers. *Chem. Eng. Prog.* 60(8), 43-45.
- [19] Croce G, D'Agaro P. Numerical analysis of forced convection in plate and frame heat exchangers. *International Journal of Numerical Methods for Heat and Fluid Flow* 2002; 12(6):756–71.
- [20] Cui, W., Li, L., Xin, M., Jen, T., Chen, Q., & Liao, Q. (2006). A heat transfer correlation of flow boiling in micro-finned helically coiled tube. *International Journal of Heat and Mass Transfer*, 49(17-18), 2851-2858.
- [21] Deb K. *Multi-objective optimization using evolutionary algorithms*. New York: John Wiley and Sons press; 2001.
- [22] Djordjevic E, Kabelac S. Flow boiling of R134a and ammonia in a plate heat exchanger. *International Journal of Heat and Mass Transfer* 2008;51:6235-42.
- [23] Dupont, V. (2004). Heat transfer model for evaporation in microchannels. Part II: comparison with the database. *International Journal of Heat and Mass Transfer*, 47(14-16), 3387-3401.
- [24] Dutto, T., Blaise, J. C., and Benedic, T., Mise (1991) Performance of Brazed Plate Heat Exchanger Set in Heat Pump, *Proc. 18th Int. Congr. Refrigeration*, Montreal, Quebec, Canada, vol. III, pp. 1284–1288, August 10–17.
- [25] Fonseca DJ, Navarrese DO, Moynihan GP Simulation metamodeling through artificial neural networks. *Engineering applications of artificial intelligence* 2003; 16:177-183.

- [26] Friedel, L., 1979. Improved friction pressure drop correlations for horizontal and vertical two-phase pipe flow. European Two-Phase Flow Group Meeting, paper E2. Ispra, Italy.
- [27] Fernandez-Seara, J., Uhia, F., Sieres, J., Campo, A., 2007. A general review of the Wilson plot method and its modifications to determine convection coefficients in heat exchange devices. *Appl. Therm. Eng.* 27, 2745-2757.
- [28] Freund, S., & Kabelac, S. (2010). Investigation of local heat transfer coefficients in plate heat exchangers with temperature oscillation IR thermographs and CFD. *International Journal of Heat and Mass Transfer*, 53(19-20), 3764-3781. Elsevier Ltd.
- [29] Galeazzo, F., Miura, R., Gut, J., & Tadini, C. (2006). Experimental and numerical heat transfer in a plate heat exchanger. *Chemical Engineering Science*, 61(21), 7133-7138.
- [30] Gungor, K. E., & Winterton, R. H. S. (1986). A general correlation for flow boiling in tubes and annuli. *International Journal of Heat and Mass Transfer*, 29(3), 351-358.
- [31] Han, D.H., Lee, K.J., Kim, Y.H., 2003. Experiments on characteristics of evaporation of R410a in brazed plate heat exchangers with different geometric configurations. *Appl. Therm. Eng.* 23, 1209-1225.
- [32] Han W, Saleh K, Aute V, Ding G, Hwang Y, Radermacher R. Numerical simulation and optimization of single-phase turbulent flow in chevron-type plate heat exchanger with sinusoidal corrugations, *HVAC&R Research* 2011;17:186–97.
- [33] Hayes, N., Jokar, A., 2009. Dynalene/Water correlations to be used for condensation of CO₂ in brazed plate heat exchangers. ASHRAE research project RP-1394.
- [34] Heavner, R.L., Kumar, H., Wanniarachchi, A.S., 1993. Performance of an industrial heat exchanger: Effect of chevron angle. *AIChE Symposium Series New York*. 89(295), 262-267.
- [35] Hesselgreaves, J.E., 2001. Compact heat exchangers: selection, design and operation. Oxford, Pergamon Press.
- [36] Holman, J.P., 2001. Experimental methods for engineers. McGraw-Hill companies.
- [37] Hsieh, Y.Y., Lin, T.F., 2002. Saturated flow boiling heat transfer and pressure drop of refrigerant R410a in a vertical plate heat exchanger. *Int. J. of Heat and Mass Transfer*. 45, 1033-1044.

- [38] Jackson, B.W., Troupe, R.A., 1964. Laminar flow in a plate heat exchanger. Chem. Eng. Prog. 60(7), 65–67.
- [39] Jain, S., Joshi, A., & Bansal, P. K. (2007). A New Approach to Numerical Simulation of Small Sized Plate Heat Exchangers With Chevron Plates. Journal of Heat Transfer, 129(3), 291.
- [40] Jung, D. S., McLinden, M., Radermacher, R., & Didon, D. (1989). A study of flow boiling heat transfer with refrigerant mixtures. International Journal of Heat and Mass Transfer, 32(9), 1751-1764.
- [41] Jung, D. S., McLinden, M., Radermacher, R., & Didon, D. (1998). Horizontal flow boiling heat transfer experiments with a mixture of R22/R114. International Journal of Heat and Mass Transfer, 32(1), 131-145.
- [42] Jung, D. S., & Radermacher, R. (1991). Prediction of heat transfer coefficient of various refrigerants during evaporation. ASHRAE Transactions, 97.
- [43] Kandlikar, S. (2002). Fundamental issues related to flow boiling in minichannels and microchannels. Experimental Thermal and Fluid Science, 26(2-4), 389-407.
- [44] Kandlikar, S. G. (1990). A general correlation for saturated two-phase flow boiling heat transfer inside horizontal and vertical tubes. Journal of Heat Transfer, 112, 219-228.
- [45] Kandlikar, Satish, & Balasubramanian, P. (2004). An Extension of the Flow Boiling Correlation to Transition, Laminar, and Deep Laminar Flows in Minichannels and Microchannels. Heat Transfer Engineering, 25(3), 86-93.
- [46] Kew, P. A., & Cornwell, K. (1997). CORRELATIONS FOR THE PREDICTION HEAT TRANSFER IN SMALL-DIAMETER OF BOILING. Applied Thermal Engineering, 17, 705-715.
- [47] Kho T, Muller-Steinhagen H. An experimental and numerical investigation of heat transfer fouling and fluid flow in flat plate heat exchangers. Chemical Engineering Research and Design 1999; 77:124-30.
- [48] Kim Y.S., 1999. An experimental study on evaporation heat transfer characteristics and pressure drop in plate heat exchanger, M.S. thesis, Yonsei University.
- [49] Kumar, V., Saini, S., Sharma, M., & Nigam, K. (2006). Pressure drop and heat transfer study in tube-in-tube helical heat exchanger. Chemical Engineering Science, 61(13), 4403-4416.

- [50] Kutateladze, S. S. (1961). Boiling heat transfer. *International Journal of Heat and Mass Transfer*, 4, 31-45.
- [51] Lazarek, G. M., & Black, S. H. (1982). Evaporative heat transfer, pressure drop and critical heat flux in a small vertical tube with R-113. *International Journal of Heat and Mass Transfer*, 25(7), 945-960.
- [52] Lee, H. J., & Lee, S. Y. (2001). Heat transfer correlation for boiling flows in small rectangular horizontal channels with low aspect ratios. *International Journal of Multiphase Flow*, 27, 2043-2062.
- [53] Lee, K. (2001). Optimal shape and arrangement of staggered pins in the channel of a plate heat exchanger. *International Journal of Heat and Mass Transfer*, 44(17), 3223-3231.
- [54] Lee, P., & Garimella, S. (2008). Saturated flow boiling heat transfer and pressure drop in silicon microchannel arrays. *International Journal of Heat and Mass Transfer*, 51(3-4), 789-806.
- [55] Li G. Online and Offline Approximations for Population Based Multi-Objective Optimization, Ph. D. Dissertation, University of Maryland, College Park, MD, 2007.
- [56] Li, M., Li, G., & Azarm, S. (2008). A Kriging Metamodel Assisted Multi-Objective Genetic Algorithm for Design Optimization. *Journal of Mechanical Design*, 130(3), 031401.
- [57] Lie, Y., Su, F., Lai, R., & Lin, T. (2006). Experimental study of evaporation heat transfer characteristics of refrigerants R-134a and R-407C in horizontal small tubes. *International Journal of Heat and Mass Transfer*, 49(1-2), 207-218.
- [58] Liu, Z., & Winterton, R. H. S. (1991). A general correlation for saturated and subcooled flow boiling in tubes and annuli, based on a nucleate pool boiling equation. *International Journal of Heat and Mass Transfer*, 34(11), 2759-2766.
- [59] Longo G. Experimental heat transfer coefficients during refrigerant vaporization and condensation inside herringbone-type plate heat exchangers with enhanced surfaces. *International Journal of Heat and Mass Transfer* 2004;47:4125-36.
- [60] Longo G.A, Gasparella A. (2007). HFC-410A vaporization inside a commercial brazed plate heat exchanger, *Experimental Thermal and Fluid Science*, Volume 32, Issue 1, October 2007, Pages 107-116
- [61] Longo, G.A., 2008. Refrigerant R 134a vaporization heat transfer and pressure drop inside a small brazed plate heat exchanger. *Int. J. of Refrigerant*. 30-5, 821-830.

- [62] Longo, G.A., 2009. R410A condensation inside a commercial brazed plate heat exchanger. *Exp. Therm. and Fluid Sci.* 284-291.
- [63] Longo, G.A., 2010. Heat transfer and pressure drop during HFC refrigerant saturated vapour condensation inside a brazed plate heat exchanger. *Int. J. of Heat and Mass Transfer.* 53, 1079-1087.
- [64] Marriott, J., 1971. Where and how to use plate heat exchangers. *Chem. Eng.* 78, 127-134.
- [65] Martin, H., 1996. A theoretical approach to predict the performance of chevron-type plate heat exchangers. *Chem. Eng. Prog.* 35, 301-310.
- [66] Mehendal S.S, Jacobi A.M., Shah R. K., Fluid flow and heat transfer at micro- and meso-scales with application to heat exchanger design, *Appl. Mech. Rev.* 53 (2000) 175–193.
- [67] Mendrinou D, Karytsas C. Use of geothermal energy and seawater for heating and cooling of the new terminal building in the airport of Thessaloniki. *Geo-Heat Center Quarterly Bulletin* 2003; 24(3):16-22.
- [68] Muley, a, & Manglik, R. M. (1999). Experimental Study of Turbulent Flow Heat Transfer and Pressure Drop in a Plate Heat Exchanger With Chevron Plates. *Journal of Heat Transfer*, 121(1), 110.
- [69] Muller-Steinhagen, H., Heck, K., (1986). A simple friction pressure drop correlation for
- [70] two-phase flow pipes. *Chemical Engineering Progress* 20, 297–308.
- [71] Okamoto S. A heat pump system with a latent heat storage utilizing seawater installed in an aquarium. *Energy and Buildings* 2006; 38:121-8.
- [72] Ozden, E., & Tari, I. (2010). Shell side CFD analysis of a small shell-and-tube heat exchanger. *Energy Conversion and Management*, 51(5), 1004-1014. Elsevier Ltd.
- [73] Palm B., Claesson J. (2006). Plate heat exchangers: calculation methods for single and two-phase flow, *heat transfer engineering*, 27(4):88-98
- [74] Pamitran, a, Choi, K., Oh, J., & Oh, H. (2007). Forced convective boiling heat transfer of R-410A in horizontal minichannels. *International Journal of Refrigeration*, 30(1), 155-165.
- [75] Park, C., & Hrnjak, P. (2007). CO₂ and R410A flow boiling heat transfer, pressure drop, and flow pattern at low temperatures in a horizontal smooth tube. *International Journal of Refrigeration*, 30(1), 166-178.

- [76] Park, K., & Moon, S. (2005). Optimal design of heat exchangers using the progressive quadratic response surface model. *International Journal of Heat and Mass Transfer*, 48(11), 2126-2139.
- [77] Park, K., Oh, P., & Lim, H. (2006). The application of the CFD and Kriging method to an optimization of heat sink. *International Journal of Heat and Mass Transfer*, 49(19-20), 3439-3447.
- [78] Primal F., Lundqvist P. (2004). Refrigeration systems with minimized refrigerant charge: system design and performance. *Proc. IMechE Vol. 219 Part E: J. Process Mechanical Engineering*, 127-137
- [79] Qu, W., & Mudawa, I. (2003). Flow boiling heat transfer in two-phase micro-channel heat sinks—II. Annular two-phase flow model. *International Journal of Heat and Mass Transfer*, 46(15), 2773-2784.
- [80] Qu, W., & Mudawa, I. (2003). Flow boiling heat transfer in two-phase micro-channel heat sinks—I. Experimental investigation and assessment of correlation methods. *International Journal of Heat and Mass Transfer*, 46(15), 2755-2771.
- [81] Ribatski, G, Wojtan, L., & Thome, J. (2006). An analysis of experimental data and prediction methods for two-phase frictional pressure drop and flow boiling heat transfer in micro-scale channels. *Experimental Thermal and Fluid Science*, 31(1), 1-19.
- [82] Savostin, A.F., Tikhonov, A.M., 1970. Investigation of the characteristics of plate type heating surfaces. *Therm. Eng.* 17, 113–117.
- [83] Saleh K, Aute V, Azarm S, Radermacher R. Online approximation assisted multiobjective optimization with space filling, variance and Pareto measures, AIAA ISSMO/MDO Conference, Fort Worth, TX, USA, AIAA-2010-9103.
- [84] Saleh K, Radermacher R, Aute V, Azarm S. Online approximation assisted optimization of a novel air-cooled heat Exchanger, 10th IEA Heat Pump Conference 2011, Tokyo, Japan, p.00272.
- [85] Saisorn, S., Kaew-On, J., & Wongwises, S. (2010). Flow pattern and heat transfer characteristics of R-134a refrigerant during flow boiling in a horizontal circular mini-channel. *International Journal of Heat and Mass Transfer*, 53(19-20), 4023-4038. Elsevier Ltd.
- [86] Saitoh, S., Daiguji, H., & Hihara, E. (2005). Effect of tube diameter on boiling heat transfer of R-134a in horizontal small-diameter tubes. *International Journal of Heat and Mass Transfer*, 48(23-24), 4973-4984.

- [87] Saitoh, S., Daiguji, H., & Hihara, E. (2007). Correlation for boiling heat transfer of R-134a in horizontal tubes including effect of tube diameter. *International Journal of Heat and Mass Transfer*, 50(25-26), 5215-5225.
- [88] Schmid F. Sewage water : Interesting heat source for heat pumps and chillers, 9th International IEA Heat Pump Conference, Zürich, Switzerland, 2008.
- [89] Shah, M.M. (1982). Chart correlation for saturated boiling heat transfer: equations and further study. *ASHRAE Transactions*, 88(1), 185-196.
- [90] Shah, Mirza M. (1976). A new correlation for heat transfer during boiling flow through pipes. *ASHRAE Transactions*, 81, 66-86. ASHRAE.
- [91] Shewry MC, Wynn HP. Maximum entropy sampling. *Journal of Applied Statistics* 1987;14: 165-170.
- [92] Shiferaw, D., Huo, X., Karayiannis, T., & Kenning, D. (2007). Examination of heat transfer correlations and a model for flow boiling of R134a in small diameter tubes. *International Journal of Heat and Mass Transfer*, 50(25-26), 5177-5193.
- [93] Simpson TW, Poplinski JD, Koch PN, Allen JK. Metamodels for Computer-based Engineering Design: Survey and recommendations. *Engineering with Computers* 2001; 17(2):129-50.
- [94] Song Y, Akashi Y, Yee J. Effects of utilizing seawater as a cooling source system in a commercial complex. *Energy and Buildings* 2007; 39:1080-7.
- [95] Stephan, K., & Abdelsalam, M. (1978). Heat transfer correlations for natural convection boiling, 23, 73-87.
- [96] Sun, L, & Mishima, K. (2009). Evaluation analysis of prediction methods for two-phase flow pressure drop in mini-channels. *International Journal of Multiphase Flow*, 35(1), 47-54. Elsevier Ltd.
- [97] Sun, Licheng, & Mishima, Kaichiro. (2009). An evaluation of prediction methods for saturated flow boiling heat transfer in mini-channels. *International Journal of Heat and Mass Transfer*, 52(23-24), 5323-5329. Elsevier Ltd.
- [98] Sundén, B. (2007). Computational Fluid Dynamics in Research and Design of Heat Exchangers. *Heat Transfer Engineering*, 28(11), 898-910.
- [99] The MathWorks Inc. MATLAB® The Language of Technical Computing, User Manual; 2007.
- [100] Thome, J. (2004). Boiling in microchannels: a review of experiment and theory. *International Journal of Heat and Fluid Flow*, 25(2), 128-139.

- [101] Thome, J. (2004). Heat transfer model for evaporation in microchannels. Part I: presentation of the model. *International Journal of Heat and Mass Transfer*, 47(14-16), 3375-3385.
- [102] Thonon, B., 1995. Design method for plate evaporators and condensers. 1st Int. Conf. on Process Intensification for the Chem. Industry, BHR Group Conference Series Publication, 18, 37–47.
- [103] Thonon B., Vidil R., Marvillet C., 1995. Recent research and developments in plate heat exchangers. *J. of Enhanced Heat Transfer*. 2, 149-155.
- [104] Tibiriçá C. B., & Ribatski, Gherhardt. (2010). Flow boiling heat transfer of R134a and R245fa in a 2.3mm tube. *International Journal of Heat and Mass Transfer*, 53(11-12), 2459-2468. Elsevier Ltd.
- [105] Tran, T. N., Wambsganss, M. W., & France, D. M. (1996). small circular and rectangular channel boiling with two refrigerants. *International Journal of Multiphase Flow*, 22(3), 485-498.
- [106] Wanniarachchi, A. S., Ratnam, U., Tilton, B. E., Dutta-Roy, K., (1995) Approximate Correlations for Chevron-Type Plate Heat Exchangers, 30th National Heat Transfer Conference, Vol. 12, HTD vol. 314, ASME, New York, pp. 145–151.
- [107] Wang, C. (1997). Two-phase heat transfer characteristics for R-22/R-407C in a 6.5-mm smooth tube. *International Journal of Heat and Fluid Flow*, 18(6), 550-558.
- [108] Wang K, Cao F, Xing Z. Experimental investigation on the performance of a high temperature water source heat pump. 9th International IEA Heat Pump Conference, Zürich, Switzerland, 2008.
- [109] Wang, L., Sunden, B., Manglik, R.M., 2007. Plate heat exchangers: design, applications and performance. USA: WIT press.
- [110] Yan, Y., & Lin, T.-F. (1998). Evaporation heat transfer and pressure drop of refrigerant R-134a in a small pipe. *International Journal of Heat and Mass Transfer*, 41(24), 4183-4194.
- [111] Yu, W., France, D. M., Wambsganss, M. W., & Hull, J. R. (2002). Two-phase pressure drop, boiling heat transfer, and critical heat flux to water in a small-diameter horizontal tube. *International Journal of Multiphase Flow*, 28(6), 927-941.
- [112] Yun R., 2002. Convective boiling of carbon dioxide in mini tubes and micro channels. Ph.D. thesis, Korea University.

- [113] Yun, R., Hyeok Heo, J., & Kim, Y. (2006). Evaporative heat transfer and pressure drop of R410A in microchannels. *International Journal of Refrigeration*, 29(1), 92-100.
- [114] Zhang, J.-F., He, Y.-L., & Tao, W.-Q. (2009). 3D numerical simulation on shell-and-tube heat exchangers with middle-overlapped helical baffles and continuous baffles – Part I: Numerical model and results of whole heat exchanger with middle-overlapped helical baffles. *International Journal of Heat and Mass Transfer*, 52(23-24), 5371-5380. Elsevier Ltd.
- [115] Zhang, W., Hibiki, T., & Mishima, K. (2004). Correlation for flow boiling heat transfer in mini-channels. *International Journal of Heat and Mass Transfer*, 47(26), 5749-5763.